

Max-Planck-Institut für Physik komplexer Systeme

Biaxial Nematic Order in Liver Tissue

D I S S E R T A T I O N

zur Erlangung des akademischen Grades

Doctor rerum naturalium

(Dr. rer. nat.)

vorgelegt

dem Bereich Mathematik und Naturwissenschaften
der Technischen Universität Dresden

von

Dipl.-Phys. André Scholich

geboren am 17. Dezember 1986 in Crivitz



**TECHNISCHE
UNIVERSITÄT
DRESDEN**



Dresden, 2018

Betreuender Hochschullehrer: Prof. Dr. Frank Jülicher

Eingereicht am 5. Februar 2018

Gutachter:

- Prof. Dr. Frank Jülicher
- Prof. Dr. Stephan Grill
- Prof. Dr. Samuel Safran

Prüfungskommission:

- Prof. Dr. Clemens Laubschat (Vorsitz)
- Prof. Dr. Frank Jülicher
- Prof. Dr. Stefan Grill
- Dr. Benjamin Friedrich

Verteidigt am 30. Mai 2018 in Dresden

Abstract

Understanding how biological cells organize to form complex functional tissues is a question of key interest at the interface between biology and physics. The liver is a model system for a complex three-dimensional epithelial tissue, which performs many vital functions. Recent advances in imaging methods provide access to experimental data at the subcellular level. Structural details of individual cells in bulk tissues can be resolved, which prompts for new analysis methods. In this thesis, we use concepts from soft matter physics to elucidate and quantify structural properties of mouse liver tissue.

Epithelial cells are structurally anisotropic and possess a distinct apico-basal *cell polarity* that can be characterized, in most cases, by a vector. For the parenchymal cells of the liver (hepatocytes), however, this is not possible. We therefore develop a general method to characterize the distribution of membrane-bound proteins in cells using a multipole decomposition. We first verify that simple epithelial cells of the kidney are of vectorial cell polarity type and then show that hepatocytes are of second order (nematic) cell polarity type. We propose a method to quantify orientational order in curved geometries and reveal lobule-level patterns of aligned cell polarity axes in the liver. These lobule-level patterns follow, on average, streamlines defined by the locations of larger vessels running through the tissue. We show that this characterizes the liver as a nematic liquid crystal with biaxial order. We use the quantification of orientational order to investigate the effect of specific knock-down of the adhesion protein Integrin- $\beta 1$.

Building upon these observations, we study a model of nematic interactions. We find that interactions among neighboring cells alone cannot account for the observed ordering patterns. Instead, coupling to an external field yields cell polarity fields that closely resemble the experimental data. Furthermore, we analyze the structural properties of the two transport networks present in the liver (sinusoids and bile canaliculi) and identify a nematic alignment between the anisotropy of the sinusoid network and the nematic cell polarity of hepatocytes. We propose a minimal lattice-based model that captures essential characteristics of network organization in the liver by local rules. In conclusion, using data analysis and minimal theoretical models, we found that the liver constitutes an example of a living biaxial liquid crystal.

Contents

1. Introduction	1
1.1. From molecules to cells, tissues and organisms: multi-scale hierarchical organization in animals	1
1.2. The liver as a model system of complex three-dimensional tissue . .	2
1.3. Biology of tissues	5
1.4. Physics of tissues	9
1.4.1. Continuum descriptions	11
1.4.2. Discrete models	11
1.4.3. Two-dimensional case study: planar cell polarity in the fly wing	15
1.4.4. Challenges of three-dimensional models for liver tissue	16
1.5. Liquids, crystals and liquid crystals	16
1.5.1. The uniaxial nematic order parameter	19
1.5.2. The biaxial nematic ordering tensor	21
1.5.3. Continuum theory of nematic order	23
1.5.4. Smectic order	25
1.6. Three-dimensional imaging of liver tissue	26
1.7. Overview of the thesis	28
2. Characterizing cellular anisotropy	31
2.1. Classifying protein distributions on cell surfaces	31
2.1.1. Mode expansion to characterize distributions on the unit sphere	31
2.1.2. Vectorial and nematic classes of surface distributions	33
2.1.3. Cell polarity on non-spherical surfaces	34
2.2. Cell polarity in kidney and liver tissues	36
2.2.1. Kidney cells exhibit vectorial polarity	36
2.2.2. Hepatocytes exhibit nematic polarity	37
2.3. Local network anisotropy	40
2.4. Summary	41

3. Order parameters for tissue organization	43
3.1. Orientational order: quantifying biaxial phases	43
3.1.1. Biaxial nematic order parameters	45
3.1.2. Co-orientational order parameters	51
3.1.3. Invariants of moment tensors	52
3.1.4. Relation between these three schemes	53
3.1.5. Example: nematic coupling to an external field	55
3.2. A tissue-level reference field	59
3.3. Orientational order in inhomogeneous systems	62
3.4. Positional order: identifying signatures of smectic and columnar order	64
3.5. Summary	67
4. The liver lobule exhibits biaxial liquid-crystal order	69
4.1. Coarse-graining reveals nematic cell polarity patterns on the lobule-level	69
4.2. Coarse-grained patterns match tissue-level reference field	73
4.3. Apical and basal nematic cell polarity are anti-correlated	74
4.4. Co-orientational order: nematic cell polarity is aligned with network anisotropy	76
4.5. RNAi knock-down perturbs orientational order in liver tissue	78
4.6. Signatures of smectic order in liver tissue	81
4.7. Summary	86
5. Effective models for cell and network polarity coordination	89
5.1. Discretization of a uniaxial nematic free energy	89
5.2. Discretization of a biaxial nematic free energy	91
5.3. Application to cell polarity organization in liver tissue	92
5.3.1. Spatial profile of orientational order in liver tissue	93
5.3.2. Orientational order from neighbor-interactions and boundary conditions	94
5.3.3. Orientational order from coupling to an external field	99
5.4. Biaxial interaction model	101
5.5. Summary	105

6. Network self-organization in a liver-inspired lattice model	107
6.1. Cubic lattice geometry motivated by liver tissue	107
6.2. Effective energy for local network segment interactions	110
6.3. Characterizing network structures in the cubic lattice geometry . . .	113
6.4. Local interaction rules generate macroscopic network structures . .	115
6.5. Effect of mutual repulsion between unlike segment types on network structure	118
6.6. Summary	121
7. Discussion and Outlook	123
A. Appendix	127
A.1. Mean field theory fo the isotropic-uniaxial nematic transition	127
A.2. Distortions of the Mollweide projection	129
A.3. Shape parameters for basal membrane around hepatocytes	130
A.4. Randomized control for network segment anisotropies	130
A.5. The dihedral symmetry group D_{2h}	131
A.6. Relation between orientational order parameters and elements of the super-tensor	134
A.7. Formal separation of molecular asymmetry and orientation	134
A.8. Order parameters under action of axes permutation	137
A.9. Minimal integrity basis for symmetric traceless tensors	139
A.10. Discretization of distortion free energy on cubic lattice	141
A.11. Metropolis Algorithm for uniaxial cell polarity coordination	142
A.12. States in the zero-noise limit of the nearest-neighbor interaction model	143
A.13. Metropolis Algorithm for network self-organization	144
A.14. Structural quantifications for varying values of mutual network seg- ment repulsion	146
A.15. Structural quantifications for varying values of self-attraction of network segments	148
A.16. Structural quantifications for varying values of cell demand	150
Bibliography	152
Acknowledgements	175

1. Introduction

The study of biaxial liquid crystal order in liver tissue, as presented in this thesis, is an interdisciplinary endeavor at the interface between biology and physics and contributes to the broader topic of how cells organize into complex functional tissues. Over the past decades, the study of physical principles in biology has been developed into a research field of its own. The capability of living matter to self-organize and replicate makes it an especially appealing research topic. The present introduction provides an overview over the key concepts of biology and physics of tissues that the main part of the thesis is founded on.

1.1. From molecules to cells, tissues and organisms: multi-scale hierarchical organization in animals

The structural organization of animals spans multiple scales ranging from molecules on the nano-meter scale to whole organisms on the order of meters (cf. Fig. 1.1). Over these scales, the cell takes a prominent role, as it forms the basic building block of all living organisms [1].

A cell's interior, the cytoplasm, consists of biomolecules such as proteins, lipids and nucleic acids. These molecular constituents organize into sub-cellular structures. In eukaryotic¹ cells, important examples of sub-cellular structures are the nucleus, mitochondria, vesicles, the cytoskeleton and the cell membrane. Each of these organelles provide a specific function to the cell. The cell membrane, for example, forms the interface between the cytoplasm and the cell's environment. It consists of a lipid bilayer and membrane-bound proteins that regulate exchange of chemicals and mediate mechanical interactions with the cell's environment [1, 2]. This chemical and mechanical interaction is important for the formation of tissues.

A tissue is a higher-level structure consisting of multiple cells with identical or complementary function. The proper function of a tissue requires cells to be connected or associated in a specific way and is an important step in the formation of complex, multi-cellular organisms [3]. There are four basic types of animal tissue: connective, muscle, nervous and epithelial tissue [4]. The connection between cells

¹Cells of eukaryotic organisms are distinguished from prokaryotic ones, in that they possess organelles enclosed within membranes, especially a nucleus.

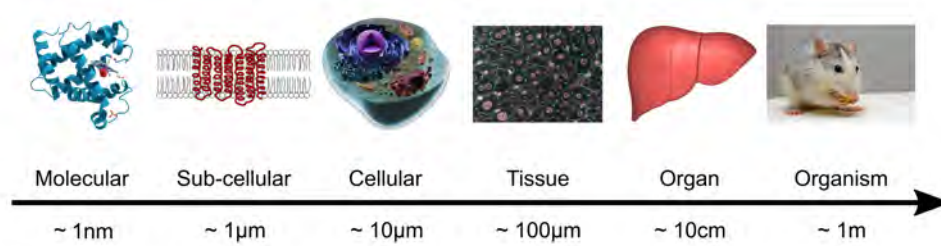


Figure 1.1. From molecules to organisms: the multi-scale hierarchical organization of animals. Macromolecules, such as proteins, DNA and lipids are the basic constituents of a biological cell. They are organized into sub-cellular structures, such as the cell membrane, vesicles, filaments and organelles. The cell is the basic organizational unit of life and capable of self-replication. Many identical cells, or similar cells working towards a common goal, are organized into a tissue. Organs are a collection of tissues that form a structural unit and perform certain functions within an organism.

Image credits (from left to right): Myoglobin protein structure (Wikimedia Commons, public domain), Schematic of FSHR protein in plasma membrane (Wikimedia Commons, public domain), 3D rendering of an animal cell cut in half (Zaldua I., Equisoain J.J., Zabalza A., Gonzalez E.M., Marzo A., Public University of Navarre, CC-BY-SA 4.0), Fluorescence-microscopy image of liver tissue (Zerial Group, MPI-CBG), Rendering of liver lobes (Wikipedia, User:Was_a_bee, CC-BY-SA 2.1 JP), a mouse (pixabay.com, public domain).

is characteristic for each tissue type. In connective tissues, for example, cells are only loosely associated with each other and separated by an extracellular matrix. In stark contrast, the connection between cells in epithelial tissues is very tight and cells are arranged in one or more layers, or sheets. When several tissues come together, they may form a structure of higher-level organization: an organ.

Organs are composed of two tissue types: a main tissue (*parenchyma*) and sporadic tissues (*stroma*) [3]. The main tissue is unique to a specific organ, such as hepatocytes in the liver, while the stroma includes nerves, blood vessels and connective tissues [3]. The collection of all organs and tissues finally make up a whole organism (cf. Fig. 1.1).

1.2. The liver as a model system of complex three-dimensional tissue

The biological model system of this thesis, the liver, is a vital organ and found in all vertebrates [5]. It is the largest internal organ and located in the center of the body, right behind the rib cage and performs a wide variety of vital functions. In the body, it is the central storage for glucose and vitamins and neutralizes many potentially harmful substances from the blood [3, 6, 7]. Furthermore, it generates

many different hormones, enzymes and blood clotting factors, as well as immune molecules [3, 8–11]. All these important functions demand a proper working of the liver at all times, which possesses astonishing regenerative capabilities: after removal of more than two thirds of the liver, it can grow back to its original mass and work as well as before [12]. This remarkable ability to regenerate is demanded by the liver’s pivotal role in blood detoxification, making liver tissue particularly susceptible to intoxication damage. Because the liver is the entry point of many medical drugs, it is of great interest to understand the underlying mechanisms that play into toxicity damage and how recovery is enabled. While, for example the kidney can be substituted by dialysis, the function of the liver can so far not be substituted by mechanical devices. This is partly due to the complex architecture of the liver, which remains a great challenge for building in-vitro systems that could be used in pharmaceutical applications [13–18]. Furthermore, how regeneration and liver development [19] is orchestrated is not well understood in terms of molecular and physical mechanisms. This thesis takes a step towards that understanding by charactering the so-far unrecognized orientational order of cell polarity in the liver, which might serve as a structural benchmark during liver development and regeneration and by that help in unraveling the underlying mechanisms.

We now describe the main anatomical features of the liver. When examining the liver as a whole it appears as a homogeneous, dark reddish brown tissue [20]. Upon closer examination, a subdivision into functional subunits called *lobules*, with typical size of about 1 mm, is observed. They are shown, schematically, in Fig. 1.2. Each lobule consists of a central vein in the middle and approximately six *portal triads* arranged in a hexagonal fashion around it. A portal triad consists of a *proper hepatic artery* (also *portal arteriole*), *hepatic portal vein* and a *bile duct* [21, 22]. The hepatic artery supplies oxygen-rich blood directly from the heart, whereas the portal vein delivers blood, which contains toxins and nutrients from other organs. The blood from these two afferent vessels mixes in a region close to the portal triad. It then flows through a network of fenestrated² blood vessels, called *sinusoids* towards the *central vein* in the center of the lobule, from where it is drained towards the heart [21, 22]. On the way through the sinusoidal network, blood flows past hepatocytes, which are immersed between the

²Fenestration means that sinusoids contain “holes” or “windows”, which enable efficient exchange of blood with hepatocytes.

1. Introduction

sinusoidal network. *Hepatocytes* are the parenchymal cells that carry out most of the metabolic and synthetic function of the liver. They account for about 80% of liver weight and about 70% of all liver cells [23, 24]. Bile, which is produced in hepatocytes, is secreted towards and transported through the *bile canaliculi* network, which is completely separate from the blood-transporting sinusoidal network. Bile canaliculi are formed as lumina between adjacent hepatocytes and are held together by specialized transmembrane proteins, called *tight junctions*. These lumina form a continuous network that transports bile from hepatocytes towards the bile duct near the portal triad through from where it is further drained towards the gall bladder. There, the bile is stored until it is needed during digestion. The

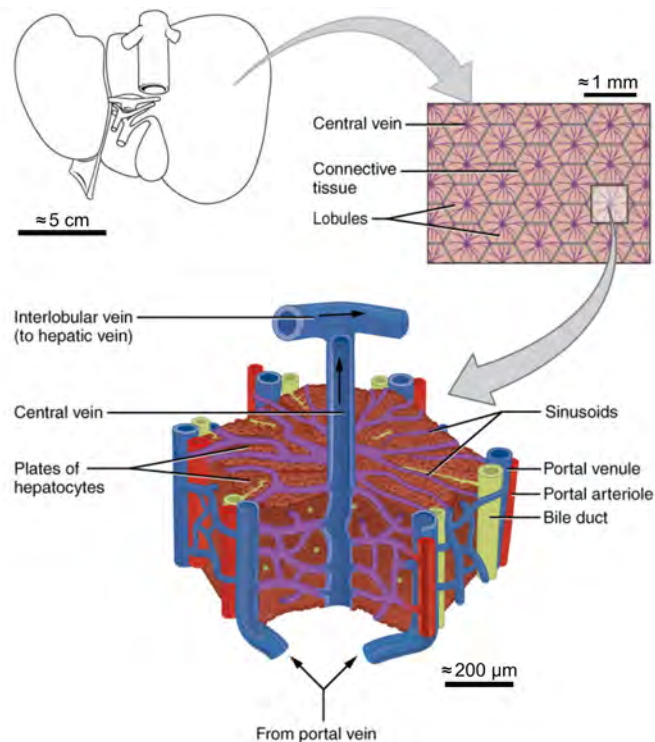


Figure 1.2. Schematic of hierarchical organization structure of the liver.

The liver (top right) consists of many thousands functional unit cells, which are called *lobules*. Each lobule consists of a central vein in the center and approximately six portal triads arranged in a hexagonal fashion around it. The hepatocytes are the parenchymal cells and dispersed between portal triad and central vein together with two transport networks: the sinusoid and bile canaliculi network. Image modified from: OpenStax College (CC-BY-3.0)

architecture of the liver lobule therefore consists of mainly hepatocytes that are dispersed between two inter-digitating transporting networks: sinusoids and bile

canaliculi³. Because hepatocytes are of epithelial origin, the liver can be regarded as an epithelial tissue but with a complex three-dimension organization. In the following sections of this introduction, we therefore review fundamental aspects of epithelia tissue architecture and cell polarity and discuss previous approaches to describe biological tissues.

1.3. Biology of tissues

As a complex organ, the liver as a whole does not fall into a single category of the four basic tissue types (connective, muscle, nervous and epithelial), mentioned above. However, the main characteristic of the liver is that of an exocrine gland [3]. Glandular tissues derive from epithelium and the parenchymal cells of the liver (hepatocytes) share important features of epithelial cells [3]. We therefore review relevant aspects of epithelial tissues now.

Epithelial tissues are found at the surface of the body or body cavities, such as the gut, the airway lumen, or the skin. They are lining tissues and typically separate the outside or a lumen from the inside of the body or an underlying tissue. Their main functions are absorption, filtration and the organization of directed transport of macromolecules. The cells that form the epithelium are tightly joined, so that almost no inter-cellular space is left. These cell-cell connections are realized by tight junctions, which effectively seal the lumen-facing side from the rest of the tissue [3]. This enables the epithelium to serve as a gatekeeper and a protective shield of the underlying tissue. It can regulate transport from one side to the other or perform more complex sorting tasks, e.g. taking in material from one side, processing it and directing the products to either side in a controlled way.

Epithelial tissue is classified by the number of cell layers and the shape of individual cells, see Fig. 1.3. One can distinguish three principal cell shapes: *squamous*, *cuboidal* and *columnar*. Squamous cells are wider than they are tall, cuboid cells are cube-like and columnar cells are taller than they are wide. Using a coordinate system, where the epithelial sheet lies in the xy-plane, *simple epithelia* are single-layered, and multi-layered epithelia are called *stratified*. When nuclei of a simple epithelium appear on different heights, they might be confused with stratified epithelia. For these cases there is the separate category of *pseudo-stratified*

³Other parts of the stroma of the liver, e.g. Kupffer cells and stellate cells, are not considered in this thesis.

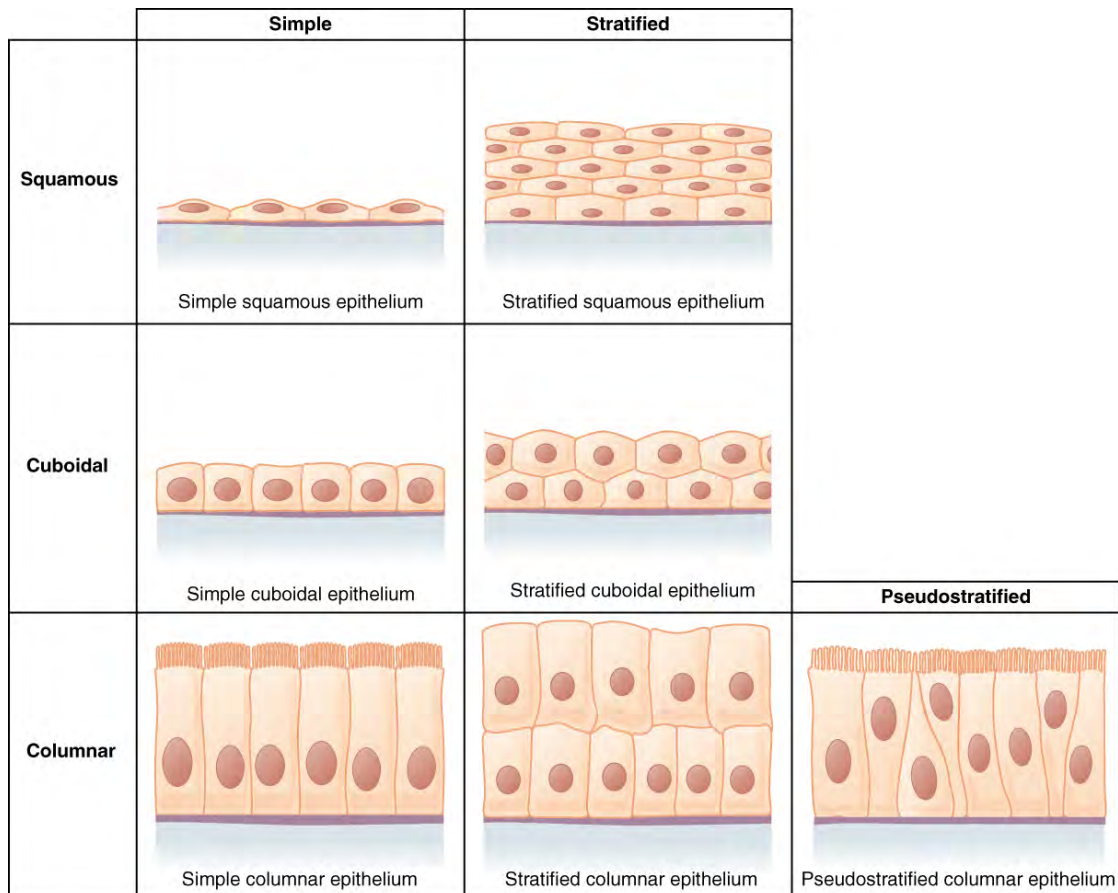


Figure 1.3. Schematic types of epithelial tissue. Epithelial tissue is classified by cell shape and number of layers. For each tissue, the lumen-facing side is located on the top and the body-facing side on the bottom. Image taken from: OpenStax College (CC-BY-4.0)

epithelia.

It is important to note that the three-dimensional organization of epithelial tissue can be more intricate than the picture of stacked flat sheets shown above. Kidney collecting ducts, for example, are simple epithelia that form cylindrical structures [20, plate 1133][3]. Hepatocytes of the liver are cuboidal epithelial cells that exhibit a peculiar three-dimensional arrangement that was first described by Hans Elias around 1950 [25, 26]. He proposed that hepatocytes are arranged into sheets, one cell thick, spanning the space between portal triad and central vein [3, 25, 26]. These cell sheets are branched and regularly anastomose with neighboring sheets. This peculiar arrangement of cells does not fit any of the classical categories of epithelial sheets mentioned above and is also reflected in the apicobasal cell polarity of hepatocytes.

Apicobasal polarity of epithelial cells. For proper function of epithelial tissue, it is important for specific proteins to be located at the correct region of the membrane of the epithelial cells. Imagine a protein pump that selectively transports material from the cell's cytoplasm into a lumen. This pump must be in the part of the membrane facing the lumen as otherwise the material would be transported into the wrong direction. Junctions forming connection between cells, specifically tight junctions, inhibit lateral diffusion of membrane proteins and thereby facilitate the compartmentalization of the membrane into distinct domains [1, 2]. Specifically, *apical* domains form on the sides of the tissue that faces the outside of a body or lumen of a cavity and are separated from other domains by tight junctions [3, 27]. *Lateral* domains provide cell-cell adhesion and *basal* domains form the interface with the basement membrane and extracellular matrix [3, 28, 29]. This anisotropic distribution of apical and basal membrane domains on the surface of cells is termed *apicobasal* cell polarity [2]. The locations of these functional domains have been found to respond to cues from the environment around a cell [30]. Disruption of the organization of membrane proteins leads to serious problems for cell function within a tissue, such as misdirection of transport [31–33], mis-specification [34, 35], or errors in cell sorting [36] and is implicated in the onset of diseases such as cholestasis [37], multiple sclerosis [33] and cancer [35, 38].

The term “cell polarity”. Cells that exhibit anisotropies in physical properties, such as the distribution of membrane-bound proteins, are said to be polarized. At this point, it is imperative to be precise about the usage of the terms *polar* and *polarity*. In physics, the term *polarity* usually refers to vectorial quantities describing, for example, electric or magnetic fields. This needs to be distinguished from the term *cell polarity* used in biology, where the term is used in a broader sense to describe differences in cell shape, structure or function of cells, that are not necessarily vectorial [2]. The present thesis deals specifically with anisotropic distributions of membrane proteins on the surfaces of cells and will thus use the term *cell polarity* to denote this particular form of cellular anisotropy, unless stated otherwise. To avoid confusion, we will be explicit about the type of polarity and will not equate *polar* with *vectorial*.

Types of apicobasal cell polarity. Schematically, there are two main types of apicobasal cell polarity documented in the literature [2, 29].

Simple epithelial sheets typically exhibit a vectorial cell polarity (also called columnar or prismatic cell polarity [3, 29]), where one side of the cell is of apical identity while the opposite side is of basal type, see Fig. 1.4A. However, there are also tissues with more complex 3D architecture than simple epithelial sheets, such as liver tissue. In these cases, the organization of cell polarity is more intricate and cannot be characterized by a single vector.

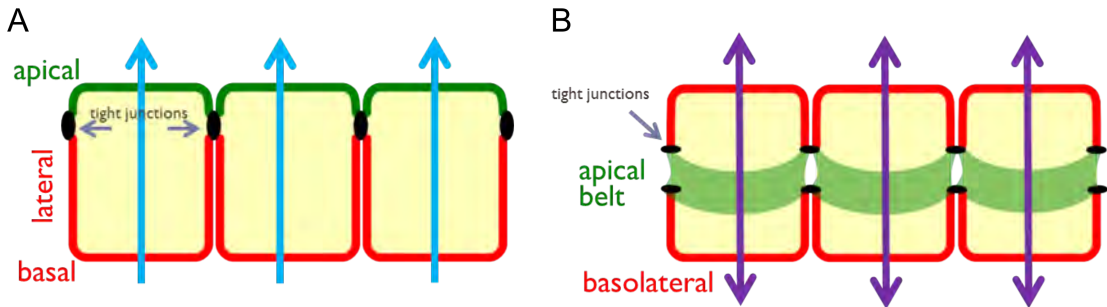


Figure 1.4. Schematic of apico-basal cell polarity. (A) Columnar cell polarity. An apical domain (green) is segregated from the basolateral (red) domain by tight junctions at the geometrical apex of the cells. This type of cell polarity typically forms in densely packed monolayer epithelial tissues [29]. This cell polarity type can, schematically, be represented by a vector. (B) Hepatic cell polarity. Apical domains form around the perimeter of cells at the sites of lateral contact between neighboring cells in a belt-like fashion. Basolateral domains are located at opposite poles of the cell. Schematically, this polarity type can be represented by a nematic axis.

One example of this type of multi-faceted cell polarity are hepatocytes of the liver. Each hepatocyte possesses multiple apical membrane domains forming narrow lumina with adjacent cells, into which bile is excreted. Together, these lumina constitute the lobule-spanning bile canaliculi network (cf. section 1.2). Additionally, each hepatocyte has multiple basal domains that face the blood-transporting sinusoidal network [29]. This type of apicobasal cell polarity is referred to as “hepatic cell polarity” in the literature [29] and schematically shown in Fig. 1.4B. This picture of hepatic cell polarity is certainly oversimplified and will be investigated systematically in chapter 2.

The schematic is nevertheless useful to illustrate the qualitative difference between columnar and hepatic cell polarity with respect to the symmetry of the protein distribution. As indicated in Fig. 1.4 columnar cell polarity can be described by a single vector pointing from the basal to the apical side of the cell. In contrast to that, the idealized hepatic cell polarity can be described by an undirected axis connecting both basal sides. In this simple case, this axis is also perpendicular to the ring of apical domain. The undirected axis of this idealized picture represents a nematic object that is invariant with respect to mirroring on a plane perpendicular to it [39]. The formalization and systematic study of this intuition will be a core subject in the present thesis.

1.4. Physics of tissues

Tissues are a form of complex matter that share common characteristics. The physics of tissues aims to find general laws describing these systems of living matter. The study of the physics of tissues is a broad field and we only provide a coarse overview here and highlight some particularly useful examples.

The physics of tissues includes inter-cellular processes of cells and the mechanical and chemical interaction between them. From the perspective of physics, a cell can be regarded as a complex machinery that, among other tasks, converts chemical energy from fuel molecules (e.g. ATP) into useful work [1]. This work can drive different processes, including cell migration [40–42], inter-cellular trafficking processes [43], and cell division [44–46]. On the sub-cellular scale, processes such as DNA replication and transcription [47] and the physics of the acto-myosin cytoskeleton [48, 49], as well as the emergent mechanical properties of the cell as a whole [50, 51] have been studied. Cells in the tissue constantly consume

1. Introduction

chemical energy, which keeps the system from reaching thermodynamic equilibrium and requires the characterization of the material as *active matter* [52]. A complete description of all degrees of freedom in a tissue is neither achievable nor desirable [52]. Instead, it is useful to apply global principles, such as conservation laws and symmetries, to constrain the possible dynamics of the system [52]. The wealth of possible descriptions can be classified into (i) continuum models that do not consider details on the cellular scale and (ii) discrete models where some degree of single-cell behavior is retained [52–54].

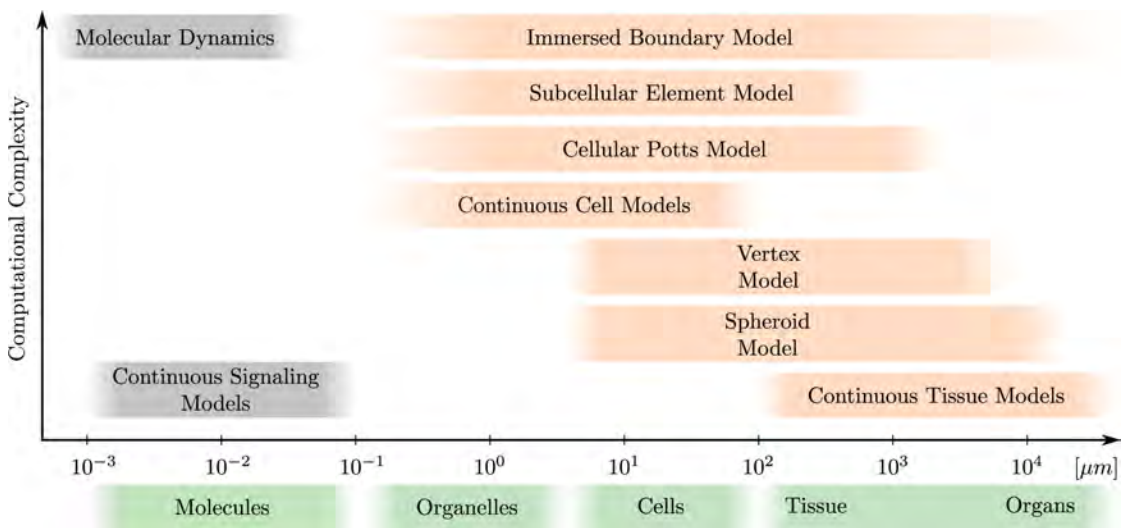


Figure 1.5. Selection of physical models for tissues morphogenesis. Physical models for tissues morphogenesis differ by computational complexity and the span of lengths scales they may describe. Image from [53] (CC-BY-4.0)

The complexity of the description of the physics of tissues can also be reduced by focusing on a subset of biological processes and providing the rest as external driving of the system. For example, many physical descriptions of tissues aim to understand morphogenesis and pattern formation of tissues and organs [53, 55–63]. Morphogenesis describes the process of the genesis of form, which is the result of the interplay between mechanical properties of the tissue, the genetic program of cells and chemical signaling. There, it is possible to focus on the study of mechanical properties and provide the genetic program and chemical signaling as external parameters to the model [53, 64]. Both, tissue mechanics and chemical signaling, have been described by a variety of physical models to different levels of detail, see Fig. 1.5 [53].

1.4.1. Continuum descriptions

At the coarsest level, a tissue can be described as a macroscopic continuous material with potentially viscous, elastic and plastic properties, depending on the timescale of interest [53, 65–67]. The tissue is characterized by a constitutive equation that describes how “slow” hydrodynamic variables respond to external stimuli, such as forces or other applied fields. These hydrodynamic variables are given by conservation laws or, in the case of ordered systems, by “continuous broken symmetries” and represent collective modes that describe the long-wavelength, long-time scale relaxation towards thermodynamic equilibrium after an initial perturbation [68]. The constitutive equation can either be determined phenomenologically [69–71] or derived from an underlying “microscopic description” of cellular processes, such as directed cell division, extrusion, migration and adhesion [72]. Given the mathematical form of the constitutive equation, the material parameters are determined by comparison to experimental data or result directly from coarse-grained “microscopic” interaction parameters between individual cells [52, 72]. The resulting ordinary or partial differential equations are typically solved using finite element methods in general, and analytical tools in special cases [52, 53, 72]. Continuum models are particularly useful for the study of processes on large time and length scales, when the separation of tissue into individual cells can be neglected. Coarse-graining a realistic microscopic description is difficult and typically involves simplifications and approximations [52].

In the context of liver tissue, continuum models have been used to study fluid flow and deformation of decellularized liver tissue [73, 74] and for the development of surgery simulation systems [75].

1.4.2. Discrete models

Discrete models typically retain the cell as a structural unit of a tissue and by that possess many more degrees of freedom than continuum descriptions [53]. There are many variants of discrete models (see Fig. 1.5) and only a subset, namely the vertex model, spheroid model and cellular Potts model, is discussed here. For more detailed reviews, see [53, 76, 77].

The vertex and spheroid models consider the cell as the smallest unit in a tissue. In the (two-dimensional) vertex model, cells are described as polygons [78–80]. The interface between neighboring cells is represented by a common edge and the points

of intersection are the location of graph vertices. Stable and stationary network configurations result from force balance on each vertex. Given N_C polygonal cells, numbered by $\alpha = 1, \dots, N_C$ and N_V vertices, numbered $i = 1, \dots, N_V$, the force balance corresponds to a local minimum of an energy function [79]

$$E(\{\mathbf{r}_i\}) = \sum_{\alpha} \frac{K_{\alpha}}{2} (A_{\alpha} - A_{\alpha}^{(0)})^2 + \sum_{\langle i,j \rangle} \Lambda_{ij} l_{ij} + \sum_{\alpha} \frac{\Gamma_{\alpha}}{2} L_{\alpha}^2. \quad (1.1)$$

Thus, $\mathbf{f}_i = -\partial E / \partial \mathbf{r}_i$ is the total force acting on vertex i . This energy function describes forces due to cell elasticity, actin-myosin bundles and adhesion molecules [79, 81]. The first term on the right hand side describes area elasticity of cells with elastic coefficients K_{α} and preferred cell area $A_{\alpha}^{(0)}$. The second term describes line tensions on the edges $\langle i, j \rangle$ of the graph with line-tension coefficient Λ_{ij} and edge length l_{ij} . Line tensions result from cell-cell adhesion and activity of actin-myosin bundles [79]. Actin-myosin bundles are combinations of actin filaments with myosin molecular motors that generate contractile forces [82]. These bundles are found at the interfaces between cells and may thus be responsible for line tensions on the edges in the vertex model. The third term describes the contractility of the cell perimeter L_{α} by a coefficient Γ_{α} . It is motivated by the observation of an actin-myosin ring around the perimeter of many epithelial cells. Vertex models have been used to study epithelial morphogenesis [79, 83, 84], cell sorting [85–87] and planar cell polarity [67, 88]. Interstitial space between cells is not described by the model, which makes it a good approximation for tightly packed epithelia.

Spheroid models are built on conceptual analogies to colloidal particles and a cell is represented by a homogeneous isotropic elastic sticky object, which is capable of migration, growth, division and change of orientation [76]. Cell adhesion has recently been shown to be well explained by Johnson-Kendall-Roberts theory of adhesive spheres [89], which includes a hysteresis effect in that the distance where cells are pulled apart is larger than the distance an initial contact is formed [53]. The JKR theory and other variants, such as the Hertz contact model [90], harmonic interaction potentials [91] and dashpot-spring elements [92] have been used in spheroids models [53, 76]. Cell movement in this framework is described by overdamped dynamics with stochastic contributions and multiple schemes to treat them in the statistical context of Langevin equations can be derived [76]. A variant of the spheroid model has been used to describe liver regeneration after intoxication

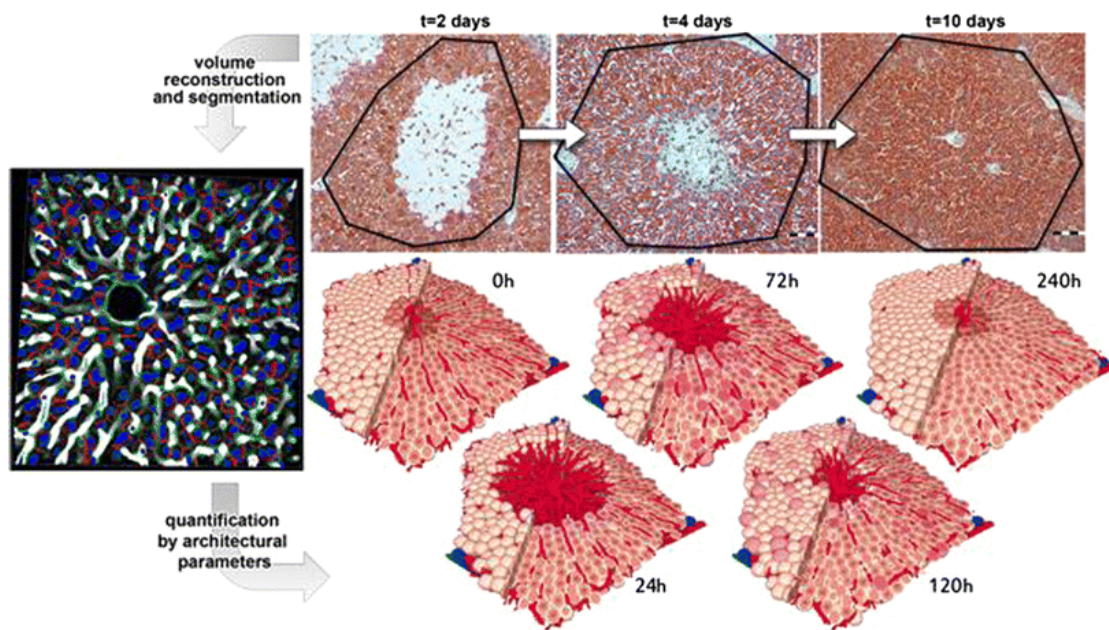


Figure 1.6. Example application of a spheroid model to study liver regeneration. Model parameters are obtained by image analysis of confocal micrographs (left) in conjunction with quantification of dynamical processes in the regenerating liver after intoxication with tetrachloride (CCl_4) (top row: hepatocytes shown in brown and central necrosis in blue). The bottom row shows a computational model where individual hepatocytes (brown) can be in different stages (light rose: quiescent hepatocyte, dark rose: proliferating hepatocyte, brown: glutamine synthetase positive hepatocyte, red: sinusoids, central and portal vein). Image credit: Godoy et al. [14] (CC-BY)

with carbon tetrachloride (CCl_4) [14, 93], see Fig 1.6.

Cellular Potts models (CPM) are generalizations of the Ising spin model [94] and were first introduced by Graner and Glazier [95, 96]. In contrast to the vertex and spheroid model discussed before, the cellular Potts model is a lattice-based model. Each lattice site x carries a spin $\sigma(x) \in \mathbb{N}^0$ that represents a cell identity. All spins carrying the same identity thus belong to the same cell. The configuration of spins and thereby the configuration of cells is governed by an interaction energy, which is the sum of an area constriction term H_v and a cell-cell adhesion term H_a [53, 95]

$$\begin{aligned} H &= H_v + H_a \\ &= \sum_{\sigma} \lambda_v (A_{\sigma} - A_{\sigma}^T)^2 + \sum_{(x,x')} J(\tau(\sigma(x)), \tau(\sigma(x'))) [1 - \delta(\sigma(x), \sigma(x'))] \end{aligned} \quad (1.2)$$

with A_{σ} and A_{σ}^T the actual and target area of cell σ , respectively. The coefficient λ_v specifies the strength of the area constraint. The term $J(\tau, \tau')$ describes cell adhesion between two cell types τ and τ' , with $\tau(\sigma(x))$ denoting the cell type of cell σ at lattice position x . The inverse Kronecker delta $1 - \delta(\cdot, \cdot)$ is non-zero only when cells are of different type and summation $\sum_{(x,x')}$ runs over all lattice sites x and its direct neighbors x' . The cell-adhesion term thus contributes only across cell-cell interfaces and only when cells are of a different type. Spin configurations are generated using the Metropolis Monte-Carlo procedure [97]. The main idea of the Metropolis algorithm is to randomly propose a new spin configuration. If the new configuration has lower total energy, it is accepted right away and if it has higher total energy, it is accepted only with probability proportional to the Boltzmann factor of the energy difference.

The CPM shows phase transition behavior that depends on the effective temperature that enters the Boltzmann factor [53]. This “temperature” is considered to be “effective” because it subsumes processes that generate disorder and its direct biophysical interpretation is often difficult [98]. Nevertheless, variants and extensions (e.g. to include reaction diffusion equations) of the CPM have been applied in a wide variety of biophysical problems, such as blood vessel formation [64, 99, 100], cell sorting [95] and cell migration [101]. In chapter 6, we will use a similar generalized spin model for networks to describe formation of the sinusoid and bile canaliculi networks in liver tissue.

1.4.3. Two-dimensional case study: planar cell polarity in the fly wing

As stated in section 1.3, this thesis deals with the peculiar cell polarity of hepatocytes in liver tissue. Organization of cell polarity has been studied previously in the context of planar cell polarity (PCP) in the planar simple epithelium of the fly wing. Proper establishment of PCP is an important prerequisite in controlling the direction of hair growth in the developing fly. In contrast to apicobasal cell polarity, PCP describes the anisotropic localization of proteins of the Frizzled system⁴ on the apical side of the fly wing epithelium and can thus be captured by an effective 2D geometry, see Fig. 1.7. The planar geometry of the tissue suits itself for an effective two-dimensional description and lead to the development of a mechanical model for two-dimensional cell packing [83] and the study of reorientation of planar cell polarity by cell flow [88]. This study of PCP in the fly wing highlights the importance of physical processes in the context of cell polarity. It is a useful reference case when attempting the description of cell polarity in bulk liver tissue, which requires a genuinely three-dimensional description.

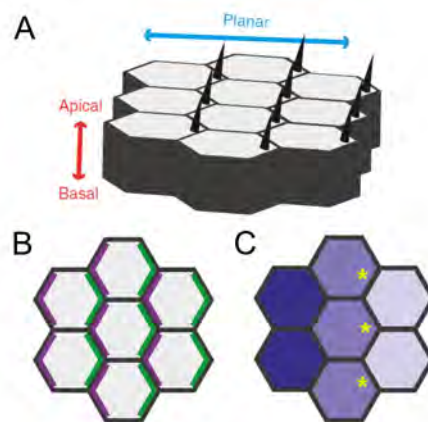


Figure 1.7. Schematic of planar cell polarity guiding hair growth in the fly wing. (A) Simple epithelium of the fly wing with apical side on the top and basal side on the bottom. Planar cell polarity works perpendicular to apico-basal polarity in the plane of the tissue. (B) Top view of (A) with highlighted localization of specific PCP proteins on opposing sides of the cells (purple and green). (C) Hairs grow at the side of cells, where one PCP protein species (depicted in green) is enriched.

Image credit: Marcinkevicius et al. 2009 [102] (CC-BY-4.0)

⁴Frizzled is a family of receptor proteins involved in the organization of planar cell polarity, the Wnt/ β -catenin pathway and Wnt/calcium pathway. For details see, for example, [67, 83, 88].

1.4.4. Challenges of three-dimensional models for liver tissue

Many studies investigating physical principles in tissues have been performed on simple epithelial sheets [2, 55, 60, 83, 88, 103, 104], because they are experimentally more easily accessible than bulk tissue. The study of complex three-dimensional organs, such as the liver [105], has become feasible only recently due to advances in microscopy techniques, such as fluorescence microscopy with its many improvements and variants (confocal, two-photon and light sheet microscopy [106, 107]), as well as advances in protocols that render tissue optically transparent to enable imaging of relatively thick specimen [108, 109]. The newfound wealth of data demand for appropriate biophysical descriptions.

So far, physical descriptions of liver tissue have involved organ-level continuum models [73, 75, 110, 111] and spheroid-based lobule-level models [93, 112]. In this thesis, we first categorize the liver as a biaxial nematic liquid crystal. We then use a discrete model of nematic cell orientations to describe the observed order. Building on this, we then develop a generalized spin model to study the formation of transport networks in the liver. In both cases, an interaction energy, similar in spirit to the vertex model and CPM, is formulated and configurations are sampled using the Monte-Carlo approach.

Biological tissues represent complex, amorphous materials with mesoscopic structure conferring interesting physical properties. From a physical point of view, their structure and order lies between the limiting cases of isotropic liquids and three-dimensional crystals. Another type of mesoscopic material, liquid crystals, falls into the same range and the concepts developed there are likely to be suitable for the description of biological tissues as well.

1.5. Liquids, crystals and liquid crystals

The solid, liquid, and gas phase are the three classical phases of matter, one is very much familiar with from everyday experience. Solids are rigid objects with definite shape and volume, due to strong attractive forces among their molecular constituents. In liquids and gases, inter-molecular forces are weaker and the material is able to adapt to the shape of a container and they are collectively referred to as fluids. Between liquids and crystalline solids, there exists a range of mesophases that can be distinguished with respect to their mechanical and symmetry properties [39].

According to Chandrasekhar, the first observations of liquid crystalline behavior were made by Reinitzer and Lehmann at the end of the 19th century [113]. The common characteristic of liquid crystalline states is that they are strongly anisotropic in certain properties, while retaining a substantial amount of fluidity in others. This macroscopic property originates in the typical shape of the constituent molecules that form liquid crystal phases, which are geometrically highly anisotropic, like a rod or a disc [113]. There is a wide variety of liquid-crystal phases, which have been classified by different experimental techniques, including refractive index studies, NMR spectroscopy as well as X-ray and Neutron scattering [114]. A liquid crystal system may be driven through multiple nematic phases by changes in temperature (thermotropic) or by the influence of solvents (lyotropic) before arriving at the isotropic liquid state.

It is instructive to review the limiting cases of crystalline order and liquids and place the liquid crystal mesophases therein. In crystals, the constituents (atoms, molecules or groups of molecules) are arranged on a three-dimensional periodic lattice. Liquids, on the other hand, flow easily and do not display a periodic arrangement. The regular ordering in crystals is reflected by the fact that, if a primitive pattern (or basis) is located at a point \mathbf{r}_0 , the probability to find an equivalent pattern at a point $\mathbf{r} = \mathbf{r}_0 + n_1\mathbf{a}_1 + n_2\mathbf{a}_2 + n_3\mathbf{a}_3$ with $n_i \in \mathcal{N}_0$, $i \in \{1, 2, 3\}$ and $\{\mathbf{a}_i\}$ the basis vectors of the crystal, remains finite even for large separations $|\mathbf{r} - \mathbf{r}_0| \rightarrow \infty$ [39]. This leads to sharp Bragg reflections in X-ray diffraction patterns that are characteristic for a given crystal and reflect the limiting behavior of the density-density correlation function [39]

$$\lim_{|\mathbf{r} - \mathbf{r}'| \rightarrow \infty} \langle \rho(\mathbf{r})\rho(\mathbf{r}') \rangle = F(\mathbf{r} - \mathbf{r}') , \quad (1.3)$$

which approaches a periodic function $F(\mathbf{r} - \mathbf{r}')$ of the crystal lattice basis vectors $\{\mathbf{a}_i\}$. Liquids, on the other hand, flow easily and individual constituents can pass each other and change neighbor relations. Liquids are isotropic and show translational symmetry in all three spatial directions. The density-density correlation function [39]

$$\lim_{|\mathbf{r} - \mathbf{r}'| \rightarrow \infty} \langle \rho(\mathbf{r})\rho(\mathbf{r}') \rangle = \bar{\rho}^2 \quad (1.4)$$

therefore approaches the square of the average density $\bar{\rho}$. In a liquid, there is an isotropic length scale ξ over which correlations between constituents are lost.

Mesophases in-between these two limiting cases are collectively called *liquid crystals* [39]. In contrast to crystals, they show liquid-like order in at least one direction of space. In contrast to liquids, they are anisotropic. De Gennes distinguishes two qualitatively different ways to obtain these mesophases [39].

The first considers the number of dimensions in which periodic positional order is found. A crystal exhibits positional order in all three spatial dimensions. If a phase shows positional order in only two dimensions, one speaks of a *columnar phase*. As the name suggests, columns are arranged on a two-dimensional lattice with no positional order of constituents along the axes of the columns. If two dimensions are unordered and only one spatial dimension shows a periodic structure, the *smectic phase* is encountered. This phase corresponds to two-dimensional layers that are stacked on top of each other with no positional order within each layer. Finally, there exists a liquid crystal mesophase without long-range positional order. In contrast to the classical isotropic liquid, however, the correlation function is anisotropic and there are two lengths scales, ξ_{\parallel} (parallel) and ξ_{\perp} (perpendicular) with respect to a macroscopically defined direction, over which correlations decay. This is the *nematic phase* [39].

The second way to obtain a mesophase between liquid and crystalline order is to include other degrees of freedom in addition to the centers of gravity of individual constituents. For non-spherical molecules, the obvious candidate is their orientation in space. If elongated molecules in a liquid align in a preferred direction, positional correlations along that direction will be different than perpendicular to it. The liquid is thus anisotropic and a nematic phase is encountered. Further mesophases can be obtained by combining positional and orientational order.

This classification of liquid crystals does not clearly separate between positional and orientational order. If one aims to study orientational order that is distinct from shape anisotropy, it is useful to modify the terminology slightly. In the above definition, anisotropic liquids and nematic liquid crystals are equivalent as any orientational order of non-spherical constituents will break isotropy of the liquid. If one now considers an anisotropy different from the constituent's shape, there is a possibility to find an orientationally ordered phase with complete isotropic positional order. In the case of molecules, magnetic moments can provide this kind of shape-independent anisotropy. In this thesis, we study mesoscopic objects (biological cells) and consider their cell polarity (cf. section 1.3) as anisotropy that is distinct and, in principle, independent from the cell's shape. It proves useful,

and will be done in this thesis, to reserve the term *nematic* for orientational order and use the term *anisotropic liquid* for anisotropic positional correlations.

1.5.1. The uniaxial nematic order parameter

The most widely studied nematic system is the *uniaxial nematic* [39, 115]. There, the constituent particles possess axial symmetry and are often represented by simple rods. Fig. 1.8 shows schematics of four fundamental types of (uniaxial) nematic ordering. Panel A shows an isotropic system with both translational and orientational symmetry. Particles are distributed randomly in space and orientations are equally likely in all directions. Hence, the locations of particles, indicated by dashes, are isotropic in space and orientations are homogeneously distributed, as shown by the spherical orientation plot in the upper right corner of Fig. 1.8A. When orientational symmetry is broken, for example due to application of an external field [116] or by spontaneous symmetry breaking upon cooling a thermotropic system, particles tend to align preferentially along a common direction. This direction is termed *director* and the state is called *uniaxial prolate* [39, 117]. In Fig. 1.8B this director is chosen to be in z-direction (indicated by the blue axis). Particles show preferential orientation in that direction but particle locations remain randomly distributed in space. There are many chemical systems exhibiting this kind of orientational ordering, in an intermediate regime, during the transition from an isotropic liquid state to a crystalline state [39, 115].

A second type of uniaxial ordering is the *oblate nematic* shown in Fig. 1.8C. Here, particles are oriented in a plane perpendicular to the director and positions are uniformly distributed. The view on the system in this example is chosen intentionally to show the ambiguity of three-dimensional visualizations in static form as the oblate state in this case can hardly be distinguished from the isotropic state in Fig. 1.8A. Also an alternative viewing direction as shown in Fig. 1.8D is ambiguous as this can hardly be distinguished from the prolate nematic case. This is why a quantitative analysis of orientational structures using objective order parameters is needed.

We now turn to the definition of the uniaxial nematic order parameter [39, 117]. We denote the orientation of a single axial-symmetric object, such as a rod or a disc, by a unit vector \mathbf{a} . As we cannot distinguish the direction of a nematic object, \mathbf{a} and the opposite vector $-\mathbf{a}$ are equivalent. We write the direction of \mathbf{a} in spherical coordinates $a_x = \sin \theta \cos \varphi$, $a_y = \sin \theta \sin \varphi$, $a_z = \cos \theta$, where

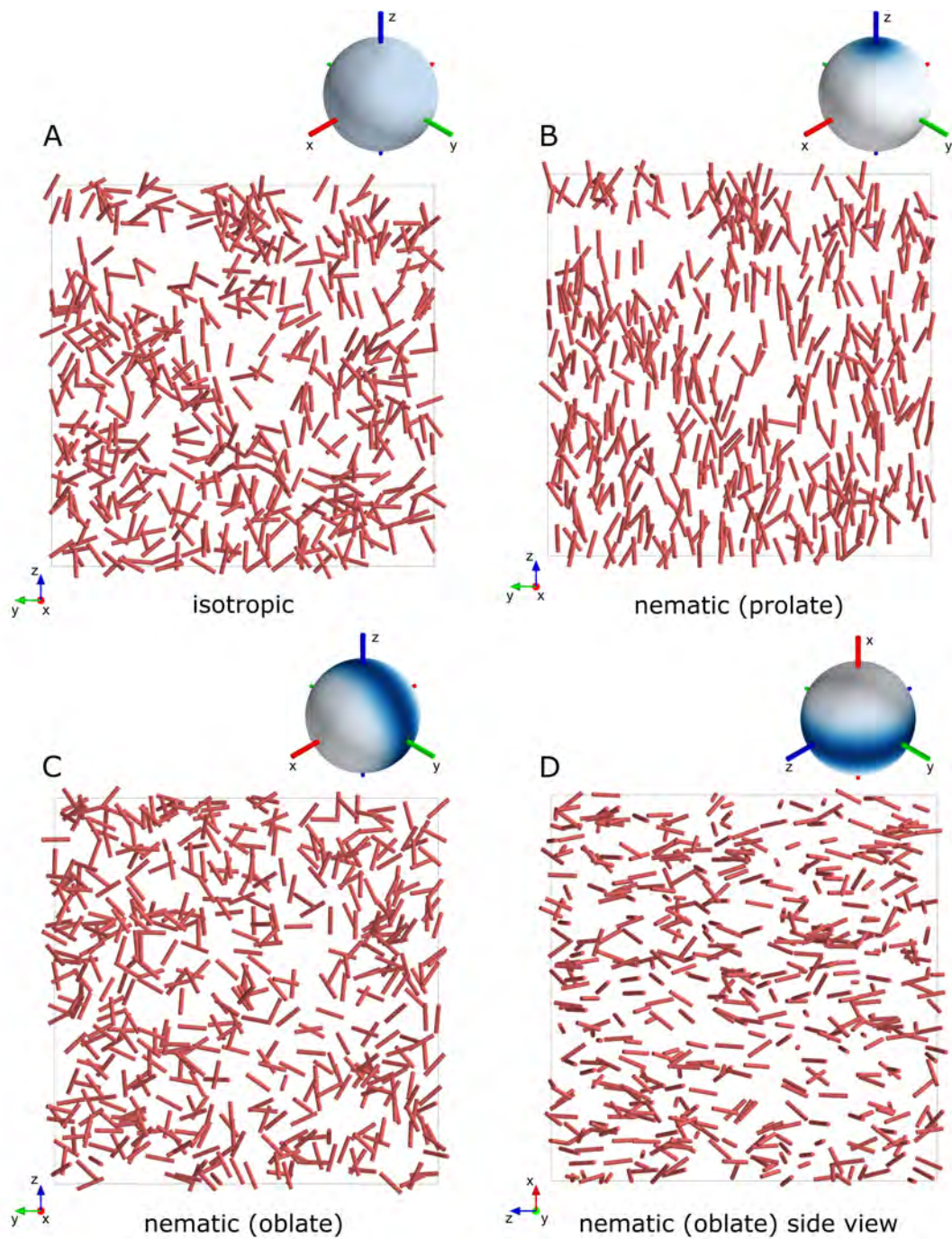


Figure 1.8. Schematics of nematic order. (A) Isotropic systems with no preferential orientation. (B) Prolate nematic ordering with director in z-direction (blue). (C) Oblate nematic ordering with director in x-direction (red). (D) Oblate nematic ordering with director in x-direction (red) viewed from the side. For each type a snapshot of orientations is shown exhibiting the nematic ordering type. Additionally, the orientational distribution functions are shown on a sphere. Note that the prolate distribution has an antipodal point on the opposite of the sphere that is occluded from the view.

the z -axis is chosen in the direction of the mean alignment of the molecules. Let $f(\theta, \varphi)$ be the distribution function of molecular orientations, where $f(\theta, \varphi)d\Omega$ is the probability to find a molecule in the infinitesimal solid angle $d\Omega = \sin\theta d\theta d\varphi$ around the direction (θ, φ) . In the uniaxial phase, the distribution function of orientations $f(\theta, \varphi)$ is independent of φ and $f(\pi - \theta) = f(\theta)$, because \mathbf{a} and $-\mathbf{a}$ are equivalent. To quantify the state of alignment of the system, one could naively take the thermal or time average over all orientations $\langle \cos\theta \rangle = \int f(\theta) \cos\theta d\Omega$. This average, however, vanishes by the symmetry property $f(\pi - \theta) = f(\theta)$. The next higher moment is the quadrupolar moment [117]

$$S = \left\langle \frac{1}{2} (3 \cos^2 \theta - 1) \right\rangle = \int f(\theta) \frac{1}{2} (3 \cos^2 \theta - 1) d\Omega \quad . \quad (1.5)$$

This moment gives a non-trivial average and is the most common order parameter used when describing uniaxial nematic systems [39, 115].

When the direction of mean alignment is unknown, it is useful to introduce a tensor order parameter [117]

$$Q_{\alpha\beta} = \frac{1}{2} \langle 3 a_\alpha a_\beta - \delta_{\alpha\beta} \rangle \quad (1.6)$$

It vanishes in the isotropic phase but becomes non-zero in the nematic phase. If the distribution of axes has axial symmetry around a preferred direction, represented by a unit vector \mathbf{n} , it can be rewritten as [117]

$$Q_{\alpha\beta} = \frac{1}{2} S (3 n_\alpha n_\beta - \delta_{\alpha\beta}) \quad (1.7)$$

with the scalar order parameter S defined above⁵. Thus, for an uniaxial system, the tensor order parameter $Q_{\alpha\beta}$ contains information about (1) the mean direction of nematic order (the *director* \mathbf{n}) and (2) how strong the molecules are aligned, quantified by S .

1.5.2. The biaxial nematic ordering tensor

So far, we have considered the orientational order of a single nematic axis. The state of alignment of non-axially symmetric objects within a system can be quantified by a generalization of eq. 1.5, which is often called “super-tensor” (also

⁵Note that because of the nematic symmetry, the directors \mathbf{n} and $-\mathbf{n}$ are equivalent.

“ordering tensor” or “ordering matrix”) [39, 115, 118]

$$S_{\alpha\beta}^{ij} = \frac{1}{2} \langle 3i_{\alpha}j_{\beta} - \delta_{\alpha\beta}\delta_{ij} \rangle, \quad (1.8)$$

where j_{α} denotes the direction cosine $j_{\alpha} = \mathbf{e}_j \cdot \mathbf{E}_{\alpha}$ between object axes $\mathbf{e}_j = \mathbf{a}, \mathbf{b}, \mathbf{c}$ and laboratory axes $\mathbf{E}_{\alpha} = \mathbf{x}, \mathbf{y}, \mathbf{z}$. Further, $\delta_{\alpha\beta}$ and δ_{ij} are Kronecker symbols and the brackets denote the thermal average. This ordering matrix is, by construction, real-valued, symmetric in both i, j and α, β , and traceless in either index pair, specifically $S_{\alpha\alpha}^{ij} = 0$ and $S_{\alpha\beta}^{ii} = 0$. It therefore diagonalizes for a special choice of the orthogonal reference frame, which we call $\mathbf{l}, \mathbf{m}, \mathbf{n}$ [39]. In its eigenframe, $S_{\alpha\beta}^{ij}$ has nine non-zero components $S_{\alpha\alpha}^{ii}$, which are not independent and can be reduced to four orientational order parameters. This is discussed in section 3.1.1, where we make explicit use of the symmetries of the individual constituents and the biaxial nematic phase [115, 119].

For objects that are axially-symmetric around one axis (e.g. \mathbf{a}), the only non-zero components of the super-tensor are

$$Q_{\alpha\beta} = S_{\alpha\beta}^{aa} = \frac{1}{2} \langle 3a_{\alpha}a_{\beta} - \delta_{\alpha\beta} \rangle \quad (1.9)$$

which is exactly the form given in equation (1.6) for axially-symmetric objects. If the distribution of object axes \mathbf{a} does not possess axial symmetry (as was assumed in eq. (1.7)), an additional order parameter P , measuring the deviation from axial symmetry of the orientational distribution, becomes non-zero and the ordering tensor is given by

$$Q_{\alpha\beta} = S n_{\alpha}n_{\beta} - \frac{S+P}{2} m_{\alpha}m_{\beta} - \frac{S-P}{2} l_{\alpha}l_{\beta} \quad (1.10)$$

with a primary director \mathbf{n} and secondary director \mathbf{m} . The third director \mathbf{l} is given by the orthogonality relation of the reference frame $\mathbf{l}, \mathbf{m}, \mathbf{n}$ in which $Q_{\alpha\beta}$ is diagonal. While in the uniaxial case there is only one symmetry axis, in the biaxial case there is some ambiguity about which axis to choose as the primary and which to choose as the secondary director. We will discuss this issue in more detail in section 3.1.1

1.5.3. Continuum theory of nematic order

We review important aspects of orientational order in the context of liquid crystals. This will provide us with the necessary tools that are applied to biological tissue in subsequent chapters.

Let us consider a uniaxial nematic, which is characterized by a scalar order parameter S and a nematic director \mathbf{n} . The total free energy E_T of this nematic can be split in into two parts

$$E_T = E_u + E_d \quad (1.11)$$

where E_u is the free energy of a uniformly aligned nematic and E_d denotes the contribution to the free energy due to gradients in the director field $\mathbf{n}(\mathbf{r})$. Typically, the uniform state is the ground state of a nematic system and therefore distortions of the director field lead to an increase of the free energy of the system [39, 120, 121]. These gradual changes may be due to constraints on the limiting surfaces of the sample (e.g. walls of a container) or external fields.

For a uniaxial system, described by a spatially varying director field $\mathbf{n}(\mathbf{r})$, the so-called *Frank free energy*⁶ is given by [39]

$$E_d = \int d^3r \frac{1}{2} K_1 (\nabla \cdot \mathbf{n})^2 + \frac{1}{2} K_2 [\mathbf{n} \cdot (\nabla \times \mathbf{n})]^2 + \frac{1}{2} K_3 |\mathbf{n} \times (\nabla \times \mathbf{n})|^2, \quad (1.12)$$

with three elastic constants that correspond to three bending modes: splay (K_1), twist (K_2) and bend (K_3). Previous measurements on nematic materials have shown that the elastic constants are of equal order of magnitude [39]. In situations, where the relative values of the elastic constants are unknown, it is therefore a good approximation to set the three elastic constants equal to $K := K_1 = K_2 = K_3$. This is known as the *one-constant approximation*⁷, which is adopted here. In this case, the Frank free energy simplifies to (neglecting surface terms) [39]

$$E_d = \int d^3r \frac{K}{2} \partial_\alpha n_\beta \partial_\alpha n_\beta. \quad (1.13)$$

⁶Named after Frederick Charles Frank and also called *distortion free energy*. In this formulation of the distortion free energy, it is assumed that the overall nematic alignment, characterized by the order parameter S , is not influenced by the distortions of the director \mathbf{n} and constant throughout the system.

⁷The elastic constants have also been calculated for a lattice model [122, 123] and using density functional theory [124]. There, equal constants correspond to an isotropic two-particle correlation function.

An important feature of the one-constant approximation is that the distortion free energy is now invariant under simultaneous rotation of all individual nematic spins \mathbf{n} while keeping their positions fixed⁸. For unequal elastic constants, the Frank free energy is invariant only under simultaneous rotation of both nematic axes and their respective positions [39]. This equation forms the starting point of the theory developed in chapter 5. There, we will discretize the continuum equations and use them to study nematic cell polarity in the liver.

Above, we assumed that nematic order is generated through some process and is constant throughout the system. The relevant contribution to the free energy then results from gradients in the director field $\mathbf{n}(\mathbf{r})$. As a side note, we now briefly mention existing statistical theories describing the emergence of nematic order in the first place (typically assuming a spatially uniform system and by that ignoring gradient terms). One can broadly distinguish macroscopic and microscopic approaches. First, axially-symmetric nematogens subject to steric interactions have been considered by Onsager in 1949 [126]. Later, in 1958, Meier and Saupe formulated a mean-field theory for the same axially-symmetric system and showed the existence of a first-order transition from the isotropic to the uniaxial nematic state [127]. This theory was extended by Freiser in 1970 to include non-axially symmetric (biaxial) nematogens [128]. For a short summary of the Meier-Saupe theory and its extension to biaxial systems, see appendix A.1.

An Onsager-type theory for the steric interaction between rigid plates was provided in 1974 by Straley [119], which was later extended to investigate the effect of polydispersity of particle sizes [129, 130]. Also, mixtures of rod-like and plate-like molecules were studied [131–134]. In these cases, stable biaxial mixtures are unlikely due to demixing prior to the biaxial phase [134–137]. Furthermore, Landau-type phenomenological theories have been developed for both uniaxial and biaxial systems [39, 118, 138–142]. Complementary, computer simulations (typically using Monte-Carlo methods) have been performed to study more complex systems that go beyond analytical and perturbative treatments mentioned above [133, 134, 143–147].

⁸The form of the free energy in one-constant approximation is also equivalent to a cubic Heisenberg ferromagnet [125, §39][39]

1.5.4. Smectic order

In liquid crystals it is also possible that translational symmetry is broken. Historically, G. Friedel coined the term *smectic* (derived from the greek word for “soap”) for all mesophases, which have mechanical properties reminiscent of soaps [148, 149]. All smectic systems have the common property that particles are arranged in a *layered structure* with a well-defined inter-layer spacing [39, p. 18]. An example is shown schematically in Fig. 1.9A. In this case, particles are oriented preferen-

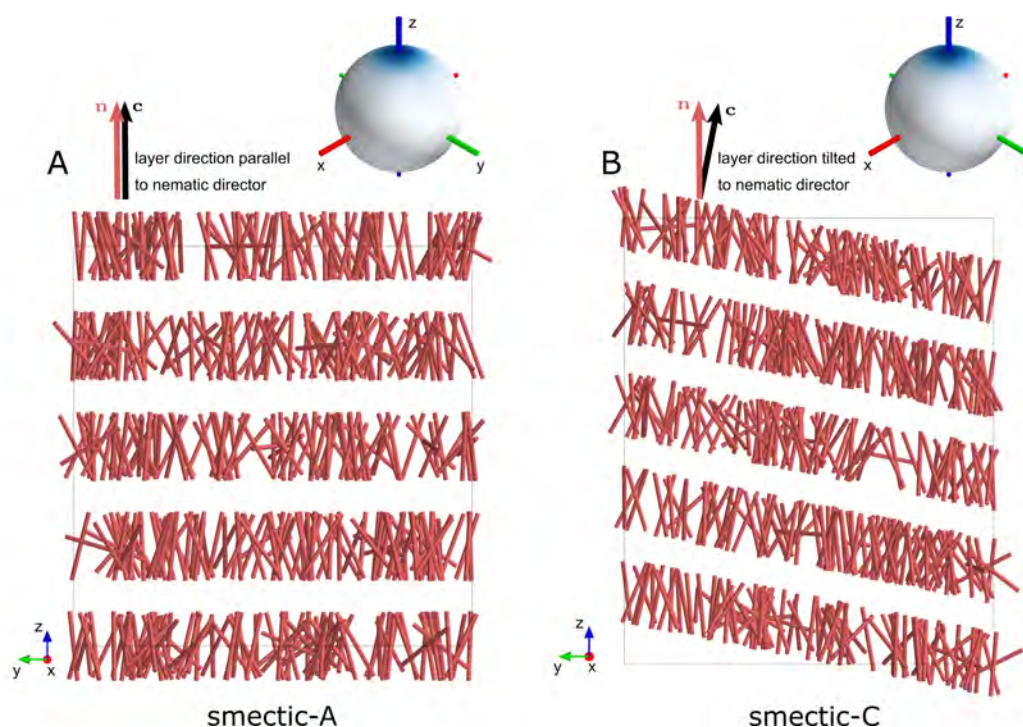


Figure 1.9. Schematics of smectic order. (A) Smectic-A order with layer normal parallel to the director of orientational order. (B) Smectic-C order with layer normal at an angle to the director of orientational order. For each type a snapshot of orientations is shown exhibiting the nematic ordering type. Additionally, the orientational distribution functions are shown on a sphere. Note that the prolate distribution has an antipodal point on the opposite of the sphere that is occluded from the view.

tially in one direction as in Fig. 1.8B, but also translational symmetry is broken and objects are arranged in layers. This case is distinct from a crystal, because individual objects are still free to move within each layer as a two-dimensional liquid. In the smectic-A phase, the layer normal is parallel to the director of orientational ordering. Systems, where the director of preferential alignment is inclined with respect to the layering direction, are called smectic-C and one example is shown in Fig. 1.8B. Besides these two most relevant forms of smectic liquid crystals, there

are more variants of smectic order (see for example Chandrasekhar [113] Table 5.1.1.).

1.6. Three-dimensional imaging of liver tissue

Imaging biological tissues across multiple length-scales is a continuing challenge within the life sciences. The data used throughout this thesis was acquired in the group of Marino Zerial at the Max Planck Institute of Molecular Cell Biology and Genetics (MPI-CBG) in Dresden. This section briefly reviews the parts of the data acquisition pipeline relevant for the purpose of this thesis. Details of the experimental procedure and computational segmentation of the images can be found in [105]. The workflow of the image acquisition pipeline is: (1) tissue preparation, (2) confocal microscopy of the tissue, and (3) computational analysis of the acquired data.

Tissue sample preparation and multi-resolution imaging. The data used in this thesis was obtained from fixated tissues. Fixated tissues are obtained by perfusion of the vascular system of the tissue with a paraformaldehyde solution. This stops all biological processes, while preserving the structural integrity of the tissue [150]. The sample is then cut into serial slices with thickness of approximately $100\mu\text{m}$ to maximize antibody penetration for fluorescent labeling. The used antibodies are engineered to bind to key subcellular structures, namely nuclei (DAPI), the apical surfaces of hepatocytes (CD13), the sinusoidal endothelial cells (Flk1), and the extra-cellular matrix (Laminin and Fibronectin), as well as the cell cortex (F-actin stained by phalloidin). These antibodies are combined with fluorescent markers to effectively image the tissue. Stained sections are imaged sequentially (generating z-stacks) by one- and two-photon laser scanning confocal microscopy, yielding multiple images of the same tissue volume with different extent and resolution, see Fig. 1.10. This enables the reconstruction of large volumes using low-magnification and low-resolutions images to provide a tissue-level context and registration for the high-magnification images located therein.

Image processing and reconstruction. Multi-resolution image stacks were further processed by the MotionTracking software [151]. The result of the image analysis pipeline is summarized in Fig. 1.10B. Tissue-level reconstruction em-

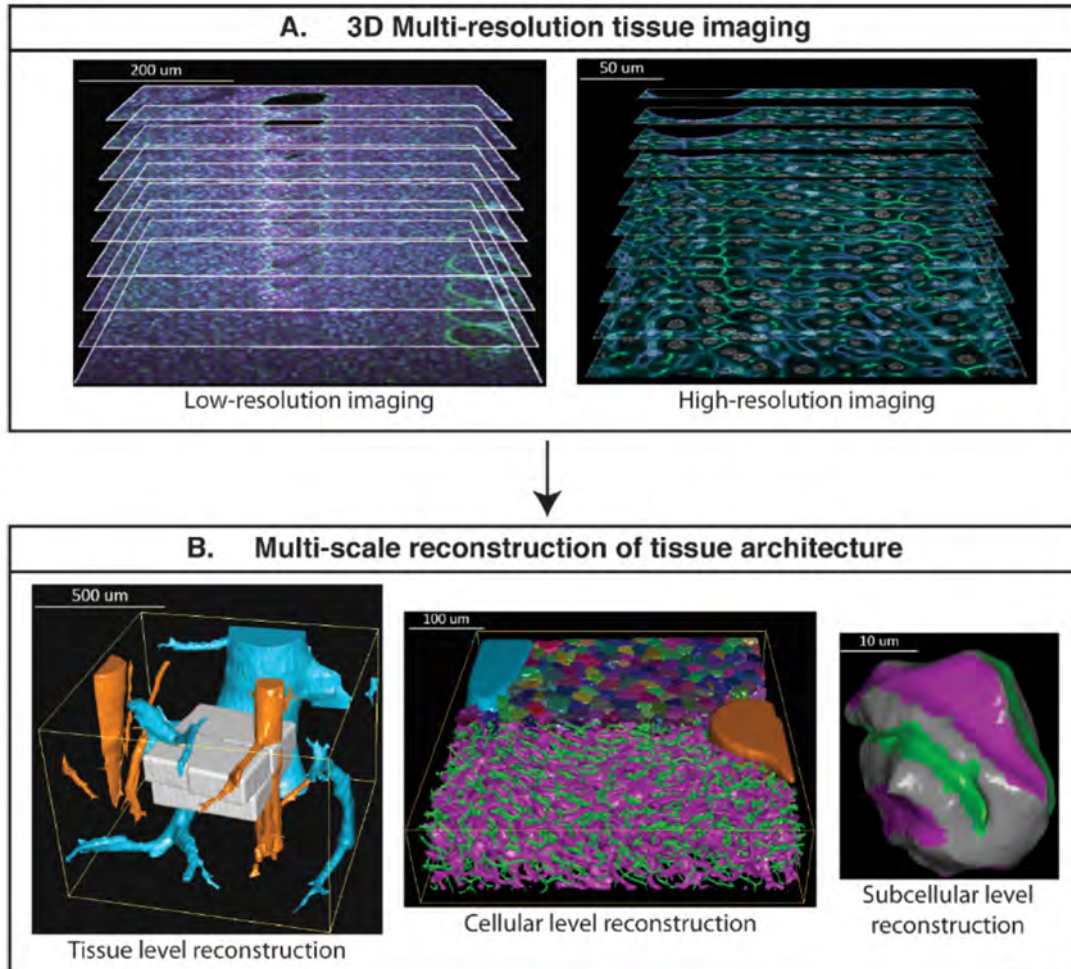


Figure 1.10. Overview of the data acquisition pipeline. (A) Low-resolution ($1\ \mu\text{m} \times 1\ \mu\text{m} \times 1\ \mu\text{m}$ per voxel) and high-resolution ($0.3\ \mu\text{m} \times 0.3\ \mu\text{m} \times 0.3\ \mu\text{m}$ per voxel) images of fixated and fluorescently stained slices of liver tissue are taken with fluorescence microscopy. (B) Segmentation, using the MotionTracking software, provides reconstructions of biological structure on different length-scales. Most notable are the reconstructions of the afferent vessels (portal veins, PV, orange) and efferent vessels (central veins, CV, cyan), hepatocytes (middle panel, colored meshes) and sinusoid and bile canaliculi networks (middle panel, magenta and green, respectively). The surface distribution of basal (magenta) and apical (green) membrane domains of each individual cell can be reconstructed (right panel). Image credit: Morales-Navarrete et al. [105] (CC-BY 4.0)

employs the low-resolution images to identify large vessels, namely portal veins and central veins to provide landmarks to identify the liver lobule (cf. section 1.2). Within these vessel structures, the high-resolution images are registered. The high-resolution images are then used for reconstruction on the cellular level (middle panel). This yields a triangulated mesh for each cell, the sinusoidal endothelial network and the bile canaliculi network [152]. Due to the high-quality of the imaging it is even possible to identify distributions of polarity proteins on the cell surface, namely domains of apical and basal membrane. We take this opportunity to also introduce a color-scheme that is used throughout this thesis to denote certain structures of the liver lobule. Central veins are shown in cyan, portal veins are shown in orange, bile canaliculi in green and the sinusoidal network in magenta. On the surface of hepatocytes, the apical domains are shown in green and basal domains in magenta (cf. Fig. 1.10B).

1.7. Overview of the thesis

At the heart of this thesis is the characterization of biaxial nematic order in liver tissue. We first turn to individual cells and establish a systematic method for the analysis of protein patterns on cell surfaces in **chapter 2**. There, we introduce the notion of vectorial and nematic cell polarity. As a reference case for vectorial cell polarity found in simple epithelia tissue, we apply this method to cells of the proximal and distal tubules of the kidney. Next, we turn to the main study subject of this thesis, the hepatocytes of the liver, and find them to be of predominantly nematic cell polarity type. Each hepatocyte in the liver is in close contact with the sinusoidal and bile canaliculi network. We therefore also characterize the local network around hepatocytes by a method that is analogous to the characterization of cell surface polarity. Having established the concept of nematic cell polarity for individual hepatocytes, we next turn to the tissue level.

In **chapter 3**, we introduce order parameters for tissues based on concepts from liquid crystal theory. There, we focus on characterizing orientational order of nematic objects and introduce scalar order parameters and invariants of moment tensors. At the end of the chapter, we turn to characterization of translational order, showcasing the relevant signatures of smectic and columnar order.

We use the tissue-level order parameters to study the structure of liver tissue in **chapter 4**. We find that the orientational order of nematic cell polarity in the

liver corresponds to a biaxial liquid crystal. Furthermore, we observe co-alignment between nematic cell polarity and the structure of the sinusoid transport network. The translational order of cells in the liver shows signatures of smectic order. We show that cell layers are co-localized with the bile canaliculi network and alternate with layers of high sinusoid network density. We report alterations of tissue polarity pattern in genetic knock-down experiments and quantify them using orientational order parameters. The specific form of the structural alterations hint at bi-directional cell communication with its environment.

We develop a simple nematic interaction model in **chapter 5**, to study the emergence of orientational order found in the liver lobule. We first discuss a uniaxial interaction model and test two hypothetical mechanisms: a global alignment field and surface anchoring. We provide evidence that a global alignment field is more consistent with observations in the liver. We then proceed to describe the biaxial co-alignment between nematic cell polarity and an alignment field given by the local sinusoid network around hepatocytes. In **chapter 6**, we devise a generalized lattice-based Ising model, which shares some characteristics with cellular Potts models, to study network generation in liver tissue. We show that this provides a possible mechanism for the spontaneous emergence of layered order from local rules.

2. Characterizing cellular anisotropy

It is crucial for proper functioning of a cell that proteins in the membrane are aggregated into functional domains (cf. section 1.3). It is therefore of great interest to quantitatively characterize the spatial distribution of membrane proteins on the surfaces of cells. In this chapter, we present a general method to systematically characterize cellular anisotropy. We first consider the case of surface distributions on the unit sphere, which are expanded into spherical modes (section 2.1.1). The power spectrum of these modes is used to characterize the anisotropy and classify it into two classes: vectorial and nematic, as shown in section 2.1.2. In section 2.1.3 we turn to biological cells, which are, in general, non-spherical and discuss projection methods of the membrane protein distribution on the cell surface onto a sphere. We then apply the developed classification technique by mode expansion to experimental data of kidney and liver cells in section 2.2. In the last section of this chapter, we extend the analysis to encompass the immediate environment around a cell and show how to quantify the anisotropy of transport networks in the vicinity of a cell.

2.1. Classifying protein distributions on cell surfaces

We first illustrate how to characterize surface distributions on a sphere, and afterwards show how membrane protein distributions of cells with non-spherical shape can be treated.

2.1.1. Mode expansion to characterize distributions on the unit sphere

Let us first assume that cells were unit spheres. Let further $f(\theta, \varphi)$ represent a binary surface density of the unit sphere, with polar angle θ and azimuthal angle φ . Similar to the two-dimensional Fourier transform for functions defined on a plane, we decompose $f(\theta, \varphi)$ into spherical harmonics

$$f(\theta, \varphi) = \sum_{l=0}^{\infty} \sum_{m=-l}^l f_l^m Y_l^m(\theta, \varphi) \quad , \quad (2.1)$$

with $Y_l^m(\theta, \varphi)$ denoting the spherical harmonic of degree l and order m normalized to unity. Using the ortho-normality of the spherical harmonics, the expansion coefficients f_l^m are given by $f_l^m = \int_{\mathcal{S}^2} d\Omega f(\theta, \varphi) Y_l^{m*}(\theta, \varphi)$. Here, integration is over the unit sphere \mathcal{S}^2 , the star denotes the complex conjugate and $d\Omega = \sin \theta d\theta d\varphi$ the differential solid angle. We also introduce orthogonal modes F_l for each degree l of the spherical harmonics, given by

$$F_l(\theta, \varphi) = \sum_{m=-l}^l f_l^m Y_l^m(\theta, \varphi) . \quad (2.2)$$

A visual representation of this spherical decomposition is given in Fig. 2.1. For

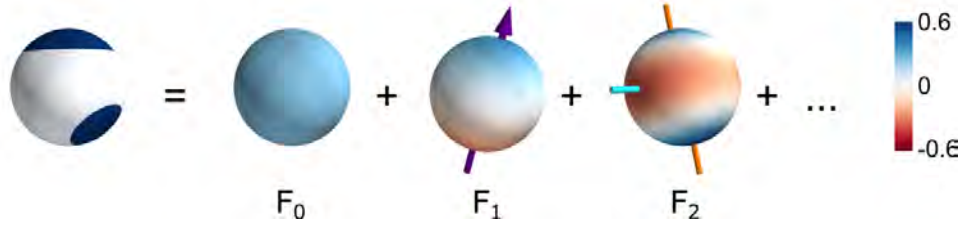


Figure 2.1. Multipole decomposition of surface patterns.

An example distribution is decomposed into spherical modes F_l (cf. eq. 2.1). The full spherical distribution is reconstructed by taking the sum over all individual spherical modes.

degree $l = 0$, the zeroth mode F_0 is isotropic and encodes the total solid angle covered by the binary distribution $\frac{1}{4\pi} \int_{\mathcal{S}^2} d\Omega f(\theta, \varphi)$. For degree $l = 1$, the first mode F_1 can be represented by a vector in the direction of the spherical average of the surface distribution¹ $\mathbf{p} = \int_{\mathcal{S}^2} d\Omega \mathbf{u} f(\theta, \varphi)$, where we introduced a unit vector \mathbf{u} in the direction of (θ, φ) . This polar vector also represents the symmetry axis of the first mode F_1 . The second mode F_2 of degree $l = 2$ corresponds to a moment of inertia tensor and can thus be represented by a tripod of nematic axes $\mathbf{a}_1, \mathbf{a}_2, \mathbf{a}_3$. Specifically, the nematic axes are given by the eigenvectors of the nematic cell polarity tensor that we define by

$$a_{\alpha\beta} = \frac{1}{2} \int d\Omega f(\theta, \varphi) (3u_\alpha u_\beta - \delta_{\alpha\beta}) , \quad (2.3)$$

where $\delta_{\alpha\beta}$ is the Kronecker delta. The eigenvectors $\mathbf{a}_1, \mathbf{a}_2, \mathbf{a}_3$ correspond to the symmetry axes of the second mode F_2 . We denote the respective eigenvalues of

¹This mode was analyzed extensively in the context of dispersion on spheres by Fisher [153].

the nematic cell polarity tensor by $\sigma_1, \sigma_2, \sigma_3$ and take $\sigma_1 \geq \sigma_2 \geq \sigma_3$ without loss of generality. The characteristic of a nematic axis is that it represents an undirected orientation. It can be represented by an equivalence class $\{\mathbf{n}, -\mathbf{n}\}$ with a unit vector \mathbf{n} and its antipodal vector $-\mathbf{n}$ [39]. Higher modes with $l > 2$ may exist but are not discussed here.

In analogy to Fourier analysis of linear signals, we define the power $S_{ff}(l)$ of each spherical mode F_l as the L^2 -norm over the spherical domain, normalized to the area of the domain, as

$$S_{ff}(l) = \|F_l\|^2 = \frac{1}{4\pi} \int_{S^2} d\Omega |F_l|^2 = \frac{1}{4\pi} \sum_{m=-l}^l |f_l^m|^2 \quad . \quad (2.4)$$

This defines the *spherical power spectrum*, which fulfills a generalized Parseval's theorem $\|f\|^2 = \sum_l \|F_l\|^2 = \sum_l S_{ff}(l)$.

2.1.2. Vectorial and nematic classes of surface distributions

We now introduce a vectorial and nematic class of surface distributions according to their spherical power spectrum. Specifically, we term a surface distribution “vectorial” if the power in the first mode is larger than the power in the second one $S_{ff}(1) > S_{ff}(2)$ and term it “nematic” otherwise. To illustrate this classification, Fig. 2.2 shows prototypical vectorial and nematic distributions, a spherical cap and bipolar caps, together with their respective spherical power spectra. Additionally, geographic Mollweide projections of these distributions are shown to provide a view on the whole spherical distribution². The geographic projection is useful for qualitatively examining the spherical distribution while keeping in mind the appreciable distortions on the boundaries of the map (see appendix A.2 for Tissot's indicatrix of the Mollweide map). The spherical power spectrum of the cap-like distribution has a prominent peak at the first mode, corresponding to a vectorial polarity type. In contrast to that, in the power spectrum for a bipolar pattern with two antipodal caps, all odd modes, including the first mode, vanish by symmetry and the second mode contains most of the power. We use this characteristic spectrum to classify this configuration as being of nematic type.

In general, we will encounter a combination of both vectorial and nematic cell polarity types. The main distinguishing feature between both types are the mag-

²The Mollweide projection is an equal-area, pseudocylindrical projection [154].

nitudes of the first and second mode of the power spectrum.

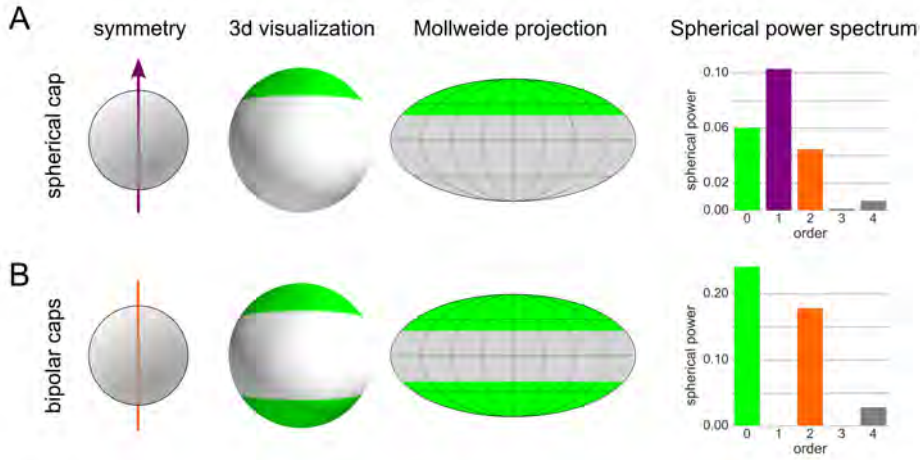


Figure 2.2. Idealized cases of vectorial and nematic surface pattern.

(A) The spherical cap is shown as a prototypical example of a vectorial surface pattern distribution, which is characterized by a peak at first mode in the spherical power spectrum. It can be represented by a vector pointing towards the center of the cap as indicated in the schematic on the left. (B) Two opposing (bipolar) spherical caps are shown as a prototypical example of a nematic surface pattern distribution. This surface distribution is characterized by a peak at the second mode in the spherical power spectrum. Additionally, all odd modes vanish by symmetry. It can be represented by a dash (an undirected line segment) pointing from the center of one cap to the center of the other as indicated in the schematic on the left.

2.1.3. Cell polarity on non-spherical surfaces

In general, the surfaces of cells are not unit spheres and we need to decide for a projection method when analyzing protein distributions on non-spherical cells. We restrict our treatment to three-dimensional volumes that are star-convex with respect to their center of mass³. To simplify notation, we choose the origin of our coordinate system to be at the center of mass of the volume. Then, by definition of a star-convex volume, for every point \mathbf{r} on the surface, there exists a line segment from the origin to \mathbf{r} that does not include any point from the surface other than \mathbf{r} . The restriction to star-convex shapes of this type is useful, because every point \mathbf{r} on the surface can be mapped bijectively on a point on the unit sphere, characterized by a polar angle θ and an azimuthal angle φ .

³A volume V in \mathcal{R}^3 is called star convex, if there exists a point $x_0 \in V$ such that every line segment from x_0 to any point in V is contained in V . Note that every non-empty convex volume is also star-convex.

We consider two methods for the projection of surface density from a star-convex shape onto the unit sphere, shown schematically in Fig. 2.3. Denote the surface density on the cell (which may represent a protein concentration) by $\rho(\mathbf{r})$ and the two methods of projections on the unit sphere by $f_A(\theta, \varphi)$ and $f_B(\theta, \varphi)$. For variant A, the nominal value of the surface distribution is retained and the projected area density on the unit sphere is defined as

$$f_A(\theta, \varphi) = \rho(\mathbf{r}) , \quad (2.5)$$

see also Fig. 2.3A. For variant B, the local surface density is weighted by the relative change in area. Thus, the total mass of the distribution is preserved. The distribution projected on the unit sphere is given by

$$f_B(\theta, \varphi) = \frac{4\pi}{A_{\text{total}}} \rho(\mathbf{r}) \frac{dA}{d\Omega} , \quad (2.6)$$

see also Fig. 2.3B.

In this work, we choose the projection variant A because it has the property that a homogeneous distribution on the cell membrane yields an isotropic projected distribution on the unit sphere.

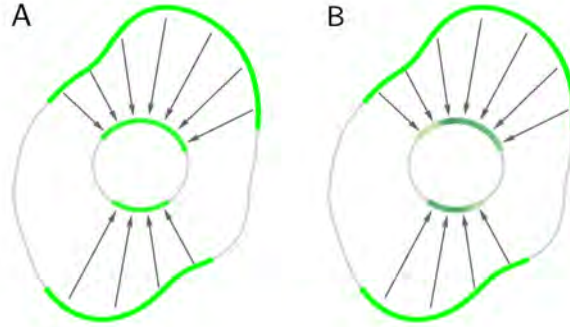


Figure 2.3. Schematic of the projection method.

A surface distribution (indicated in green) on a star-convex domain is radially projected on a co-centric sphere. (A) In variant A, the nominal value of the surface distribution is retained, see equation (2.5). (B) Alternatively, for method B, the local surface density is multiplied by the relative change in area upon projection, see equation (2.6). Thereby, the total mass of the distribution would be retained. However, the resultant spherical distribution would then confound anisotropy of the original distribution and anisotropy of domain shape.

2.2. Cell polarity in kidney and liver tissues

Experimental data for protein distributions on the membrane of cells are given as three-dimensional triangle meshes. Each triangle has a binary value ρ_i according to presence of a specific domain type in that part of the membrane (cf. section 1.6). The continuous surface distribution $\rho(\mathbf{r})$ is thus approximated by

$$\rho(\mathbf{r}) \approx \sum_i \rho_i A_i \delta(\mathbf{r} - \mathbf{r}_i) \quad (2.7)$$

with A_i the area of triangle i , \mathbf{r}_i the triangle center and ρ_i the binary value signifying the presence of a specific membrane domain type. The projected distribution on the unit sphere is given by

$$f(\theta, \varphi) \approx \sum_i \rho_i \Omega_i \delta(\theta - \theta_i) \delta(\varphi - \varphi_i) \quad (2.8)$$

where Ω_i is the area of the projection of the respective triangle area A_i on the unit sphere and θ_i, φ_i the polar and azimuthal angles of \mathbf{r}_i . The discretized version of equation (2.3) for triangle meshes is obtained by integrating over the approximate surface distribution, which gives

$$a_{\alpha\beta} = \frac{1}{2} \sum_i \rho_i \frac{\Omega_i}{4\pi} \left(3 u_\alpha^{(i)} u_\beta^{(i)} - \delta_{\alpha\beta} \right) . \quad (2.9)$$

2.2.1. Kidney cells exhibit vectorial polarity

To verify the general validity of the approach, we apply the characterization method to a simple epithelium: the proximal and distal tubules of the kidney. One example of these kidney cells is shown Fig. 2.4A. On the left, the three-dimensional mesh of a representative cell is shown, where green areas denote membrane parts which are identified to be of apical type and white represents other membrane domains. This mesh is projected onto a unit sphere, the result of which is shown as a three-dimensional rendering and a geographic projection. The spherical power spectrum of the example cell, shown in Fig. 2.4B, shows a clear peak at the first mode and resembles the power spectrum of a spherical cap (cf. 2.2), as expected from the visual inspection of the Mollweide map, where a single patch is located on the side of the cell. Finally, the average of the power spectra over $n = 286$ measured cells exhibits the same characteristic as the single example cell, see Fig. 2.4C.

From this, we conclude that the investigated cells in kidney tissue display vectorial cell surface polarity.

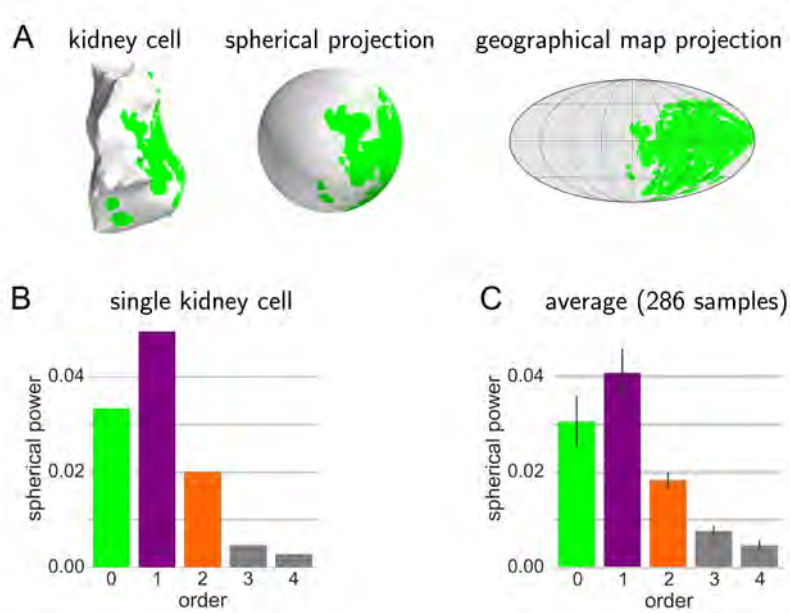


Figure 2.4. Mode expansion for kidney cells. (A) The three-dimensional mesh of a kidney cell with apical protein distribution (green) together with its spherical projection and geographical Mollweide projection. The Mollweide projection of this spherical projection shows that the apical membrane identity of the cell is aggregated one one side of the cell, reminiscent of a spherical cap as shown in Fig. 2.2. (B) The spherical power spectrum of the mode expansion of a single cell shows a clear peak in the first mode. (C) The average distribution over all cells in the tissue sample also exhibits a clear peak at the first mode. Experimental data: Zerial group at MPI-CBG.

2.2.2. Hepatocytes exhibit nematic polarity

An analogous analysis for hepatocytes of the liver is shown in Fig. 2.5. In contrast to the case of kidney, a dominant second mode is found. This is due to the approximate two-fold symmetry of the distribution about the north-south axis as seen in the Mollweide projection. Thus, hepatocytes display nematic cell surface polarity.

There are two interesting limit cases for second-order spherical anisotropies, which we will use to name the nematic axis. One is the case of two opposing spherical caps, already introduced in Fig. 2.2. The nematic axis corresponding to this limiting case is identified by the largest eigenvalue of the nematic cell polarity tensor (cf. equation (2.3)) and shall henceforth be denoted as *bipolar axis*.

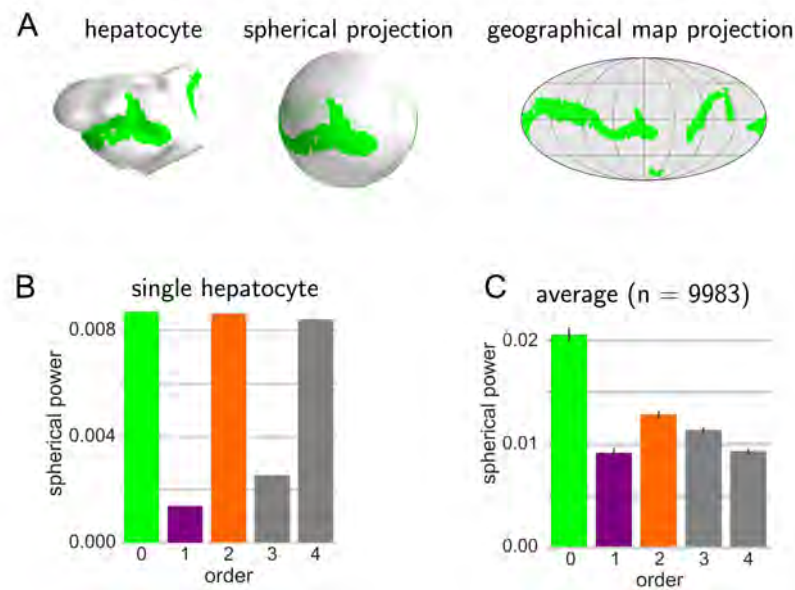


Figure 2.5. Mode expansion for hepatocytes in liver tissue. (A) The three-dimensional mesh of a hepatocyte with apical protein distribution (green) together with its spherical projection and geographical Mollweide projection. The Mollweide projection of this spherical projection shows that the apical membrane identity of the cell is clustered around the equator the cell. This indicated the same 2-fold symmetry as found in the example of bipolar caps in Fig. 2.2. (B) The spherical power spectrum of the mode expansion of this cell shows clear peaks in the even modes and high suppression of odd modes. (C) The average distribution over all cells in the tissue sample also exhibits a peak at the second mode, although less pronounced as for the individual cell shown. Experimental data: Zerial group at MPI-CBG.

The second limiting case is when the distribution is localized at a great circle of the sphere. The nematic axis characterizing this configuration belongs to the smallest eigenvalue of the nematic cell polarity tensor and is termed *ring axis* here, see Fig. 2.6A.

The degree of nematic anisotropy can be quantified by the two eigenvalues σ_1 and σ_3 , since the third one follows as $\sigma_2 = -\sigma_1 - \sigma_3$. As these eigenvalues effectively characterize the shape of the surface distribution, we also refer to them as *polarity weights*. The vast majority of polarity weights describing the apical membrane hepatocytes (gray dots) lie in between the ideal bipolar (orange line) and ring case (blue line), see Fig. 2.6B. Thus, two axes are needed to characterize the orientation of one single hepatocyte. The spatial distribution of individual cell polarity orientations will be discussed in section 4.

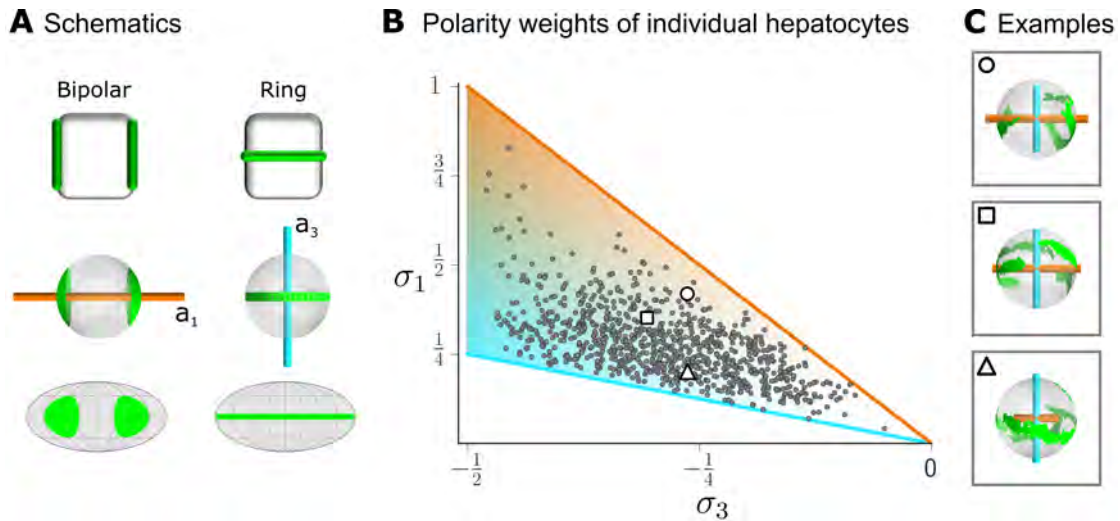


Figure 2.6. Polarity weights characterizing anisotropic apical membrane distribution on hepatocytes. (A) Limiting cases of the surface distribution used to name the nematic axes. Two opposing caps (left) with bipolar axis. The ring-axis is degenerate in that case. A ring forming a great circle (right) with ring-axis. In this case, the bipolar axis is degenerated. (B) Gray dots indicate values for the polarity weights σ_1 and σ_3 of hepatocytes in liver tissue. The orange line on the top of the triangle corresponds to the ideal bipolar case and the blue line corresponds to the ideal ring pattern. (C) Examples of real hepatocyte surface patterns with bipolar and ring axis indicated. Symbols correspond to location in the space of polarity weights in panel (B). Experimental data: Zerial group at MPI-CBG.

2.3. Local network anisotropy

In addition to the quantification of anisotropic distribution of membrane proteins, it is also interesting to analyze the immediate environment of cells. In particular, the organization of the sinusoidal transport network around cells is studied here. Sinusoids are highly-specialized blood vessels forming a network within the liver lobule (cf. section 1.2). The central lines of the sinusoids for a section of a liver lobule are shown in Fig 2.7A. Additionally, one hepatocyte is shown and the inset shows a magnified view of that particular hepatocyte together with the local segments of the sinusoid central lines. The hepatocytes are embedded in the sinusoid network in such a way that every hepatocyte is in contact with the network to be supplied with blood.

We determine the nematic order of the local network in the vicinity of a single cell. We define a unit vector \mathbf{e}_k parallel to a straight network central line segment with midpoint position \mathbf{x}_k and length l_k and define a rank-2 tensor

$$\mathbf{s} = \frac{1}{2} \sum_k w(\mathbf{x}_k) l_k (3 \mathbf{e}_k \otimes \mathbf{e}_k - \mathbb{1}) \quad . \quad (2.10)$$

Here, $w(\mathbf{x}_k)$ is a weighting function normalized as $\sum_k w(\mathbf{x}_k) l_k = 1$. We choose $w(\mathbf{x}_k)$ as a binary cutoff with fixed radius around the center of each hepatocyte to obtain, for each cell location, a nematic tensor \mathbf{s} characterizing the local anisotropy of the sinusoid network. We again sort the eigenvalues $\sigma_1, \sigma_2, \sigma_3$ of \mathbf{s} by magnitude and take $\sigma_1 \geq \sigma_2 \geq \sigma_3$.

The geometric meaning of \mathbf{s} can be understood as follows: The eigenvector \mathbf{s}_1 , corresponding to the largest eigenvalue, characterizes the direction of preferred sinusoid orientation and will be referred to as “preferred axis” in the following. The eigenvector \mathbf{s}_3 , corresponding to the smallest eigenvalue, defines the normal to a plane in which sinusoids orientations are preferentially distributed and will be referred to as “plane axis” in the following. The respective eigenvalues are a measure for the amount of anisotropy, similar to the polarity weights of membrane distributions introduced in the previous section. The eigenvalues of all local sinusoid anisotropy tensors for a liver data set are shown in Fig. 2.7B. We find pronounced biaxial anisotropy, reflected by data points far away from the uniaxial boundary lines indicated in orange and cyan. Note that due to the relatively small number of segments around each hepatocyte, random orientations can also yield

non-zero anisotropies. These are, however, much smaller than the ones observed in actual liver data, see appendix A.4 for details.

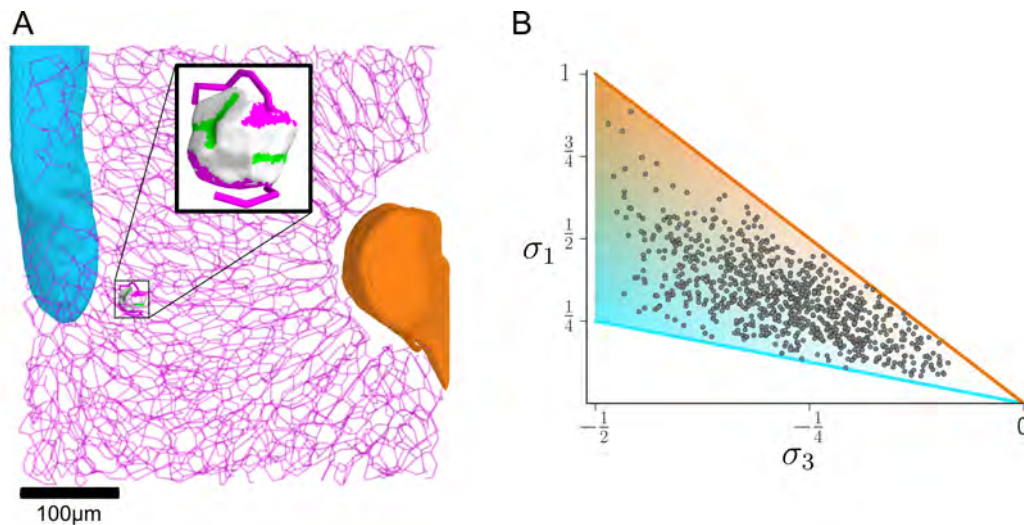


Figure 2.7. Local network anisotropy around cells. (A) Central lines of the sinusoid network (cf. section 1.6) shown for a section of a liver lobule between central vein (cyan) and portal vein (orange). Inset shows one hepatocyte together with the segments of the central lines with node positions within a sphere of $20\ \mu\text{m}$ around the center of the hepatocyte. (B) Eigenvalues of the nematic tensor \mathbf{s} for local sinusoid network around hepatocytes that characterize the amount of nematic anisotropy. Experimental data: Zerial group at MPI-CBG.

2.4. Summary

In this chapter, we defined and characterized two types of cell polarity: vectorial and nematic. These types represent symmetry types of surface patterns of (apical) membrane proteins. We showed that the cells of the kidney exhibit vectorial apico-basal cell polarity and cells in the liver exhibit nematic cell polarity. This is, to our knowledge, the first time that nematic cell polarity of hepatocytes has been quantified systematically in this way. Furthermore, we introduced a tool to quantify nematic anisotropy of networks around cells. These methods open up new possibilities to analyze structure order in tissue and will be applied to liver tissue in chapter 4 to identify biaxial liquid crystal ordering of apical nematic cell polarity of hepatocytes.

3. Order parameters for tissue organization

For individual cells, we established in chapter 2 that membrane protein distributions around individual cells of kidney and liver tissue are anisotropic. We now consider many cells that together constitute a biological tissue and study translational and orientational order of this composite material. In the present chapter, we introduce the necessary tools for this structural analysis. These tools will be applied to the study of liver tissue in chapter 4.

Regarding orientational order, we discuss two approaches: (i) scalar order parameters used in liquid crystal theory (cf. section 1.5.3) and (ii) invariants of tensor fields. We then extend the description to treat orientational order in curved geometries. This generalization is motivated by the lobular structure of liver tissue (cf. section 1.2). Complementary to this, we propose the concept of co-orientational order to compare two biaxial nematic fields within the same system. This approach will prove useful in the analysis of orientational order in tissues with spatially varying director fields, presented in chapter 4. In the last section of this chapter, we turn to translational order by providing concepts to quantify smectic and columnar order.

3.1. Orientational order: quantifying biaxial phases

In this section, we characterize orientational order of homogeneous systems by two methods: (i) four orientational order parameters S, P, D, C and (ii) invariants of moment tensors I_k . This analysis of orientational order of nematic objects is motivated by the finding that hepatocytes of the liver exhibit a second-order anisotropy that is captured by the nematic tensor $a_{\alpha\beta}$ (cf. equation (2.3)), which was presented in section 2.2.2. The analysis of orientational order outlined below is not specific to cell polarity but instead more general. We therefore use the generic term “object” to refer to individual constituents and denote the corresponding nematic tensor by $t_{\alpha\beta}$ (cf. Fig. 3.1).

We denote the tripod of ortho-normalized eigenvectors of this tensor by $\mathbf{l}, \mathbf{m}, \mathbf{n}$ with respective eigenvalues $\sigma_l, \sigma_m, \sigma_n$. The eigenvectors $\mathbf{l}, \mathbf{m}, \mathbf{n}$ are only defined up

3. Order parameters for tissue organization

to sign and the eigenvalues are ordered according to their magnitude, e.g. $\sigma_l \leq \sigma_m \leq \sigma_n$ or $\sigma_n \leq \sigma_l \leq \sigma_m$. A change in the ordering of eigenvalues corresponds to a permutation of the labels of nematic axes $\mathbf{l}, \mathbf{m}, \mathbf{n}$. This permutation of axes will be discussed in more detail in section 3.1.1.

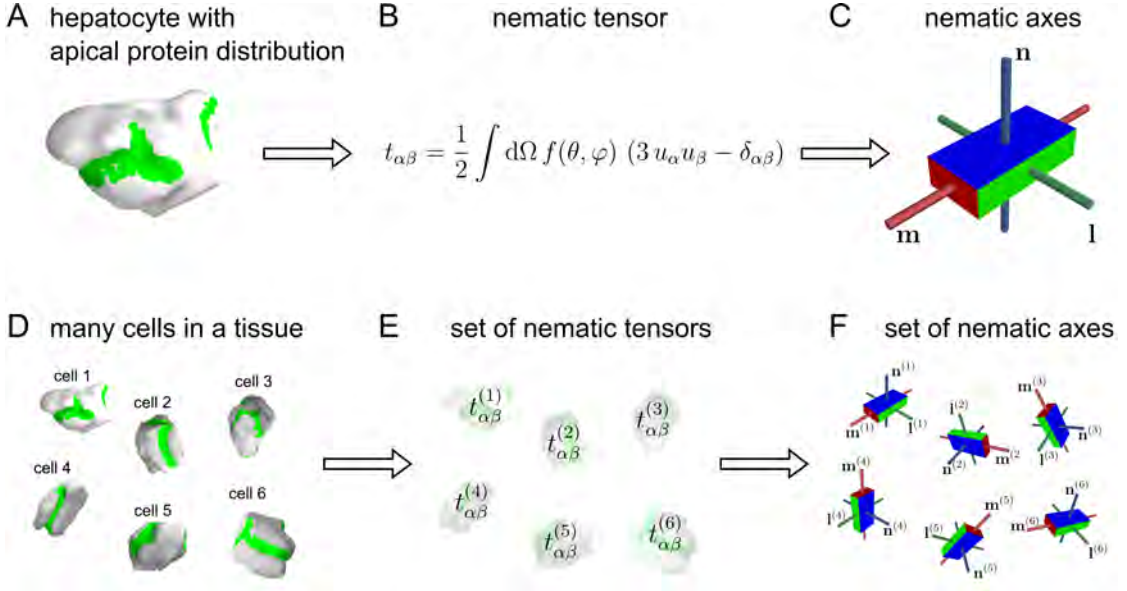


Figure 3.1. Hepatocytes in the liver: from surface distributions to nematic axes. The apical protein distribution of hepatocytes in the liver (A) exhibits a second-order anisotropy that is captured by the nematic tensor (B), as presented in section 2.2.2. The eigenvectors $\mathbf{l}, \mathbf{m}, \mathbf{n}$ of the nematic tensor define the nematic symmetry axis of each cell (C). Given many cells in a tissue (D), each nematic cell polarity is represented by a nematic tensor (E), which gives rise to a tripod of oriented, undirected nematic axes (F). The naming of the nematic axes $\mathbf{l}, \mathbf{m}, \mathbf{n}$ corresponds to an ordering of their respective eigenvalues, which is arbitrary but fixed for all cells in a tissue.

For many cells in a tissue, the nematic cell polarity of each cell i is represented by a nematic tensor $t_{\alpha\beta}^{(i)}$, see Fig. 3.1D and 3.1E. The corresponding nematic axes $\mathbf{l}^{(i)}, \mathbf{m}^{(i)}, \mathbf{n}^{(i)}$ are named according to their respective eigenvalues $\sigma_l^{(i)}, \sigma_m^{(i)}, \sigma_n^{(i)}$. The ordering of eigenvalues is arbitrary but fixed for all nematic tensors in the system. We will show that the four classical order parameters S, P, D, C have a direct geometrical interpretation but depend on a specific choice of axes permutation. The direct geometrical interpretation is absent for the invariants of moment tensors I_k but they do not depend on a specific permutation of axes. To simplify notation, we will drop the superscript i unless it is needed to resolve ambiguity between individual and averaged quantities.

3.1.1. Biaxial nematic order parameters

In section 1.5.1, we introduced three fundamental types of uniaxial nematic order: prolate, oblate and smectic. In general, individual objects do not exhibit axial symmetry and instead possess three distinct axes (see Fig. 2.6). In order to characterize orientational order of these biaxial objects¹, we employ the concept of biaxial nematic order parameters. In the following, we derive four scalar order parameters to characterize the orientational order of biaxial objects in a biaxial phase, discuss the subtle issue of permutation of object and reference axes, and provide a geometrical meaning for each of the four order parameters.

Four scalar orientational order parameters S , P , D , C for biaxial systems

Every nematic tensor \mathbf{t} of an individual nematic object can be written as a superposition of two traceless, irreducible orthogonal tensors \mathbf{q} and \mathbf{b} ([155, 156] and appendix A.7)

$$\mathbf{t} = \xi_0 \mathbf{q} + \xi_1 \mathbf{b} . \quad (3.1)$$

This decomposition separates the orientational part encoded in the tensors \mathbf{q} and \mathbf{b} from the anisotropy of the tensor \mathbf{t} , quantified by two shape parameters $\xi_0 = \sigma_n$ and $\xi_1 = \frac{1}{3}(\sigma_l - \sigma_m)$, which are given as linear combinations of the eigenvalues $\sigma_l, \sigma_m, \sigma_n$ of \mathbf{t} . The shape parameters characterize the second-order anisotropy of an object, represented by the tensor \mathbf{t} . We consider them as constant parameters, the same for all objects in the system². The orientation tensors \mathbf{q} and \mathbf{b} are given as linear combinations of dyadics of the eigenvectors \mathbf{l} , \mathbf{m} , \mathbf{n} of the nematic tensor \mathbf{t} and the identity matrix $\mathbb{1}$

$$\mathbf{q} = \frac{1}{2} (3 \mathbf{n} \otimes \mathbf{n} - \mathbb{1}) \quad , \quad \mathbf{b} = \frac{3}{2} (\mathbf{l} \otimes \mathbf{l} - \mathbf{m} \otimes \mathbf{m}) \quad . \quad (3.2)$$

Here, \otimes denotes the outer product. The advantage of this decomposition is that we can perform ensemble averages over the orientational parts

$$\mathbf{Q} = \langle \mathbf{q} \rangle \quad \text{and} \quad \mathbf{B} = \langle \mathbf{b} \rangle \quad (3.3)$$

¹The symmetry group of the biaxial nematic objects studied here is D_{2h} , which is the point group of ethene. It can be represented by three nematic axes (cf. appendix A.5).

²A similar expansion has been considered by Freiser [157].

3. Order parameters for tissue organization

separately from the shape anisotropy. The eigenvalues of these averaged tensors represent the relevant invariants S, P, D, C of orientational order for biaxial nematic objects

$$\mathbf{R}_Q^T \mathbf{Q} \mathbf{R}_Q = \begin{pmatrix} -\frac{1}{2}(S - P) & 0 & 0 \\ 0 & -\frac{1}{2}(S + P) & 0 \\ 0 & 0 & S \end{pmatrix}, \quad (3.4)$$

$$\mathbf{R}_B^T \mathbf{B} \mathbf{R}_B = \begin{pmatrix} -\frac{1}{2}(D - 3C) & 0 & 0 \\ 0 & -\frac{1}{2}(D + 3C) & 0 \\ 0 & 0 & D \end{pmatrix}. \quad (3.5)$$

Here, \mathbf{R}_Q and \mathbf{R}_B are rotation matrices that diagonalize \mathbf{Q} and \mathbf{B} , respectively.

We now consider the important special case that the system is in a phase exhibiting D_{2h} symmetry. Phases with this symmetry group exhibit three mutually orthogonal symmetry planes. For example, any ensemble of nematic objects, following a Boltzmann distribution for a Hamiltonian describing either local interactions or coupling to an external field, exhibits D_{2h} -symmetry, provided this Hamiltonian possesses D_{2h} symmetry itself [156, 158, 159]. In this case, \mathbf{Q} and \mathbf{B} diagonalize in the same eigenframe and one can set $\mathbf{R}_Q = \mathbf{R}_B$. The eigenvectors of \mathbf{Q} and \mathbf{B} thus coincide and specify normal vectors of the symmetry planes of the ensemble (also termed *director frame* [39, 115]). We denote them by $\mathbf{x}, \mathbf{y}, \mathbf{z}$. Equations (3.4) and (3.5) define four scalar orientational order parameters S, P, D, C . The exact normalization of these order parameters is subject to convention. An overview over normalizations that are common in the literature is provided by Rosso [160]

The order parameters can also be written as averages over direction cosines as [115, 160]

$$\begin{aligned} S &= \frac{1}{2} \langle 3(\mathbf{n} \cdot \mathbf{z})^2 - 1 \rangle, \\ P &= \frac{3}{2} \langle (\mathbf{n} \cdot \mathbf{x})^2 - (\mathbf{n} \cdot \mathbf{y})^2 \rangle, \\ D &= \frac{3}{2} \langle (\mathbf{l} \cdot \mathbf{z})^2 - (\mathbf{m} \cdot \mathbf{z})^2 \rangle, \\ C &= \frac{1}{2} \langle (\mathbf{l} \cdot \mathbf{x})^2 - (\mathbf{l} \cdot \mathbf{y})^2 + (\mathbf{m} \cdot \mathbf{y})^2 - (\mathbf{m} \cdot \mathbf{x})^2 \rangle. \end{aligned} \quad (3.6)$$

Where brackets $\langle \dots \rangle$ denote an ensemble average. Note that the reference frame

$\mathbf{x}, \mathbf{y}, \mathbf{z}$ is given by the symmetry properties of the phase and constant with regard to the ensemble average. In case of a discrete set of nematic tensors, as will be the case of cells in liver tissue in the next chapters, the ensemble average is replaced by a sum over all the tensors

$$\begin{aligned}
 S &= \frac{1}{2N} \sum_i \left(3 (\mathbf{n}^{(i)} \cdot \mathbf{z})^2 - 1 \right) \\
 P &= \frac{3}{2N} \sum_i \left((\mathbf{n}^{(i)} \cdot \mathbf{x})^2 - (\mathbf{n}^{(i)} \cdot \mathbf{y})^2 \right) \\
 D &= \frac{3}{2N} \sum_i \left((\mathbf{l}^{(i)} \cdot \mathbf{z})^2 - (\mathbf{m}^{(i)} \cdot \mathbf{z})^2 \right) \\
 C &= \frac{1}{2N} \sum_i \left((\mathbf{l}^{(i)} \cdot \mathbf{x})^2 - (\mathbf{l}^{(i)} \cdot \mathbf{y})^2 + (\mathbf{m}^{(i)} \cdot \mathbf{y})^2 - (\mathbf{m}^{(i)} \cdot \mathbf{x})^2 \right) \quad (3.7)
 \end{aligned}$$

This representation of the order parameters highlights the fact that they are averages over squares of direction cosines and are therefore restricted to lie in a specific four-dimensional domain given by [158]

$$\begin{aligned}
 -\frac{1}{2} \leq S \leq 1, & \quad -(1-S) \leq P \leq (1-S), \\
 -(1-S) \leq D \leq (1-S), & \quad C_{\min} \leq C \leq C_{\max} \quad (3.8)
 \end{aligned}$$

with

$$\begin{aligned}
 C_{\min} &= -\frac{1}{3} \min(2 + S + P + D, 2 + S - P - D), \\
 C_{\max} &= -\frac{1}{3} \min(2 + S + P - D, 2 + S + D - P). \quad (3.9)
 \end{aligned}$$

Equation (3.6) also provides the mapping of the order parameters S, P, D, C to the elements of the super-tensor $S_{\alpha\beta}^{ij}$ (cf. section 1.5.2). Using the property of direction cosines $\sum_{\alpha} j_{\alpha} j_{\alpha} = 1$, for all j and $\sum_j j_{\alpha} j_{\alpha} = 1$, for all α , one can solve the linear system in equation (3.6) for the squares of the direction cosines. These can then be substituted in equation (1.8) to yield the elements of the super-tensor in terms of the orientational order parameters S, P, D, C . This is performed explicitly in appendix A.6.

Permutation of symmetry axes

The numerical values of S, P, D, C depend on a chosen ordering of the object axes $\mathbf{l}, \mathbf{m}, \mathbf{n}$ and symmetry axes $\mathbf{x}, \mathbf{y}, \mathbf{z}$ and change under permutation of these axes. This ambiguity complicates the comparison of order parameters between different systems. There are two main issues: (1) two different 4-tuples S, P, D, C may, in fact, describe the same system and (2) the permutation ambiguity complicates the distinction between a biaxial and uniaxial system. In principle, both issues can be addressed by testing all permutations given in table A.1.

We first note that the restrictions on the range of accessible order parameters, given in eq. 3.8, define a polytope $\mathcal{P} \subset \mathbb{R}^4$ in the four-dimensional (S, P, D, C) -space. Permutation of the object axes $\mathbf{l}, \mathbf{m}, \mathbf{n}$ and reference axes $\mathbf{x}, \mathbf{y}, \mathbf{z}$ define a permutation group $G = S_3 \times S_3$ containing 36 elements (cf. table A.1). Each element $g \in G$ maps a point $p = (S, P, D, C) \in \mathcal{P}$ of the polytope \mathcal{P} onto another point $g(p) \in \mathcal{P}$. The images of a single point under all group elements form an orbit $\mathcal{O} = \{g(p), g \in G\}$ of that point. All points of an orbit describe the same state of orientational order and are thus equivalent.

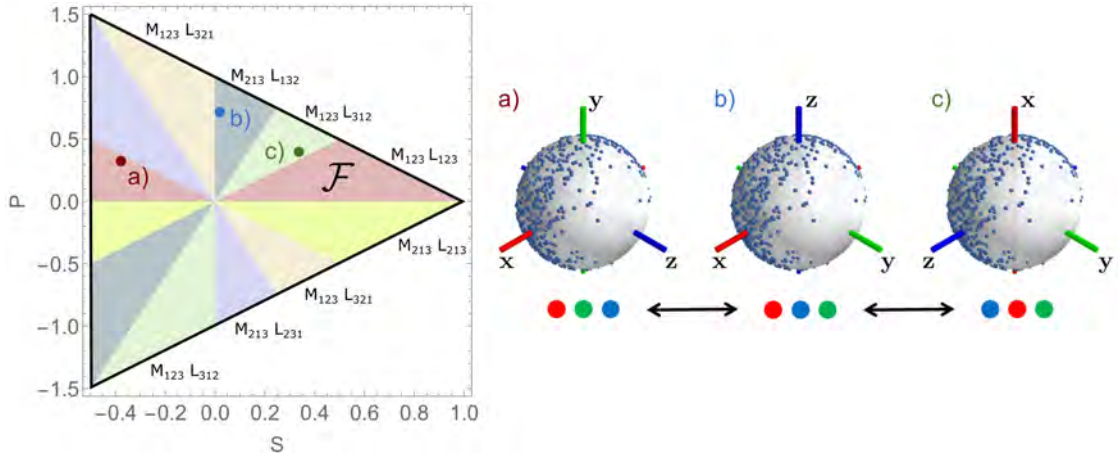


Figure 3.2. Action of axes permutation on the order parameters. Left: cut through the polytope \mathcal{P} for $D = 2\varepsilon$ and $C = \varepsilon$. A small perturbation $\varepsilon = 10^{-4}$ is used to avoid cutting along boundary surfaces. Colors indicate tessellation of this space into fundamental domains. The classical fundamental domain \mathcal{F} is shown in red. Labels on the domains denote the group element g of permutation of object axes (M) and reference axes (L) that transforms \mathcal{F} onto this domain (see also appendix A.8). Right: Distribution of orientations of uniaxial objects with phase-biaxial order in three different permutations of the symmetry axes of the phase. Letters correspond to points in the order parameter space on the left.

One conventional choice for a particular permutation of axes is the one that fulfills [161]

$$|S| = \text{maximal}, P \geq 0, C \geq 0 \text{ as well as } D \geq 0, \text{ if } C = 0. \quad (3.10)$$

These requirements define a fundamental domain $\mathcal{F} \subset \mathcal{P}$, which contains one point of each orbit. Note that only the first condition, namely requiring $|S|$ to be maximal, influences the magnitude of the order parameters, whereas the remaining conditions set the signs of the order parameters to a specific convention. For all points in \mathcal{F} , the order parameter S is identical to the uniaxial order parameter for systems with axial symmetry, which makes this choice particularly appealing [115]. Applying a group action $g \in G$ (excluding the identity operation) to all points in \mathcal{F} results in a different fundamental domain \mathcal{F}_g . Doing this for all elements in G results in 36 fundamental domains, which together give a tessellation of \mathcal{P} such that $\mathcal{P} = \bigcup_{g \in G} \mathcal{F}_g$. This tessellation is shown in Fig. 3.2 for a two-dimensional cut through \mathcal{P} .

The classical fundamental domain is also useful in determining, whether a given system is in a uniaxial or biaxial phase. For uniaxial systems $P = C = 0$ and a single reference axis \mathbf{z} is sufficient to characterize the phase (cf. equation (3.6)). Any deviation from axial symmetry is reflected in either P or C becoming non-zero. This is, in general, not the case for other fundamental domains.

Geometric meaning of orientational order parameters

We illustrate the geometric meaning of the orientational order parameters chosen to lie in the classical fundamental domain in Fig. 3.3. When $S > 0$ and the three remaining order parameters vanish (as shown in panel (A)), the ensemble is said to possess *uniaxial prolate order*³ [115]. Uniaxial orderings are axially symmetric around the main director. If fluctuations of the first principal axis are anisotropic, as shown in panel (B), the ensemble is said to possess *phase-biaxial order*⁴. This is quantified by the magnitude of the order parameter P . In panel (C), the other extreme of an axially-symmetric distribution is shown, where the directions of the first principal axis are concentrated on a great circle, which is termed *uniaxial oblate order*⁵. So far, we only examined the distribution of

³This type of order is also called *cluster order* [162].

⁴This type of biaxiality was first characterized by Freiser [157], see also appendix A.1.

⁵This type of order is also called *girdle order* [162].

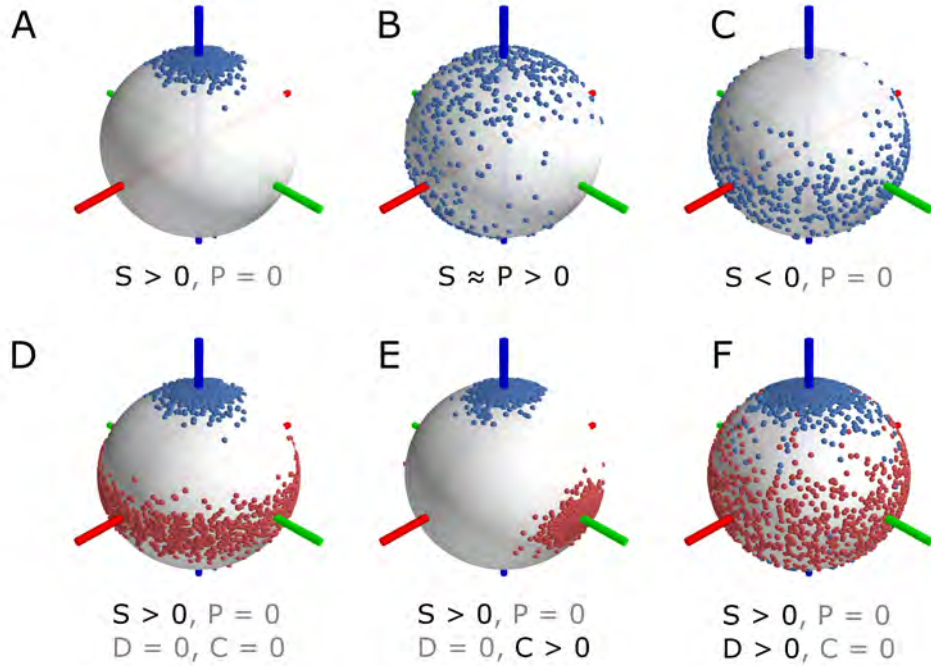


Figure 3.3. Schematics to illustrate orientational order parameters. (A) Distribution of a single axis with prolate nematic order relative to the main director axis (blue). Sample axes are indicated by pairs of antipodal blue points. (B) Example of a phase biaxial distribution with nematic alignment (towards the main director) and strong anisotropic fluctuations with bias towards the medium director (red). (C) Distribution of a single axis with oblate nematic order around a great circle about the main director. (D) Distribution of a tripod of axes with prolate nematic order of the first principal axis (blue) and no additional order of the second principal axis (red), third axis not shown. (E) Example of biaxial order measured by the order parameter C , where the first principal axis displays prolate nematic order as in panel (D) while the second principal axis (red) is additionally biased towards the minor director (green). (F) Illustration of molecular biaxiality, where the first principal axis (blue dots) exhibits nematic order with respect to the blue director, while fluctuations of the second principal axis (red dots) are biased in the direction of the same reference axes to an extent measured by D . In this case, the biaxial nature of individual objects is not reflected in the phase, which remains uniaxial.

one principal axis of the object’s anisotropy, which is quantified by the two order parameters S and P . We now turn to the full description of biaxial nematic order, characterizing the distribution of a tripod of axes for each individual object. For that we show in panels (D), (E), and (F) the effect of an additional ordering of a second principal axis indicated by red points on the sphere and explain how this effects the remaining two order parameters D and C . Fig. 3.3D shows the reference case in which a sample of an uniaxial prolate distribution is shown in blue. In absence of any additional ordering, the second principal axis (drawn in red) is in the uniaxial oblate state, as it is required to be perpendicular to the main axis⁶.

We now consider the case of an additional ordering on the second principal axis in panels (E) and (F). In panel (E), the second principal axis is biased towards a direction perpendicular to the main director. This breaks the axial symmetry around the main director for the second principal axis (red) but not for the first principal axis (blue). Therefore, the order parameter P describing the phase biaxiality of the first principal axis remains zero but the molecular biaxiality parameter C becomes nonzero. The parameter C therefore describes the deviation from axial symmetry of the distribution of the second principal axis around the main director. In contrast to that, it is possible that both nematic axes of individual objects compete for the same director as shown in panel (F) while their distribution remains axially symmetric around that axis. This case is captured by both P and C being zero and the competition is quantified by the molecular ordering parameter D being non-zero⁷. In this case, the phase remains axially symmetric but two molecular axes compete for alignment with the same director.

3.1.2. Co-orientational order parameters

The reference axes $\mathbf{x}, \mathbf{y}, \mathbf{z}$ used in the calculation of the orientational order parameters S, P, D, C are determined by the symmetry axes of a phase of biaxial objects. In a similar manner, we can consider the case where the reference axes are given by a second biaxial field. We now introduce the concept of *co-orientational order parameters*. For that, we consider two sets of nematic tensors $T_{\alpha\beta}^{(i)}$ and $K_{\alpha\beta}^{(i)}$. The basic idea is to calculate the orientational order parameters of one field in

⁶This example also demonstrates that the type of order (prolate or oblate) depends on the choice of which axis is taken as the first principal axis.

⁷This type of “molecular” biaxiality was first considered by Alben, McColl and Shih in [163]

the reference frame provided by the other. Formally, this is achieved by replacing the symmetry axes of the phase $\mathbf{x}, \mathbf{y}, \mathbf{z}$ in equation (3.6) by the object axes frame of the second tensor field. Specifically, denoting by $\mathbf{l}^{(i)}, \mathbf{m}^{(i)}, \mathbf{n}^{(i)}$ the eigenvectors of tensor $T_{\alpha\beta}^{(i)}$ with an arbitrary but fixed ordering of their respective eigenvalues and $\mathbf{u}^{(i)}, \mathbf{v}^{(i)}, \mathbf{w}^{(i)}$ the respective eigenvectors of tensor $K_{\alpha\beta}^{(i)}$, we define the co-orientational order parameters analogously to equation (3.6)

$$\begin{aligned}
 \text{co-}S &= \frac{1}{2N} \sum_i \left(3 (\mathbf{n}^{(i)} \cdot \mathbf{w}^{(i)})^2 - 1 \right) \\
 \text{co-}P &= \frac{3}{2N} \sum_i \left((\mathbf{n}^{(i)} \cdot \mathbf{u}^{(i)})^2 - (\mathbf{n}^{(i)} \cdot \mathbf{v}^{(i)})^2 \right) \\
 \text{co-}D &= \frac{3}{2N} \sum_i \left((\mathbf{l}^{(i)} \cdot \mathbf{w}^{(i)})^2 - (\mathbf{m}^{(i)} \cdot \mathbf{w}^{(i)})^2 \right) \\
 \text{co-}C &= \frac{1}{2N} \sum_i \left((\mathbf{l}^{(i)} \cdot \mathbf{u}^{(i)})^2 - (\mathbf{l}^{(i)} \cdot \mathbf{v}^{(i)})^2 + (\mathbf{m}^{(i)} \cdot \mathbf{v}^{(i)})^2 - (\mathbf{m}^{(i)} \cdot \mathbf{u}^{(i)})^2 \right)
 \end{aligned} \tag{3.11}$$

where we explicitly noted the index i , which runs over all N pairs of nematic tensors $(T_{\alpha\beta}^{(i)}, K_{\alpha\beta}^{(i)})$. This highlights the main difference to the classical orientational order parameters (cf. equation (3.6)). There, the reference axes $\mathbf{x}, \mathbf{y}, \mathbf{z}$ were given by the symmetry of the biaxial phase and were the same for all nematic objects in the system. In contrast to that, for co-orientational order parameters, the reference axes are given by a second tripod of nematic axes $\mathbf{u}^{(i)}, \mathbf{v}^{(i)}, \mathbf{w}^{(i)}$, which need not be constant throughout the system.

3.1.3. Invariants of moment tensors

An alternative to the classical order parameters introduced above is to quantify the state of orientational order of a nematic tensor field by constructing invariants of its moment tensors. The benefit of this approach is that tensor invariants are independent of the choice of ordering of axes. Here, we focus on the invariants of the first three moment tensors. The moment tensors are given by

$$\begin{aligned}
 \text{first moment:} & \quad T_{\alpha\beta} = \langle t_{\alpha\beta} \rangle \\
 \text{second moment:} & \quad V_{\alpha\beta\gamma\delta} = \langle t_{\alpha\beta} t_{\gamma\delta} \rangle \\
 \text{third moment:} & \quad K_{\alpha\beta\gamma\delta\epsilon\nu} = \langle t_{\alpha\beta} t_{\gamma\delta} t_{\epsilon\nu} \rangle \quad .
 \end{aligned} \tag{3.12}$$

Note that, because nematic tensors of individual objects $t_{\alpha\beta}$ are traceless ($t_{\gamma\gamma} = 0$), only some contractions are non-zero. Specifically, the only non-vanishing contraction of the second moment is $V_{\alpha\beta} = V_{\alpha\gamma\gamma\beta}$. From these moment tensors, invariants can be constructed as

$$T_{\alpha\alpha}, T_{\alpha\beta}T_{\beta\alpha}, T_{\alpha\beta}T_{\beta\gamma}T_{\gamma\alpha}, V_{\alpha\alpha}, V_{\alpha\beta}V_{\beta\alpha}, T_{\alpha\beta}V_{\beta\alpha}, \dots$$

When the ordered phase exhibits at least D_{2h} symmetry, the average tensor and its higher moments diagonalize in the same eigenframe (see appendix A.5). The invariants are then given by polynomials of the eigenvalues of the averaged tensor and higher moments. Specifically, denoting the eigenvalues of $T_{\alpha\beta}$ by $\sigma_1, \sigma_2, \sigma_3$ and $V_{\alpha\gamma\gamma\beta}$ by μ_1, μ_2, μ_3 , the invariants defined above are given as

$$\begin{aligned} I_1 = T_{\alpha\alpha} &= \sum_i \sigma_i, & I_2 = T_{\alpha\beta}T_{\beta\alpha} &= \sum_i \sigma_i^2, & I_3 = T_{\alpha\beta}T_{\beta\gamma}T_{\gamma\alpha} &= \sum_i \sigma_i^3, \\ I_4 = V_{\alpha\alpha} &= \sum_i \mu_i, & I_5 = V_{\alpha\beta}V_{\beta\alpha} &= \sum_i \mu_i^2, & I_6 = V_{\alpha\beta}V_{\beta\gamma}V_{\gamma\alpha} &= \sum_i \mu_i^3, \\ I_7 = T_{\alpha\beta}V_{\alpha\beta} &= \sum_i \sigma_i \mu_i, & I_8 = T_{\alpha\beta}T_{\beta\gamma}V_{\gamma\alpha} &= \sum_i \sigma_i^2 \mu_i, & I_9 = T_{\alpha\beta}V_{\beta\gamma}V_{\gamma\alpha} &= \sum_i \sigma_i \mu_i^2, \\ & \dots & & & & \dots \end{aligned} \tag{3.13}$$

In turn, the eigenvalues can either be determined by diagonalization of $T_{\alpha\beta}$ and $V_{\alpha\beta}$ or by solving a polynomial system of the tensor invariants. In general, infinitely many invariants can be constructed from the series of moment tensors. However, a finite number of them is sufficient to describe biaxial nematic systems (cf. appendix A.9). We will address this issue in detail when comparing the approach of tensor invariants with the approach of scalar order parameters in the next section.

3.1.4. Relation between these three schemes

Above, we introduced three methods to characterize the orientational order of a field of nematic tensors: (1) by four orientational order parameters S, P, D, C , (2) by co-orientational order parameters $\text{co-}S, \text{co-}P, \text{co-}D, \text{co-}C$, and (3) by invariants I_k of moment tensors. The main difference between the classical order parameters S, P, D, C and the co-orientational order parameters $\text{co-}S, \text{co-}P, \text{co-}D, \text{co-}C$ is that with the former, the permutation of symmetry axes is obtained by bounds on the values of the order parameters, whereas in the second method, the permutation

3. Order parameters for tissue organization

is postulated a priori (cf. section 3.1.2). The relation between the order parameters S, P, D, C and tensor invariants I_k is less obvious and will be discussed now.

For identical object anisotropies ξ_0 and ξ_1 , as considered here, the averaged nematic tensor $T_{\alpha\beta}$ is related to the averaged orientation tensors $Q_{\alpha\beta}$ and $B_{\alpha\beta}$ by

$$\langle t_{\alpha\beta} \rangle = T_{\alpha\beta} = \xi_0 Q_{\alpha\beta} + \xi_1 B_{\alpha\beta} . \quad (3.14)$$

Because $q_{\alpha\beta}, b_{\alpha\beta},$ and $\delta_{\alpha\beta}$ span the space of symmetric traceless tensors in three dimensions (cf. appendix A.7 and [156]), the second moment can also be given as a linear combination and reads $V_{\alpha\beta} = \xi'_0 Q_{\alpha\beta} + \xi'_1 B_{\alpha\beta} + \xi'_c \delta_{\alpha\beta}$ with $\xi'_0 = \frac{1}{2}(\xi_0^2 - 3\xi_1^2),$ $\xi'_1 = -\xi_0\xi_1$ and $\xi'_c = \frac{1}{2}(\xi_0^2 + 3\xi_1^2).$ A similar statement also holds for higher moments. Because of the linearity of the trace operation, the invariants of the moment tensors I_k can be expressed by the invariants of the ordering tensors $Q_{\alpha\beta}$ and $B_{\alpha\beta}.$ Note that due to the vanishing trace of the nematic tensor, $I_1 = T_{\alpha\alpha} = 0$ and $I_4 = V_{\alpha\alpha} = 3\xi'_c$ are independent of the orientational order of the system.

The eigenvalues of the first and second moment of the tensor field can be expressed in terms of the orientational order parameters as

$$\begin{aligned} 2\sigma_1 &= -\xi_0 S + \xi_0 P - \xi_1 D + 3\xi_1 C \\ 2\sigma_2 &= -\xi_0 S - \xi_0 P - \xi_1 D - 3\xi_1 C \\ 2\mu_1 &= -\xi'_0 S + \xi'_0 P - \xi'_1 D + 3\xi'_1 C + \xi'_c \\ 2\mu_2 &= -\xi'_0 S - \xi'_0 P - \xi'_1 D - 3\xi'_1 C + \xi'_c \end{aligned} \quad (3.15)$$

This system can be inverted to express the scalar orientational order parameters S, P, D, C in terms of invariants of the tensor field. Note that this shows explicitly that the average of the tensor field $T_{\alpha\beta}$ is not sufficient to quantify the state of biaxial nematic order. To determine all four scalar order parameters, at least the second moment tensor is needed⁸. It is now interesting to understand the relative benefits and downsides of both approaches.

As shown in section 3.1.1, the order parameters S, P, D, C have a direct geometrical meaning, which is not apparent for the invariants of moment tensors. On the other hand, the invariants of the moments tensors respect the permutation symmetry of the system and can be used directly for the construction of a Landau free energy. It is, however, possible to construct invariants from the scalar order

⁸If the nematic shape parameters are such that $\xi'_0 = \xi_0$ and $\xi'_1 = \xi_1,$ the third moment has to be considered in order to arrive at four linearly independent equations.

parameters as well. In fact, Matteis [140] pointed out that there are at most eight independent invariants of the two ordering tensors $Q_{\alpha\beta} = \langle q_{\alpha\beta} \rangle$ and $B_{\alpha\beta} = \langle b_{\alpha\beta} \rangle$, because both are symmetric traceless tensors. The arguments for that upper limit are summarized in appendix A.9.

3.1.5. Example: nematic coupling to an external field

We now show orientational order parameters, co-orientational order parameters and invariants of moment tensors for systems of biaxial objects subject to an externally applied field, to highlight the differences between these methods. The three-dimensional orientation of the external field is described by a tripod of ortho-normalized axes $\mathbf{e}_k = \mathbf{e}_x, \mathbf{e}_y, \mathbf{e}_z$. The interaction of the nematic axes $\mathbf{m}_i = \mathbf{m}_1, \mathbf{m}_2, \mathbf{m}_3$ of each individual object with that external field is described by a nematic interaction term $(\mathbf{m}_i \cdot \mathbf{e}_k)^2$ that is invariant under a flip of any molecular axis $\mathbf{m}_i \rightarrow -\mathbf{m}_i$ or an external field axis $\mathbf{e}_k \rightarrow -\mathbf{e}_k$. The interaction strength is controlled by coupling constants α_{ik} and the free energy of a single nematic object in an external field is given by

$$F_{\text{int}} = -U_0 \sum_{ik} \alpha_{ik} (\mathbf{m}_i \cdot \mathbf{e}_k)^2, \quad (3.16)$$

with an overall interaction strength $U_0 > 0$. The sign is chosen such that positive values of the coupling constants α_{ik} favor alignment of the specific axis with the respective reference axis. A particular realization of this biaxial nematic interaction model of molecules in an external field was considered by Carlsson and Leslie [116] in a theoretical study of nematogenic molecules in electric and magnetic fields.

We assume that the statistics of the system can be described by the Boltzmann distribution⁹

$$f(\varphi, \theta, \psi) = \frac{1}{Z} e^{-F_{\text{int}}(\varphi, \theta, \psi)/\nu}, \quad (3.17)$$

where ν controls the noise strength, which induces disorder in the system, and Z is the partition sum. Observables of the system, such as the order parameters S, P, D, C and invariants of moment tensors I_k , are given by averages over

⁹Note that the Boltzmann distribution describes canonical ensembles in thermodynamic equilibrium. Therefore, the statistical ensemble of the orientational distributions discussed here are equivalent to a system of particles interacting with an external field according to equation (3.16), coupled to a heat bath at temperature ν .

3. Order parameters for tissue organization

this orientational distribution function, which we determine numerically by discretizing the space of orientations φ, θ, ψ . We can now study how the microscopic interaction parameters α_{ik} influence the macroscopic phase of the system and how this is reflected in the orientational order parameters S, P, D, C and invariants of the moment tensors I_k . We will consider four cases: (A) uniaxial objects in an uniaxial phase, (B) uniaxial objects in a biaxial phase, (C) biaxial objects in a uniaxial phase and (D) biaxial objects in a biaxial phase. The classical order parameters S, P, D, C for these cases are shown in Fig. 3.4. To simplify notation, the

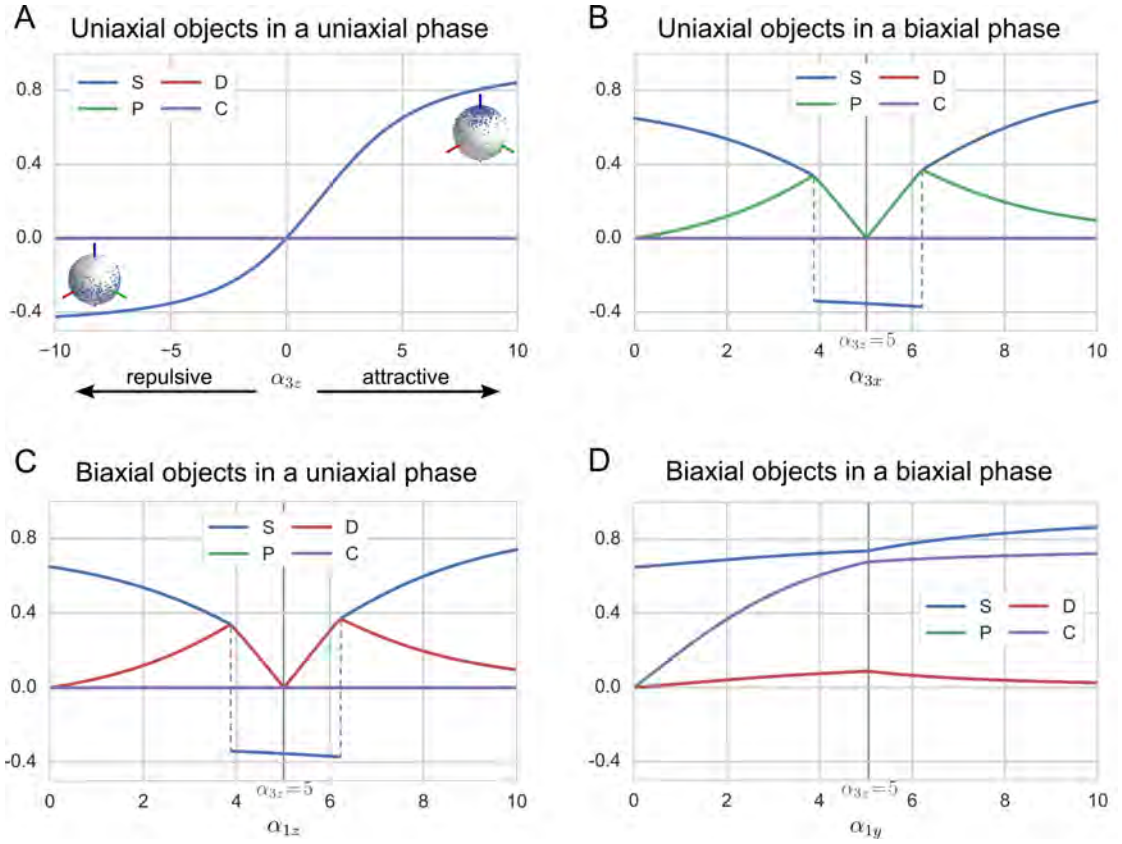


Figure 3.4. Classical order parameters S, P, D, C for four types of external biaxial fields. (A) Uniaxial ordering of uniaxial objects. (B) Biaxial phase of uniaxial objects. (C) Uniaxial phase of biaxial objects. (D) Biaxial phase of biaxial objects.

coefficients α_{ik} are given in units of U_0/ν .

(A) Uniaxial ordering of uniaxial objects. We start with the simplest case of one axis of the objects interacting with one axis of the reference frame. Hence, we have $\alpha_{3z} \neq 0$ and set all other interaction parameters to zero. The result is a uniaxial phase, characterized by the single non-zero uniaxial order parameter

S . For negative values of α_{3z} , the interaction between the object's axis and the external field axis is repulsive and the resulting orientational order is oblate ($S < 0$). For positive values of α_{3z} , the interaction between the object's axis and the external field axis is attractive and the resulting orientational order is prolate ($S > 0$).

(B) Phase biaxial ordering of uniaxial objects. If a single object axis interacts with more than one reference axes, the observed phase becomes biaxial. We illustrate this by setting $\alpha_{3z} = 5$ and varying α_{3x} instead. For $\alpha_{3x} = 0$ the system is in a uniaxial phase but for increasing α_{3x} it becomes phase biaxial, characterized by the order parameter P . The dominant order is prolate, meaning, that the object axis is preferentially aligned with the z -direction. This is captured by a positive order parameter S . When α_{3x} crosses a threshold value. the dominant order becomes oblate, which means that the object axes is preferentially in the xz -plane. This is characterized by a negative value of S . At this point, the maximum of the phase biaxiality is reached. When α_{3x} is increased further and approaches $\alpha_{3z} = 5$, the phase biaxiality decreases and for the point $\alpha_{3x} = \alpha_{3z} = 5$ the system is in the uniaxial oblate phase. Upon further increase of the second interaction parameter α_{3x} , phase biaxiality increases again and the dominant order type switches back to prolate but with alignment preferential in the x -direction. Phase biaxiality decreases asymptotically to zero for $\alpha_{3x} \rightarrow \infty$, because the deviation from axial symmetry is only possible in non-perfectly ordered systems.

(C) Uniaxial ordering of biaxial objects. If two axes of the object interact with a single reference axis, the microscopic biaxiality is not propagated to the phase, which remains uniaxial. This is achieved by setting $\alpha_{3z} = 5$ and varying α_{1z} . An increase of α_{1z} leads to a competition of two molecular axes about aligning with the reference z -direction, which reduces the dominant ordering parameter S . When both interaction parameters are of comparable magnitude, the dominant order type switches to be oblate, characterized by negative values of S . This case is very similar to the one of phase biaxial ordering in that they are mapped onto each other by exchange of the roles of biaxial object and reference axes.

(D) Biaxial ordering of biaxial objects. If two axes of the object interact with two reference axes in a non-competing way, the molecular biaxiality is translated to the phase, which then also become biaxial. This is markedly different from the

3. Order parameters for tissue organization

case of phase biaxiality, where a single axis interacts with a two reference axis. Here, we set $\alpha_{3z} = 5$ and change α_{1y} . Again, starting at the uniaxial prolate phase an increase of α_{1y} changes the dominant order type characterized by S only slightly. Instead, the biaxial order parameter C becomes non-zero, characteristic of this phase. Interestingly, also the order parameters D and P become non-zero through the additional interaction parameter. However, both D and P approach zero in the limit of perfect biaxial ordering, whereas S and C approach unity.

The convention to choose the order parameters S, P, D, C in the classical fundamental domain has the drawback that these order parameters may jump discontinuously, although the orientational order of the system changes continuously. The co-orientational order parameters, however, do not change discontinuously. A direct comparison between both values is given in Fig. 3.5 for the case of phase biaxiality. We can see that for this particular choice of axes ordering in the co-

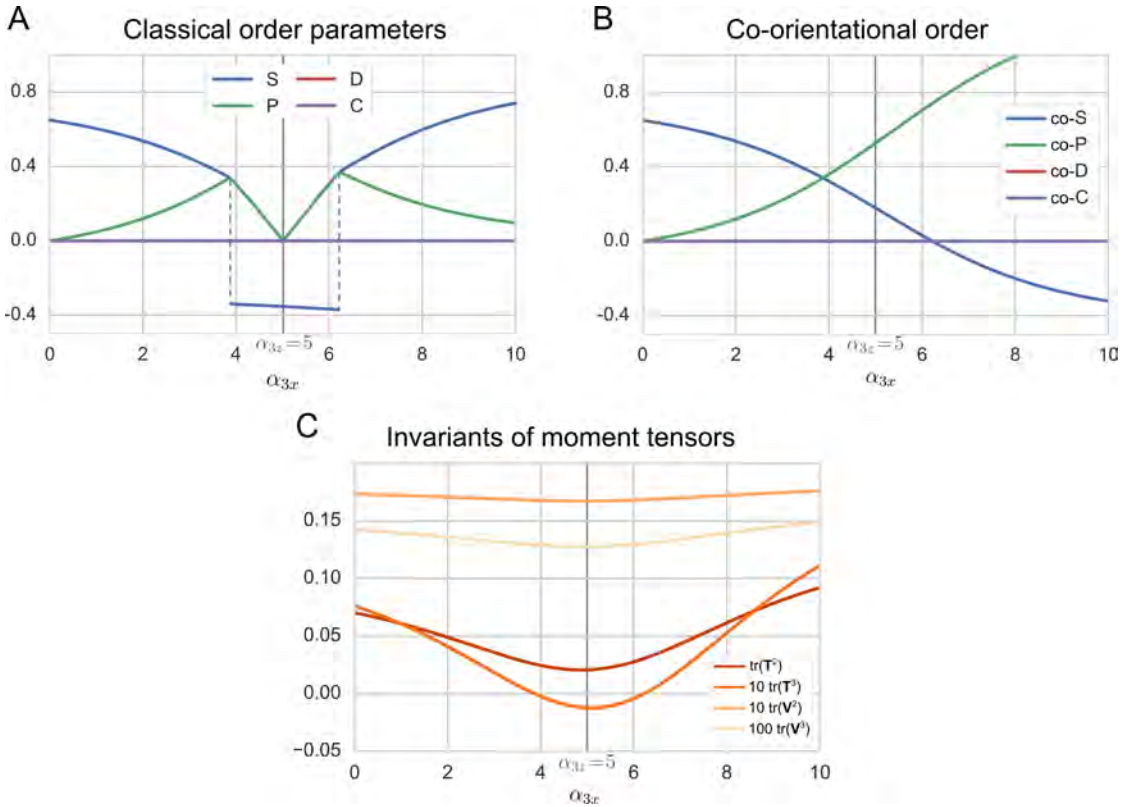


Figure 3.5. Direct comparison of classical order parameters, co-orientational order parameters and invariants of moment tensors for phase biaxial order. (A) Classical order parameters and (B) co-orientational order parameter for phase biaxial system. The classical order parameters may jump discontinuously upon a continuous change of the microscopic interaction parameters, whereas the co-orientational order parameters vary smoothly.

orientational order parameters, they are identical to the classical order parameters for small values of α_{3x} . At the point where the orientational order parameters have a discontinuity, however, the co-orientational order parameters vary smoothly, which makes them more suitable to describe orientational order for systems, where a control parameter is varied continuously. Their geometrical meaning, however, is less transparent than for the conventional order parameters. The same applies to the invariants of moment tensors.

3.2. A tissue-level reference field

We introduce the concept of a tissue-level reference field, which will be useful to analyze biological data in chapter 4. Spatially varying director fields are often related to structural landmarks that either provide boundary conditions [164] or are the organizing centers for external ordering fields, such as morphogen gradients [60].

In the liver, a tissue-level reference field has so far not been observed directly. However, the locations of afferent (portal veins and arteries) and efferent (central veins) blood vessels provide natural candidates for organizing centers. We therefore define a reference coordinate system that encodes a relative distance between the locations of portal and central veins.

To that end, we construct a scalar potential $\chi(\mathbf{r})$ as a solution to Laplace's equation

$$\Delta\chi(\mathbf{r}) = 0 \tag{3.18}$$

with boundary conditions $f(\mathbf{r})$ on the surfaces of the portal and central veins as defined below. This generic equation describes phenomena ranging from electrostatics to stationary diffusion profiles. As explained in section 1.6 the locations of the veins are given as triangulated meshes. We therefore describe the boundary conditions $f(\mathbf{r})$ as a superposition of point sources and sinks. Specifically, point sources are placed at locations of triangle centers \mathbf{r}_i of meshes belonging to afferent vessels (portal veins) with magnitude proportional to the relative area of the triangle with respect to the total area of the corresponding vessel $q_i = A_i / \sum_i A_i$. Correspondingly, point sinks with magnitude $\bar{q}_j = A_j / \sum_j A_j$ are placed on the triangle centers $\bar{\mathbf{r}}_j$ of efferent vessels (central veins). We therefore define the boundary

3. Order parameters for tissue organization

conditions $f(\mathbf{r})$ on a discrete set of points as

$$f(\mathbf{r}) = -4\pi \sum_{i \in I_{PV}} q_i \delta(\mathbf{r} - \mathbf{r}_i) + 4\pi \sum_{j \in I_{CV}} \bar{q}_j \delta(\mathbf{r} - \bar{\mathbf{r}}_j), \quad (3.19)$$

where the index $i \in I_{PV}$ runs over the triangles of the mesh constituting portal veins and $j \in I_{CV}$ runs over triangles constituting the mesh of central veins.

The Green's function $G(\mathbf{r}, \mathbf{r}') = -|\mathbf{r} - \mathbf{r}'|^{-1}/4\pi$ of the Laplace operator describes the response of the system to a unit point source $\Delta G(\mathbf{r}, \mathbf{r}') = \delta(\mathbf{r} - \mathbf{r}')$. The total field χ is then given as a superposition

$$\chi(\mathbf{r}) = \sum_{i \in I_{PV}} \frac{q_i}{|\mathbf{r} - \mathbf{r}_i|} - \sum_{j \in I_{CV}} \frac{\bar{q}_j}{|\mathbf{r} - \bar{\mathbf{r}}_j|}. \quad (3.20)$$

The value at a specific location is a measure of distance between the two vessel types. Positive values correspond to positions near the portal veins, whereas negative values indicate closeness to the central vein. The gradient of this scalar field, $\nabla\chi$ gives a reference direction throughout the lobule represented by the unit vector $\mathbf{e}_\chi = \nabla\chi/|\nabla\chi|$. To illustrate the resulting tissue-level reference field, we show the streamlines of this vector field $\nabla\chi$ for a simple configuration of cylindrical vessels in Fig. 3.6. In an analogy with potential flow in fluid dynamics, these streamlines correspond to paths that particles in an incompressible fluid would take, where the velocity field of the flow is given by $\mathbf{v}(\mathbf{r}) = \nabla\chi(\mathbf{r})$. In this analogy, the boundary conditions introduced above represent sources and sinks of the flow field.

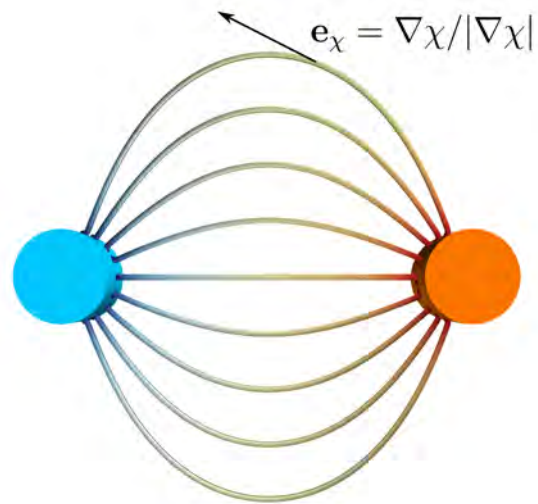


Figure 3.6. Streamlines of tissue-level reference field for idealized synthetic configuration of veins. Idealized cylindrical central vein (blue) and portal vein (orange) are used to define a tissue-level reference system interpolating the locations between opposing vessels. The color of the streamline encodes the value of the scalar field. Orange color indicates closeness to the portal vein and blue color indicates closeness to the central vein. The gradient of this scalar field $\nabla\chi$ provides a reference direction represented by the unit vector $\mathbf{e}_x = \nabla\chi/|\nabla\chi|$ and is the local tangent on the streamlines.

3.3. Orientational order in inhomogeneous systems

So far, we have considered homogeneous systems, where the director frame and strength of orientational order are uniform in the system. We now turn to the study of systems with spatially-varying orientational order. The purpose of this section is to provide a methodology to estimate a spatially-varying director field from data.

There are, in general, three approaches to estimate a spatially-varying director field from data: (i) temporal averages, (ii) ensemble averages, and (iii) spatial averages over small regions. The experimental data considered in this thesis consist of fixated tissue samples (cf. section 1.6), which rules out temporal and ensemble averages for analysis. We therefore turn to spatial averages over small regions to approximate the local director field.

Coarse-graining spatially discrete nematic tensor fields. Given a set of nematic tensors $T_{\alpha\beta}^{(i)}$ at positions \mathbf{r}_i , we define a coarse-grained nematic tensor field using a kernel function $g_\sigma(\mathbf{r}, \mathbf{r}')$, that is localized to a length-scale σ , by

$$\langle T_{\alpha\beta} \rangle_\sigma(\mathbf{r}_k) = \frac{\sum_{i \neq k} g_\sigma(\mathbf{r}_k, \mathbf{r}_i) T_{\alpha\beta}^{(i)}}{\sum_{i \neq k} g_\sigma(\mathbf{r}_k, \mathbf{r}_i)} \quad (3.21)$$

where we introduced the notation $\langle \dots \rangle_\sigma$ to indicate a localized average over a length-scale σ . Below, we will use the (isotropic) Gaussian normal distribution in three dimensions $g_\sigma(\mathbf{r}, \mathbf{r}') = (2\pi\sigma^2)^{3/2} \exp\left(-\frac{|\mathbf{r}-\mathbf{r}'|^2}{2\sigma^2}\right)$ with standard deviation σ as the local averaging kernel. In the definition of the coarse-grained tensor in equation (3.21), we have omitted the tensor at the location \mathbf{r}_k , where the local director is estimated, from the average. This is done to avoid over-estimation of orientational order as the nematic tensor at location \mathbf{r}_k would enter the average with the largest weight¹⁰.

The resulting locally averaged tensor $\langle T_{\alpha\beta} \rangle_\sigma(\mathbf{r}_k)$ is traceless and symmetric and can therefore be diagonalized. We denote the eigenvectors of the locally averaged

¹⁰In other words, if one would choose not to eliminate the tensor at the center point and let the standard deviation σ of the Gaussian kernel go to zero, the averaged tensor would be identical to the one in the center. If one then compares the individual nematic orientations to the averaged ones with the co-orientational order parameters introduced above, one would always obtain perfect alignment, even if in reality orientations are uncorrelated. This is not possible, if one eliminates the center tensor, which is the strategy adopted here.

tensors by $\bar{\mathbf{t}}_1, \bar{\mathbf{t}}_2, \bar{\mathbf{t}}_3$ and taken them as the local director, where the ordering of eigenvalues is arbitrary but fixed. The co-orientational order parameters (cf. section 3.1.2) between the object nematic axes, resulting from individual tensors $T_{\alpha\beta}^{(i)}$, and the estimate of the local director frame are used to characterize the orientational state of systems with curved director fields.

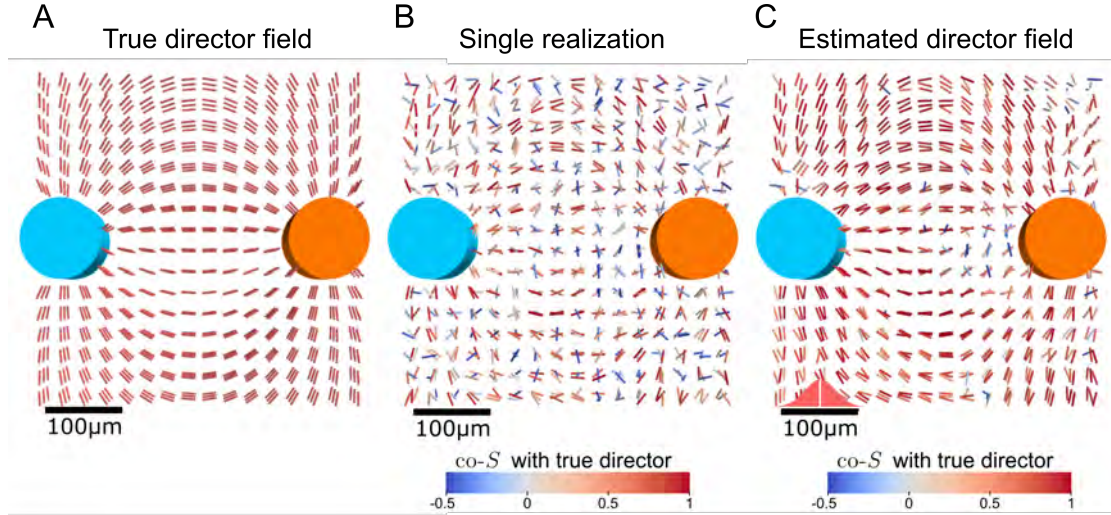


Figure 3.7. Estimation of director orientation for synthetic data. (A) Spatial distribution of true director field $\mathbf{e}_z(\mathbf{r}_i)$ at positions \mathbf{r}_i on a simple cubic lattice. (B) Single realization of uniaxial order following the Boltzmann distribution given in equation (3.17) with $U_0 \alpha_{3z}/\nu = 2$. This describes an uniaxial nematic coupling between an object axis $\mathbf{m}_3(\mathbf{r}_i)$ and the curvilinear field $\mathbf{e}_z(\mathbf{r}_i)$ at individual lattice positions \mathbf{r}_i (cf. section 3.1.5). (C) Estimated director field using coarse-graining with Gaussian kernel with $\sigma = 20 \mu\text{m}$ (shown for reference above the scale bar).

Coarse-graining in a simple curvilinear director field To illustrate the method, we show a simplified example of uniaxial order around a director given by the tissue-level reference field introduced in the previous section and shown in Fig. 3.7A. The systems consists of two cylindrical veins, as introduced in the previous section. Positions of nematic tensors are distributed on a regular grid with a lattice spacing comparable to the cell distance of hepatocytes in the liver¹¹. For this illustration, we use the Boltzmann distribution given in equation (3.17) with $U_0 \alpha_{3z}/\nu = 2$ as the only non-zero interaction between the object axes and the external field, which describes an uniaxial nematic coupling between an object axis $\mathbf{m}_3(\mathbf{r}_i)$ and

¹¹Specifically, cylinder centers are $330 \mu\text{m}$ apart and each cylinder has a radius of $50 \mu\text{m}$. Nematic objects are located on a simple cubic lattice with lattice constant $25 \mu\text{m}$ and three layers of nematic objects (in viewing direction) are considered.

the curvilinear field $\mathbf{e}_z(\mathbf{r}_i)$ at individual lattice positions \mathbf{r}_i . Sample configurations are obtained by inverse transform sampling on a discretization of orientation space. A single realization is shown in Fig. 3.7B. There, the order is not prevalent and the director field cannot be made out visually. Nevertheless, using the estimation procedure introduced above it is possible to get an estimated director field that closely follows the true director field from just a single realization, as shown in Fig. 3.7C.

The choice of coarse-graining length scale σ depends on the specific system at hand. It should be large enough to achieve a good statistic for the local director estimate. On the other hand, σ should be chosen small enough, in order to describe spatial variations of the local director.

3.4. Positional order: identifying signatures of smectic and columnar order

We use the structure function to characterize positional order of tissue structures. The structure function is a central quantity in the classification of matter [165]. It is used to discriminate between liquids and crystals and the mesophases between them (see section 1.5). One can distinguish four broad classes of positional order: liquids, columnar liquid crystals, smectic liquid crystals and crystals [39, pp. 34, 409]. In liquids, there is no long-range positional order, whereas in crystals, constituents are arranged on a three-dimensional lattice [165]. If positional order is present in one dimension, we speak of a smectic phase and when positional order is observed in two dimensions a columnar phase is encountered [39].

The structure function is the Fourier transform of the two-point density-density correlation function $\langle \rho(\mathbf{r})\rho(\mathbf{r}') \rangle$ [165]

$$I(\mathbf{q}) = \int e^{-i\mathbf{q}\cdot(\mathbf{r}-\mathbf{r}')} \langle \rho(\mathbf{r})\rho(\mathbf{r}') \rangle d^3r d^3r' \quad . \quad (3.22)$$

The data to be analyzed consists of binarized voxel¹² images, where the value indicates the presence or absence of a cell. The density is therefore given as $n(\mathbf{r}) = \sum_{\alpha} \delta(\mathbf{r} - \mathbf{r}_{\alpha})$, where $\{\mathbf{r}_{\alpha}\}$ is the set of voxel locations, where cells are present.

¹²Voxels are the three-dimensional generalizations of pixels, familiar from two-dimensional images.

In this case, the structure function simplifies to the absolute square of the Fourier transform of the number density

$$I(\mathbf{q}) \propto S(\mathbf{q}) = \left\langle \sum_{\alpha, \beta} e^{-i\mathbf{q} \cdot (\mathbf{r}_\alpha - \mathbf{r}_\beta)} \right\rangle = \left\langle \sum_{\alpha} e^{-i\mathbf{q} \cdot \mathbf{r}_\alpha} \sum_{\beta} e^{i\mathbf{q} \cdot \mathbf{r}_\beta} \right\rangle = \langle |\rho(\mathbf{q})|^2 \rangle \quad (3.23)$$

with the Fourier transform¹³ of the density $\rho(\mathbf{q})$. Periodic structures in the distribution of cells¹⁴ lead to characteristic peaks of the structure function at non-zero wave-vectors \mathbf{q} . The peaks form a lattice in the reciprocal space of wave-vectors and the dimensionality of this lattice reflects the type of positional order between a liquid and a crystal, as detailed above.

Three-dimensional structure functions cannot be easily visualized and interpreted. We therefore project the densities along different directions and calculate the two-dimensional structure function of these images. We subtract the mean of the input images to avoid the otherwise dominating peak at zero wave-vector.

To illustrate this approach to structural analysis on voxelized binary data, we consider idealized arrangements of smectic and columnar order. In Fig. 3.8A, three orthogonal cut-planes through an idealized system of smectic order is shown. Cells (red voxels) are arranged into layers, which are stacked in z-direction. There is no positional order of cells within each layer. The cube is summed along each axis individually and the two-dimensional structure function is calculated. The layered order is characterized by two peaks in the structure function for the summed densities in x- and y-direction. The absence of order within the layers is quantified by a diffuse peak at the center of the structure function when considering the density summed in z-direction.

In the idealized case of columnar order, shown in Fig. 3.8B, cells are arranged into columns on a two-dimensional grid, with no positional order along the direction of the columns. Again, this order is reflected in the structure functions of the summed densities. The two-dimensional grid is easily visible in x-direction, whereas an apparent layered order is seen in the other two directions.

¹³We write the Fourier transform as $\rho(\mathbf{q}) = \int n(\mathbf{r})e^{-i\mathbf{q} \cdot \mathbf{r}}d^3r$, which yields for a discrete set of voxel locations, as considered above, $\rho(\mathbf{q}) = \sum_{\alpha} e^{-i\mathbf{q} \cdot \mathbf{r}_\alpha}$. Taking the absolute square of this leads to the last equality in equation (3.23).

¹⁴Note that, due to the limitation of experimental imaging to fixated samples (cf. section 1.6), we are not able to perform an ensemble average and instead perform the analysis on single realizations of the system.

3. Order parameters for tissue organization

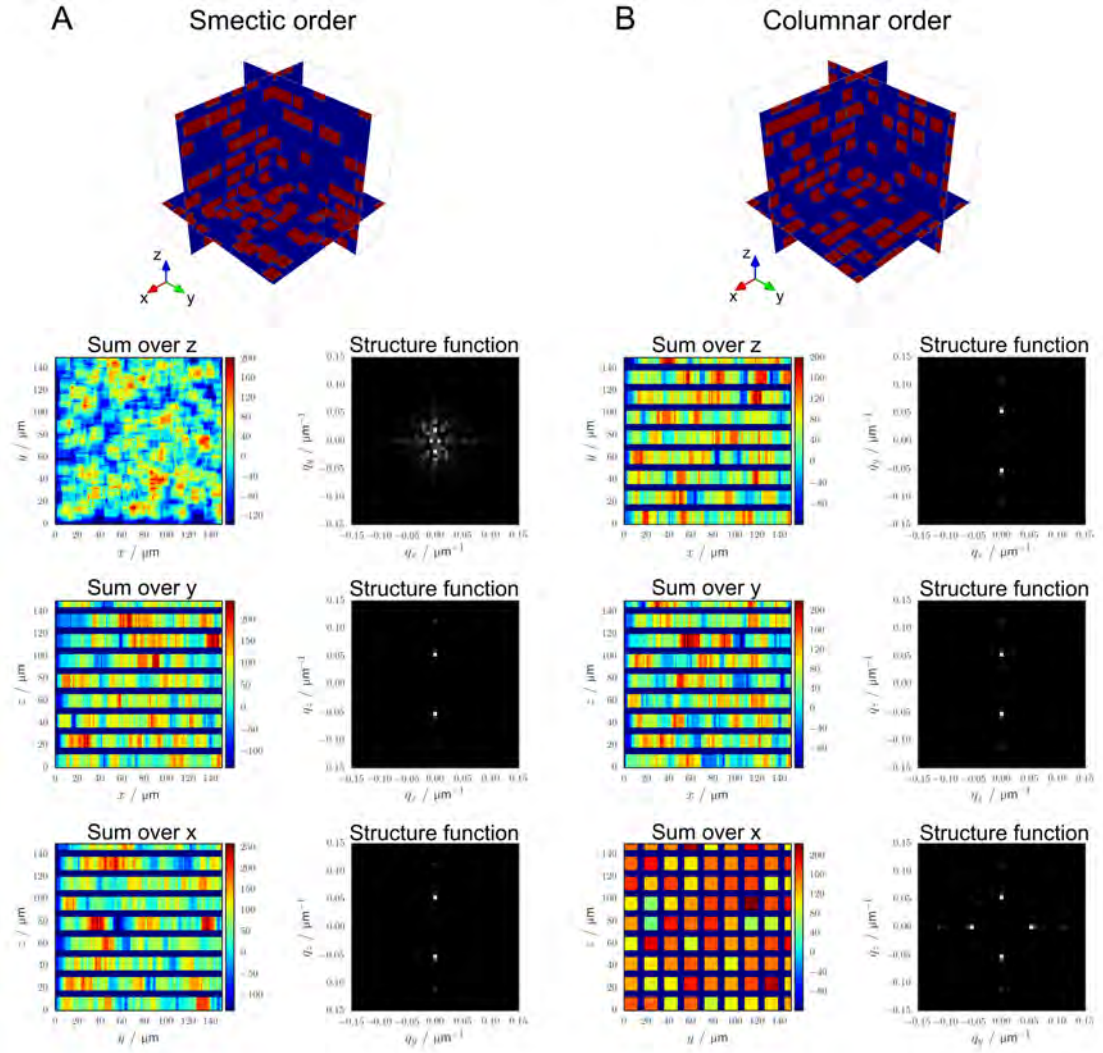


Figure 3.8. Examples to illustrate structure function of smectic and columnar order. (A) Random distribution of cubes in layers in z -direction with fixed distance. Smectic order is reflected by characteristic peaks of the structure function (cf. eq.(3.23)) at non-zero wavelengths. (B) Random distribution of cubes in columns with perfect square ordering in y - z plane. Columnar order is reflected by characteristic peaks at non-zero wavelengths, see text for details.

By this analysis, signatures of smectic and columnar order can be identified in binarized voxelized cell distributions.

3.5. Summary

In the present chapter, we introduced mathematical tools for the subsequent analysis of structural order of liver tissue in chapter 4. We addressed orientational and positional order. To characterize orientational order in spatially homogeneous systems, we reviewed classical orientational order parameters S, P, D, C , and introduced invariants of moment tensors I_k and co-orientational order parameters $co-S, co-P, co-D, co-C$ as alternative measures. We showed that all three schemes are directly related for systems in which all objects have identical anisotropies. To showcase how uniaxial and biaxial orientational order is captured by these three different types of order parameters, we used a simple model of nematic coupling to an external field¹⁵. We showed that the classical orientational order parameters provide an intuitive geometrical interpretation at the expense of discontinuous jumps¹⁶ upon gradual changes of orientational order (cf. Fig. 3.4). In contrast, the tensor invariants do not jump discontinuously but in turn lack an intuitive geometric interpretation (cf. Fig. 3.5). Finally, with a suitable choice of nematic reference frame, the co-orientational order parameters change continuously and also yield a geometrical meaning through their relation to the classical order parameters.

Equipped with these orientational order parameters for homogeneous systems, we turned to characterize orientational order in curved geometries. The basic approach is to find a suitable nematic reference field to define co-orientational order parameters. In this chapter, we introduced two possibilities. First, we defined a tissue-level reference field based on locations of landmarks, e.g. large blood vessels, within a tissue¹⁷. Secondly, we introduced a coarse-graining procedure to obtain estimates for a local director in systems with curved directors. Additionally to the two presented options, the nematic reference field can be given by other tissue structures, e.g. orientation of anisotropy of transport networks surrounding the

¹⁵We will return to this model in section 5.4, where we study biaxial alignment of cell polarity with local anisotropy of the sinusoid network in liver tissue.

¹⁶The reason for these jumps is their restriction to a specific fundamental domain in the parameters space, which is motivated by the equivalence with the common uniaxial order parameter S (see section 3.1.1).

¹⁷Evaluating the direction of the gradient of this field at the positions of cells provides a nematic reference axis.

3. Order parameters for tissue organization

cells (cf. section 2.3), which are co-located with the positions of cells. These three variants of co-orientational order are used in the next chapter for the analysis of cell polarity in liver tissue.

In the last section of the present chapter, we introduced a method to identify signatures of smectic and columnar order from experimental data using the structure function.

4. The liver lobule exhibits biaxial liquid-crystal order

In chapter 2, we saw that the distribution of membrane-bound proteins on cell surfaces is anisotropic. In particular, hepatocytes of the liver exhibit a *nematic cell polarity* characterized by a dominant second mode in the spherical power spectrum. This anisotropy defines an orientation of a cell within the tissue that is characterized by a tripod of nematic cell polarity axes. In this chapter, we study orientational order of hepatocytes within the liver, using concepts from liquid-crystal theory introduced in chapter 3. Our analysis identifies so far unrecognized tissue-level ordering patterns within liver tissue. We relate these ordering patterns to positions of anatomical landmarks in the liver lobule. Section 4.4 compares these newly found nematic cell polarity fields with fields of anisotropies of the blood-supplying sinusoid network around hepatocytes. This provides a comprehensive view on both the global and relative orientational order of cell polarity within the liver. Section 4.5 deals with the analysis of experiments involving genetic perturbations. The knock-down of a cell-adhesion protein (Integrin- β 1) reduces orientational order of the liver in a characteristic way that indicates a bi-directional feedback between cell polarity organization and sinusoidal network structure. The chapter closes with a discussion of translational order, where we find evidence for smectic order of liver tissue. All experimental data shown in this chapter was obtained and pre-processed (cf. section 1.6) by members of the Zerial lab at the Max Planck Institute of Molecular Cell Biology and Genetics (MPI-CBG) in Dresden, Germany.

4.1. Coarse-graining reveals nematic cell polarity patterns on the lobule-level

In this section, we analyze the spatial distribution of nematic tensors as defined in equation 2.3, which characterizes the distribution of apical membrane proteins on the hepatocyte surfaces. To get a visual impression of the spatial distribution of nematic cell polarity, we employ two complementary three-dimensional visualizations approaches: individual nematic cell polarity axes and colored cubes. We

4. The liver lobule exhibits biaxial liquid-crystal order

recall our convention that eigenvalues are ordered as $\sigma_1 \geq \sigma_2 \geq \sigma_3$ with their respective eigenvectors denoted by $\mathbf{a}_1, \mathbf{a}_2, \mathbf{a}_3$ and the terminology of bipolar axis (\mathbf{a}_1) and ring axis (\mathbf{a}_3), see section 2.1.1.

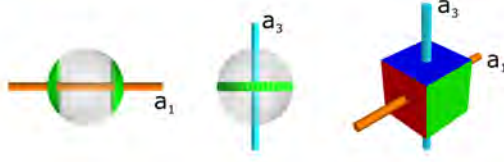


Figure 4.1. Cubic representation of a tripod of nematic cell polarity axis.

The colored cube shown in this figure will be used below to indicate the orientation of the tripod of nematic cell polarity axis, e.g. $\mathbf{a}_1, \mathbf{a}_2, \mathbf{a}_3$, for apical cell polarity (cf. Fig. 2.6). The cube faces are aligned with the nematic cell polarity axes, such that the bipolar axis \mathbf{a}_1 is normal to the red faces of the cube and the ring axis \mathbf{a}_3 is normal to the blue faces of the cube.

Panel (A) of Fig. 4.2 shows tubes parallel to the bipolar axis \mathbf{a}_1 (largest eigenvalue) of apical nematic cell polarity tensors¹. Visual inspection alone does not give a robust evaluation of orientational order. Hence, we estimate the underlying director field by making use of the coarse-graining procedure, which was introduced in section 3.3. We choose a punctured Gaussian kernel with a standard deviation of $20 \mu\text{m}$, which is the typical distance between neighboring hepatocytes [105]. The resulting approximate director field is shown in panel (B) of Fig. 4.2 and reveals a lobule-level pattern of cell polarity in the liver. These ordering fields are non-uniform, because the estimated director changes direction throughout the liver lobule.

After having recognized orientational order in the bipolar nematic cell polarity axis \mathbf{a}_1 , we now turn to the ring-axis \mathbf{a}_3 , the spatial visualization of which is shown in panels (C) and (D) of Fig. 4.2. Upon coarse-graining, lobule-level ordering patterns emerge again. In this case, however, the ordering is such that the director points in the viewing direction, which makes it visually hard to see. In this case, a better approach is to use colored cubes for visualization of individual nematic cell polarity orientations. Panels (E) and (F) of Fig. 4.2 show the three-dimensional renderings for individual cell nematic tensors and averaged tensors, respectively. The ordering of the \mathbf{a}_3 axis is more easily recognized as the corresponding faces of the cubes can be seen directly. This shows that both visualization methods

¹Note that directions are not indicated because of the nematic symmetry, which means that \mathbf{a}_1 and $-\mathbf{a}_1$ are equivalent.

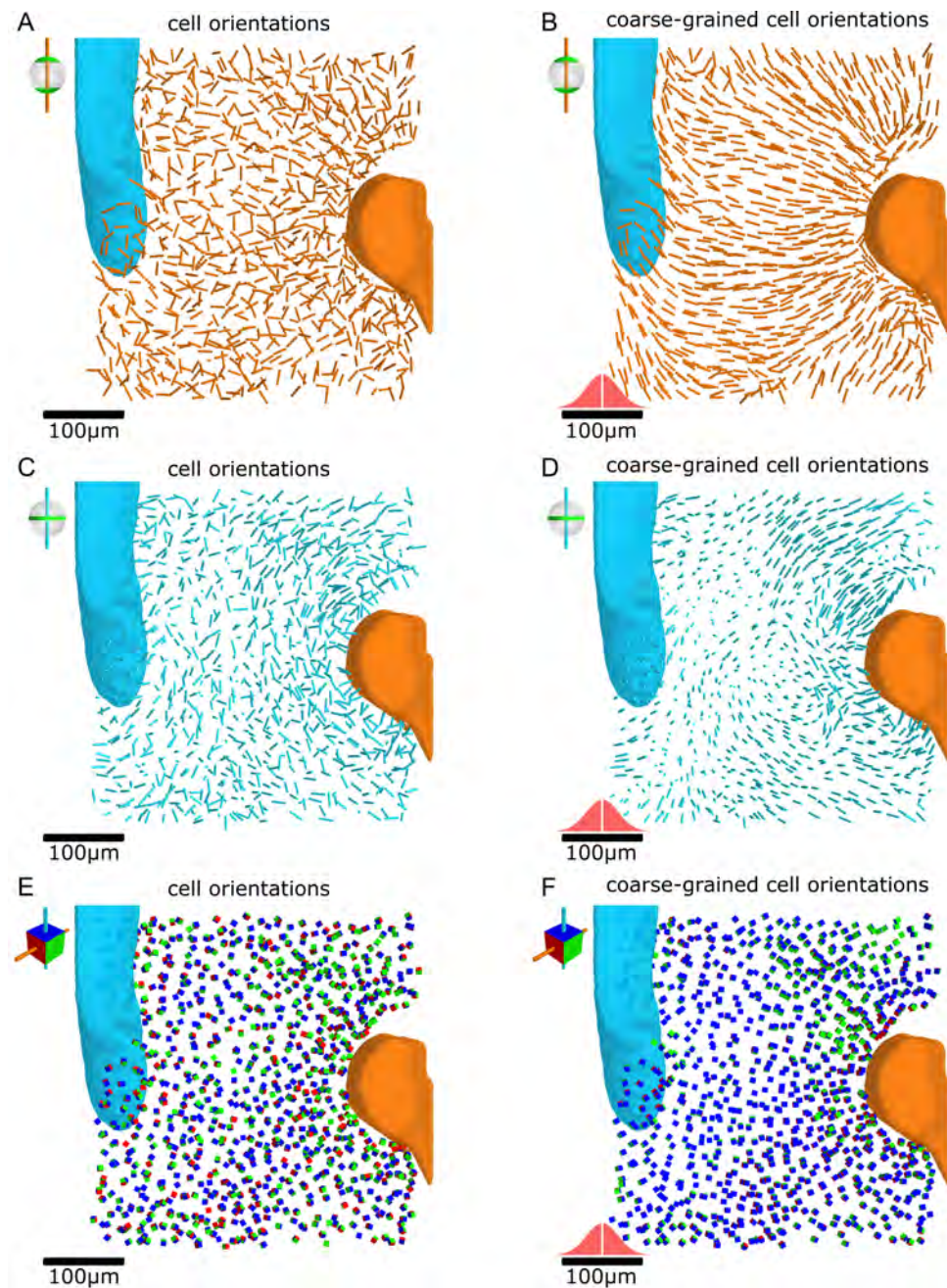


Figure 4.2. Nematic cell polarity axes of hepatocytes in a liver lobule.

(A) Three-dimensional renderings of axes representing bipolar axes of apical nematic cell polarity resulting from individual cell polarity tensors. (B) Same as panel A, but from cell polarity tensors averaged with a Gaussian kernel ($\sigma = 20\ \mu\text{m}$, profile indicated above the scale bar of all plots showing averages). (C, D) Same as panels A and B, respectively, for ring axes of apical nematic cell polarity. (E, F) Three-dimensional renderings of cubes representing individual (E) and averaged (F) apical nematic cell polarity tensors. Cube faces are colored as: red normal to \mathbf{a}_1 (bipolar axis), green normal to \mathbf{a}_2 , and blue normal to \mathbf{a}_3 , (ring axis), see also Fig. 4.1. Experimental data: Zerial group at MPI-CBG.

4. The liver lobule exhibits biaxial liquid-crystal order

are complementary and can be used to highlight different aspects of the three-dimensional orientational order of nematic cell polarity in tissue. We can now use these insights to identify the relevant concepts from liquid crystal theory to quantify the observed orientational ordering. We note two qualitative features of the patterns:

1. The order is biaxial, e.i. the bipolar and also the ring axes exhibit orientational order.
2. The average direction changes throughout the lobule, making the director field non-uniform.

We therefore employ the quantification of orientational order in curved geometries developed in section 3.3. Specifically, we calculate the co-orientational order parameters $co-S$, $co-P$, $co-D$, $co-C$ of orientations of each individual cell nematic polarity with a local reference system, given by a local average of the tensors $A_{\alpha\beta}$ with a punctured Gaussian kernel (as shown in Fig 4.2).

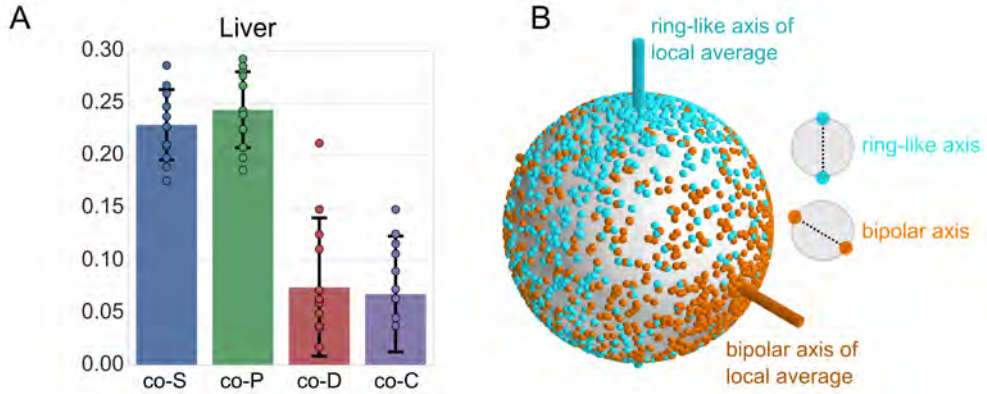


Figure 4.3. Biaxial order parameter in liver tissue. (A) Co-orientational order parameters quantify biaxial order of hepatocytes in liver tissue (average over $n = 11$ data sets). The local reference system was chosen as a local average with punctured Gaussian kernel, see text for details. Error bars denote standard error ($n = 11$ tissue samples). (B) Spherical distribution of apical ring-like axis (blue dots) and apical bipolar axis (red dots) corresponding to the quantitative analysis in panel (A). Experimental data: Zerial group at MPI-CBG.

This calculation requires the commitment to an ordering of axes (cf. sections 3.1.2 and 3.3). Using the notation introduced in section 3.1.2, we choose \mathbf{n} to point in the direction of the apical ring-like axis \mathbf{a}_3 and \mathbf{m} to point in the direction of the apical bipolar axis \mathbf{a}_1 of each individual cell. Similarly, we choose \mathbf{w} to point along

the direction of ring axis $\bar{\mathbf{a}}_3$ and \mathbf{v} to point along the bipolar axis $\bar{\mathbf{a}}_1$ of the local averaged cell polarity tensor (cf. section 3.3).

With this choice, we compute the four co-orientational order parameters $\text{co-}S$, $\text{co-}P$, $\text{co-}D$, $\text{co-}C$ as shown in Fig 4.3A. To further illustrate the order of nematic cell polarity in liver tissue, we show the distribution of the nematic axes of cell polarity relative to the local reference system as a spherical distribution plot in Fig 4.3B. We observe that the ring-like axes (blue dots) are clustered around the blue reference axis. This is reflected by the scalar order parameter $\text{co-}S$ being larger than zero. Additionally, we find a significant phase biaxiality quantified by non-zero values of $\text{co-}P$, which is also apparent in the spherical distribution plot of Fig 4.3B. The second principal axis $\mathbf{m} = \mathbf{a}_1$ (bipolar axis, red dots) also exhibits a weak ordering, which becomes apparent in the non-zero values of $\text{co-}D$ and $\text{co-}C$. Thus, using co-orientational order parameters that compare nematic axes with a local average (omitting the central cell), we have quantified biaxial orientational ordering in the presence of curved director fields.

4.2. Coarse-grained patterns match tissue-level reference field

In the previous section, we studied coarse-grained patterns of apical nematic cell polarity. By visual inspection, a clear resemblance with the lobule-wide reference field is apparent as is shown in Fig. 4.4 for one example data set. As shown in section 3.2, the locations of the central and portal veins in the lobule can be used to define a tissue-level reference coordinate system. In this chapter, we use the term *lobule-level reference system* to refer to the specific realization for a given geometrical configuration of large veins in liver tissue, as shown in Fig. 4.4B. Additionally, a quantification of the alignment of the coarse-grained directors with the lobule-level reference frame is shown in panel (C) of Fig. 4.4. There, a color-coding is used to distinguish between parallel (red) and perpendicular alignment (blue). The coarse-grained cell polarity pattern matches the reference system well throughout most parts of the lobule (indicated by red color in the figure). Deviations from the parallel alignment are most notable near the portal vein and at the boundary of the imaging volume. We will return to this spatial dependence of orientational order throughout the lobule in section 5.3.3, where we compare a minimal model of nematic order generation to the orientational order found in

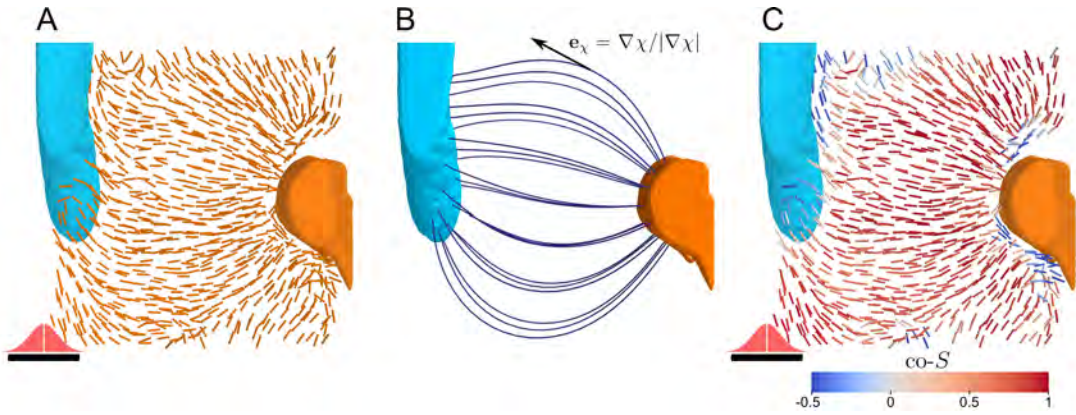


Figure 4.4. Big veins define a curvilinear reference coordinate system. (A) Pattern of averaged orientations (same as Fig. 4.2B). (B) Lobule-level reference field determine by the location of the big veins, e.i. the portal and the central vein as explained in the text, see also section 3.2. (C) Orientation field of panel (A) with color code indicating uniaxial co-alignment to the lobule-level reference field \mathbf{e}_x of panel (B). Experimental data: Zerial group at MPI-CBG.

liver tissue.

4.3. Apical and basal nematic cell polarity are anti-correlated

The study so far has focused on apical nematic cell polarity of hepatocytes and their spatial patterns on the lobule-level. We turn back to the scale of individual cells and investigate the relative orientation of nematic cell polarity axes stemming from apical domains with respect to the ones from basal domains. We recall that the apical bipolar axis is denoted by \mathbf{a}_1 and ring-axis is denoted by \mathbf{a}_3 as they correspond the largest σ_1 and smallest eigenvalue σ_3 of the apical nematic cell polarity tensor, respectively (cf. Fig. 2.6). We now introduce a similar notation for nematic cell polarity axes for the basal membrane distribution, i.e. \mathbf{b}_1 for the bipolar axis and \mathbf{b}_3 for the ring-axis resulting from the basal membrane distribution. The corresponding eigenvalue distribution is shown in appendix A.3 and is qualitatively similar to the eigenvalue distribution of apical membrane.

We now examine correlations between the cell polarity axes originating from apical and basal domains using the uniaxial order parameter $\text{co-}S$. In Fig. 4.5, we show the values of S for four different axes pairs. Schematics in the figure illustrate the limiting configurations of idealized bipolar and ring-patterns. The first pairing,

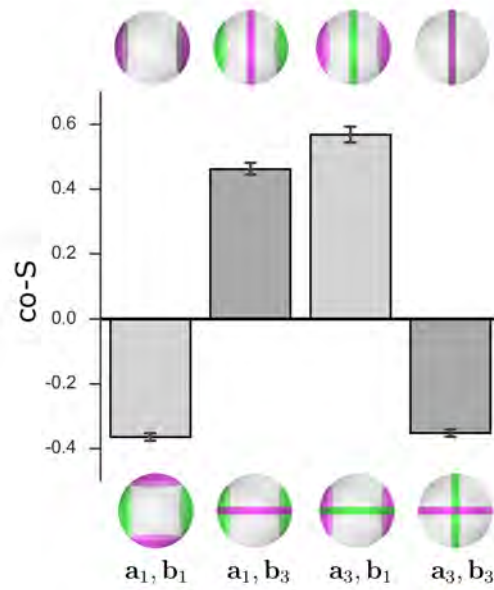


Figure 4.5. Correlations between nematic cell polarity axes of apical and basal membrane domains. Uniaxial order parameters $co-S$ for four pairs of apical and basal nematic cell polarity axes. High values of S for the pairs $(\mathbf{a}_1, \mathbf{b}_3)$ and $(\mathbf{a}_3, \mathbf{b}_1)$ indicate that these axes pairs are aligned in a parallel fashion, which is schematically shown on the top of the figure above the respective columns. In contrast, low values of $co-S$ for the pairs $(\mathbf{a}_1, \mathbf{b}_1)$ and $(\mathbf{a}_3, \mathbf{b}_3)$ indicate a preferentially perpendicular configuration of these axes pairs, which is schematically shown at the bottom of the figure below the respective columns. Experimental data: Zerial group at MPI-CBG.

($\mathbf{a}_1, \mathbf{b}_1$) shows that the apical bipolar axis is preferentially perpendicular to the basal bipolar axis. The same holds true for the pairing of ring axes \mathbf{a}_3 and \mathbf{b}_3 . In contrast to that, the mixed pairings show that the basal ring axis \mathbf{b}_3 is mostly parallel to the apical bipolar axis \mathbf{a}_1 . Vice versa, the apical ring axis \mathbf{a}_3 is mostly parallel to the basal bipolar axis \mathbf{b}_1 .

Taken together, this implies an anti-correlation between the directions of nematic axes from apical and basal cell polarity. This finding reflects a putative competition between apical and basal membrane domains, which is indicated by the observation that nematic axes of the same kind (bipolar, ring) but of different membrane domain appear to repel each other and instead align with their counterpart.

4.4. Co-orientational order: nematic cell polarity is aligned with network anisotropy

We defined a method to determine a nematic tensor of local network anisotropy around cells in section 2.3. This nematic tensor is now calculated for the sinusoid network around hepatocytes in liver tissue. The preferred direction of the local sinusoid network anisotropy is shown for one dataset in Fig 4.6A. Complementary to that, we plot the spatial distribution of all three nematic axes by the approach of aligned cubes in Fig 4.6B. The cube sides are aligned to the nematic axes of the nematic tensor of sinusoidal network anisotropy analogously to Fig. 4.1. The red side is normal to the “preferred axis” \mathbf{s}_1 and the blue face is normal to the “plane axis” \mathbf{s}_3 (cf. section 2.3). The pattern of network anisotropy is similar to the averaged pattern of apical cell polarity and qualitatively resembles the lobule-level reference field.

To quantitatively assess the alignment between apical nematic cell polarity and local sinusoid network anisotropy, we calculate co-orientational order parameters (cf. section 3.1.2) between the nematic fields of apical cell polarity of hepatocytes and local sinusoid anisotropy around each hepatocyte. The resulting values are shown in Figure 4.6C (averaged over nine different data sets). We find that the ring axis of the apical cell polarity is well-aligned with the plane axis of the local sinusoid anisotropy, as quantified by the co-orientational order parameter $co-S$. We can identify a phase-biaxial character of this co-alignment, too. Deviations from perfect co-alignment between apical ring axis and local sinusoid plane axis are less pronounced in the direction of the preferred sinusoid axis than perpendicular to

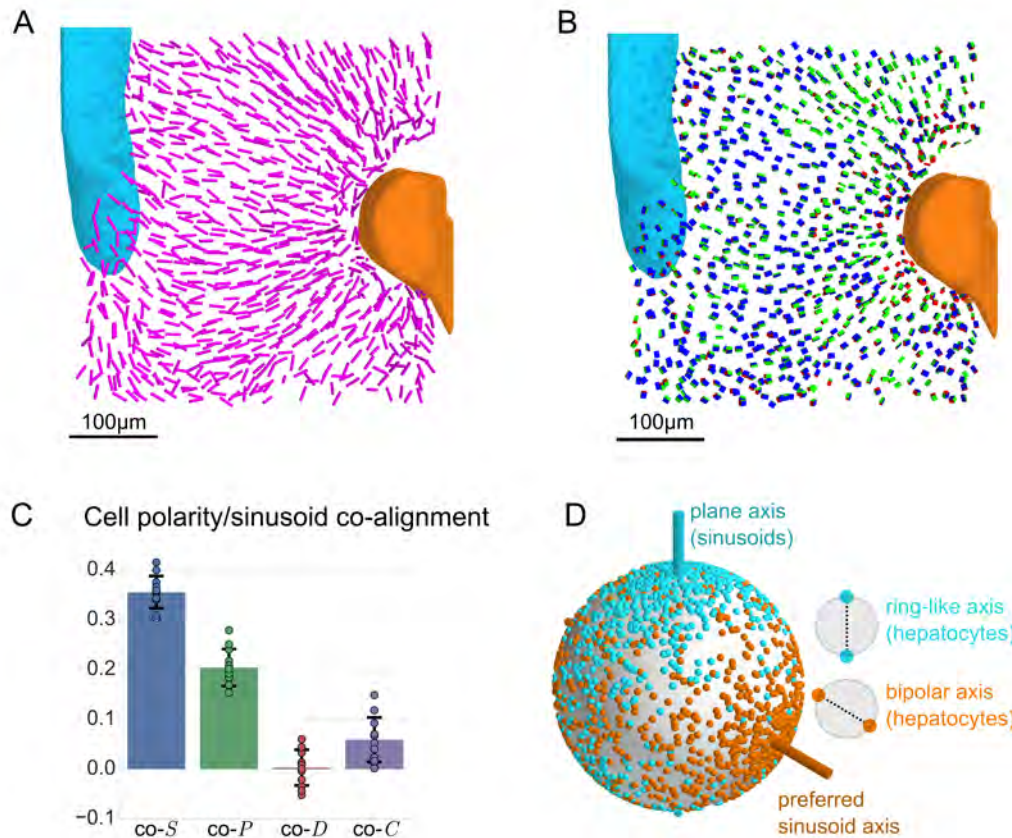


Figure 4.6. Co-orientational order between network anisotropy of sinusoid blood-vessel network and nematic cell polarity of hepatocytes. (A) Preferred direction of local sinusoid network anisotropy. (B) The local anisotropy of the sinusoidal network is visualized with the equivalent cuboid visualization. Specifically, the average orientation tensor of the network at the centers of the hepatocytes with a Gaussian with standard deviation of 20 µm is computed and a colored cube, representing the directions of the tripod of nematic axes, is shown. (C) Co-orientational order of apical nematic cell polarity with local sinusoid network. (D) Spherical distribution of apical ring-like axis (blue dots) and apical bipolar axis (red dots) in the reference frame of local sinusoid network anisotropy. Experimental data: Zerial group at MPI-CBG.

it as reflected by a non-zero value of $\text{co-}P$. The co-orientational order parameters $\text{co-}D$ and $\text{co-}C$ are close to zero. This co-orientational order is also visualized in a spherical distribution plot in Fig 4.6D. The co-alignment between apical ring axis and local sinusoid plane axis can be seen visually. The anisotropic distribution of apical ring axes around the local sinusoid plane axis is also clearly observed. This shows the applicability of our method to identify co-alignment between two different local nematic anisotropies in a tissue.

4.5. RNAi knock-down perturbs orientational order in liver tissue

Inhibiting gene expression through RNA interference (RNAi) is a powerful tool of genetic engineering and functional genomics [166]. During the last 30 years it has been used successfully, in conjunction with physical modeling and computer simulations, to investigate a wide array of basic biological processes, e.g. [51, 67, 88, 167–171].

Here, the main idea is to compare structural order under unperturbed conditions (often termed “wild-type”) with a genetic knock-down. We focus on the cell’s communication with its environment, in particular the extra-cellular matrix (ECM). It has been shown that cells can sense the location of ECM and react to it by changing their position [172] or modify their cell polarity [30]. Using the quantification of cell polarity presented here, we are able to investigate the effect of a disruption of communication between hepatocytes and ECM.

In the experiment, communication between hepatocytes and ECM was disturbed by injection of lipidoid-based nanoparticles (LNP) into the tail vein of mice. The LNP contained small interfering RNAs (siRNAs) to inhibit the expression of the protein Integrin- β 1 (Itgb1) specifically in hepatocytes and not in other cells of the tissue [173]. This resulted in a much lower concentration (about 90% reduction in expression levels [173]) of the Itgb1 protein. Integrin- β 1 (Itgb1) is a ubiquitous trans-membrane protein of the integrin family and found in all animals. It has a signaling role in the recognition process of ECM by cells [173]. Inhibition of Integrin- β 1 expression (knock-down) therefore effectively disturbs communication between hepatocytes and the ECM. In principle, the injection of lipidoid-based nanoparticles itself could have an impact that is unrelated to the specific action of silencing expression of Integrin- β 1. To account for these potential non-specific

effects, LPNs with siRNAs against a protein that is not expressed in hepatocytes (luciferase) were injected as a control.

We address two specific questions:

1. Do individual hepatocytes retain their cell polarity upon loss of communication with the ECM?
2. How is the lobule-level coordination of cell polarity influenced?

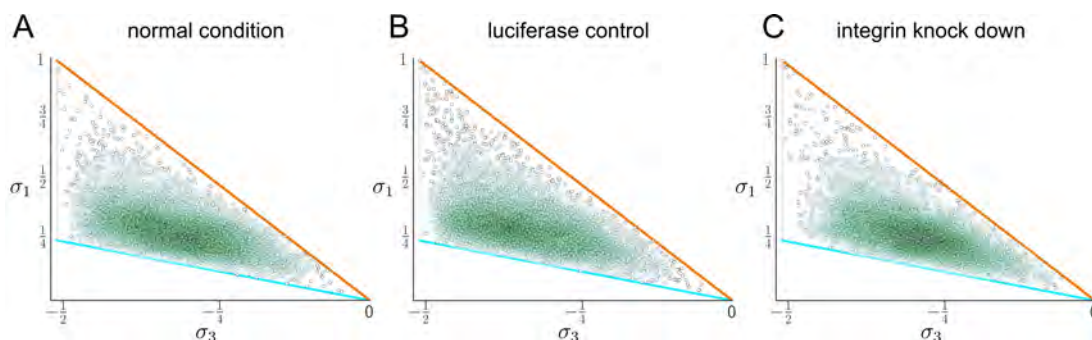


Figure 4.7. Apical nematic cell polarity of individual hepatocytes is retained upon Integrin- β 1 knock-down. (A-C) Distributions of apical nematic polarity weights σ_1 and σ_3 for three conditions. Shown are individual cells as points (gray) and a kernel density estimate of the distribution (green) to facilitate comparison between the distributions. The orange line on the top of the triangle corresponds to the ideal bipolar case and the blue line corresponds to the ideal ring pattern, see Fig. 2.6. (A) Adult “wild-type” mice without injection of RNAi. (B) Control injection of RNAi against a non-expressed protein (luciferase). (C) Knock-down of Integrin- β 1 by RNAi injection. Kernel density estimates were obtained using the method `kdeplot` from the `seaborn` package [174] with standard parameters. Experimental data: Zerial group at MPI-CBG.

To investigate the influence of cell-ECM communication on nematic cell polarity of individual hepatocytes, we examine the distributions of polarity weights σ_1 and σ_3 (cf. section 2.2.2) that quantify the magnitude of nematic anisotropy, see Fig. 4.7. Comparing the distributions of nematic cell polarity parameters, we find no change in the distribution of nematic cell polarity weights between normal condition, luciferase control and integrin knock down. We therefore conclude that individual nematic cell polarity is retained and not affected by communication of hepatocytes with ECM. Furthermore, alignment between nematic axes of apical and basal cell polarity is also not affected by knock down of Integrin- β 1, as shown in Fig. 4.8A. This suggests that the antagonistic configuration of apical and basal nematic cell polarity of individual hepatocytes is also retained.

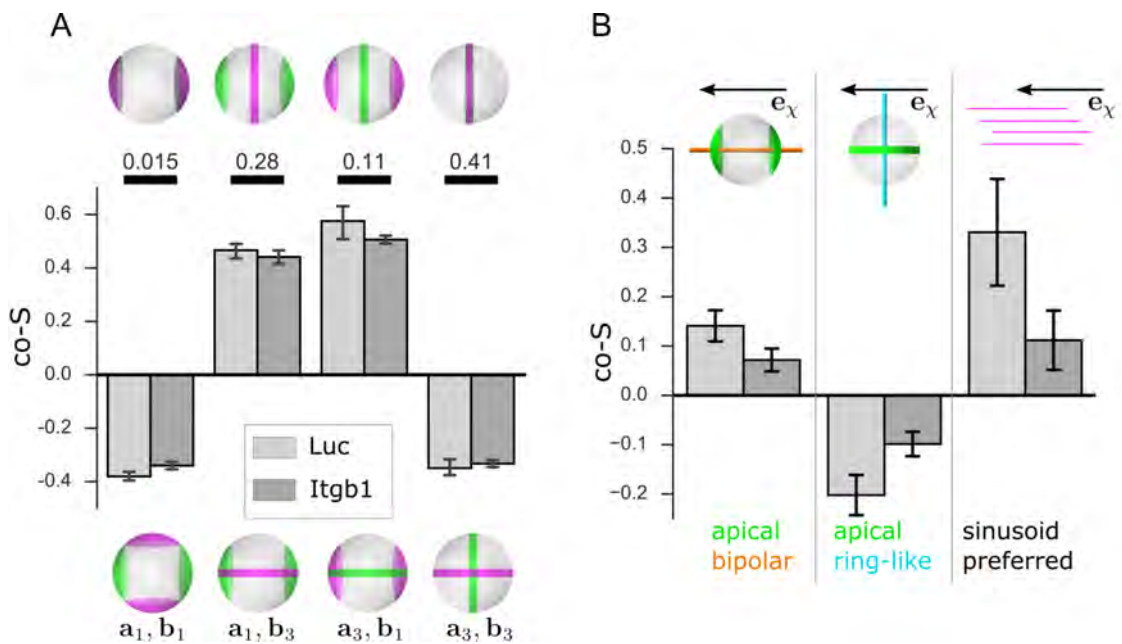


Figure 4.8. Impact of Integrin- β 1 knock down by RNAi on coordination of nematic cell polarity. (A) Alignment between nematic axes of apical and basal cell polarity averaged over individual hepatocytes for two experimental conditions: luciferase control (Luc) and Integrin- β 1 knock-down (Itgb1). (B) Alignment of apical bipolar, apical ring-like and sinusoid preferred axis with the lobule-level reference field averaged over individual cells and grouped by treatment condition as in panel A. The unit vector \mathbf{e}_χ points in the direction of the gradient of the lobule-level field χ , see section 3.2. Experimental data: Zerial group at MPI-CBG.

In contrast to the nematic cell polarity of individual cells, the alignment of nematic cell polarity axes with the lobule-level reference field is strongly perturbed in knock-down conditions, as is shown in Fig. 4.8B. Both the alignment of apical bipolar axis and apical ring-like axis were affected. This suggests that communication of hepatocytes with their surrounding extra-cellular matrix is needed in order to properly position cellular nematic cell polarity. Moreover, the alignment of the local sinusoid anisotropy around hepatocytes is disrupted in the knock-down as is shown in the rightmost panel of Fig. 4.8B. The reduction of sinusoid alignment suggests a feedback of cell polarity organization on the structure of the sinusoid transport network.

This is in contrast to previous belief, where sinusoids have been suggested to organize autonomously with hepatocytes strictly following sinusoidal cues [30, 93]. If this would have been true, communication between hepatocytes and ECM should not affect sinusoid organization. Instead, our finding of sinusoid disruption upon Integrin- β 1 knock-down contrarily suggests a bi-directional feedback between cell polarity organization and the structure of the sinusoid transport network.

4.6. Signatures of smectic order in liver tissue

So far, we have focused on orientational order of nematic cell polarity and local network anisotropy in liver tissue. We now turn to translational order, which gives insight into the spatial arrangement of the constituents of the tissue. In section 4.1, we have seen that orientational order follows a curvilinear pattern, i.e. is not uniform throughout the lobule. To investigate translational order, we have to resort to selecting a subset of data, within which the tissue is approximately homogeneous. The location of this subset is indicated in Fig. 4.9. Due to experimental constraints, the available images of liver tissue have a much smaller extension in z -direction than in the x - y plane (cf. section 1.6). The portal and central veins in the images are approximately oriented along the z -direction and the direction of the lobule-level reference field is approximately in the x - y plane of the image.

To analyze positional order, we follow the procedure introduced in section 3.4. We calculate summed densities along the three spatial directions, from which two-dimensional structure functions are obtained, see Fig. 4.10. Compared to the idealized cases presented in section 3.4, the structure function of liver tissue is more complex.

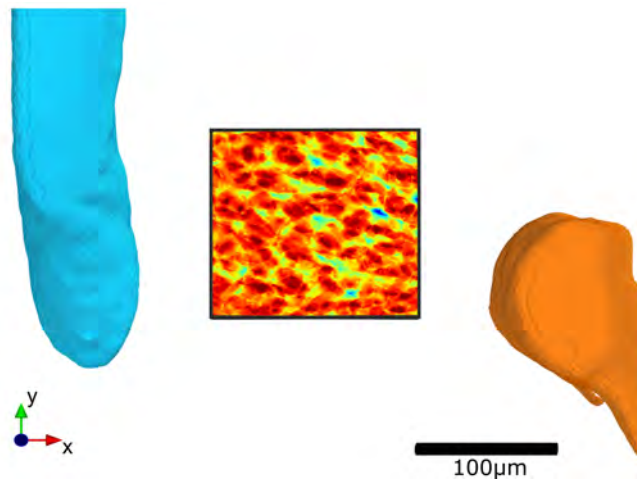


Figure 4.9. Schematic of the location of the data subset used to analyze translational order in the liver. Shown are the locations of the central vein (cyan, left) and portal vein (orange, right) together with the sum over z -indices of the binary sub-stack of the data for locations of segmented cells within the lobule (same as Fig. 4.10) to illustrate the placement of the data subset between the larger veins. Experimental data: Zerial group at MPI-CBG.

For smectic order, we would expect a broadened peak around the center for one direction and antipodal peaks in the other two directions (compare Fig. 3.8A). Indeed, the structure function for the x - y plane of the liver tissue shows pronounced antipodal peaks. The peaks corresponds to a wavelength of about $20\mu\text{m}$, which compares well with the cell diameter of a hepatocyte plus the diameter of a sinusoid in the tissue². The interpretation of the structure function for the other two directions is less clear. This could be either due to the restricted width of the tissue in z -direction or, alternatively, to a putative additional periodic order in that z -direction.

We conclude that there are signatures of layered order. Together with the orientational order of nematic cell polarity, discussed in section 4.1, this classifies liver tissue as a smectic liquid crystal. There is also the possibility of an additional translational order in z -direction, which is not accessible so far due to experimental limitations. In that case, there would be additional periodic structures within the layers, which would indicate a potential columnar order in liver tissue (cf. Fig. 3.8).

²The diameter of a hepatocytes is about $12\mu\text{m}$ and the diameter of sinusoids about $8\mu\text{m}$ [105].

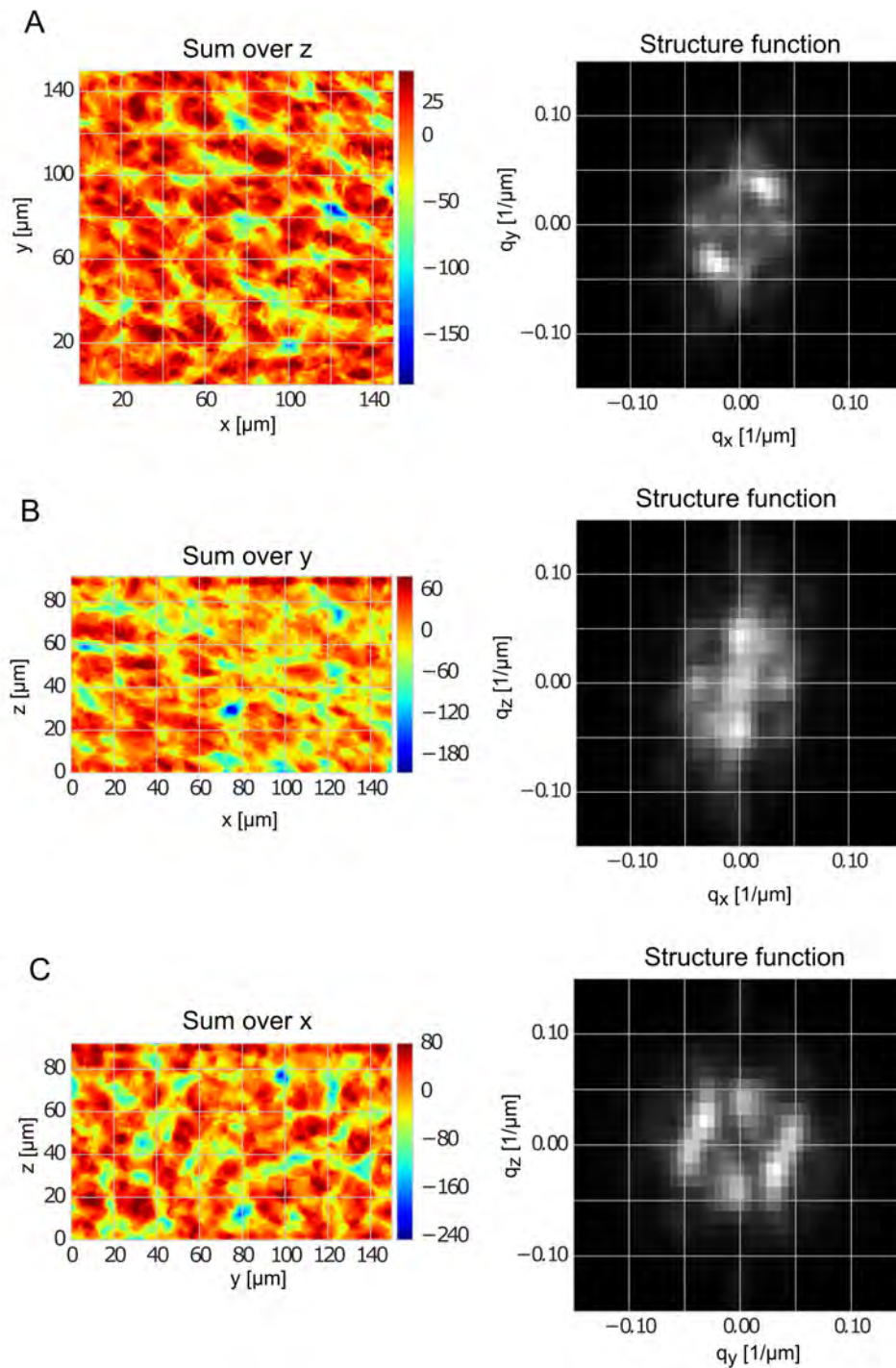


Figure 4.10. Structure factor of cells in liver tissue. (A-C) The voxelized data of cell locations is summed along one axis and the mean signal is subtracted, prior to calculation of the structure function, see equation (3.23) for the definition of the structure function. (A) Sum along the z-axis. (B) Sum along the y-axis. (C) Sum along the x-axis. Note that the data is not cubic because of experimental limitations for the imaging height Experimental data: Zerial group at MPI-CBG.

4. The liver lobule exhibits biaxial liquid-crystal order

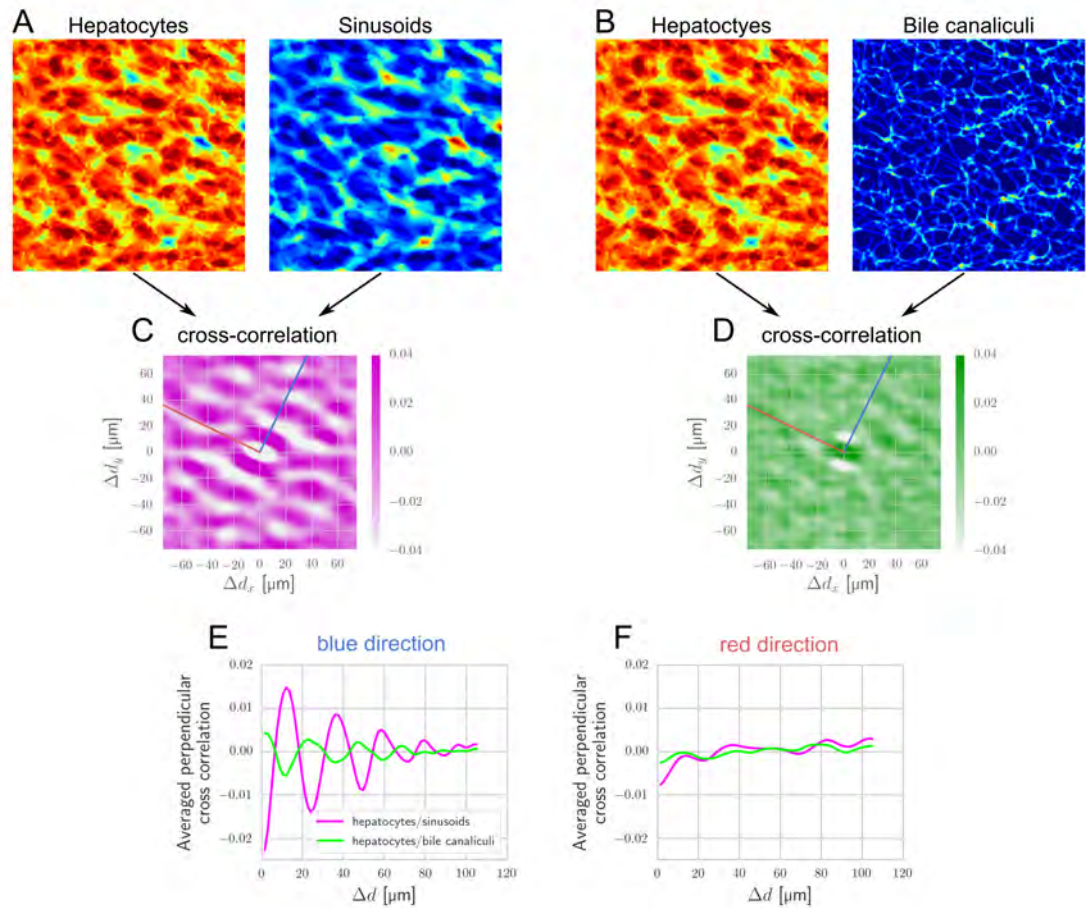


Figure 4.11. Cross-correlations between positions of hepatocytes, sinusoids and bile canaliculi reveal smectic order.

(A, B) Original images of densities of cells, sinusoids and bile canaliculi, summed over the z-direction of the image. (C, D) Normalized two-dimensional cross-correlations (cf. eq (4.1)) of hepatocytes with sinusoids (C) and hepatocytes with bile canaliculi (D). Blue and red lines indicate directions used in the panels below.

(E, F) Average normalized cross correlations along the blue direction (E) and red direction (F). The damped oscillations visible in the cross-correlation of panel E and absence of undulations in panel F indicate the presence of smectic order in liver tissue. Experimental data: Zerial group at MPI-CBG.

Relative positioning of hepatocytes, sinusoids and bile canaliculi. We now turn to positional correlations between different structures in liver tissues, namely the hepatocytes and the two transport networks: the sinusoidal network and the bile canaliculi network.

We define the normalized two-dimensional cross-correlation between two real-valued, discrete signals (images) $f[n, m]$ and $g[n, m]$ as

$$C_{fg}[k, l] = (f \star g)[k, l] = \frac{1}{N_f + N_g} \sum_{n, m} \frac{1}{\sigma_f \sigma_g} (f[n, m] - \bar{f}) (g[n + k, m + l] - \bar{g}) \quad (4.1)$$

where N_f is the number of pixels in f , \bar{f} is the average of f , σ_f the standard deviation³ and \star denotes the cross-correlation. Analogous definitions apply to N_g , σ_g , and \bar{g} . Finite signals are zero-padded for arguments outside of the domains, where shifted signals overlap. We use this normalized cross-correlation function to investigate the relative positioning of hepatocytes and the sinusoid network as well as hepatocytes and the bile canaliculi network, see Fig. 4.11. We focus on cross-correlating densities that were summed along the z-direction, because layered order of cells is most pronounced within that plane.

Both cross-correlations reflect the layered order of the tissue, which was already implicated in the analysis of hepatocytes alone (cf. Fig. 4.10A). Additionally, we can now make statements about co-localization of hepatocytes and the two different transport networks. Sinusoids are shifted with respect to the positions of hepatocytes along the layer direction, indicated by low values of the cross-correlation for zero shift and higher values for finite shifts in layer direction, see Fig. 4.11C. In contrast to that, bile canaliculi are co-located with hepatocytes, as shown in Fig. 4.11D.

To make this shift in co-localization with hepatocytes more apparent, we calculate the averaged cross-correlations along two different directions. The directions are indicated by blue and red lines in panels C and D and the resulting plots are shown in panels E and F of Fig. 4.11. For the blue direction, the cross-correlations of hepatocytes/sinusoid as well as hepatocytes/bile canaliculi show periodic undulations in the line plots (panel E). This is consistent with a periodic layering in that direction, where hepatocytes and sinusoids are anti-correlated and hep-

³We define the standard deviation over all pixels as $\sigma_f = \sqrt{\sum_{k, l} (f[k, l] - \bar{f})^2 / N_f}$ and analogously for g .

atocytes and bile canaliculi are co-localization. In the red direction (panel F of Fig. 4.11), the undulation is more irregular and has lower amplitude, which is consistent with a direction perpendicular to normal direction of putative layers. This implies the presence of alternating layers of sinusoid and bile canaliculi networks in the liver, which is consistent with the finding that apical and basal nematic cell polarity are anti-correlated (cf. section 4.3).

The layer distance derived from the maximum-to-maximum distance in the line plot of hepatocyte/sinusoid cross-correlation is approximately $24\ \mu\text{m}$. This compares well with the value of $20\ \mu\text{m}$ obtained by the structure function of hepatocytes shown in Fig. 4.10A. The structure function is the inverse Fourier transform of the cross-correlation of an input signal with itself (also called auto-correlation), which is also known as the Wiener-Kinchin theorem [175, 176]. The different representations highlight distinct features of the tissue structure. While the structure function is useful to access the general presence of layered order in the system, the cross-correlations emphasizes the relative phase between different structures. The quantification of the layer spacing distance of both approaches give comparable results that are close to the value of the sum of one hepatocyte diameter plus one sinusoid diameter⁴.

4.7. Summary

This chapter investigated the structural properties of liver tissue with focus on orientational order of nematic cell polarity. We found that apical nematic cell polarity of hepatocytes exhibit lobule-level patterns in liver tissue. We used tools from liquid crystal theory to quantify the orientational order and found it to be phase biaxial. We showed that the coarse-grained patterns of apical nematic cell polarity match a curvilinear reference field that is given by the locations of larger vessels in the liver lobule.

We then investigated co-orientational order between different types of cellular anisotropies. We found that apical and basal nematic cell polarity are anti-correlated, which indicates a putative competition between apical and basal membrane domains. The co-orientational order of apical cell polarity and local sinusoid anisotropy was found to be of phase biaxial type. These quantifications of co-orientational order between different cell anisotropies was then used to investigate

⁴The diameter of a hepatocytes is about $12\ \mu\text{m}$ and the diameter of sinusoids about $8\ \mu\text{m}$ [105].

genetic knock-down experiments.

We found that the knock-down of Integrin- $\beta 1$, a protein involved in cell adhesion and recognition, has no impact on apical-basal anti-correlation but does disrupt the co-orientational order between apical cell polarity and local sinusoid network anisotropy. This finding, together with the previously known influence of external cues on hepatic cell polarity, indicates a bi-directional feedback between cell polarity organization and sinusoidal network structure.

In the last section of this chapter, we examined the translational order of hepatocytes and found evidence for smectic order. Furthermore, we investigated cross correlations and found indications for alternating layers of sinusoids and bile canaliculi.

5. Effective models for cell and network polarity coordination

In this chapter, we investigate physical principles underlying the observed architecture in the liver, which was presented in chapter 4. Motivated by the observation of biaxial nematic liquid crystal order of cell polarity made there, we first derive a minimal nematic interaction model¹ by discretizing a continuum theory of nematic elasticity (cf. section 1.5.3). This procedure yields a uniaxial nematic interaction model and we show how it naturally generalizes to the biaxial case.

We then apply this nematic interaction model to the case of coordinated nematic cell polarity found in liver tissue. Using the uniaxial variant of the model, we address two basic mechanisms to coordinate nematic cell polarity axes throughout the liver lobule: neighbor-interaction and coupling to an external ordering field. We show that both mechanisms are, in principle, able to generate ordered patterns reminiscent of the cell polarity fields in liver but only the external field mechanism is consistent with spatial profiles of orientational order found in liver tissue. Building on this observation, we focus the external field mechanism and use its biaxial variant to study co-orientational order between apical nematic cell polarity and local sinusoid around hepatocytes. This reproduces the observed phase-biaxial order of apical cell polarity in liver tissue, which was shown in section 4.4.

The work presented in this section was done in collaboration with Simon Syga. Some preliminary results of the uniaxial interaction model were published in his Bachelor thesis titled “Nematic Order in Complex Tissues” [179].

5.1. Discretization of a uniaxial nematic free energy

Starting from a continuum theory of nematic liquid crystals, we obtain a discretization, which we will use to describe the discrete organization of cells in tissues. For this, we restate the Frank free energy in one-constant approximation (cf. eq. (1.13))

¹Meier and Saupe [127, 177, 178] derived a formally equivalent nematic interaction model by expanding dispersion forces between individual molecules up to second order.

and [39])

$$F_d = \int d^3r \frac{K}{2} (\partial_\alpha n_\beta)(\partial_\alpha n_\beta) , \quad (5.1)$$

which describes the contribution of gradients in the uniaxial director field $\mathbf{n}(\mathbf{r})$ with $\mathbf{n}^2 = 1$ to the total free energy. We now discretize this continuum energy, which will yield a sum over pairwise nematic interactions. For this, it is convenient to rewrite it in tensorial form. We introduce the tensor $N_{\alpha\beta} = n_\alpha n_\beta$ as the dyadic product of the nematic director \mathbf{n} with itself. Using that \mathbf{n} is a unit vector, we can also write [121]

$$F_d = \int d^3r \frac{K}{4} (\partial_\gamma N_{\alpha\beta}) (\partial_\gamma N_{\alpha\beta}) . \quad (5.2)$$

The tensorial form of the Frank free energy, eq.(5.2), has the advantage that it allows for a straight-forward discretization. This is due to the fact that the individual gradient $\partial_\gamma N_{\alpha\beta} = n_\alpha \partial_\gamma n_\beta + n_\beta \partial_\gamma n_\alpha$ is invariant under the nematic symmetry operation $\mathbf{n} \rightarrow -\mathbf{n}$. In contrast, only the square of the gradient of the nematic director $\partial_\alpha n_\beta$ is invariant under the nematic symmetry operation. We first consider discretization on a cubic lattice with lattice constant a , which yields (cf. appendix A.10)

$$F_d \approx -\frac{K a}{2} \sum_{\langle i,j \rangle} N_{\alpha\beta}^{(i)} N_{\alpha\beta}^{(j)} \quad (5.3)$$

where $\langle i, j \rangle$ runs over all pairs of neighbors on the cubic lattice and $N_{\alpha\beta}^{(i)}$ denotes the dyadic tensor of the nematic director located at lattice point i . The parameter K controls the interaction strength between neighboring nematic tensors.

The discretized distortion free energy, eq (5.3), can be restated² in terms of the nematic director \mathbf{n} and the second Legendre polynomial $P_2(x) = \frac{1}{2}(3x^2 - 1)$

$$F_d \approx -\varepsilon \sum_{\langle i,j \rangle} P_2(\mathbf{n}^{(i)} \cdot \mathbf{n}^{(j)}) \quad (5.4)$$

with $\varepsilon = K a/3$. This form is known as the *Lebwohl-Lasher* model in the literature [180–182] and resembles the definition of the uniaxial order parameter

²Here, we ignored an irrelevant additive constant to the interaction energy.

(cf. section 1.5.1). For $\varepsilon > 0$, this pairwise interaction energy favors nematic alignment, because it is minimized for either parallel or anti-parallel configurations of neighboring directors $\mathbf{n}^{(i)}$ and $\mathbf{n}^{(j)}$.

As an alternative to neighbor-interactions, we consider interactions of the nematic directors with an external nematic field $G_{\alpha\beta}$, which can align the nematic directors and is described by the following contribution to the free energy

$$F_{\text{int}} = - \int d^3r N_{\alpha\beta}(\mathbf{r}) G_{\alpha\beta}(\mathbf{r}) \approx - a^3 \sum_i N_{\alpha\beta}^{(i)} G_{\alpha\beta}^{(i)}, \quad (5.5)$$

where i runs over all lattice sites. Equation (5.5) can be restated in terms of unit vectors, by introducing $G_{\alpha\beta} = \lambda g_\alpha g_\beta$, with a unit vector \mathbf{g} pointing parallel to the externally applied field³ and λ the strength of the external field

$$F_{\text{int}} \approx -\varepsilon_{\text{int}} \sum_i P_2(\mathbf{n}^{(i)} \cdot \mathbf{g}^{(i)}) \quad (5.6)$$

with $\varepsilon_{\text{int}} = \frac{2}{3} a^3 \lambda$ and the second Legendre polynomial P_2 to make the definition similar to the one for the neighbor-interaction given in eq. (5.4).

5.2. Discretization of a biaxial nematic free energy

We generalize the Frank free energy in one-constant approximation, eq. (5.2) by formally replacing the dyadic $N_{\alpha\beta}$ by a generic symmetric traceless tensor $T_{\alpha\beta}$ that describes the orientation of a tripod of axes (cf. Fig. 3.1) instead of a single axis

$$F_d = \int d^3r \frac{K}{4} (\partial_\gamma T_{\alpha\beta}) (\partial_\gamma T_{\alpha\beta}) . \quad (5.7)$$

This simple biaxial interaction does not include all terms allowed by symmetry and more involved descriptions exist⁴. These descriptions, however, require more detailed knowledge about the system and are too detailed for the present initial investigations into biaxial orientational order found in liver tissue.

Discretization of eq. (5.7) follows the same approach as discretization of eq. (5.2)

³Note that we assume nematic symmetry for the externally applied field and hence \mathbf{g} and $-\mathbf{g}$ are equivalent.

⁴More general distortion energies for biaxial systems with up to 12 elastic constants can be found in [124, 183–186].

and leads to

$$F_d \approx -\frac{aK}{2} \sum_{\langle i,j \rangle} T_{\alpha\beta}^{(i)} T_{\alpha\beta}^{(j)} \quad (5.8)$$

To couple the symmetric traceless tensors $T_{\alpha\beta}$ to a biaxial external field, described by a tensor $G_{\alpha\beta}$, we use an analogous generalization of eq. (5.5)

$$F_{\text{int}} = - \int d^3r T_{\alpha\beta}(\mathbf{r}) G_{\alpha\beta}(\mathbf{r}) \approx - a^3 \sum_i T_{\alpha\beta}^{(i)} G_{\alpha\beta}^{(i)}. \quad (5.9)$$

In section 5.4, we will consider the specific case of coordination between biaxial cell polarity and local network anisotropy of the sinusoid network in liver tissue.

5.3. Application to cell polarity organization in liver tissue

We now put the nematic interaction model derived above into the context of interacting cell polarity axes. Each cell polarity is represented by a nematic director $\mathbf{n}^{(i)}$ and interacts with the nematic director $\mathbf{n}^{(j)}$ representing the cell polarity of a second cell, when they are in direct physical contact. The cell positions and contacts are taken from experimental data. We use an *effective free energy* F_d of the form given in equation (5.4) to capture the coordination between cell polarities in a tissue motivated by equilibrium systems. For simplicity, the distribution of cell polarity axes is chosen to be a Boltzmann distribution $f(\{\mathbf{n}^{(i)}\}) \propto \exp(-F_d/\nu)$, with noise strength ν that controls the amount of disorder of cell polarity orientations⁵.

Cells in tissues are, in general, far from thermodynamic equilibrium (cf. section 1.4) and we want to stress that we do not regard the orientations of cell polarity in tissues to be at thermodynamic equilibrium. Instead, we consider equilibrium-like models in a probabilistic sense. We therefore consider the Boltzmann distribution given above as a parameterized probability distribution by which ordered states are more likely than disordered states and which also accounts for the combinatorics of all possible states. This equilibrium-like probability distribution is now studied to obtain insights into basic mechanisms generating ordered patterns

⁵Some authors identify the noise strength ν with an effective temperature T_{eff} that subsumes biophysical processes generating disorder [98].

of cell polarity in tissues. In this section, we use the Metropolis algorithm to draw sample configurations that follow the Boltzmann distribution given above. Details of the algorithm can be found in appendix A.11.

In the same spirit, we test whether alignment of cell polarities with respect to an external reference field according to equation (5.6) is consistent with observations. For that, we make use of the coupling energy given in equation (5.6). In section 4.2, we have seen that the apical bipolar axes of hepatocytes follow a lobule-level reference field. This motivates us to consider the lobule-level reference field as a potential guide for nematic cell polarity orientation in section 5.3.3. Based on our observation of co-orientational order between apical nematic cell polarity and local sinusoid network anisotropy (cf. section 4.4), we will consider the local network anisotropy of the sinusoidal blood vessels as a second potential external alignment field in section 5.3.3.

5.3.1. Spatial profile of orientational order in liver tissue

As a benchmark to judge whether a given model variant is consistent with experimental data of cell polarity coordination in liver tissue, we use the spatial dependency of apical bipolar axis (cf. section 2.2.2 for definition) alignment with the lobule-level reference field. This spatial dependence of orientational order is computed by dividing the lobule into eight zones according to the value of the scalar reference field χ , thus measuring relative distance between portal and central veins⁶. The resulting lobule-adapted binning is shown by color-code for the cell centers of hepatocytes in Fig. 5.1A. We calculate the co-orientational parameter $co-S$ (cf. section 3.1.2) of each apical bipolar cell polarity axes with the direction of the lobule-level reference field \mathbf{e}_χ and average them according to their cell-center position in the lobule-level binning. This results in the profile shown in Fig. 5.1B and we observe a characteristic spatial dependence of this co-orientational order. The apical bipolar axes of hepatocytes is co-aligned with respect the lobule-level reference field with prolate order ($co-S > 0$) far away from the portal and central veins⁷. Close to both central and portal veins, the co-alignment type changes from prolate to oblate ($co-S < 0$).

⁶For numerical convenience, we linearly re-scaled the values of χ such that the hepatocyte closest to the portal vein carries a value of $\chi = 1$ and the hepatocyte closest to the central vein a value of $\chi = -1$.

⁷See section 1.5.1 for definitions of prolate and oblate order.

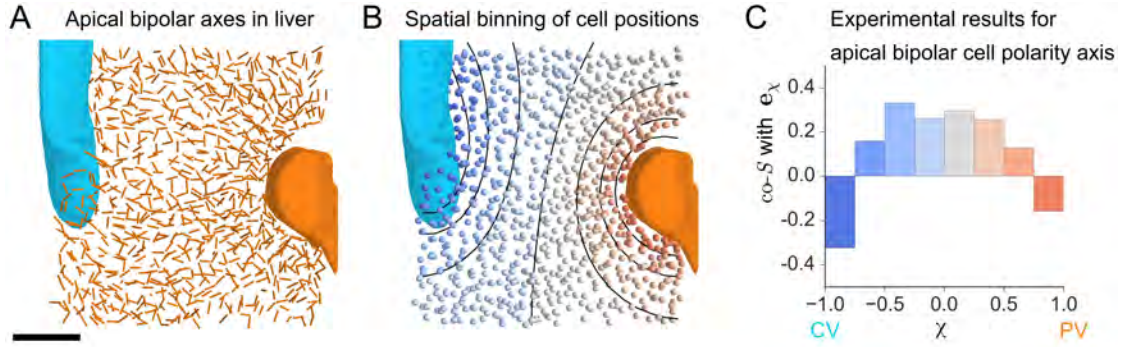


Figure 5.1. Experimental reference: orientations of apical bipolar cell polarity in liver tissue. (A) Orientations of apical bipolar axes in the liver lobule (cf. Fig. 4.2, scale bar: $100\ \mu\text{m}$). (B) Locations of cell centers color-coded by a division of the lobule into eight zones according to the value of the scalar reference field χ (see section 3.2). (C) Co-orientational order parameter $\text{co-}S$ of the apical bipolar axis \mathbf{a}_1 of cells with lobule-level reference field \mathbf{e}_χ within the respective regions of the lobule-level binning. Experimental data (surfaces of large vessels, cell positions and neighborhood relations): Zerial group at MPI-CBG.

5.3.2. Orientational order from neighbor-interactions and boundary conditions

One potential mechanism for orientational order in the liver is a direct nematic interaction between hepatocytes. We describe this mechanism by the effective interaction energy given in equation (5.4) and using the neighborhood relations of hepatocytes obtained from experimental data. Each nematic director \mathbf{n} in the model corresponds to a nematic cell polarity axis of a hepatocyte. The directions of the nematic director \mathbf{n} near large vessels, i.e. portal and central vein, are held fixed to point normal to the surfaces of the veins to provide boundary conditions for the other directors.

We first examine states in the zero-noise limit, which were determined through simulated annealing, see appendix A.12 for details. In Fig. 5.2, we show two typical low-energy states. Panel A shows an example of a measured vein geometry that leads to an orientational configuration that follows the lobule-level reference field well. Other vein configurations lead to more uniformly ordered systems, as shown in panel B. Generally, by examining five different data sets (cf. appendix A.12), we find that in cases where only small sections of the vessels are included in the imaging volume (the number of boundary anchoring points is low), the neighbor-interaction model does not provide physiologically plausible solutions. This observation might be due to the restricted volume of tissue imaged and does not

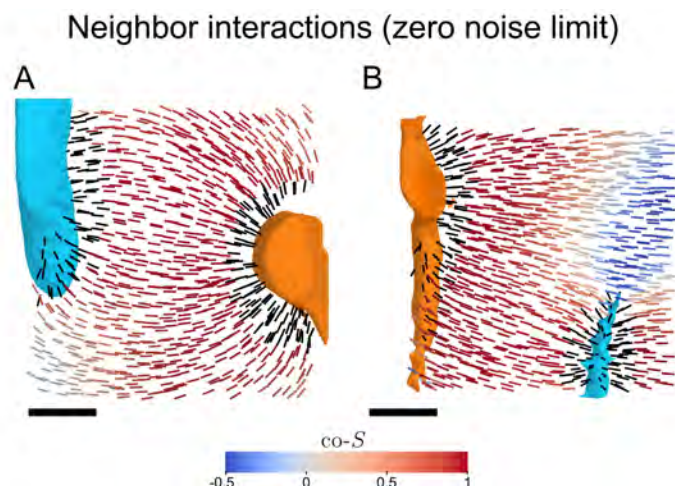


Figure 5.2. Role of boundary conditions for orientation patterns in the neighbor-interaction model governed by equation (5.4). Shown are the nematic axes, colored by co-alignment values $co-S$ with the lobule-level reference field e_χ (cf. section 3.2). Fixed directors, adjacent to large veins and normal to their respective surfaces, providing boundary conditions and are shown in black. (A) For large vessels, configuration in the zero-noise strength limit is well-aligned with the lobule-level reference field. (B) If only a small fraction of vessels is included in the imaging volume, the configuration in the zero-noise strength limit resembles a more uniformly ordered system. Experimental data (surfaces of large vessels, cell positions and neighborhood relations): Zerial group at MPI-CBG. Scale bar: $100\mu\text{m}$.

necessarily speak against the neighbor-interaction model to drive cell polarity organization in liver tissue.

After having examined the zero-noise limit, we now gradually increase the noise strength. In order to generate configurations that resemble the orientational order found in liver tissue, we start with a configuration of directions perfectly aligned with the lobule-level reference field e_χ and gradually increase⁸ the noise strength ν . Fig. 5.3 shows 4 example realizations of the neighbor-interaction system at different noise strengths. In general, the overall orientational order decreases for increasing noise strength ν . For finite noise strengths, the alignment with the lobule-level reference field is strongest near the imposed boundary conditions. The nematic directors, representing cell polarity, become more disordered, the farther away they are from the anchoring points at the large veins. This is reflected in the spatial ordering profile shown in Fig. 5.4B for a noise strength of $\nu/\varepsilon = 2.0$. As expected, it shows a characteristic dip between the veins, which serve as boundary anchoring

⁸The noise strength (given relative to the local interaction strength ε) is increased in discrete steps $\nu/\varepsilon = 0.01, 0.1, 0.2, 0.3, \dots, 1.9, 2.0$. At each value of the noise strength, 10000 MCS are performed.

points in the neighbor-interaction model.

The spatial profile of the co-alignment order parameter is very different from the spatial order profile observed for experimental data of liver tissue (cf. Fig. 5.1B). This indicates that the neighbor-interaction mechanism is not able to explain coordination of bipolar apical cell polarity in liver tissue.

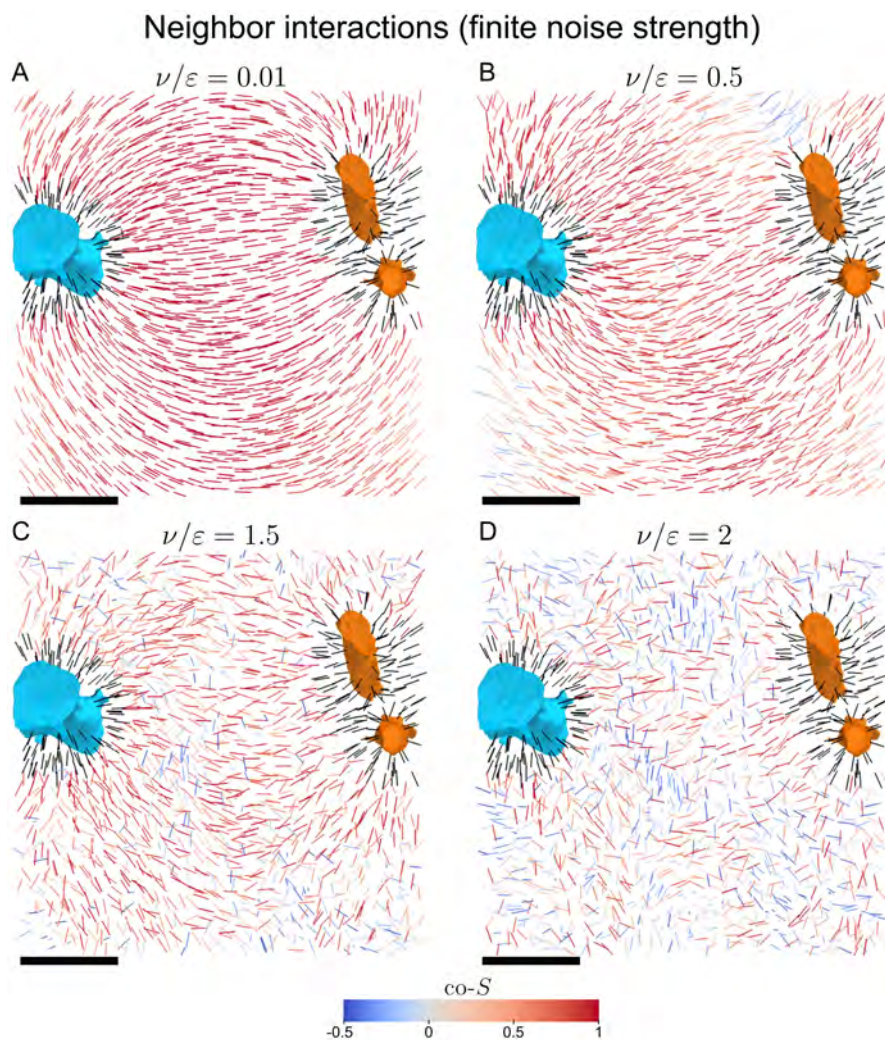


Figure 5.3. Noise strength controls disorder of director patterns in the neighbor-interaction model. (A) When the noise strength is much smaller than the energetic interaction constant, $\nu/\varepsilon = 0.01$, the director configuration closely resembles the lobule-level reference field e_χ , indicated by co-alignment values $co-S$ (cf. section 3.2) close to 1 (red colors). (B-C) For increasing values of ν/ε , the orientational order decreases and alignment with the lobule-level reference field is reduced. Experimental data (surfaces of large vessels, cell positions and neighborhood relations): Zerial group at MPI-CBG. Scale bar: $100\ \mu\text{m}$.

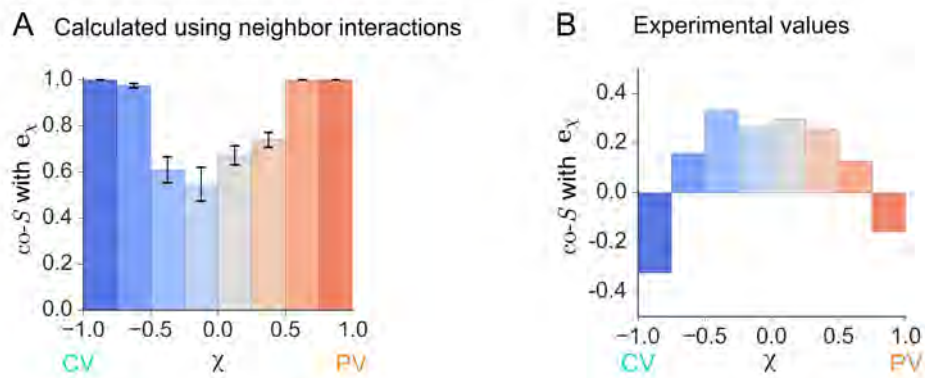


Figure 5.4. Spatial ordering profile resulting from nematic neighbor-interactions. (A) Spatial profile of co-orientational order parameter $co-S$ of directors resulting from nematic interaction model (cf. equation (5.4)) with neighbor-interactions and noise strength $\nu/\varepsilon = 2.0$. Error bars indicate standard deviation of a grand average over 1000 samples. Bar colors correspond to binning of cell-center positions shown in Fig. 5.1B. A snapshot configuration at the same noise strength is shown in Fig. 5.3D. (B) For reference, the spatial profile of orientational order of apical bipolar cell polarity as obtained from experimental data, see Fig. 5.1C. Experimental data (surfaces of large vessels, cell positions and neighborhood relations): Zerial group at MPI-CBG.

5.3.3. Orientational order from coupling to an external field

We now study the orientational order of nematic cell polarity axes by coupling it to an external guidance field. We will consider two different external guidance fields here. First, we will consider the lobule-level reference field (cf. section 3.2) according to equation (5.6). Second, we will take the preferred direction of the local sinusoid as local external field directions. Here, in contrast to the previous section, we do not impose boundary conditions at the large veins and there are no interactions between the directors, which allows us to treat each director independently. In the limit of zero noise strength, the orientations are always perfectly aligned with the external field. For increasing noise strengths⁹ $\nu/\varepsilon_{\text{int}} > 0$, the directors fluctuate around the perfectly aligned state as shown in Fig. 5.5.

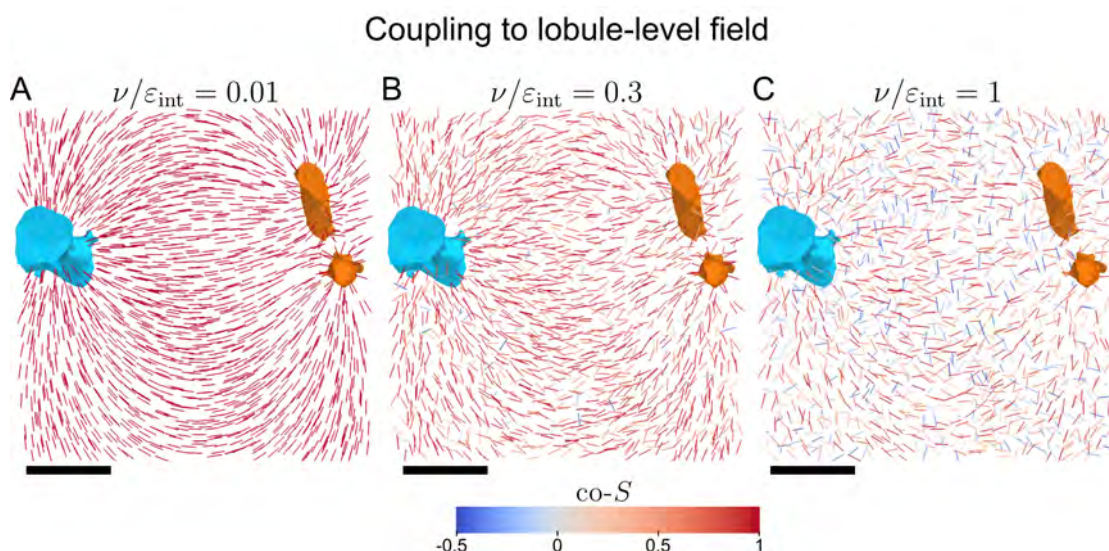


Figure 5.5. Nematic director fields for nematic coupling to an external field at finite noise strengths. (A-C) For small noise strengths, the director field closely follows the external guidance field. For increasing values of $\nu/\varepsilon_{\text{int}}$, the overall orientational order decreases. See section 3.2 for the definition of the lobule-level reference field. Experimental data (surfaces of large vessels, cell positions and neighborhood relations): Zerial group at MPI-CBG. Scale bar: 100 μm .

In contrast to the case of neighbor-interaction, there is no spatial dependence of the ordering, which is reflected by a flat spatial ordering profile, shown in Fig. 5.6. This still deviates from the experimentally observed spatial dependence (cf. Fig. 5.1B), but is qualitatively more similar than the case of neighbor interac-

⁹The relevant energy scale in this section is the coupling constant ε_{int} of individual directors with the external field. We therefore note the noise strength relative to this energy scale.

tions. This already indicates that an external guidance field is more likely to be involved in the coordination of orientational order in liver tissue.

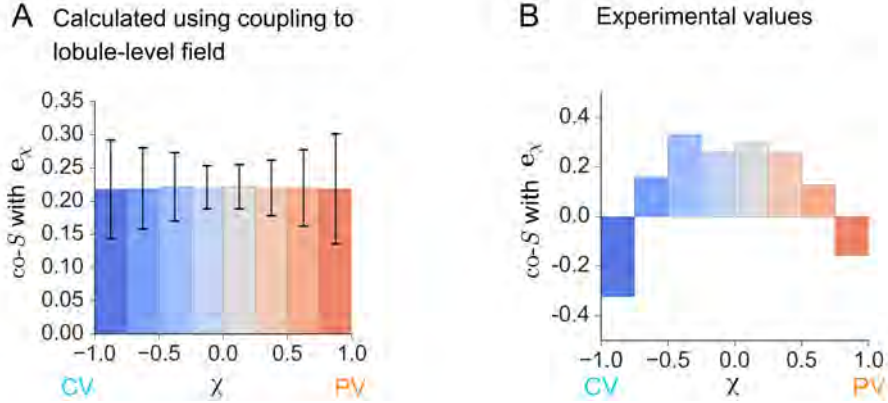


Figure 5.6. Spatial ordering profile resulting from nematic coupling with the lobule-level reference field e_χ . (A) Spatial profile of co-orientational order parameter $co-S$ of directors resulting from nematic coupling with the lobule-level reference field e_χ as external field (cf. equation (5.6)). Error bars indicate standard deviation of a grand average over 1000 samples at $\nu/\varepsilon_{\text{ext}} = 1$. Bar colors correspond to binning of cell-center positions shown in Fig. 5.5B. A snapshot configuration at the same noise strength is shown in Fig. 5.5C. (B) For reference, the spatial profile of orientational order of apical bipolar cell polarity as obtained from experimental data, see Fig. 5.1C. Experimental data (surfaces of large vessels, cell positions and neighborhood relations): Zerial group at MPI-CBG.

In the third uniaxial model variant considered here, we assume that nematic cell polarity of hepatocytes is guided by the local anisotropy of the sinusoidal blood transport network. This choice is motivated by observations of apical lumen elongation in response to extracellular matrix scaffolding by Li et al. [30]. When we provide the preferred local sinusoid orientation as an external field for directors to align, we find that the resulting spatial profile closely resembles the qualitative behavior observed in experiment, as shown in Fig. 5.1B. Together with the findings of the previous model variants, this suggests that apical bipolar cell polarity is unlikely to be autonomously organized through neighbor-interactions between hepatocytes. Instead, the organization of apical bipolar cell polarity may be guided by a nematic interaction with the preferred axis of the local sinusoidal network.

In section 4.4 we showed that co-alignment between apical cell polarity of hepatocytes and local sinusoidal networks is not uniaxial but phase-biaxial, which cannot be explained by the uniaxial nematic interaction model considered so far.

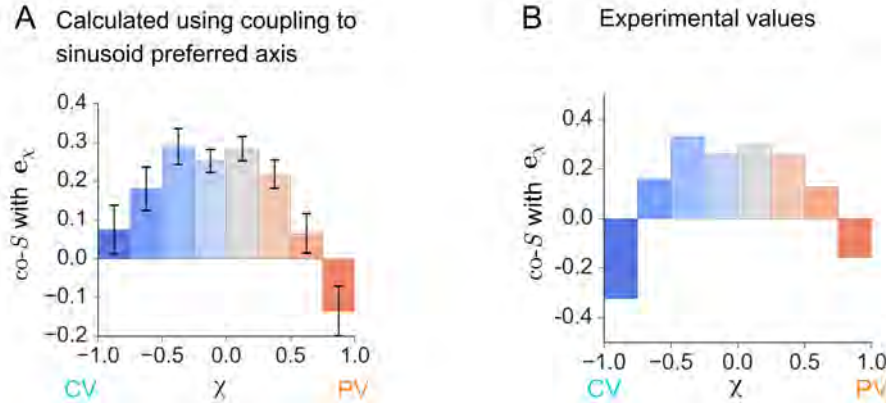


Figure 5.7. Spatial ordering profile resulting from nematic coupling with sinusoid preferred axis. (A) Spatial profile of co-orientational order parameter $co-S$ of directors resulting from nematic coupling, as described by equation (5.6), with the local sinusoid preferred axis \mathbf{s}_1 (cf. section 2.3) as external field. Error bars indicate standard deviation of a grand average over 1000 samples at $\nu/\varepsilon_{\text{ext}} = 0.5$. Bar colors correspond to binning of cell-center positions shown in Fig. 5.5B. (B) For reference, the spatial profile of orientational order of apical bipolar cell polarity as obtained from experimental data, see Fig. 5.1C. Experimental data (surfaces of large vessels, cell positions and neighborhood relations): Zerial group at MPI-CBG.

In the present section, we have found that the uniaxial coupling to the local sinusoid agrees best with experimental observations for the spatial dependence of nematic order. In the next section, we will hence consider biaxial interactions between apical nematic cell polarity and local sinusoid anisotropy.

5.4. Biaxial interaction model reproduces co-orientational order between hepatocytes and sinusoids

In the previous section, we have seen that a simple model of uniaxial coupling between apical bipolar axis and local sinusoid preferred orientation leads to spatial patterns of co-alignment between apical bipolar axis and lobule-level reference frame that resembles experimental data well. For this particular case, we now turn to biaxial interactions and aim to reproduce the phase-biaxial co-orientational order found in liver tissue (cf. Fig. 4.6).

We employ the discretized external interaction energy of equation (5.9) and replace $T_{\alpha\beta}$ by the apical cell polarity tensors $a_{\alpha\beta}$ (cf. eq. (2.9)). These cell polarity

tensors are subject to an external field $G_{\alpha\beta} = \lambda/a^3 s_{\alpha\beta}$ given as the product of a field strength λ and the anisotropy $s_{\alpha\beta}$ of the local sinusoid network (cf. eq. (2.10)). This leads to the interaction energy

$$F_{\text{int}} = -\lambda \sum_i a_{\alpha\beta}^{(i)} s_{\alpha\beta}^{(i)} = \sum_i F_{\text{int}}^{(i)}. \quad (5.10)$$

The interaction strength¹⁰ λ with the external field effectively controls the coupling between the orientation of the biaxial cell anisotropy, described by $a_{\alpha\beta}$, and the orientation of the sinusoid network anisotropy $s_{\alpha\beta}$, which takes the role of an external field¹¹. Again, we assume that the probability of finding a relative orientation between an apical cell polarity and a respective local sinusoid is proportional to the Boltzmann distribution at a noise strength ν that subsumes dynamic processes that reduce spatial order. For simplicity, we introduce the normalized interaction strength $\bar{\lambda} = \frac{\lambda}{\nu}$ as the parameter that controls the overall amount of order in the system. As we consider only the coupling to an external reference field here, the directions of apical nematic cell polarity of individual cells decouple and we can obtain the co-orientational parameters by direct numerical integration without needing to resort to Monte-Carlo methods.

We now use the minimal biaxial interaction model to study co-orientational order between apical nematic cell polarity and local sinusoid anisotropy of hepatocytes

¹⁰Here, we defined the coupling in a way that the field strength λ has units of energy.

¹¹To show this more explicitly, each tensor contraction in (5.10) can be written in terms of the principle axis of the apical cell polarity tensor $a_{\alpha\beta}$ and the sinusoid network anisotropy tensor $s_{\alpha\beta}$. For simplicity, we assume all cells and network anisotropies to be identical. and consider only a single cell subject to the external field and drop the superscript i . Denoting the eigenvalues of $a_{\alpha\beta}$ by $\sigma_1^a, \sigma_2^a, \sigma_3^a$ and the respective eigenvectors by $\mathbf{a}_1, \mathbf{a}_2, \mathbf{a}_3$ and an analogous naming for the eigenvalues and eigenvectors of tensor \mathbf{s} , we note

$$\begin{aligned} F_{\text{int}}^{(1)} = \lambda \mathbf{a} : \mathbf{s} &= \lambda \left(\sum_i \sigma_i^a \mathbf{a}_i \otimes \mathbf{a}_i \right) : \left(\sum_k \sigma_k^s \mathbf{s}_k \otimes \mathbf{s}_k \right) \\ &= \lambda \sum_{ik} \sigma_i^a \sigma_k^s (\mathbf{a}_i \otimes \mathbf{a}_i) : (\mathbf{s}_k \otimes \mathbf{s}_k) \\ &= \lambda \sum_{ik} \sigma_i^a \sigma_k^s (\mathbf{a}_i \cdot \mathbf{s}_k)^2 = \sum_{ik} \alpha_{ik} (\mathbf{a}_i \cdot \mathbf{s}_k)^2. \end{aligned} \quad (5.11)$$

Comparison with equation (3.16) shows that the functional form is similar to the case of a biaxial object in an external field discussed in section 3.1.5. Both descriptions become equivalent, when the eigenvectors of the tensor \mathbf{s} take the role of the external reference frame and the interaction parameters α_{ik} are given by the eigenvalues of \mathbf{a} and \mathbf{s} as $\alpha_{ik} = \lambda \sigma_i^a \sigma_k^s$. The biaxial nematic interaction energy thus depends on the eigenvalues of both tensors, encoded in the interaction parameters α_{ik} as well as the mutual orientation of the eigenframes of the tensors given by direction cosines $\mathbf{a}_i \cdot \mathbf{s}_k$.

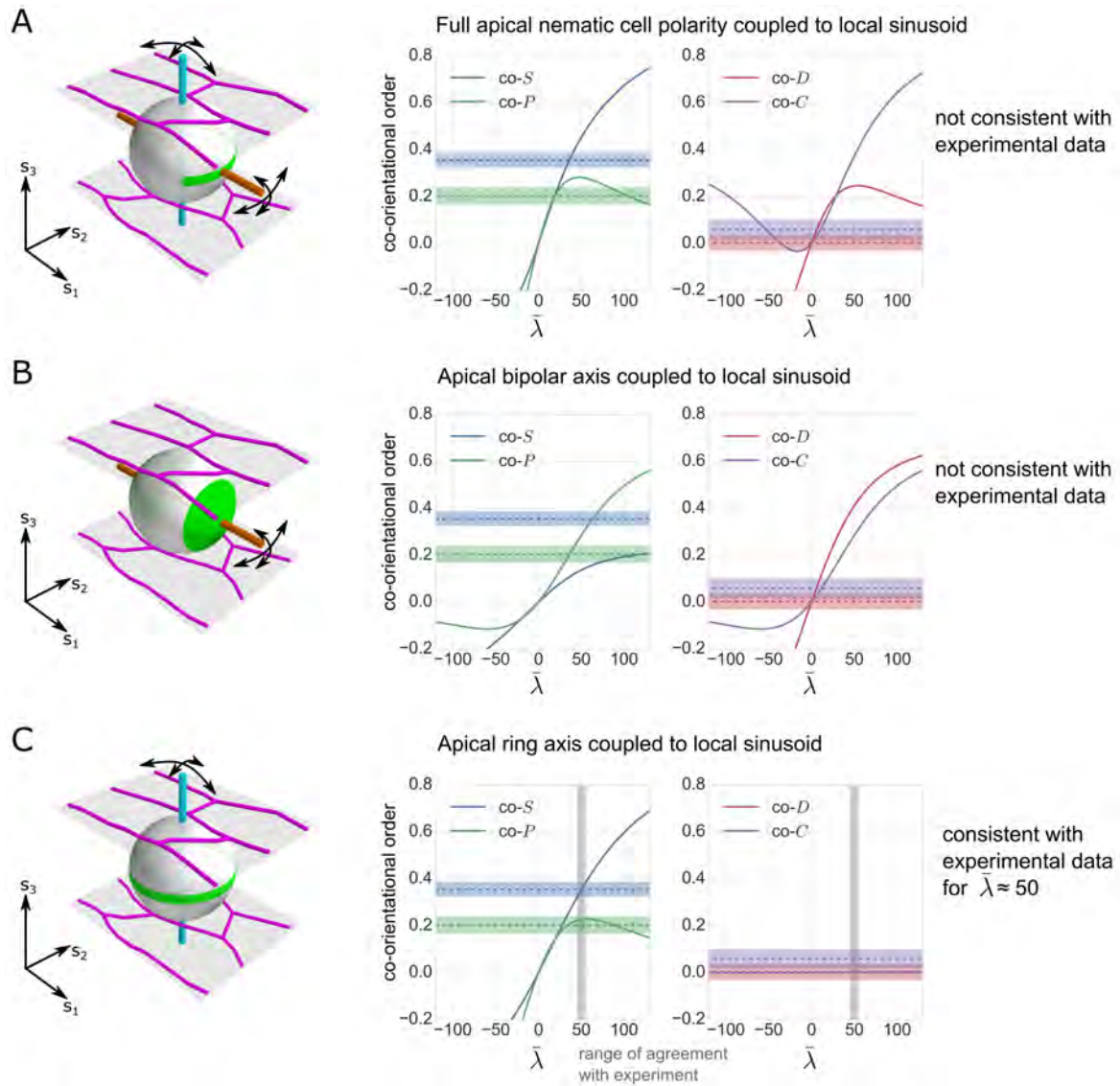


Figure 5.8. Co-orientational order parameters for three model calculations.

(A) Schematic nematic interactions (left) and resulting co-orientational order parameters (right) for coupling of the full apical nematic cell polarity to the local sinusoid. Solid lines show co-orientational order parameters for the model calculations. Dashed lines represent experimental values of co-orientational order (means over 12 experimental data sets with shaded areas indicating one standard deviation). (B) Same as panel A but with interaction only between the apical bipolar axis and the local sinusoid. (C) Same as panels A and B but with interaction only between the apical ring axis and the local sinusoid. Here, the range of normalized interaction strength $\bar{\lambda}$ where the model calculations agree with experimental data is highlighted in gray. Experimental data: Zerial group at MPI-CBG.

in the liver. For that, the averaged eigenvalues of the apical nematic cell polarity tensor and local sinusoid tensor are used for $a_{\alpha\beta}$ and $s_{\alpha\beta}$, respectively. Below, we will consider three variants of the model. While the first two cannot explain the experimental data, the third compares very well.

Let us first consider the case, where the biaxial interaction parameters are derived from the full (averaged) apical nematic cell polarity tensor. The resulting co-orientational order parameters for varying values of the normalized interaction strength $\bar{\lambda}$ are shown in Fig. 5.8A together with a schematic of an apical cell polarity interacting with its local sinusoid. Because the sign of the interaction energy (5.10) is not known a priori, both positive and negative values of the control parameter are considered. For comparison, the mean co-orientational order parameters for liver tissue (cf. Fig. 4.6) averaged over 12 data sets are shown by a dashed line. The shaded area around the dashed line indicates one standard deviation of the experimental values. It can be seen that for no value of the normalized interaction strength $\bar{\lambda}$ consistency with the experimental values is achieved. In particular, for the region in which co- S is in agreement with experiment, the other co-orientational order parameters are much higher in the model calculations than what is observed in liver tissue.

This leads us to test an intermediate approach between the uniaxial and biaxial model, where only one axis of apical cell polarity interacts with the local sinusoid. For an interaction of only the bipolar nematic axis with the local sinusoid anisotropy, we formally set $\sigma_2^a = \sigma_3^a = 0$, see schematic in Fig. 5.8B. Likewise, to let only the apical the ring axis interact with the local sinusoid anisotropy, we formally set $\sigma_1^a = \sigma_2^a = 0$, see schematic in Fig. 5.8C. The resulting co-orientational order parameters are shown in panels B and C of Fig. 5.8, respectively. In the case of coupling the apical bipolar axis with the local sinusoid, again, the co-orientational order parameters of the model calculations (solid lines) are different from the experimental values observed in liver data (dashed lines) for all values of the normalized interaction strength $\bar{\lambda}$. However, for the last considered variant, where the apical ring axis of cell polarity interacts with the local sinusoid anisotropy, we observe a range of normalized interaction strengths $\bar{\lambda}$, where the co-orientational order parameters obtained from the model calculations (solid lines) are in good agreement with experimental results (dashed lines).

This indicates that the interaction of the ring-axis of apical nematic cell polarity with the local sinusoid network is sufficient to account for the experimentally

observed co-orientational order, which motivates the schematic picture of sinusoid-hepatocyte co-alignment in liver tissue shown in Fig 5.8C. There, we propose a simplified view of co-alignment with the ring-axis of apical nematic cell polarity of hepatocytes aligned preferentially parallel to the plane axis of the local sinusoid \mathbf{s}_3 (see section 2.3 for definition). Fluctuations break axial symmetry and are biased towards the corresponding network axis \mathbf{s}_2 .

5.5. Summary

In this chapter, we investigated potential mechanisms that could underly orientational order of nematic cell polarity found in liver tissue (cf. chapter 4). With a uniaxial nematic interaction model (derived by discretizing the Frank distortion free energy) we studied neighbor-interactions and coupling to an external field. We showed that, for certain boundary conditions, the orientations obtained in the zero-noise strength limit of the uniaxial nematic neighbor-interactions agree with the lobule-level reference field, which can be seen as an idealization of the orientational order of cell polarity found in liver tissue (see section 4.2). For finite noise strength, however, the spatial distribution of orientational order of cell polarity, as found in liver data, could not be reproduced. Coupling to an external reference field, given by the lobule-level reference field, gave slightly better agreement (cf. section 5.3.3). By far the best agreement with experimental data was obtained using the preferential direction of the local sinusoid network as a global alignment field. This indicates that nematic cell polarity of hepatocytes is spontaneous, yet requires global alignment cues for correct lobule-level organization, which may be provided by the anisotropy of the local sinusoid network. Building on these observations, we considered a biaxial nematic interaction model that couples anisotropy of the local sinusoid network and nematic cell polarity of hepatocytes. This last model was able to reproduce the phase biaxial co-orientational order between both structures.

6. Network self-organization in a liver-inspired lattice model

The main focus of this short chapter are the two transport networks of the liver, namely the sinusoid and bile canaliculi network, which were introduced in section 1.2. One important aspect of the bile canaliculi network is that it is formed directly as a lumen between two adjacent cells, which is hold together by tight junctions (cf. section 1.3). It is therefore not possible that the sinusoid and bile canaliculi networks cross each other. Furthermore, all hepatocytes are in contact with both transport networks and each network is by itself fully connected.

The aim of the present chapter is to reproduce the basic principles of these three biological observations of the two transport networks in liver tissue in a minimal model. For that, we devise a simple lattice-based model, which is a generalized Ising model. The proposed energetic interactions are similar to the one in the Cellular Potts Model introduced in section 1.4.2, which is able to spontaneously generate ordered structures.

6.1. Cubic lattice geometry motivated by liver tissue

We propose a simple and abstract model to study the generation of the network structure observed in liver tissue. As a first simplification, we neglect all dynamic rearrangement of cells, such as cell movement or cell division. We further simplify the arrangement of cells by regarding them as cubes arranged on a simple cubic lattice. On the surfaces of these cubes, which represent cells in an abstract way, we allow network segments to form in a particular fashion. Specifically, network segments representing sinusoids may form on the edges of the cube and will be referred to as *edge segments* below. Network segments representing bile canaliculi connect midpoints of opposing edges on the faces of the cube and are termed *face segments*, see Fig. 6.1. This peculiar topology is chosen because it is relatively simple, while retaining the number of cells adjacent to each segment found in real liver tissue. We now provide analysis of experimental data to support that claim.

In the cubic model, it is apparent that each edge segment, representing a sinusoid, is surrounded by four different hepatocytes, while each face segment, repre-

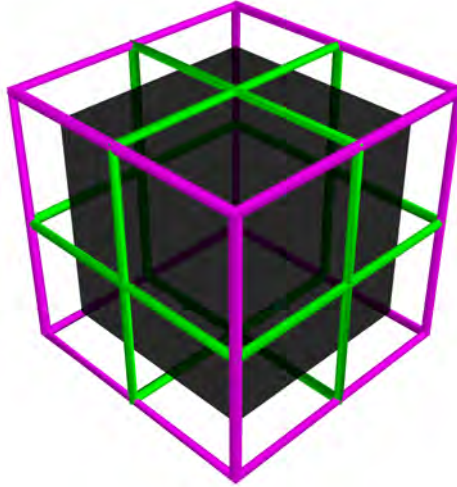


Figure 6.1. One cubic cell with all possible sinusoid segments shown in magenta and bile canaliculi segment shown in green. We represent a tissue cell, in an abstract sense, by a cube. Network segments can be located on the cube under two conditions. (1) Segments representing sinusoids (magenta) may be located on the edges of the cube and (2) segments representing bile canaliculi may be located across the faces of the cube, connecting the midpoints of two opposing edges.

senting bile canaliculi, is surrounded by two different hepatocytes. To quantify the same measures in the liver, we performed an analysis combining the information of the central lines of the network and the segmented cells. Specifically, we find the midpoint of the central lines connecting two adjacent branching points. We then determine how many different hepatocytes are within a thin disk¹. The normal axis of the disk is located at a midpoint and parallel to a central line segment and as shown in Fig. 6.2. The histogram for sinusoids shows a clear peak at four hepatocytes and the histogram for bile canaliculi a peak at two hepatocytes², which is in good agreement with the values of the cubic lattice model introduced above. Thus, the minimal cubic model approximately reproduces the number of cells adjacent to sinusoid and bile canaliculi segments, respectively, which supports the general validity of the cubic abstraction.

¹The disk had a height $h = 0.5\mu\text{m}$ and radius $r = 6.5\mu\text{m}$. The height was chosen to be slightly larger than the side-length of an image voxel of $0.3\mu\text{m}$. The radius was chosen to be 1.5 times the sum of the average sinusoid radius of $4.1\mu\text{m}$ and its standard deviation of $0.2\mu\text{m}$.

²To avoid the influence of branching points on the counts, we order the midpoints of segments by their distance to the nearest branching point (high to low) and take the first 500 segments for analysis. The distribution for the bile canaliculi is skewed, because segments can only form between at least two hepatocytes. Detection of more than two hepatocytes around bile canaliculi can be due to either physiological branching points or too-large discs, which capture hepatocytes that are not directly adjacent to the segment under question.

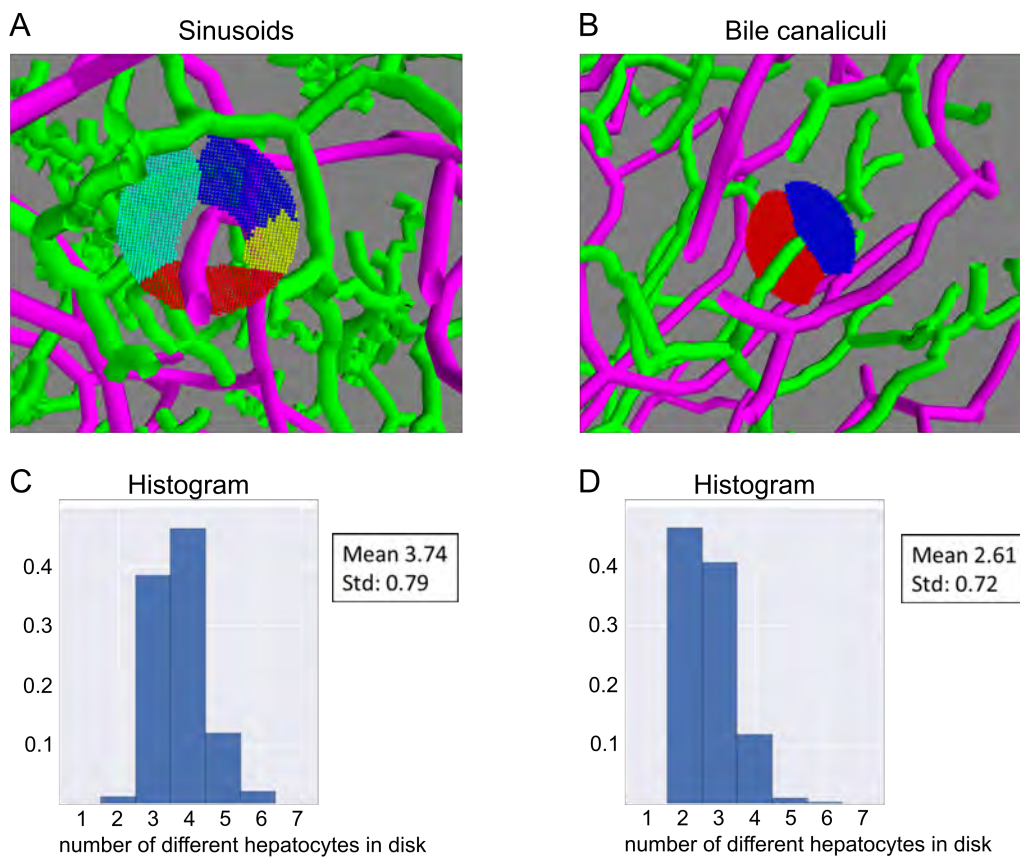


Figure 6.2. Quantification of number of hepatocytes surrounding the central lines of sinusoid and bile canaliculi. (A-B) Example disk around (A) sinusoids and (B) bile canaliculi network segment with different colors corresponding to different segmented hepatocytes. For each disk, the number of different hepatocytes is counted. The histograms over 500 data points are shown in the panels below. (C, D) Histogram of numbers of hepatocytes around (C) sinusoid and (D) bile canaliculi network segments. Experimental data: Zerial group at MPI-CBG.

We can further estimate the number of segments per cube in the model that would correspond to the network density found in liver tissue. From experimental data, we calculate the length density and obtain for the bile canaliculi network 5.8 m/mm^3 and 4.4 m/mm^3 for the sinusoid network. We assume that the cubic cell has a side-length of $a = 20 \mu\text{m}$, which corresponds to approximately one hepatocyte diameter³. With that, we estimate the density of network segments to be 2.32 bile canaliculi segments per cubic volume and 1.72 sinusoid segments per cubic volume.

6.2. Effective energy for local network segment interactions

The geometric lattice model introduced above is now supplemented with an effective energy to describe local interactions between network segments that are motivated by observations in liver tissue. The resulting effective energy is formally equivalent to a Hamiltonian of a generalized Ising model. The interaction parameter, however, do not describe actual physical interactions between the network segments but are instead used to make biologically plausible neighborhood relations more preferable. In particular, neighboring segments of the same type should be favored while segments of different type should repel each other⁴. The conceptual novelty of the approach presented here is the biologically motivated constraint for each species of network segments to be bound to a disjoint subset of the lattice, e.i. sinusoids to “edge segments” and bile canaliculi to “face segments”.

We write the effective energy of the network configuration as a sum of pair-wise interaction between network segments E_{pair} and an energy E_{cell} favoring a specific number of segments per cell

$$E_{\text{total}} = E_{\text{pair}} + E_{\text{cell}} . \quad (6.1)$$

The probability to find a specific configuration of network segments at a noise strength ν shall be given by the Boltzmann distribution $f \propto \exp(-E_{\text{total}}/\nu)$. Here, we regard the noise strength ν as an abstract measure of how strongly biological processes generate disorder.

³This value also compares well with the layer spacing found in section 4.6.

⁴This type of local interaction is similar to the cellular Potts model introduced in section 1.4.2. They were also studied in the context of binary mixtures of liquids [187, 188], which were used by Steinberg to formulate the differential adhesion hypothesis for cell sorting [189].

Energetic contribution of neighboring network segments. To formulate the effective pair interaction between network segments, we introduce an occupation list $\sigma_i = 0, 1$, where i sequentially numbers all segments of the lattice and segment i is empty if $\sigma_i = 0$ and occupied if $\sigma_i = 1$. Denoting the energetic interaction between segment i and segment j by J_{ij} , we write the interaction energy

$$E_{\text{pair}} = \sum_{ij} J_{ij} \sigma_i \sigma_j . \quad (6.2)$$

While this formulation is appealing due to its simplicity, it is impractical to allow for arbitrary interaction energies between any segments in the whole lattice. We therefore modify the generic formulation above to make explicit use of the topology of the lattice. Specifically, we separate the occupation list into two parts, σ_i^S and σ_j^B , where the index i runs over all edge segments of the lattice, $i \in \mathcal{I}_E$, and the index j runs over all face segments of the lattice $j \in \mathcal{I}_F$. With this, we effectively separated the energetic contributions from segments of the same type, J^{SS} and J^{BB} , and of different types J^{BS} , yielding $E_{\text{pair}} = \sum_{i,j \in \mathcal{I}_E} J_{ij}^{\text{SS}} \sigma_i^S \sigma_j^S + \sum_{i,j \in \mathcal{I}_F} J_{ij}^{\text{BB}} \sigma_i^B \sigma_j^B + \sum_{i \in \mathcal{I}_F, j \in \mathcal{I}_E} J_{ij}^{\text{BS}} \sigma_i^B \sigma_j^S$. The total number of occupied network segments representing sinusoids is thus given by $N^S = \sum_i \sigma_i^S$, and the number of occupied network segments representing bile canaliculi is given by $N^B = \sum_i \sigma_i^B$.

We further impose that the energetic interactions are the same for all neighbors defined by adjacency matrices $\{K^{\text{SS}}, K^{\text{BB}}, K^{\text{BS}}\}$. Hence, we can write $J^{\text{SS}} = \frac{\epsilon_{\text{SS}}}{2} K^{\text{SS}}$, $J^{\text{BB}} = \frac{\epsilon_{\text{BB}}}{2} K^{\text{BB}}$, $J^{\text{BS}} = \frac{\epsilon_{\text{BS}}}{2} K^{\text{BS}}$, which gives for the effective interaction energy

$$E_{\text{pair}} = \frac{\epsilon_{\text{SS}}}{2} \sum_{i,j \in \mathcal{I}_E} K_{ij}^{\text{SS}} \sigma_i^S \sigma_j^S + \frac{\epsilon_{\text{BB}}}{2} \sum_{i,j \in \mathcal{I}_F} K_{ij}^{\text{BB}} \sigma_i^B \sigma_j^B + \epsilon_{\text{BS}} \sum_{i \in \mathcal{I}_F, j \in \mathcal{I}_E} K_{ij}^{\text{BS}} \sigma_i^B \sigma_j^S . \quad (6.3)$$

We have thus separated the parameters for the energetic interaction from the topology of the lattice. The topology of the lattice is incorporated solely in the set of adjacency matrices $\{K^{\text{SS}}, K^{\text{BB}}, K^{\text{BS}}\}$. The constraint of segments representing sinusoids being located on the edges of cubes and segments representing bile canaliculi on the face of cubes leads to particular neighborhood relations between different segment types. To illustrate that we show the 4 possible neighborhoods that are encoded in the adjacency matrices $\{K^{\text{SS}}, K^{\text{BB}}, K^{\text{BS}}\}$ in Fig. 6.3.

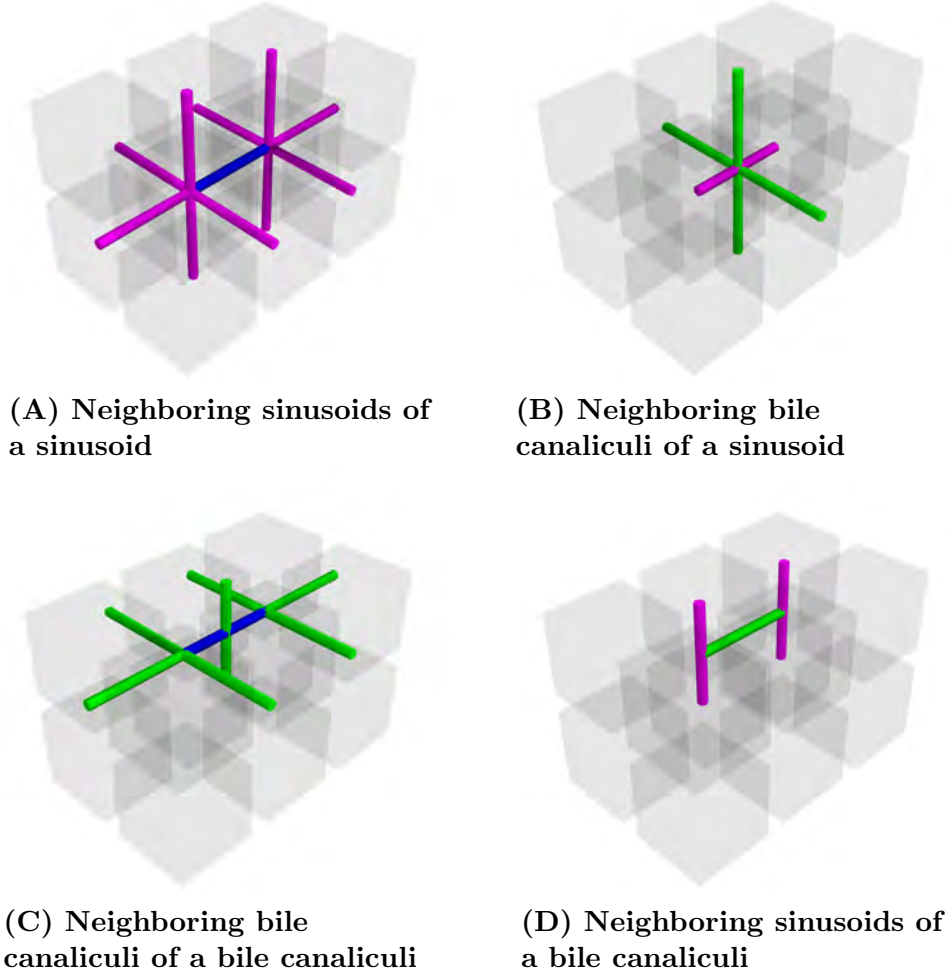


Figure 6.3. Segment neighborhoods considered in the lattice model. Shown are 12 cells in shaded gray arranged into four rows of three cells each. (A) Segment neighbors representing sinusoids (magenta) of a specific “sinusoid” segment (blue). This corresponds to the non-zero entries in the respective row i (or column j) in the adjacency matrix K_{ij}^{SS} . (B) Segment neighbors representing bile canaliculi (green) of a specific “sinusoid” segment (magenta). This corresponds to the non-zero entries in the respective column j in the adjacency matrix K_{ij}^{BS} . (C) Segment neighbors representing bile canaliculi (green) of a specific “bile canaliculi” segment (blue). This corresponds to the non-zero entries in the respective row i (or column j) in the adjacency matrix K_{ij}^{BB} . (D) Segment neighbors representing sinusoids (magenta) of a specific “bile canaliculi” segment (green). This corresponds to the non-zero entries in the respective row i in the adjacency matrix K_{ij}^{BS} .

Energetic contribution to favor a given network segment number per cell.

As every cell needs to be in contact with both types of network it is useful to introduce a cell-based control parameter to enforce this requirement. We choose an energy contribution similar to the area constraint of the cellular Potts model (cf. equation 1.2).

$$E_{\text{cell}} = \sum_{\alpha} \lambda_{\alpha}^{\text{S}} \left(n_{\alpha}^{\text{S}} - c_{\alpha}^{\text{S}} \right)^2 + \sum_{\alpha} \lambda_{\alpha}^{\text{B}} \left(n_{\alpha}^{\text{B}} - c_{\alpha}^{\text{B}} \right)^2. \quad (6.4)$$

Here, we introduced the index α that runs over all N_{cells} cubes that represent cells in the abstract lattice model. For a compact notation, we defined shorthands for the number of occupied segments representing sinusoids $n_{\alpha}^{\text{S}} = \sum_{i \in \mathcal{C}_{\alpha}^{\text{S}}} \sigma_i^{\text{S}}$ and the number occupied segments representing bile canaliculi $n_{\alpha}^{\text{B}} = \sum_{i \in \mathcal{C}_{\alpha}^{\text{B}}} \sigma_i^{\text{B}}$ that are adjacent to the cube α . The set $\mathcal{C}_{\alpha}^{\text{S}}$ includes all edge segments and the set $\mathcal{C}_{\alpha}^{\text{B}}$ holds all face segments adjacent to the cube α . The parameter c_{α}^{S} is the target number of occupied edge segments representing sinusoids and c_{α}^{B} is the target number of face segments representing bile canaliculi for cube α . Any deviation of the actual number of occupied segments around cube α from their respective target number yields a unfavorable contribution to the total effective energy. The parameters $\lambda_{\alpha}^{\text{S}} \geq 0$ and $\lambda_{\alpha}^{\text{B}} \geq 0$ control the strength of the energetic penalty. For simplicity, we assume that all cells share the same preference for the number of surrounding segments. Thus, we set $\lambda_{\alpha}^{\text{S,B}} = \lambda^{\text{S,B}}$ and $c_{\alpha}^{\text{S,B}} = c^{\text{S,B}}$ in equation (6.4).

6.3. Characterizing network structures in the cubic lattice geometry

For the analysis of network structures on the cubic lattice employed here, we define suitable order parameters. Motivated by the observations in liver data, we are interested in the amount of connectivity between the two transport networks (sinusoids and bile canaliculi) and structural order parameters, such as cell polarity and smectic order of the cell-network density correlations (cf. section 4.6).

From liver data, we know that each cell has an interface with both types of networks. In the cubic lattice model, we therefore investigate the fraction of cells that is in contact with at least one segment representing a sinusoid and the fraction of cells that is in contact with at least one segment representing a bile canaliculi.

When both of these numbers are one, every cell has a contact to both network types, which corresponds to the results found in liver tissue. Fractions lower than one indicate that some cubes in the model are not connected to the networks. Next, we observe in experimental data of liver tissue that the sinusoid and bile canaliculi networks are both fully connected. In the abstract cubic lattice model, we calculate the number of connected components as well as the relative size of the largest one. When this relative size is one, all the segments form one giant component, which is then similar to the observations in liver tissue.

From liver data, we are also aware of the impossibility of crossings between sinusoid and bile canaliculi network. We therefore count the number of crossings in segment configurations in the cubic lattice model. Any deviation from zero indicates a deviation from typical liver structure.

Finally, we calculate a structural anisotropy parameter similar to identify layered structures, for which we found evidence in liver tissue (cf. section 4.6). Due to the underlying specific geometry of a cubic lattice, we now introduce a layering order parameter for this specific case. To that end, we consider a binary array \mathbf{p} of dimension $2n_x \times 2n_y \times 2n_z$, where n_x, n_y, n_z are the numbers of cubes in the respective spatial direction. The indices of that array represent all node positions of both network types and the midpoints of the cubes they surround. Each network segment is thus associated with three indices in that array, corresponding to its endpoints and midpoint. Starting at a zero-array, we iterate through all segments of a given network type (either edge or face segments) and all occupied nodes from zero to one. We then calculate an intermediate quantity

$$q_x = \sum_{i_x \in [0, 2, 3, \dots, 2n_x - 2]} \sum_{i_y, i_z = 0}^{2n_y - 1, 2n_z - 1} \mathbf{p}_{i_x, i_y, i_z} + \mathbf{p}_{i_x + 2, i_y, i_z} - 2\mathbf{p}_{i_x + 1, i_y, i_z}$$

and analogous values q_y and q_z for the other spatial directions. We sort these intermediate values as $q_1 \leq q_2 \leq q_3$ and take

$$q = q_3 - \frac{1}{2}(q_2 + q_1) \tag{6.5}$$

as the layering order parameter. In accordance with the notation introduced for the interaction energy between network segments, we term the layering order parameter for the edge network representing sinusoids q^S and the respective layering order parameter for the face network representing bile canaliculi q^B .

6.4. Local interaction rules generate macroscopic network structures

We now introduce the effects of the individual contributions of the interaction parameters on the qualitative properties of the structure of the resulting transport networks. For simplicity, we fix the total number of sinusoid N_S and bile canaliculi segments N_B in the system. To avoid non-integer values for the number of occupied edge segments per cell c_S and occupied face segments per cell c_B , we round the respective segment numbers estimate from liver data (cf. section 6.1) to their nearest integer values, which yields 2 bile segments (located on cube faces) per cube and 2 sinusoid segments (located on cube edges) per cube⁵.

To get a qualitative picture of the how different local rules lead to different types of order in the cubic lattice model presented above, we first examine only self-attraction, only mutual repulsion and then their combined action. After that, we add the cell demand (cf. equation (6.4)), which will lead to layered network structures. To that end, we employ a Monte-Carlo method (see appendix A.13 for details) to sample configurations from the Boltzmann distribution $f \propto \exp(-E_{\text{total}}/\nu)$. For each set of parameters, we gradually decrease⁶ the noise strength ν to obtain states that correspond to (local) energetic minima. We then compare the types of order found in the network configurations corresponding to these (local) energetic minima.

We first confirm that in the absence of network segment pair interactions, random configurations are found, see Fig 6.4B. For non-zero self-attraction parameters $\epsilon_{SS} < 0$, we find that network segments of the same type aggregate into fully-connected clusters, see Fig. 6.4C. In other words, all segments of one type are part of a single connected component. The locations of the two clusters are arbitrary and they may overlap. The layering order parameters $q^S = 0.1$ and $q^B = 0.13$ for this structure are small. We now consider the case of only repulsive interaction between un-like network segment types. This corresponds to $\epsilon_{BS} > 0$ being the

⁵Due to the different total numbers of face segments and edge segments, this leads to two thirds of the edge segments (representing sinusoids) and one third of the face segments (representing bile canaliculi) being occupied. Note that the rounding has an opposite effect in both network types.

⁶The noise strength ν was first set to 100 to allow for equilibration in a highly unordered regime. It was then reduced in steps of 1 from 10 to 5 and then further reduced in steps of 0.1 from 5 to 0. For each value of the noise strength, 5000 MCS were performed. A single annealing run took about 4h on a machine with an Intel Xeon CPU with 2.5 GHz.

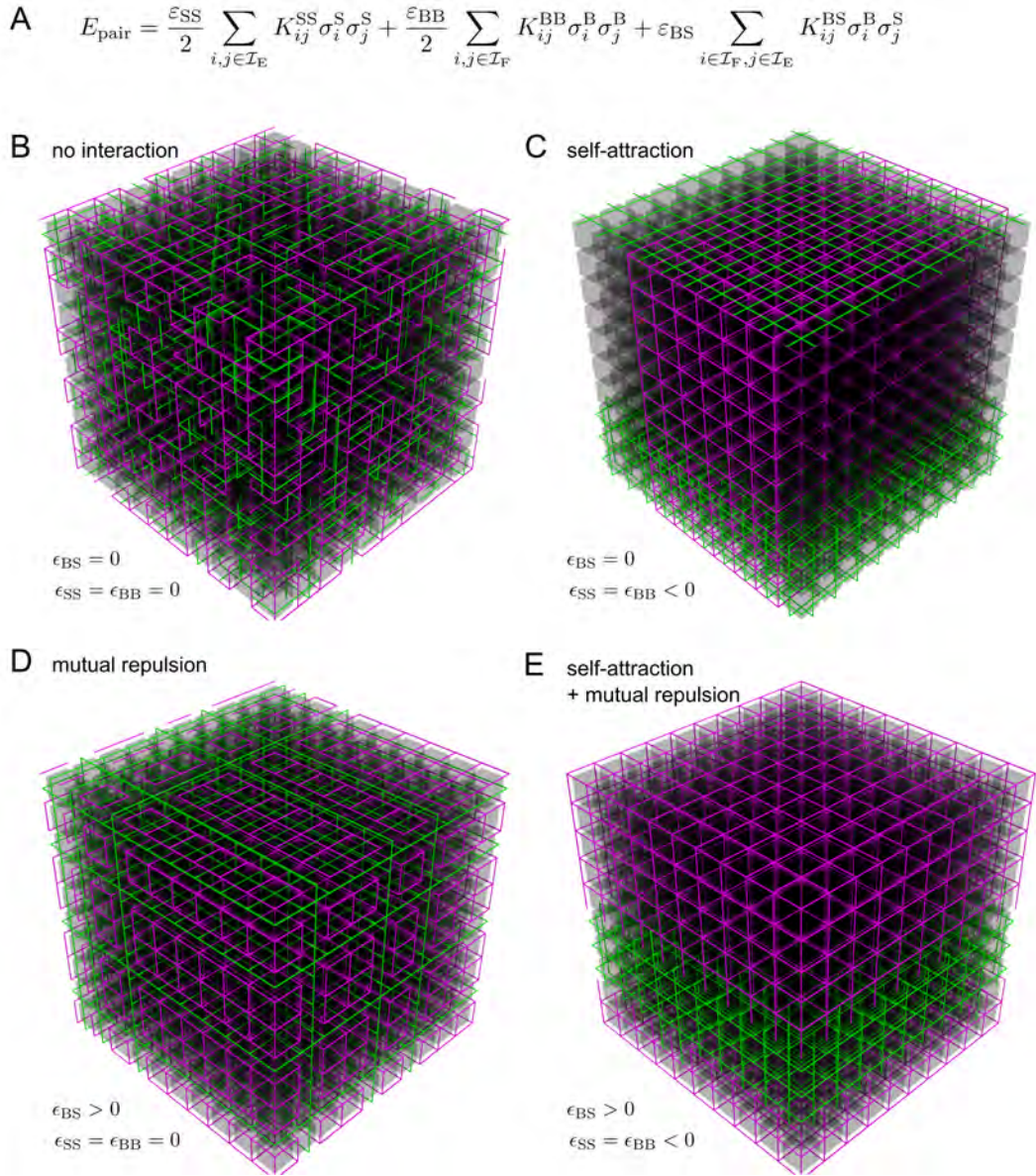


Figure 6.4. Effects of individual contributions of the effective network segment pair energy E_{pair} . (A) Equation (6.3) for direct reference. (B) In the absence of interactions between segments, the configurations of network segments are random. (C) Negative self-attraction parameters $\epsilon_{\text{SS}} = \epsilon_{\text{BB}} < 0$ lead to aggregation of network segments into two fully connected clusters that may overlap. Shown is a configuration for $\epsilon_{\text{SS}} = \epsilon_{\text{BB}} = -1$ after simulated annealing, as described in the text. (D) Mutual repulsion between unlike network segment types is induced by setting $\epsilon_{\text{BS}} > 0$. In this case, not all cells are in contact with both network types and the networks are not fully connected. Shown is a configuration for $\epsilon_{\text{BS}} = 5$ after simulated annealing, as described in the text. (E) Including both self-attraction and mutual repulsion leads to a demixing of both network segment types into two distinct and fully-connected clusters. Shown is a configuration for $\epsilon_{\text{SS}} = \epsilon_{\text{BB}} = -0.5$ after simulated annealing, as described in the text.

only non-zero interaction parameter and leads to non-overlapping but also not fully connected networks. Also, not all cells are in contact with both network cells. The configuration, shown in Fig. 6.5D, corresponds to the global energetic minimum, because no segments of different kind are in contact with each other, which is the only contribution to the energy for the selected parameters. The layering order parameters $q^S = 0.05$ and $q^B = 0.03$ for this structure are also small.

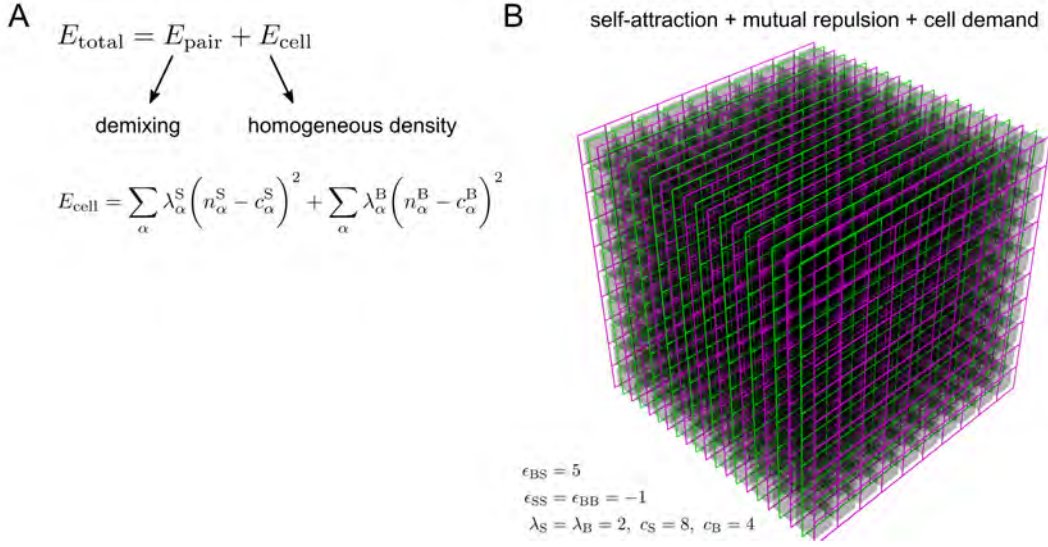


Figure 6.5. Full model including pair interactions and cell demand term.

(A) Equations (6.1) and (6.4) for direct reference. (B) Addition of a cell demand, with model parameters $\epsilon_{SS} = \epsilon_{BB} = -1$, $\epsilon_{BS} = 5$, $c_S = 8$, $c_B = 4$, $\lambda_S = \lambda_B = 2$. This leads to a alternating layers of segment types. Within each layer, the networks are fully connected, all cells are in contact with both network types and there are no intersections between network segments of different type.

If both self-attraction and mutual repulsion interaction parameters are non-zero and follow $\epsilon_{SS} < 0$, $\epsilon_{BB} < 0$ and $\epsilon_{BS} > 0$, the segments of both network kinds separate into two distinct clusters, see Fig. 6.5E. In contrast to the configuration shown in Fig. 6.5C, the clusters are now separated and there are only very few intersections between unequal network segment types⁷. Compared to the configuration found in Fig. 6.5D, the small amount of increase in effective energy due to crossings of different network types is over-compensated by the decrease in effective energy due to more self-interactions. The smectic order parameters $q^S = 0.04$ and $q^B = 0.17$ for this structure are small. The local pair interactions between network segments thus can lead to demixing of both networks into separate clusters.

⁷For the densities chosen here, it is not possible to achieve two fully-connected but separated clusters without any intersections between the two different network types.

In the liver, we also find that both networks are "demixed" in that there are no overlaps between sinusoids and bile canaliculi. However, the demixing occurs locally and still each cell is in contact with both network types. For this, we now also include the cell demand E_{cell} (cf. equation (6.4)). The addition of a non-zero cell demand with $\lambda_S > 0$ and $\lambda_B > 0$ generates alternating layers of sinusoid and bile canaliculi networks, see Fig. 6.5B. Here, we chose the cell segment numbers per cell $c_S = 8$ and $c_B = 4$ to be compatible with the fixed numbers of respective network segments in the system. Within the layers, both networks are fully connected but individual layers are not connected with each other. This configuration has the, qualitatively, best agreement with properties found in liver tissue. In particular, there are no intersection points between the two, mutually exclusive, networks. All cells are in contact with both network types and both networks are (within each layer) fully connected. The smectic order parameters $q^S = 1$ and $q^B = 1$ correspond to perfect layering and are thus much larger than in the other three examples shown.

While these layered structures in the cubic lattice model in the low-noise strength limit are much more regular than the networks found in liver tissue, they share common characteristics and open the possibility of reproducing general features of liver tissue for finite noise strengths.

6.5. Effect of mutual repulsion between unlike segment types on network structure

The analysis above shows that simple local rules can generate different types of interesting order in the cubic lattice model that can be compared to properties of liver tissue. To get more insight into the parameter space and how the qualitatively different structures are placed therein, we scans through different sections of the parameter space can be performed. An exhaustive scan is unfeasible at the moment. However, for an initial analysis, we perform a line scan through the parameter space to explore the feasibility and to learn how the ordered structures change in dependence of the repulsion parameter ε_{BS} and for varying values of the noise strength ν .

For that, we take the values used to obtain the layered structure in Fig. 6.5B

and change the repulsion parameter⁸ ε_{BS} from $\varepsilon_{BS} = 0$ to $\varepsilon_{BS} = 4$ in steps of 0.2. For each value of the repulsion parameter ε , simulated annealing⁹ was done 10 times and a grand average over the averaged values over 20 measurements of a single realization at each noise strength was taken.

The resulting values for the number of intersection events between unequal network types are shown in Fig. 6.6A and four regimes can be identified¹⁰. The first, “R1”, is encountered for high values of the noise strength and low values of the repulsion parameter ε_{BS} . A representative example is shown in Fig. 6.6D1. This corresponds to a random configuration of both networks, which features many intersections between both network types. For decreasing values of the noise strength ν , the structure becomes more ordered. In particular, the face segments representing bile canaliculi (green) representing bile canaliculi arrange into layers. This is quantified by the network order parameter $S = -0.5$ for these structures, see Fig. 6.6B, which means that all occupied face segments lie in a single plane¹¹. The edge segments representing sinusoids, however, form a structure not yet encountered. It can be best described by envisioning a fully occupied edge segment network and then removing every second layer in one direction, see Fig. 6.6D2. This is captured by the smectic order parameter $q^S = 0.25$, see Fig. 6.6C, which is clearly non-zero but far from its maximum value of 1. For increasing values of the repulsion parameter ($1 < \varepsilon < 2$), the number of intersection events between unequal segment types decreases and the bile canaliculi layers change into more line-like configurations, which is indicated by positive values of S in Fig. 6.6B. Finally, for large values of the repulsion parameter $\varepsilon > 2$, the layered configuration already encountered in the qualitative analysis, see Fig. 6.5B, is found.

We now raise the question, whether the final configurations after the annealing procedure may be the ground states for the specific parameter. For that, we compare the configuration found through simulated annealing at a specific value of the repulsion parameter ε with all other configurations encountered after simulated annealing with different values of the repulsion parameter. For high values $\varepsilon_{BS} >$

⁸The other interaction parameters are kept constant at $\varepsilon_{SS} = \varepsilon_{BB} = -1$, $c_S = 8$, $c_B = 4$ and $\lambda_S = \lambda_B = 2$.

⁹The noise strength ν was first set to 100 to allow for equilibration in a highly unordered regime. It was then reduced in steps of 1 from 10 to 5 and then further reduced in steps of 0.1 from 5 to 0. For each value of the noise strength, 20000 MCS were performed for equilibration. Then, 20 numerical measurements were taken with 100 MCS between each measurement.

¹⁰Other structural quantities can be found in appendix A.14

¹¹The smectic order parameter for face segments representing bile canaliculi is $q^B = 1$ in this case, see appendix A.14.

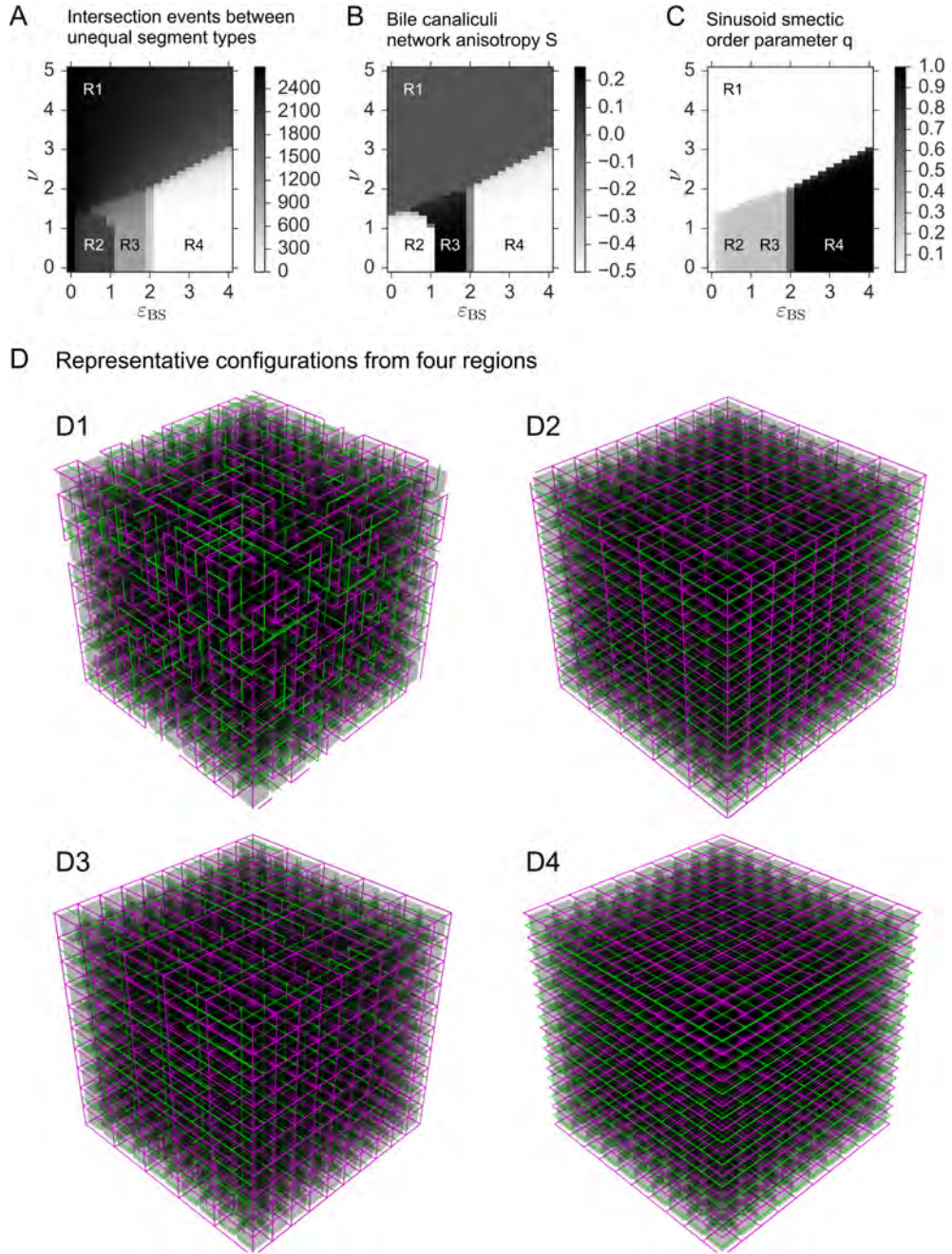


Figure 6.6. Four potential regions depending on repulsion parameter ϵ_{BS} and noise strength ν . Simulated annealing for varying values of the repulsion parameter ϵ_{BS} while keeping the other local interaction parameters fixed to $\epsilon_{SS} = \epsilon_{BB} = -1$, $c_S = 8$, $c_B = 4$ and $\lambda_S = \lambda_B = 2$ with cooling schedule as described in the text. (A) Number of intersection events between unequal segment types. Four regions in the parameter space are labeled. (B) Quantification of the network anisotropy parameter S (cf. section 2.3) for the bile canaliculi networks. (C) Quantification of the smectic order parameter q for sinusoid network. (D) Representative configurations for the four regions marked in panel A. Numbers in label correspond region number in panel A. The chosen values for the mutual repulsion parameter are $\epsilon_{BS} = 0.6$ for regions R1 and R2, $\epsilon_{BS} = 1.6$ for region R3 and $\epsilon_{BS} = 2.6$ for region R4.

2 and low values $\varepsilon_{\text{BS}} < 1$ of the repulsion parameter, the configuration found through annealing had indeed the lowest energy among all the other proposed configurations. For repulsion parameters in the intermediate regime $1 < \varepsilon_{\text{BS}} < 2$, however, the annealing procedure was not able to find the lowest energy configuration. In this parameter range, the layered configuration had lower total energy than the one found through simulated annealing. We therefore speculate that the annealing procedure was trapped in a potentially metastable state and the layered configuration is assumed to be the ground state in that parameter range.

Given the densities, the values for the network segment self-attraction and cell demand as above, the face segments representing bile canaliculi form layers even in the absence of mutual repulsion while the edge segments representing sinusoids do not. Therefore, mutual repulsion is mandatory to obtain a smectic configuration of network segments. For an intermediate region of repulsion $1 < \varepsilon < 2$, the layered configuration has the lowest energy but is not reliably found through simulated annealing, indicating other, possibly metastable, configurations. Only for larger values $\varepsilon > 2$, the layered configuration is found in all the simulated annealing trials.

6.6. Summary

In this last chapter of the thesis, we have presented an abstract model to condense the complex three-dimensional structure of liver tissue into a simplified cubic geometry. We have shown that this abstract geometry conserves the number of cells that surround the segments of the transport networks to good approximation.

On this cubic geometry, we defined a generalization of the Ising model for network self-organization, which is similar to the cellular Potts model introduced in section 1.4.2. For a specific choice of local interaction parameters, we were able to reproduce three key observations from biology: connectedness of both networks, avoidance of crossings between different network types and the connection of all cells to both network types. The configuration that reproduced these features was also smectic, and network segments of different type were organized into alternating layers. Building on this observation we tested, whether repulsion between segments is necessary for the emergence of this type of order. While for the face segment network representing bile canaliculi, the repulsion was not needed to generate a layered structure, it was indeed necessary for the formation of edge segment

layers representing sinusoids. This serves as a proof-of-concept and opens interesting avenues to explore in future.

One interesting future research is to characterize different kinds of phase separations in the system. Also, on a more technical note, it is not obvious how to best compare the simulation results on the abstract cubic geometry to experimental data of liver tissue. Alternatively to using coarse-grained data, as done here, it might provide useful to extend a mapping procedure of fluorescence data onto a lattice geometry, as proposed by Breuer et al. [190] for the two-dimensional case, to the three-dimensional geometry used here. A further future research direction is to use the cubic lattice geometry to model growth processes of the networks that may include feedback from the hepatocytes. From a biological perspective, there are indications that hepatocytes control the local density of sinusoid and bile canaliculi in liver tissue by either regulating the number of proteins involved in the formation of membrane domains that create bile canaliculi [29, 37, 191], or through chemical signaling by growth factors, such as VEGF, which was previously reported for the sinusoidal network [192–194]. Some of these approaches have been investigated in the master thesis of Marius Asal [195] on a modified version of the cubic lattice model presented here.

7. Discussion and Outlook

The over-arching question underlying this thesis is how cells organize into complex functional tissues. To address this question, we selected the liver as a model organ because of three main features: (1) it is a vital organ of vertebrates performing a wide variety of functions, (2) it is inherently three-dimensional in its structural organization and (3) novel experimental imaging methods have recently become available to provide a detailed view on the organization of cells with sub-cellular resolution. By that, the liver qualifies as being complex in both the function it provides for body homeostasis as well as in the architecture needed to provide this function. Using data analysis of high-resolution images of liver data¹ and theoretical modeling, the present thesis arrived at four important results.

The first important result of this thesis, laid out in chapter 2, is the identification of a *nematic cell polarity* of hepatocytes in the liver. In this context, cell polarity refers to the inhomogeneous distribution of membrane-bound proteins on the surface of cells. While this has been implicated before [29], we provide a rigorous quantification of this type of cell polarity by means of a multipole expansion. We showed that cell polarity of hepatocytes is best described by a nematic cell polarity, the orientation of which is represented by a tripod of undirected axes. In the future, it will be interesting to see this method applied to other tissues types and investigate, what dominant type of protein configurations are found there.

The second important result of this thesis is that the orientations of these individual nematic cell polarities are coordinated among many cells throughout the tissue. Furthermore, the patterns of oriented nematic cell polarity were found to be correlated with a lobule-level reference field that is defined by the locations of large vessels within the tissue (cf. section 4.1). We applied the structural analysis framework, which consists of analyzing single cell protein patterns and the orientational order of the thus identified nematic cell polarity, to genetic knock-down experiments, which highlights the usefulness of the quantification. We could show that the inhibition of a specific signaling protein (integrin beta1) reduces the amount of cellular coordination, making the orientational alignment less pronounced, while leaving nematic cell polarity of individual cells unchanged (cf. section 4.5). This

¹The acquisition of experimental data of mice livers as well as image segmentation was performed by collaborators in the lab of Marino Zerial at the Max Planck Institute of Molecular Cell Biology and Genetics, Dresden.

indicates a bi-directional feedback between cell polarity organization and network structures, which is contrary to previous belief. Future studies of liver tissue may use the structural benchmark presented here and investigate its changes during liver development and regeneration. The tools underlying this liver-specific analysis are generic and are summarized in a separate chapter 3. In the future, they may provide useful in their own right as they can be readily applied to other tissues to investigate phenotypes induced by genetic knock down, chemical damage or disease conditions.

The third important result of this thesis is that the coordination of nematic cell polarity is best reproduced by a theoretical model that couples cell polarity to the anisotropy of the local sinusoid network. This conclusion involved three steps. We first showed that uniaxial nematic nearest-neighbor interactions (known as the *Lebwohl-Lascher* model) was unable to reproduce the spatial distribution of orientational order of cell polarity in liver tissue, and coupling to the lobule-level reference field gave more agreeable results (cf. section 5.3.3). The best agreement with experimental data was obtained using the preferential direction of the local sinusoid network as a global alignment field. This indicates that nematic cell polarity of hepatocytes is spontaneous, yet requires global alignment cues for correct lobule-level organization, which may be provided by the anisotropy of the local sinusoid network. Building on these observations, we considered a biaxial nematic interaction model that couples anisotropy of the local sinusoid network and nematic cell polarity of hepatocytes. This last model was able to reproduce the phase biaxial co-orientational between both structures. This implicates that an autonomous organization of orientational order of cell polarity of hepatocytes in the liver is unlikely and guidance by the sinusoidal network is necessary. Whether the sinusoidal network is the only driver of structural organization in the liver or whether there is a more intricate interplay between the network structures and the cell polarity of hepatocytes, as indicated by the genetic knock-down experiments presented in section 4.5, is an interesting question for future research.

The fourth important result of this thesis is that local interaction rules can self-organize into biologically sensible transport networks on a simplified cubic tissue geometry. We mapped the complex three-dimensional structure of liver tissue to a simplified cubic geometry, which preserves typical network-cell neighbor-relations present in liver tissue. We showed that a generalized Ising model is able to reproduce three key observations from biology: connectedness of both networks,

avoidance of crossings between different network types and the connection of all cells to both network types, for a specific choice of local interaction parameters. This serves as a proof-of-concept and opens interesting avenues to explore in future work, e.g. efficient simulation of networks to study robustness and the action of morphogenetic cues.

In conclusion, this thesis used structural analysis of biological tissues to reveal biaxial nematic order in liver tissue. Furthermore, using theoretical modeling, we showed that networks on an abstract cubic lattice can self-organize into sensible structures by local rules alone. Using a nematic interaction model, we showed that it is reasonable to assume that the networks in turn influence the arrangement of cell polarity in liver tissue. A potential feedback of cell polarity on the network structure, as indicated by experimental data, opens new avenues for future explorations.

A. Appendix

A.1. Mean field theory fo the isotropic-uniaxial nematic transition

The first molecular field theory for the (uniaxial) nematic phase was developed by Wilhelm Meier and Alfred Saupe in 1959 [177]. The theory features an effective orientational potential for a single particle derived by a molecular field approximation of the van der Waals forces between molecules [117, 196]

$$U(\cos \theta) = -\bar{u}_2 S \frac{1}{2} (3 \cos^2 \theta - 1) \quad (\text{A.1})$$

where θ is the angle between the molecular symmetry axis and the director. The order parameter S is one given in equation 1.5 and \bar{u}_2 includes the averaged anisotropic interaction parameters. In general, \bar{u}_2 may depend on pressure and temperature. Following the original assumption by Meier and Saupe and for sake of simplicity, this dependence is neglected here. In equilibrium, the angular distribution function given by the interaction energy (A.1) follows the Boltzmann distribution $f(\theta) = \exp(-U/kT)/Z$ with partition function Z as the normalization factor $Z = \int_0^{\pi/2} d\theta \sin \theta \exp(-U/kT)$. The order parameter S is given as the average second moment of the distribution (see eq. (1.5)). Inserting the Boltzmann distribution for the orientational distribution function into eq. (1.5) yields

$$S = -\frac{1}{2} + \frac{3}{2Z} \int_0^1 x^2 e^{\frac{1}{2}\bar{u}_2 S (3x^2-1)/kT} dx . \quad (\text{A.2})$$

where we substituted $x = \cos \theta$. In order for equation (A.2) to be self-consistent, the values of the order parameter on the left-hand side and on the right-hand side must be equal. The solution to this self-consistency equation can be determined numerically. The Meier-Saupe theory predicts a first-order transition from an isotropic fluid to the nematic state at a critical temperature $T = T_c$, where the order parameter goes discontinuously from zero to $S_c = S(T_c) = 0.44$ [39]. Despite the simplicity of the interaction potential and assumption of axially symmetric molecules, the theory is in reasonable agreement with experimental ob-

servations (see Fig. 2.3 in [39] and [196]). The theory of Meier and Saupe was extended to also include steric interactions between molecules, higher rank interactions and deviations from molecular cylindrical symmetry that yield better quantitative agreement with experimental data [196–198].

Extensions to biaxial nematics The molecular-field theory of Meier and Saupe, describing the uniaxial nematic phase, was extended by Freiser to non-cylindrically symmetric molecules [128, 157, 199]. Specifically, the orientational part of the interaction energy between molecules i and j is written as

$$w_{ij} = -\text{Trace}(\mathbf{R}^T \mathbf{Q} \mathbf{R} \mathbf{Q}) \quad (\text{A.3})$$

where \mathbf{R} is the orthogonal rotation matrix that transforms the axes of molecule i into those of molecule j , and \mathbf{Q} characterizes the second-order molecular anisotropy of the molecules. Assuming molecules that possess dihedral symmetry (see appendix A.5), \mathbf{Q} is assumed to be symmetric and traceless. It can thus always be diagonalized, yielding two shape parameters. One parameter, Q , characterizes the uniaxial anisotropy of the molecule and the second, q , characterizes the deviation of the molecular shape from axial symmetry. Using the Schwartz inequality, he first shows that all molecules are perfectly aligned in the ground state. Two orientational order parameters can be defined from the averaged quantity $\langle \mathbf{Q} \rangle$ over the orientational distribution function $f(\Omega) = f(\alpha, \beta, \gamma)$, that are related to the uniaxial order parameter S and the phase biaxiality parameter P that are discussed in section 3.1.1. Applying the molecular field approximation, a successive transition from the isotropic to uniaxial towards the biaxial state upon cooling is found. The isotropic to uniaxial transition is shown to be of first order, whereas the uniaxial to biaxial transition is continuous. For axially symmetric molecules ($q = 0$) the theory reduces to the one of Meier and Saupe.

Shortly after Freiser, Straley proposed the use of two more order parameters (corresponding to D and C in section 3.1.1) to properly characterize the biaxial phase [119]. This revealed a richer phase diagram than the one predicted by Freiser. In particular, a direct isotropic-to-biaxial transition of either first or second order, depending on the molecular anisotropy, was found. This view was adopted by subsequent authors and formalized in considering a so-called “supertensor” [39] or two molecular tensors [200], which can be shown to be equivalent descriptions of orientational order of biaxial molecules in a biaxial phase [160]. Using this

extended description, a Landau expansion in the invariants of Straley's four order parameters gave a more complete view of the phase space for biaxial nematics [140].

A.2. Distortions of the Mollweide projection

A simple method to visualize the distortion in map projection is Tissot's indicatrix [154]. It shows how (infinitely small) circles on the sphere are, in general, deformed to ellipses in the projected view. If the projection is conformal, the ellipse is a circle and eccentricity is zero. Otherwise the ellipse has a major and minor axis which is a direct result of angular and shape distortions of the projection method. Tissot's indicatrix of the Mollweide map is given in Fig. A.1.

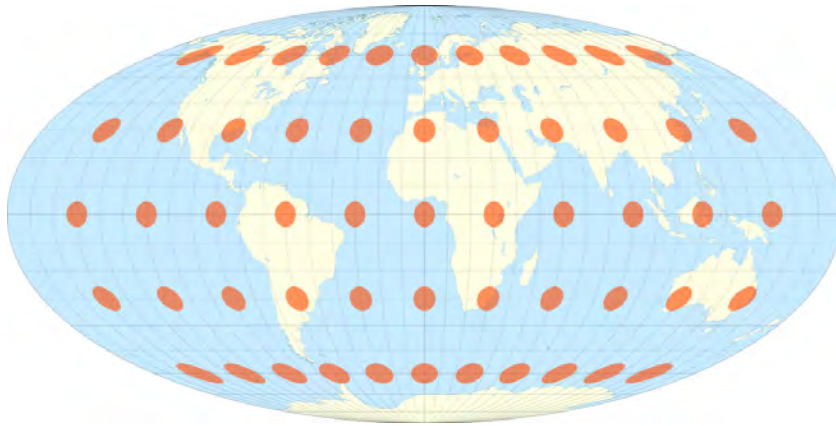


Figure A.1. Distortions of the Mollweide projection.

The Mollweide map is an equal-area, pseudo-cylindrical map projection. Pseudo-cylindrical means that the central meridian and parallel are depicted as straight lines. Also, the distance from the central meridian along a parallel is proportional to the real distance on the globe, hence the meridians on the equator are equally spaced. Equal area means that the proportion of area of an ellipse, consisting of opposing meridians, between any given parallel and the equator is the same as the proportion of area on the globe between that parallel and the equator. It therefore gives good account of the proportion of area covered throughout the whole map. This is achieved by sacrificing accuracy of angle and shape as seen by considerable distortions of the global circles on the projected map when moving away from the equator and central meridian.

Image source: Eric Gaba – Wikimedia Commons User: Sting, distributed under CC-BY-SA 4.0.

A.3. Shape parameters for basal membrane around hepatocytes

The Fig. A.2 shows a version of Fig. 2.6 for basal instead of apical membrane markers. Similar to the apical membrane protein distribution around hepatocytes, most basal membrane configurations of hepatocytes exhibit neither ideal bipolar (orange line) nor ideal ring configurations (blue line). The basal configuration shows a slight bias towards the bipolar case, while the shape parameters of apical membrane are shifted slightly towards the ring limit.

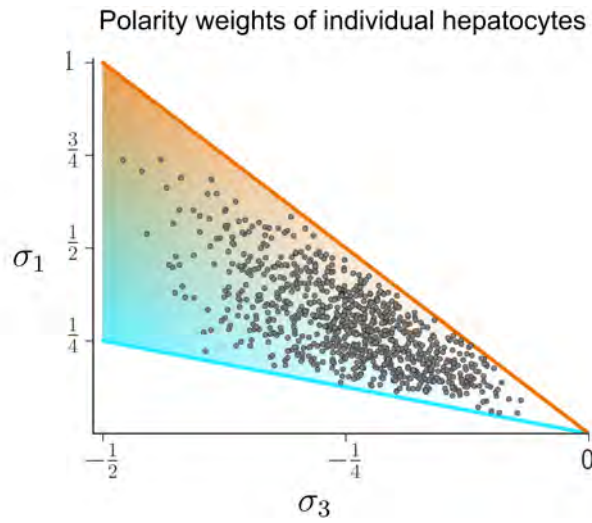


Figure A.2. Polarity weights characterizing basal membrane distribution on hepatocytes. Gray dots indicate values for the polarity weights σ_1 and σ_3 of basal membrane distributions around hepatocytes in liver tissue. The orange line on the top of the triangle corresponds to the ideal bipolar case and the blue line corresponds to the ideal ring configuration. Experimental data: Zerial group at MPI-CBG.

A.4. Randomized control for network segment anisotropies

Due to the relatively small number of segments around each cell, even randomly oriented segments yield a local nematic anisotropy. In Fig. A.3B, we show the local nematic anisotropies of a randomized version of the local sinusoid network. Specifically, we randomize the directions of local sinusoid network segments \mathbf{e}_k prior to calculation of the nematic tensor according to equation (2.10). Direct comparison

with the actual liver data (Fig. A.3A) shows a significant reduction in local network anisotropy. This provides strong evidence for non-isotropic configurations of local sinusoid segments around hepatocytes.

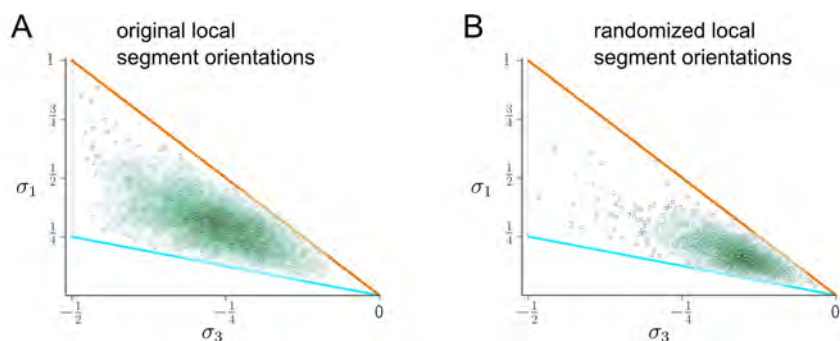


Figure A.3. Comparison of local network anisotropy between random control and actual data. (A) Same as Fig. 2.7B, showing eigenvalues of the nematic tensor \mathbf{s} for local sinusoid network around hepatocytes that characterize the amount of nematic anisotropy. Here, with kernel density estimate of the distribution. (B) Same as panel A but for randomized local direction of the network segments. Experimental data: Zerial group at MPI-CBG. Kernel density estimates were obtained using the method `kdeplot` from the `seaborn` package [174] with standard parameters.

A.5. The dihedral symmetry group D_{2h}

In this thesis, we focus on nematic objects with D_{2h} symmetry (the point group of ethene). If a collection of many of these objects (the “phase”) also enjoy D_{2h} symmetry, all averaged tensors must diagonalize in the same reference frame. This can be understood by realizing that the point group D_{2h} contains mirror symmetries about three orthogonal planes and two-fold rotation symmetries around three orthogonal axes (see Fig. A.4 for a visual representation). Any averaged tensor A describing a D_{2h} symmetric system must remain unchanged under all symmetry operations of the point group as these transform the system into itself. This is equivalent to demanding that $A = G A$, $\forall G \in D_{2h}$, or demanding that A commutes with all members of D_{2h} [156, ch. 3.3.1].

We now follow Virga’s arguments in [156], and formally construct the elements of the symmetry group. We start with the mirror symmetry about three orthonormal planes. A reflection about a plane orthogonal to the unit vector \mathbf{e}_i is given by $R_i := \mathbb{1} - 2 \mathbf{e}_i \otimes \mathbf{e}_i$. There are three orthogonal mirror planes in D_{2h} giving three orthonormalized symmetry axes $\mathbf{e}_1, \mathbf{e}_2, \mathbf{e}_3$. All these reflections are in $O(3)$ and

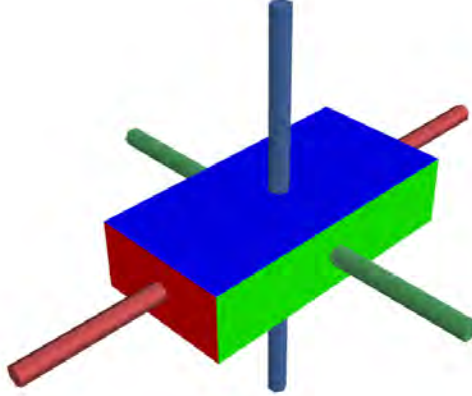


Figure A.4. Cuboid as prototypical example for the symmetry class D_{2h} . A cuboid remains unchanged under the seven non-trivial transformations: rotations of π about one of the principal axes (3), mirroring on a plane perpendicular to one of the principal axes (3) and point inversion in the center. These representations define the D_{2h} symmetry group [156].

obey $R_i^2 = \mathbb{1}$ and $R_i R_j = -R_k$ for $i \neq j \neq k \in \{1, 2, 3\}$. The matrix $-R_k$ can be identified as a rotation around \mathbf{e}_k about an angle π , which is also part of D_{2h} . Thus, the symmetry group D_{2h} can be written as

$$D_{2h} = \{\mathbb{1}, R_1, R_2, R_3, -\mathbb{1}, -R_1, -R_2, -R_3\} \quad (\text{A.4})$$

where $-\mathbb{1}$ is the central inversion. We can expand any second-rank tensor in three dimension in the reference frame given by the ortho-normalized symmetry axes:

$$A = \sum_{i,j} a_{ij} \mathbf{e}_i \otimes \mathbf{e}_j \quad (\text{A.5})$$

The nine dyads $\mathbf{e}_i \otimes \mathbf{e}_j$ hence form a basis of these second-rank tensors. For any pair $(\mathbf{e}_k, \mathbf{e}_l)$, $k \neq l$ of orthogonal unit vectors of $\mathbf{e}_1, \mathbf{e}_2, \mathbf{e}_3$ there is an element $G \in D_{2h}$ for which $G \mathbf{e}_k = -\mathbf{e}_k$ and $G \mathbf{e}_l = \mathbf{e}_l$. From that follows for the matrix element A_{kl} , $k \neq l$:

$$A_{kl} = a_{kl} \mathbf{e}_k \otimes \mathbf{e}_l = (GA)_{kl} = a_{kl} G \mathbf{e}_k \otimes G \mathbf{e}_l = -a_{kl} \mathbf{e}_k \otimes \mathbf{e}_l \quad (\text{A.6})$$

which can only be true when $a_{kl} = 0$. The symmetry axis thus coincide with

the eigenvectors of A . This is true for any averaged property of the system, and therefore all must diagonalize in the same principal axis frame, which coincides with the symmetry axis of the phase.

In that case the invariants of the tensor field can be calculated from the eigenvalues of the averaged tensors. Given two averaged tensors of the system A, B we can write

$$A = R \begin{pmatrix} \lambda_1 & & \\ & \lambda_2 & \\ & & \lambda_3 \end{pmatrix} R^T \quad \text{and} \quad B = R \begin{pmatrix} \sigma_1 & & \\ & \sigma_2 & \\ & & \sigma_3 \end{pmatrix} R^T \quad (\text{A.7})$$

where $\{\lambda_1, \lambda_2, \lambda_3\}$ are the eigenvalues of A , $\{\sigma_1, \sigma_2, \sigma_3\}$ are the eigenvalues of B , and R is the rotation matrix that transforms A and B into their common eigenframe. We first state that

$$A^k = R \begin{pmatrix} \lambda_1 & & \\ & \lambda_2 & \\ & & \lambda_3 \end{pmatrix} R^T \dots R \begin{pmatrix} \lambda_1 & & \\ & \lambda_2 & \\ & & \lambda_3 \end{pmatrix} R^T = R \begin{pmatrix} \lambda_1^k & & \\ & \lambda_2^k & \\ & & \lambda_3^k \end{pmatrix} R^T \quad (\text{A.8})$$

The invariants of any powers $k, l \in \mathbb{N}_0$ in A and B is then given as

$$\text{tr}(A^k B^l) = \text{tr} \left(R \begin{pmatrix} \lambda_1^k & & \\ & \lambda_2^k & \\ & & \lambda_3^k \end{pmatrix} R^T R \begin{pmatrix} \sigma_1^l & & \\ & \sigma_2^l & \\ & & \sigma_3^l \end{pmatrix} R^T \right) \quad (\text{A.9})$$

$$= \text{tr} \left(R \begin{pmatrix} \lambda_1^k \sigma_1^l & & \\ & \lambda_2^k \sigma_2^l & \\ & & \lambda_3^k \sigma_3^l \end{pmatrix} R^T \right) \quad (\text{A.10})$$

$$= \text{tr} \left(\begin{pmatrix} \lambda_1^k \sigma_1^l & & \\ & \lambda_2^k \sigma_2^l & \\ & & \lambda_3^k \sigma_3^l \end{pmatrix} R R^T \right) \quad (\text{A.11})$$

$$= \sum_i \lambda_i^k \sigma_i^l \quad (\text{A.12})$$

which implies that the knowledge of the eigenvalues of the averaged tensors is then sufficient to construct all tensor invariants.

A.6. Relation between orientational order parameters and elements of the super-tensor

The non-zero elements of the super-tensor $S_{\alpha\alpha}^{ii}$ in its eigenframe are given as linear combinations of the order parameters S, P, D, C as

$$\begin{aligned}
S_{zz}^{nn} &= S \\
S_{yy}^{mn} &= -\frac{1}{2}(S + P) \\
S_{xx}^{nn} &= \frac{1}{2}(-S + P) \\
S_{zz}^{mm} &= -\frac{1}{2}(S + D) \\
S_{yy}^{mm} &= \frac{1}{4}(S + P + D + 3C) \\
S_{xx}^{mm} &= \frac{1}{4}(S - P + D - 3C) \\
S_{zz}^{ll} &= \frac{1}{2}(-S + D) \\
S_{yy}^{ll} &= \frac{1}{4}(S + P - D - 3C) \\
S_{xx}^{mm} &= \frac{1}{4}(S - P - D + 3C)
\end{aligned} \tag{A.13}$$

A.7. Formal separation of molecular asymmetry and orientation

In this section, we present a formal approach to separate the orientational part of the nematic tensor from its shape anisotropy. This provides a direct connection to the scalar orientational order parameters used in the field of liquid crystals and introduced in section 3.1.1. We follow Rosso [160] and note that any symmetric traceless tensor can be written in a basis of five traceless tensors $m_{\alpha\beta}^{(k)}$ as

$$t_{\alpha\beta} = \sum_k \tilde{\xi}_k m_{\alpha\beta}^{(k)}. \tag{A.14}$$

The basis tensors $m_{\alpha\beta}^{(k)}$ are given in terms of three ortho-normalized vectors $\mathbf{m}_1, \mathbf{m}_2, \mathbf{m}_3$

$$\begin{aligned} \mathbf{m}^{(0)} &= \sqrt{\frac{3}{2}} \left(\mathbf{m}_3 \otimes \mathbf{m}_3 - \frac{1}{3} \mathbb{1} \right), & \mathbf{m}^{(1)} &= \sqrt{\frac{1}{2}} (\mathbf{m}_1 \otimes \mathbf{m}_1 - \mathbf{m}_2 \otimes \mathbf{m}_2), \\ \mathbf{m}^{(2)} &= \sqrt{\frac{1}{2}} (\mathbf{m}_1 \otimes \mathbf{m}_2 + \mathbf{m}_2 \otimes \mathbf{m}_1), & \mathbf{m}^{(3)} &= \sqrt{\frac{1}{2}} (\mathbf{m}_1 \otimes \mathbf{m}_3 + \mathbf{m}_3 \otimes \mathbf{m}_1), \\ \mathbf{m}^{(4)} &= \sqrt{\frac{1}{2}} (\mathbf{m}_2 \otimes \mathbf{m}_3 + \mathbf{m}_3 \otimes \mathbf{m}_2). \end{aligned} \quad (\text{A.15})$$

and are ortho-normalized with respect to the standard scalar product $m_{\alpha\beta}^{(k)} m_{\beta\alpha}^{(l)} = \delta_{kl}$. We can thus describe the five degrees of freedom of any symmetric traceless tensor by five coefficients $\tilde{\xi}_0, \tilde{\xi}_1, \tilde{\xi}_2, \tilde{\xi}_3, \tilde{\xi}_4$.

We have the freedom to choose a specific basis for each nematic tensor in the given set. The tensor bases themselves might be represented in an arbitrary but fixed laboratory system. We can use this freedom to choose $\mathbf{m}_1, \mathbf{m}_2, \mathbf{m}_3$ to coincide with the eigenvectors $\mathbf{l}, \mathbf{m}, \mathbf{n}$ of the nematic tensor $t_{\alpha\beta}$. The coefficients $\tilde{\xi}_2, \tilde{\xi}_3$ and $\tilde{\xi}_4$ must vanish, which can be seen by noting that $t_{\alpha\beta}$ is diagonal in its eigenframe and $\mathbf{m}^{(2)}, \mathbf{m}^{(3)}$ and $\mathbf{m}^{(4)}$ are exactly the basis tensors corresponding to the off-diagonal elements. Hence, their respective coefficients must vanish. For this choice, we can write

$$t_{\alpha\beta} = \tilde{\xi}_0 m_{\alpha\beta}^{(0)} + \tilde{\xi}_1 m_{\alpha\beta}^{(1)} \quad (\text{A.16})$$

where now the five degrees of freedom of the symmetric traceless tensor $t_{\alpha\beta}$ are encoded in two shape coefficients $\tilde{\xi}_0 = \sqrt{\frac{3}{2}} \sigma_n$ and $\tilde{\xi}_1 = \frac{1}{\sqrt{2}} (\sigma_l - \sigma_m)$, given as linear combinations of the eigenvalues $\sigma_l, \sigma_m, \sigma_n$ of $t_{\alpha\beta}$, and three rotation angles (e.g. Euler angles) describing the orientation of the eigenframe of $t_{\alpha\beta}$ that we used to define $m_{\alpha\beta}^{(0)}$ and $m_{\alpha\beta}^{(1)}$. Here, we have chosen to map $\mathbf{m}_1, \mathbf{m}_2, \mathbf{m}_3$ onto the eigenvectors $\mathbf{l}, \mathbf{m}, \mathbf{n}$ in that given order. This can be done without loss of generality, because the corresponding eigenvalues $\sigma_l, \sigma_m, \sigma_n$ of $t_{\alpha\beta}$ are ordered by magnitude in an arbitrary but fixed way. They can thus be re-ordered and re-named correspondingly. The molecular tensors \mathbf{q} and \mathbf{b} , introduced in equation 3.2, differ from $m_{\alpha\beta}^{(0)}$ and $m_{\alpha\beta}^{(1)}$ only by numerical prefactors

$$q_{\alpha\beta} = \sqrt{\frac{3}{2}} m_{\alpha\beta}^{(0)} \quad \text{and} \quad b_{\alpha\beta} = \frac{3}{\sqrt{2}} m_{\alpha\beta}^{(1)}. \quad (\text{A.17})$$

In a reciprocal manner, the respective coefficients are related by $\xi_0 = \sqrt{2/3} \tilde{\xi}_0$ and $\xi_1 = \sqrt{2/3} \tilde{\xi}_1$. This normalization is useful, as it yields simple prefactors in the relation to the order parameters S, P, D, C (cf. equation (3.5)) at the expense of normalization to unity with respect to the standard scalar product.

We have now separated the orientation from the magnitude of the second-order spherical anisotropy which the tensor $t_{\alpha\beta}$ describes. This also holds for higher moments. The square of $t_{\alpha\beta}$ is, for example, is given by

$$t_{\alpha\gamma} t_{\gamma\beta} = \frac{1}{\sqrt{6}} \left(\tilde{\xi}_0^2 - \tilde{\xi}_1^2 \right) m_{\alpha\beta}^{(0)} - \frac{2}{\sqrt{6}} \tilde{\xi}_0 \tilde{\xi}_1 m_{\alpha\beta}^{(1)} + \frac{1}{3} \left(\tilde{\xi}_0^2 + \tilde{\xi}_1^2 \right) \delta_{\alpha\beta} \quad (\text{A.18})$$

where the coefficients of the basis tensors are quadratic function of $\tilde{\xi}_0$ and $\tilde{\xi}_1$ and also the trace becomes non-zero. This treatment is useful when examining averaged quantities like the average over the tensor field and its higher moments.

To draw a connection to the treatment of orientational fluctuations in biaxial nematic liquid crystals we now make the simplifying assumption that all cell surface distributions are equal but rotated in space. This means that the coefficients $\tilde{\xi}_0$ and $\tilde{\xi}_1$ are identical for all cells and only the orientations of the eigenframe described by $m^{(0)}$ and $m^{(1)}$ vary. We can thus write the average of the nematic tensor field as $\langle \mathbf{t} \rangle = \tilde{\xi}_0 \langle \mathbf{m}^{(0)} \rangle + \tilde{\xi}_1 \langle \mathbf{m}^{(1)} \rangle$.

In this case, the information about the orientational order is captured by the two tensor averages $\langle \mathbf{m}^{(0)} \rangle$ and $\langle \mathbf{m}^{(1)} \rangle$. We now also expand these two symmetric traceless tensors in a tensor basis. To distinguish this laboratory reference frame, we call it $\{\mathbf{L}^{(0)}, \dots, \mathbf{L}^{(4)}\}$ and thus write

$$\langle \mathbf{m}^{(0)} \rangle = \sum_{p=0}^4 S_{0,p} \mathbf{L}^{(p)} \quad \text{and} \quad \langle \mathbf{m}^{(1)} \rangle = \sum_{p=0}^4 S_{1,p} \mathbf{L}^{(p)} \quad (\text{A.19})$$

with 10 coefficients $S_{\{0,1\},p}$. Three of these coefficients describe the global rotation of the frame $\{\mathbf{L}^{(0)}, \dots, \mathbf{L}^{(4)}\}$, which in turn means that 7 coefficients are relevant for the invariants that are independent of this global rotation¹. When $\langle \mathbf{m}^{(0)} \rangle$ and $\langle \mathbf{m}^{(1)} \rangle$ diagonalize in the same frame, as is the case for systems obeying D_{2h} symmetry (see appendix A.5) only 4 scalar coefficients remain. We identify these with the orientational order parameters introduced in section 3.1.1 as $S_{0,0} = S$, $S_{0,1} = \frac{1}{\sqrt{3}}P$, $S_{1,0} = \frac{1}{\sqrt{3}}D$, and $S_{1,1} = C$. The averages of the two basis tensors are

¹This is equivalent to saying that one may diagonalize $\langle \mathbf{m}^{(0)} \rangle$, giving 2 coefficients and then writing $\langle \mathbf{m}^{(1)} \rangle$ in that frame, yielding 5 more.

then given as:

$$\langle \mathbf{m}^{(0)} \rangle = S \mathbf{L}^{(0)} + \frac{P}{\sqrt{3}} \mathbf{L}^{(1)} \quad \text{and} \quad \langle \mathbf{m}^{(1)} \rangle = \frac{D}{\sqrt{3}} \mathbf{L}^{(0)} + C \mathbf{L}^{(1)} \quad (\text{A.20})$$

and thereby, the average of the nematic tensor field by

$$\langle \mathbf{T} \rangle = \left(\tilde{\xi}_0 S + \tilde{\xi}_1 \frac{D}{\sqrt{3}} \right) \mathbf{L}^{(0)} + \left(\tilde{\xi}_1 C + \tilde{\xi}_0 \frac{P}{\sqrt{3}} \right) \mathbf{L}^{(1)} \quad (\text{A.21})$$

A.8. Order parameters under action of axes permutation

Below we give the table of the transformation laws of the order parameters under the action of the permutations of the molecular and laboratory axes. The indices of the first row provides the reference for Cauchy's two-line permutation [201, p. 94] notation for the subsequent rows. We use the letter m to denote the molecular axes and l to denote the laboratory axes.

A. Appendix

m_{123}	l_{123}	S	D	P	C
m_{123}	l_{132}	$\frac{1}{2}(-S - P)$	$\frac{1}{2}(-D - 3C)$	$\frac{1}{2}(P - 3S)$	$\frac{C-D}{2}$
m_{123}	l_{213}	S	D	$-P$	$-C$
m_{123}	l_{231}	$\frac{P-S}{2}$	$\frac{1}{2}(3C - D)$	$\frac{1}{2}(-3S - P)$	$\frac{1}{2}(-D - C)$
m_{123}	l_{312}	$\frac{1}{2}(-S - P)$	$\frac{1}{2}(-D - 3C)$	$\frac{1}{2}(3S - P)$	$\frac{D-C}{2}$
m_{123}	l_{321}	$\frac{P-S}{2}$	$\frac{1}{2}(3C - D)$	$\frac{1}{2}(3S + P)$	$\frac{D+C}{2}$
m_{132}	l_{123}	$\frac{1}{2}(-S - D)$	$\frac{1}{2}(D - 3S)$	$\frac{1}{2}(-P - 3C)$	$\frac{C-P}{2}$
m_{132}	l_{132}	$\frac{1}{4}(S + P + D + 3C)$	$\frac{1}{4}(3S + 3P - D - 3C)$	$\frac{1}{4}(3S - P + 3D - 3C)$	$\frac{1}{4}(3S - P - D + C)$
m_{132}	l_{213}	$\frac{1}{2}(-S - D)$	$\frac{1}{2}(D - 3S)$	$\frac{1}{2}(P + 3C)$	$\frac{P-C}{2}$
m_{132}	l_{231}	$\frac{1}{4}(S - P + D - 3C)$	$\frac{1}{4}(3S - 3P - D + 3C)$	$\frac{1}{4}(3S + P + 3(D + C))$	$\frac{1}{4}(3S + P - D - C)$
m_{132}	l_{312}	$\frac{1}{4}(S + P + D + 3C)$	$\frac{1}{4}(3S + 3P - D - 3C)$	$\frac{1}{4}(-3S + P - 3D + 3C)$	$\frac{1}{4}(-3S + P + D - C)$
m_{132}	l_{321}	$\frac{1}{4}(S - P + D - 3C)$	$\frac{1}{4}(3S - 3P - D + 3C)$	$\frac{1}{4}(-3S - P - 3(D + C))$	$\frac{1}{4}(-3S - P + D + C)$
m_{213}	l_{123}	S	$-D$	P	$-C$
m_{213}	l_{132}	$\frac{1}{2}(-S - P)$	$\frac{1}{2}(D + 3C)$	$\frac{1}{2}(P - 3S)$	$\frac{D-C}{2}$
m_{213}	l_{213}	S	$-D$	$-P$	C
m_{213}	l_{231}	$\frac{P-S}{2}$	$\frac{1}{2}(D - 3C)$	$\frac{1}{2}(-3S - P)$	$\frac{D+C}{2}$
m_{213}	l_{312}	$\frac{1}{2}(-S - P)$	$\frac{1}{2}(D + 3C)$	$\frac{1}{2}(3S - P)$	$\frac{C-D}{2}$
m_{213}	l_{321}	$\frac{P-S}{2}$	$\frac{1}{2}(D - 3C)$	$\frac{1}{2}(3S + P)$	$\frac{1}{2}(-D - C)$
m_{231}	l_{123}	$\frac{D-S}{2}$	$\frac{1}{2}(-3S - D)$	$\frac{1}{2}(3C - P)$	$\frac{1}{2}(-P - C)$
m_{231}	l_{132}	$\frac{1}{4}(S + P - D - 3C)$	$\frac{1}{4}(3S + 3P + D + 3C)$	$\frac{1}{4}(3S - P - 3D + 3C)$	$\frac{1}{4}(3S - P + D - C)$
m_{231}	l_{213}	$\frac{D-S}{2}$	$\frac{1}{2}(-3S - D)$	$\frac{1}{2}(P - 3C)$	$\frac{P+C}{2}$
m_{231}	l_{231}	$\frac{1}{4}(S - P - D + 3C)$	$\frac{1}{4}(3S - 3P + D - 3C)$	$\frac{1}{4}(3S + P - 3(D + C))$	$\frac{1}{4}(3S + P + D + C)$
m_{231}	l_{312}	$\frac{1}{4}(S + P - D - 3C)$	$\frac{1}{4}(3S + 3P + D + 3C)$	$\frac{1}{4}(-3S + P + 3D - 3C)$	$\frac{1}{4}(-3S + P - D + C)$
m_{231}	l_{321}	$\frac{1}{4}(S - P - D + 3C)$	$\frac{1}{4}(3S - 3P + D - 3C)$	$\frac{1}{4}(-3S - P + 3(D + C))$	$\frac{1}{4}(-3S - P - D - C)$
m_{312}	l_{123}	$\frac{1}{2}(-S - D)$	$\frac{1}{2}(3S - D)$	$\frac{1}{2}(-P - 3C)$	$\frac{P-C}{2}$
m_{312}	l_{132}	$\frac{1}{4}(S + P + D + 3C)$	$\frac{1}{4}(-3S - 3P + D + 3C)$	$\frac{1}{4}(3S - P + 3D - 3C)$	$\frac{1}{4}(-3S + P + D - C)$
m_{312}	l_{213}	$\frac{1}{2}(-S - D)$	$\frac{1}{2}(3S - D)$	$\frac{1}{2}(P + 3C)$	$\frac{C-P}{2}$
m_{312}	l_{231}	$\frac{1}{4}(S - P + D - 3C)$	$\frac{1}{4}(-3S + 3P + D - 3C)$	$\frac{1}{4}(3S + P + 3(D + C))$	$\frac{1}{4}(-3S - P + D + C)$
m_{312}	l_{312}	$\frac{1}{4}(S + P + D + 3C)$	$\frac{1}{4}(-3S - 3P + D + 3C)$	$\frac{1}{4}(-3S + P - 3D + 3C)$	$\frac{1}{4}(3S - P - D + C)$
m_{312}	l_{321}	$\frac{1}{4}(S - P + D - 3C)$	$\frac{1}{4}(-3S + 3P + D - 3C)$	$\frac{1}{4}(-3S - P - 3(D + C))$	$\frac{1}{4}(3S + P - D - C)$
m_{321}	l_{123}	$\frac{D-S}{2}$	$\frac{1}{2}(3S + D)$	$\frac{1}{2}(3C - P)$	$\frac{P+C}{2}$
m_{321}	l_{132}	$\frac{1}{4}(S + P - D - 3C)$	$\frac{1}{4}(-3S - 3P - D - 3C)$	$\frac{1}{4}(3S - P - 3D + 3C)$	$\frac{1}{4}(-3S + P - D + C)$
m_{321}	l_{213}	$\frac{D-S}{2}$	$\frac{1}{2}(3S + D)$	$\frac{1}{2}(P - 3C)$	$\frac{1}{2}(-P - C)$
m_{321}	l_{231}	$\frac{1}{4}(S - P - D + 3C)$	$\frac{1}{4}(-3S + 3P - D + 3C)$	$\frac{1}{4}(3S + P - 3(D + C))$	$\frac{1}{4}(-3S - P - D - C)$
m_{321}	l_{312}	$\frac{1}{4}(S + P - D - 3C)$	$\frac{1}{4}(-3S - 3P - D - 3C)$	$\frac{1}{4}(-3S + P + 3D - 3C)$	$\frac{1}{4}(3S - P + D - C)$
m_{321}	l_{321}	$\frac{1}{4}(S - P - D + 3C)$	$\frac{1}{4}(-3S + 3P - D + 3C)$	$\frac{1}{4}(-3S - P + 3(D + C))$	$\frac{1}{4}(3S + P + D + C)$

Table A.1. Full table of transformation rules under permutations of the molecular axes (denoted by $m_{\text{permutation}}$ from 123) and laboratory axes (denoted by $l_{\text{permutation}}$ from 123)

A permutation of the molecular axes also changes the definition of the molecular anisotropies ξ_0 and ξ_1 . Combining both parameters into a vector $\xi = (\xi_0, \xi_1)^T$, we first note that the eigenvalues $\sigma = (\sigma_l, \sigma_m, \sigma_n)^T$ of $t_{\alpha\beta}$ are related to the shape parameters as

$$\sigma = \mathbf{M}\xi = \mathbf{M}'\xi' \quad (\text{A.22})$$

with

$$\mathbf{M} = \begin{pmatrix} -\frac{1}{2} & \frac{3}{2} \\ -\frac{1}{2} & -\frac{3}{2} \\ 1 & 0 \end{pmatrix} \quad (\text{A.23})$$

The permuted version is then given by a permutation of the rows of \mathbf{M} . For example

$$\mathbf{M}_{231} = P_{231}(\mathbf{M}) = \begin{pmatrix} -\frac{1}{2} & -\frac{3}{2} \\ 1 & 0 \\ -\frac{1}{2} & \frac{3}{2} \end{pmatrix} \quad (\text{A.24})$$

We can invert the permuted matrix by deleting the last row as it is linearly dependent on the first two. The shape parameters after axes permutation are then given as

$$\begin{aligned} \xi_{132} &= \begin{pmatrix} -\frac{1}{2} & -\frac{3}{2} \\ -\frac{1}{2} & \frac{1}{2} \end{pmatrix} \xi_{123}, & \xi_{213} &= \begin{pmatrix} 1 & 0 \\ 0 & -1 \end{pmatrix} \xi_{123}, & \xi_{231} &= \begin{pmatrix} -\frac{1}{2} & \frac{3}{2} \\ -\frac{1}{2} & -\frac{1}{2} \end{pmatrix} \xi_{123} \\ \xi_{312} &= \begin{pmatrix} -\frac{1}{2} & -\frac{3}{2} \\ \frac{1}{2} & -\frac{1}{2} \end{pmatrix} \xi_{123}, & \xi_{321} &= \begin{pmatrix} -\frac{1}{2} & \frac{3}{2} \\ \frac{1}{2} & \frac{1}{2} \end{pmatrix} \xi_{123} \end{aligned} \quad (\text{A.25})$$

A.9. Minimal integrity basis for symmetric traceless tensors

Matteis [140] pointed out that there are at most eight independent invariants of the two ordering tensors $Q_{\alpha\beta} = \langle q_{\alpha\beta} \rangle$ and $B_{\alpha\beta} = \langle b_{\alpha\beta} \rangle$, because both are symmetric traceless tensors. Those invariants are

$$\text{tr}(\mathbf{Q}^2), \text{tr}(\mathbf{B}^2), \text{tr}(\mathbf{Q}^3), \text{tr}(\mathbf{B}^3), \text{tr}(\mathbf{QB}), \text{tr}(\mathbf{Q}^2\mathbf{B}), \text{tr}(\mathbf{QB}^2), \text{tr}(\mathbf{Q}^2\mathbf{B}^2) \quad (\text{A.26})$$

and are termed *minimal integrity basis*. All other invariants can be expressed as polynomials in these basic ones. As already mentioned above, for biaxial phases with D_{2h} symmetry, the ordering tensors $Q_{\alpha\beta}$ and $B_{\alpha\beta}$ diagonalize in the same eigenframe. In that case, the number of independent invariants is reduced to seven, due to the relationship $\text{tr}(\mathbf{B}^2)\text{tr}(\mathbf{Q}^2) = 6\text{tr}(\mathbf{Q}^2\mathbf{B}^2) - 2(\text{tr}(\mathbf{QB}))^2$. It is important to note that these invariants are only polynomially independent but functionally

dependent. The functional dependence results from the fact that they can be given as polynomials in the four order parameters S, P, D, C . These seven invariants are thus particular polynomials in S, P, D, C from which any function that obeys the D_{2h} symmetry of the objects and the phase can be constructed.

The averaged moment tensors \mathbf{T} and \mathbf{V} (cf. section 3.1.3) can be written as a linear combination of the ordering tensors $Q_{\alpha\beta}, B_{\alpha\beta}$ and the identity matrix, as shown in section 3.1.4. The minimal number of moments needed to describe the system is met, when they can express all elements of the minimal integrity basis. In general, taking the first and second moment is sufficient (cf. equation (3.15)).

A.10. Discretization of distortion free energy on cubic lattice

The Frank distortion free energy in tensorial form is given by (cf. equation (5.2))

$$F_d = \int d^3r \frac{1}{4} K (\partial_\gamma N_{\alpha\beta})^2 . \quad (\text{A.27})$$

To discretize this free energy, we approximate the partial derivatives with finite differences

$$\partial_\gamma N_{\alpha\beta} = \frac{N_{\alpha\beta}(\mathbf{r} + a \mathbf{e}_\gamma) - N_{\alpha\beta}(\mathbf{r})}{a} \quad (\text{A.28})$$

which yields for the squared gradient term

$$(\partial_\gamma N_{\alpha\beta})^2 = -\frac{2}{a^2} \sum_{\alpha\beta\gamma} N_{\alpha\beta}(\mathbf{r} + a \mathbf{e}_\gamma) N_{\alpha\beta}(\mathbf{r}) + \text{const} . \quad (\text{A.29})$$

Aligning the cubic lattice with the directions of the reference frame $\{a \mathbf{e}_x, a \mathbf{e}_y, a \mathbf{e}_z\}$ and further approximating the volume integral by a sum over lattice vectors \mathbf{r} with substituting $\int d^3r \rightarrow a^3 \sum_{\mathbf{r}}$, we see that

$$\begin{aligned} F_d &= \int d^3r \frac{1}{4} K (\partial_\gamma N_{\alpha\beta})^2 \approx -\frac{K a}{2} \sum_{\mathbf{r}} \sum_{\alpha\beta\gamma} N_{\alpha\beta}(\mathbf{r} + a \mathbf{e}_\gamma) N_{\alpha\beta}(\mathbf{r}) + \text{const} \\ &= -\frac{K a}{2} \sum_{\langle i,j \rangle} N_{\alpha\beta}^{(i)} N_{\alpha\beta}^{(j)} + \text{const} \end{aligned} \quad (\text{A.30})$$

where $\langle i, j \rangle$ runs over all pairs of neighbors on the cubic lattice.

A.11. Metropolis Algorithm for uniaxial cell polarity coordination

The *Metropolis* algorithm was first published by Nicholas Metropolis et al. in 1953 [202]. It is used to create a *Markov* chain and with it the states of a system according to the *Boltzmann* distribution. The new state of the system does only depend on the current state. The definition of the algorithm as it is used here, can be found below. Note, that the unit vector \mathbf{n}' created in step 3 must be chosen from the uniform distribution on the surface of the unit sphere. The random value r in step 6 must be chosen from the uniform distribution in the interval $[0, 1]$.

Algorithm 1 (Metropolis algorithm for uniaxial interaction model)

1. Choose an initial state
2. Choose a random lattice site i that is not fixed by boundaries
3. Generate a random unit vector \mathbf{n}'
4. Calculate the energy change ΔF that results if the vector $\mathbf{n}^{(i)}$ at site i is replaced by the new direction \mathbf{n}' .
5. If $\Delta F \leq 0$, accept the proposed new direction \mathbf{n}' for the lattice site i and go to step 2
6. If $\Delta F > 0$, draw r from the uniform distribution in the interval $[0, 1]$
7. If $r < \exp(-\frac{\Delta F}{\nu})$, accept the proposed new direction \mathbf{n}' for the lattice site i
8. Go to step 2

Unit vectors with isotropic orientational distribution are generated by obtaining three independent coordinates from the normal distribution and then normalizing the resulting vector to unit length. One Monte-Carlo step (MCS) is defined as N Metropolis steps, where N denotes the number of lattice sites excluding those fixed by boundary conditions. One Metropolis step is defined as one proposed new direction (doing steps 2 to 7 of algorithm 1 once). Note that a rejected proposal is counted as one Metropolis step as well.

A.12. States in the zero-noise limit of the nearest-neighbor interaction model

This section provides details of the algorithms used to find the states in the zero-noise strength limit of the uniaxial nearest-neighbor interaction model presented in section 5.3.2. Namely, two strategies were used. First, the system was initialized with random director orientations and gradually “cooled” down towards smaller noise strengths. The steps of noise strength used were $\nu/\varepsilon = 10., 5.0, 2.0, 1.0, 0.5, 0.2, 0.1, 0.05, 0.02, 0.01$. For each value of the noise strength, 25000 Monte Carlo steps (MCS) were performed² and the last configuration at one noise strength was used as the first configuration for the subsequent lower noise strength. In the second strategy, the system was initialized with all the directors aligned to the lobule-level reference field \mathbf{e}_χ . Then, 50000 MCS were performed at a relatively small noise strength of $\nu/\varepsilon = 0.01$. This procedure provided two candidates for the potential states for the zero-noise strength limit of the system. In general, it is not guaranteed that the found state corresponds to the smallest effective energy of the system. However, for sake of practicality, we refer to the lower-energy state of the two candidates as the state for the zero-noise strength limit. An overview over the resulting energies for different data sets is provided in Fig. A.5.

²One MCS consists of N Metropolis steps, where N is the number of free directors in the system, see section A.11 for details.

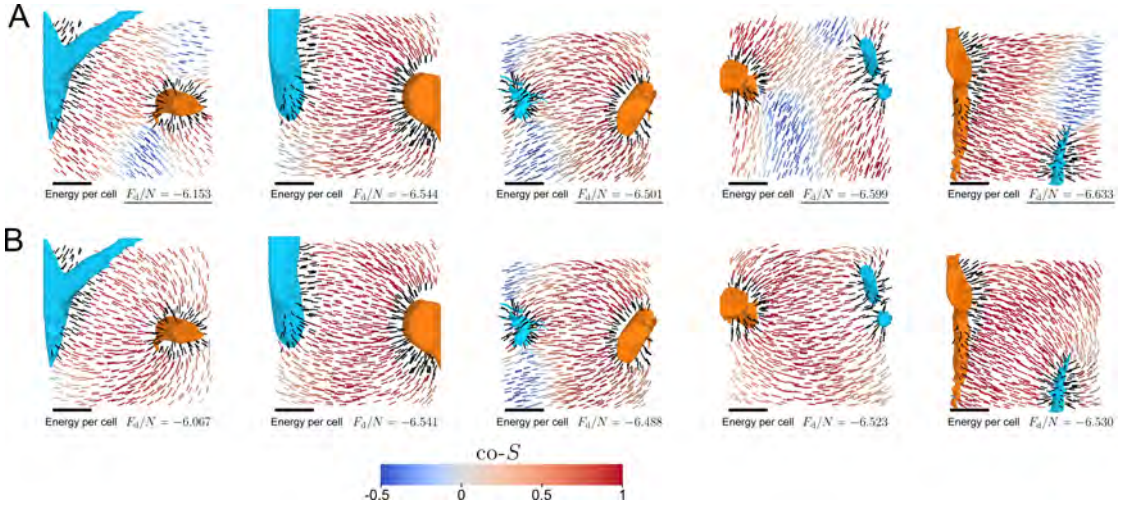


Figure A.5. Finding states in the limit of zero noise strength of the uniaxial nearest-neighbor interaction model. (A) Last configuration and energy per cell F_d/N after simulated annealing as described in the text for different vein configurations. (B) Same as panel A but for starting with alignment to the lobule-level reference field and performing 50000 MCS at $\nu/\varepsilon = 0.01$. For all vein configurations shown here, the state after simulated annealing had the lower energy. For most data sets (4 out of 5), the resulting lowest-energy state does not follow the lobule-level reference field well. Experimental data (surfaces of large vessels, cell positions and neighborhood relations): Zerial group at MPI-CBG. Scale bar: 100 μm .

A.13. Metropolis Algorithm for network self-organization

Here, we provide the Metropolis algorithm for the cubic lattice model presented in chapter 6. The version, presented as algorithm 2 below, preserves the total number of occupied edge segments (representing sinusoids) N^S and occupied face segments (representing bile canaliculi) N^B .

Algorithm 2 (Metropolis network switch)

1. Choose an initial state
2. Choose to a random number r from the uniform distribution in $[0, 1]$
3. If $r < \frac{N^S}{N^S + N^B}$, choose to update the edge-segment sub-lattice (representing sinusoids) else choose to update the face-segment sub-lattice (representing bile canaliculi)

4. Choose a random occupied segment l with $\sigma_l = 1$ and a random unoccupied segment m with $\sigma_m = 0$ from the sub-lattice chosen in step 3, the newly proposed configuration exchanges these states to $\sigma_l = 0$ and $\sigma_m = 1$, which preserves the total number of occupied segments
5. Calculate the energy difference $\Delta E_{l \rightarrow m}$ between the newly proposed network configuration and the current one for the respective sub-lattice as given in equation (A.31)
6.
 - a) If $\Delta E_{l \rightarrow m} < 0$ accept the proposed change
 - b) If $\Delta E_{l \rightarrow m} = 0$ accept the proposed change with probability $1/2$
 - c) If $\Delta E_{l \rightarrow m} > 0$ accept the proposed change with probability $\exp(-\frac{\Delta E_{l \rightarrow m}}{\nu})$
7. Go to step 2

The energy differences used in algorithm 2 are given by

$$\begin{aligned} \text{edge-segment sub-lattice: } \Delta E_{l \rightarrow m} &= \Delta E_l^S + \Delta E_m^S \\ \text{face-segment sub-lattice: } \Delta E_{l \rightarrow m} &= \Delta E_l^B + \Delta E_m^B \end{aligned} \quad (\text{A.31})$$

with

$$\Delta E_l^S = \Delta \sigma_l^S \left(\varepsilon_{SS} \sum_i K_{il}^{SS} \sigma_i^S + \varepsilon_{BS} \sum_i K_{il}^{BS} \sigma_i^B + 2 \lambda^S \sum_{\{\alpha: l \in \mathcal{C}_\alpha\}} (n_\alpha^S - c^S) \right) + \lambda^S \sum_{\{\alpha: l \in \mathcal{C}_\alpha\}} 1$$

and

$$\Delta E_l^B = \Delta \sigma_l^B \left(\varepsilon_{BB} \sum_i K_{il}^{BB} \sigma_i^B + \varepsilon_{BS} \sum_i K_{li}^{BS} \sigma_i^S + 2 \lambda^B \sum_{\{\alpha: l \in \mathcal{C}_\alpha\}} (n_\alpha^B - c^B) \right) + \lambda^B \sum_{\{\alpha: l \in \mathcal{C}_\alpha\}} 1, \quad (\text{A.32})$$

where $(\sigma_l^{S, B})^2 = 1$ was used and $\{\alpha : l \in \mathcal{C}_\alpha\}$ is the set of cells indices α that are in contact with the network segment l . One Monte-Carlo step (MCS) consists of going L times through steps 2 till 6 of algorithm 2, where $L = |\mathcal{I}_E| + |\mathcal{I}_F|$ is the total number of available lattice sites in the system.

The algorithm was implemented in Python [203] and Cython [204]. The implementation was able to go through steps 2 through 6 of algorithm around 200000

times per second for a lattice of 10x10x10 cubes, amounting to about 23 MCS/s on a single core of the Intel Xeon CPU E5-2680 v3 with 2.5 GHz.

A.14. Structural quantifications for varying values of mutual network segment repulsion

Figure 6.6 show two network measures for varying values of the repulsion strength ϵ_{BS} and noise strength ν . This appendix provides further quantifications of these structures. The values for edge segments representing sinusoids can be found in Fig. A.6 and the respective values for face segments representing bile canaliculi in Fig. A.7.

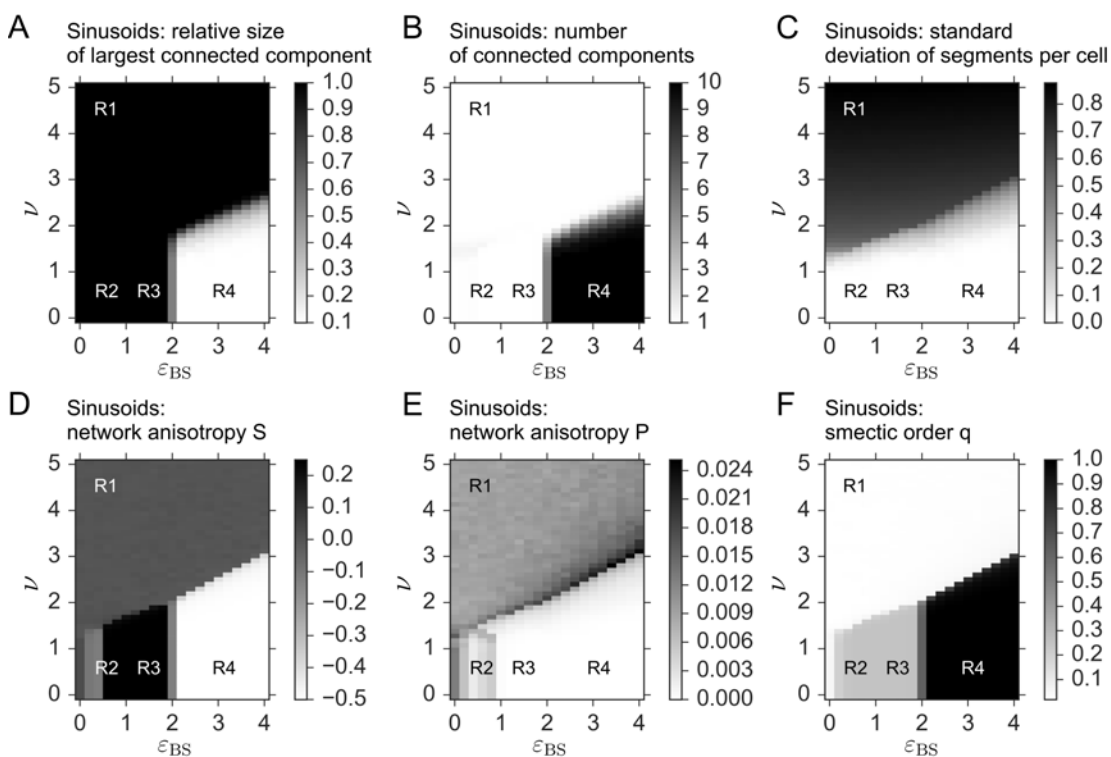


Figure A.6. Structural quantification of configurations of edge segments representing sinusoids. Supplemental quantifications of network configurations of edge segments representing sinusoids as encountered in the simulated annealing procedure used in section 6.5. For reference, the region labels from Fig. 6.6A are included.

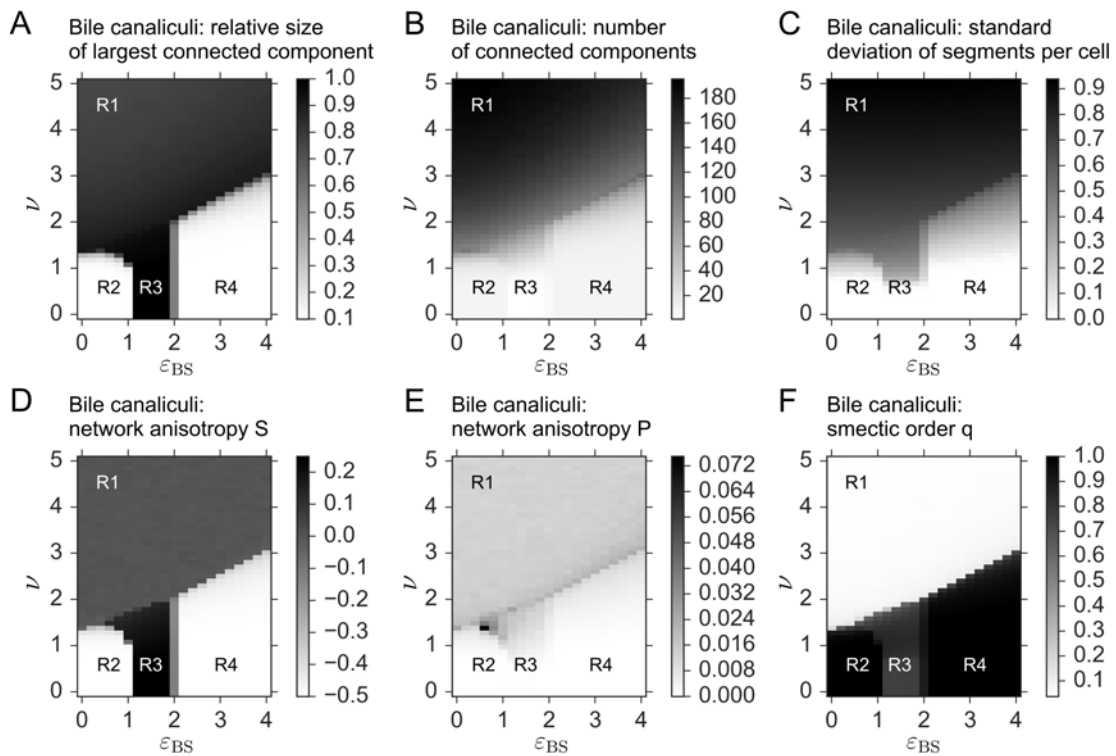


Figure A.7. Structural quantification of configurations of edge segments representing sinusoids. Supplemental quantifications of network configurations of face segments representing bile canaliculi as encountered in the simulated annealing procedure used in section 6.5. For reference, the region labels from Fig. 6.6A are included.

A.15. Structural quantifications for varying values of self-attraction of network segments

This appendix provides network measures for varying values of the self-attraction parameters $\varepsilon_{SS} = \varepsilon_{BB}$ and noise strength ν . The values for edge segments representing sinusoids can be found in Fig. A.8 and the respective values for face segments representing bile canaliculi in Fig. A.9.

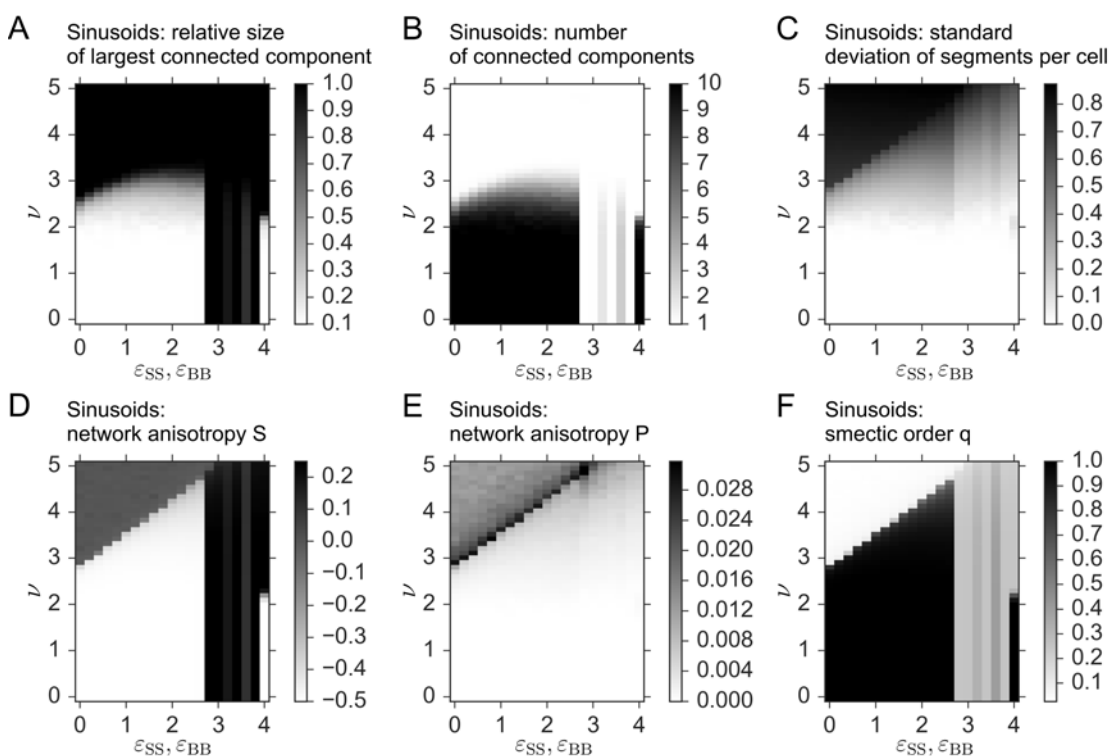


Figure A.8. Structural quantification of configurations of edge segments representing sinusoids. Quantifications of network configurations of edge segments representing sinusoids as encountered in a simulated annealing procedure as explained in section 6.5. Here, the interaction parameter for self-attraction $\varepsilon_{SS} = \varepsilon_{BB}$ are varied instead.

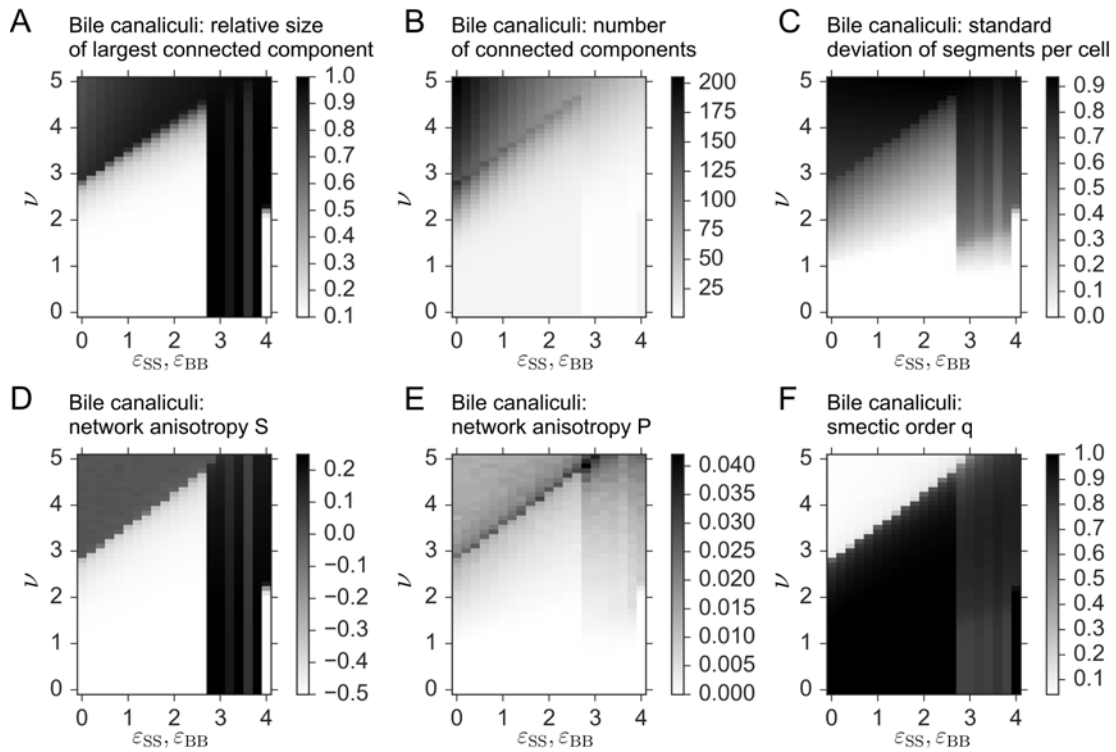


Figure A.9. Structural quantification of configurations of edge segments representing sinusoids. Quantifications of network configurations of face segments representing bile canaliculi as encountered in a simulated annealing procedure as explained in section 6.5. Here, the interaction parameter for self-attraction $\varepsilon_{SS} = \varepsilon_{BB}$ are varied instead.

A.16. Structural quantifications for varying values of cell demand

This appendix provides network measures for varying values of the parameters controlling the strength of the cell demand $\lambda_S = \lambda_B$ and noise strength ν . The values for edge segments representing sinusoids can be found in Fig. A.10 and the respective values for face segments representing bile canaliculi in Fig. A.11.

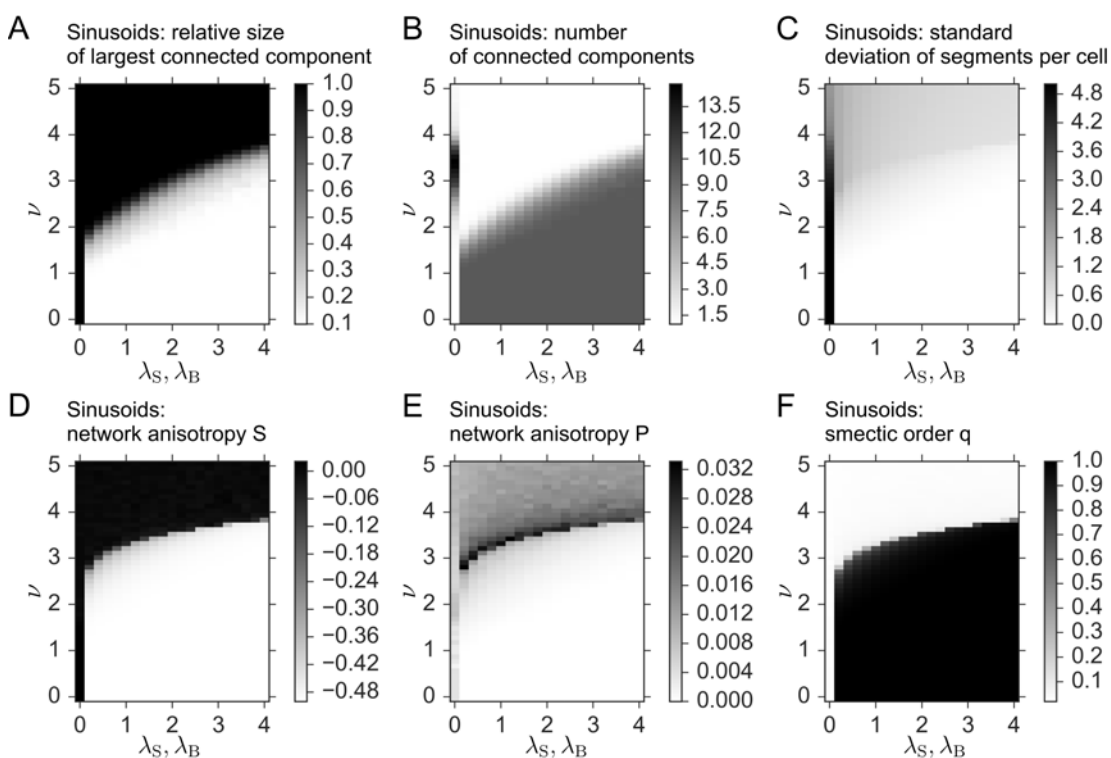


Figure A.10. Structural quantification of configurations of edge segments representing sinusoids. Quantifications of network configurations of edge segments representing sinusoids as encountered in a simulated annealing procedure as explained in section 6.5. Here, the interaction parameter for self-attraction $\lambda_S = \lambda_B$ are varied instead.

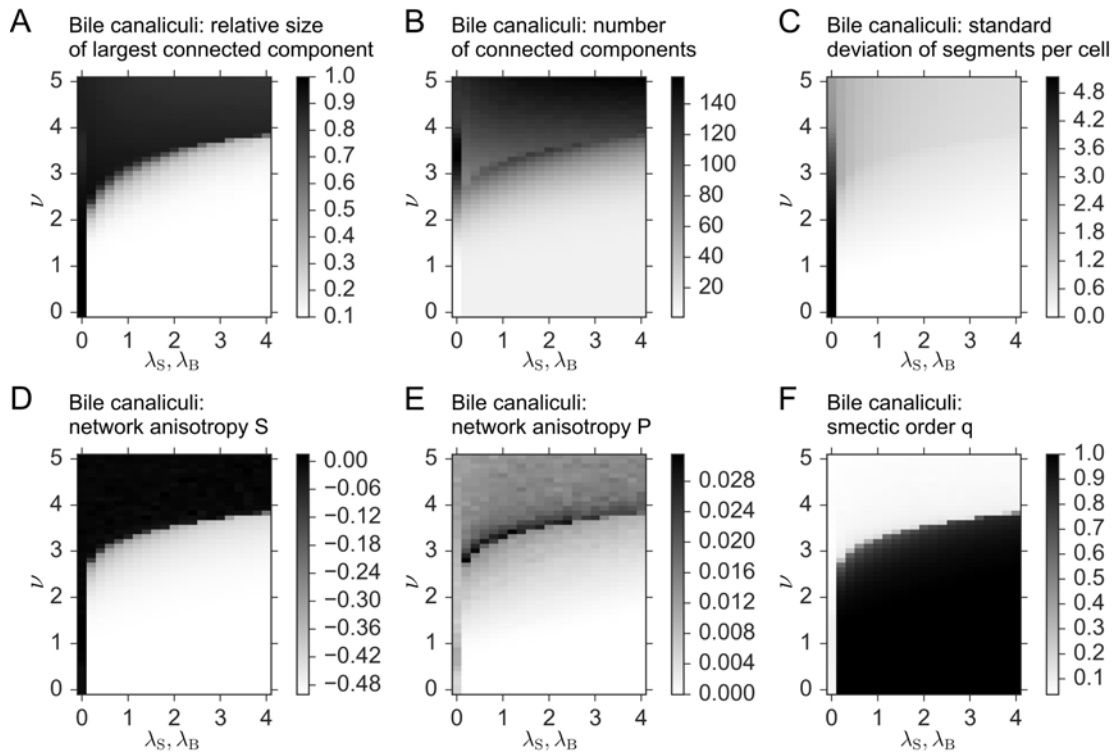


Figure A.11. Structural quantification of configurations of edge segments representing sinusoids. Quantifications of network configurations of face segments representing bile canaliculi as encountered in a simulated annealing procedure as explained in section 6.5. Here, the interaction parameter for self-attraction $\lambda_S = \lambda_B$ are varied instead.

Bibliography

1. Alberts, B., Johnson, A., Lewis, J., Raff, M., Roberts, K. & Walter, P. *Molecular Biology of the Cell* 4th ed. (Garland Science, New York, NY, USA, 2002) (cit. on pp. 1, 7, 9).
2. Bryant, D. M. & Mostov, K. E. From cells to organs: building polarized tissue. *Nature Reviews Molecular Cell Biology* **9**. doi:10.1038/nrm2523 (2008) (cit. on pp. 1, 7, 8, 16).
3. Van Lommel, A. T. L. *From Cells to Organs* doi:10.1007/978-1-4615-0353-8 (Springer US, Boston, MA, 2003) (cit. on pp. 1–3, 5, 7, 8).
4. OpenStax. *Anatomy and Physiology* 2016. <https://opentextbc.ca/anatomyandphysiology/> (2017) (cit. on p. 1).
5. Elias, H. & Bengelsdorf, H. The Structure of the Liver of Vertebrates. *Cells Tissues Organs* **14**. doi:10.1159/000140715 (1952) (cit. on p. 2).
6. Hendriks, H., Verhoofstad, W., Brouwer, A., De Leeuw, A. & Knook, D. Perisinusoidal fat-storing cells are the main vitamin A storage sites in rat liver. *Experimental Cell Research* **160**. doi:10.1016/0014-4827(85)90243-5 (1985) (cit. on p. 2).
7. Schleicher, J., Tokarski, C., Marbach, E., Matz-Soja, M., Zellmer, S., Gebhardt, R. & Schuster, S. Zonation of hepatic fatty acid metabolism — The diversity of its regulation and the benefit of modeling. *Biochimica et Biophysica Acta (BBA) - Molecular and Cell Biology of Lipids* **1851**. doi:10.1016/j.bbalip.2015.02.004 (2015) (cit. on p. 2).
8. Yamamoto, M. *et al.* SIRT1 regulates adaptive response of the growth hormone–insulin-like growth factor-I axis under fasting conditions in liver. *Proceedings of the National Academy of Sciences* **110**. doi:10.1073/pnas.1220606110 (2013) (cit. on p. 3).

9. Van den Eynden, G. G. *et al.* The Multifaceted Role of the Microenvironment in Liver Metastasis: Biology and Clinical Implications. *Cancer Research* **73**. doi:10.1158/0008-5472.CAN-12-3931 (2013) (cit. on p. 3).
10. Zorn. Liver Development. *StemBook*. doi:10.3824/stembook.1.25.1 (2008) (cit. on p. 3).
11. Boyer, J. L. Bile Formation and Secretion. In *Comprehensive Physiology* (John Wiley & Sons, Inc., Hoboken, NJ, USA, 2013). doi:10.1002/cphy.c120027 (cit. on p. 3).
12. Michalopoulos, G. K. Liver Regeneration after Partial Hepatectomy. *The American Journal of Pathology* **176**. doi:10.2353/ajpath.2010.090675 (2010) (cit. on p. 3).
13. Thomas, R. J., Bhandari, R., Barrett, D. A., Bennett, A. J., Fry, J. R., Powe, D., Thomson, B. J. & Shakesheff, K. M. The Effect of Three-Dimensional Co-Culture of Hepatocytes and Hepatic Stellate Cells on Key Hepatocyte Functions in vitro. *Cells Tissues Organs* **181**. doi:10.1159/000091096 (2005) (cit. on p. 3).
14. Godoy, P. *et al.* Recent advances in 2D and 3D in vitro systems using primary hepatocytes, alternative hepatocyte sources and non-parenchymal liver cells and their use in investigating mechanisms of hepatotoxicity, cell signaling and ADME. *Archives of Toxicology* **87**. doi:10.1007/s00204-013-1078-5 (2013) (cit. on pp. 3, 13, 14).
15. Baptista, P. M., Siddiqui, M. M., Lozier, G., Rodriguez, S. R., Atala, A. & Soker, S. The use of whole organ decellularization for the generation of a vascularized liver organoid. *Hepatology* **53**. doi:10.1002/hep.24067 (2011) (cit. on p. 3).
16. Ho, C.-T. *et al.* Liver-cell patterning Lab Chip: mimicking the morphology of liver lobule tissue. *Lab on a Chip* **13**. doi:10.1039/c3lc50402f (2013) (cit. on p. 3).
17. Montanez-Sauri, S. I., Beebe, D. J. & Sung, K. E. Microscale screening systems for 3D cellular microenvironments: platforms, advances, and challenges. *Cellular and Molecular Life Sciences* **72**. doi:10.1007/s00018-014-1738-5 (2015) (cit. on p. 3).

18. Deharde, D. *et al.*
Bile canaliculi formation and biliary transport in 3D sandwich-cultured hepatocytes in dependence of the extracellular matrix composition. *Archives of Toxicology* **90**. doi:10.1007/s00204-016-1758-z (2016) (cit. on p. 3).
19. Gordillo, M., Evans, T. & Gouon-Evans, V.
Orchestrating liver development. *Development* **142**. doi:10.1242/dev.114215 (2015) (cit. on p. 3).
20. Gray, H. *Anatomy of the human body* 20th ed. (ed Lewis, W. H.) (Lea & Febiger, Philadelphia, 1918) (cit. on pp. 3, 7).
21. Elias, H. & Petty, D.
Gross anatomy of the blood vessels and ducts within the human liver. *American Journal of Anatomy* **90**. doi:10.1002/aja.1000900104 (1952) (cit. on p. 3).
22. Mescher, A. L. *Junqueira's Basic Histology: Text and Atlas* 13th ed. doi:ark:/13960/t62553f36 (McGraw-Hill Education, 2013) (cit. on p. 3).
23. Si-Tayeb, K., Lemaigre, F. P. & Duncan, S. A.
Organogenesis and Development of the Liver. *Developmental Cell* **18**. doi:10.1016/j.devcel.2010.01.011 (2010) (cit. on p. 4).
24. Miyaoka, Y. & Miyajima, A.
To divide or not to divide: revisiting liver regeneration. *Cell Division* **8**. doi:10.1186/1747-1028-8-8 (2013) (cit. on p. 4).
25. Elias, H. A re-examination of the structure of the mammalian liver. II. The hepatic lobule and its relation to the vascular and biliary systems. *American Journal of Anatomy* **85**. doi:10.1002/aja.1000850303. (2014) (1949) (cit. on p. 7).
26. Elias, H. & Petty, D.
Gross anatomy of the blood vessels and ducts within the human liver. *American Journal of Anatomy* **90**. doi:10.1002/aja.1000900104. (2013) (1952) (cit. on p. 7).

27. Matter, K. & Mellman, I.
Mechanisms of cell polarity: sorting and transport in epithelial cells.
Current Opinion in Cell Biology **6**. doi:10.1016/0955-0674(94)90075-2
(1994) (cit. on p. 7).
28. Simons, K. & Fuller, S. D. Cell Surface Polarity in Epithelia.
Annual Review of Cell Biology **1**.
doi:10.1146/annurev.cb.01.110185.001331 (1985) (cit. on p. 7).
29. Treyer, A. & Müsch, A. Hepatocyte Polarity. *Comprehensive Physiology* **3**.
doi:10.1002/cphy.c120009 (2013) (cit. on pp. 7–9, 122, 123).
30. Li, Q. *et al.* Extracellular matrix scaffolding guides lumen elongation by
inducing anisotropic intercellular mechanical tension.
Nature Cell Biology **18**. doi:10.1038/ncb3310 (2016)
(cit. on pp. 7, 78, 81, 100).
31. Schiff, J. M., Fisher, M. M. & Underdown, B. J. Receptor-mediated biliary
transport of immunoglobulin A and asialoglycoprotein: sorting and
missorting of ligands revealed by two radiolabeling methods.
The Journal of Cell Biology **98**. doi:10.1083/jcb.98.1.79 (1984)
(cit. on p. 7).
32. Babbey, C. M., Ahktar, N., Wang, E., Chen, C. C.-H., Grant, B. D. &
Dunn, K. W. Rab10 Regulates Membrane Transport through Early
Endosomes of Polarized Madin-Darby Canine Kidney Cells.
Molecular Biology of the Cell **17**. doi:10.1091/mbc.E05-08-0799 (2006)
(cit. on p. 7).
33. Wolburg-Buchholz, K., Mack, A. F., Steiner, E., Pfeiffer, F.,
Engelhardt, B. & Wolburg, H.
Loss of astrocyte polarity marks blood–brain barrier impairment during
experimental autoimmune encephalomyelitis. *Acta Neuropathologica* **118**.
doi:10.1007/s00401-009-0558-4 (2009) (cit. on p. 7).
34. Miller, J. R. & Moon, R. T. Signal transduction through beta-catenin and
specification of cell fate during embryogenesis. *Genes & Development* **10**.
doi:10.1101/gad.10.20.2527 (1996) (cit. on p. 7).

35. Lee, M. & Vasioukhin, V. Cell polarity and cancer - cell and tissue polarity as a non-canonical tumor suppressor. *Journal of Cell Science* **121**. doi:10.1242/jcs.016634 (2008) (cit. on p. 7).
36. Cerchiari, A. E. *et al.* A strategy for tissue self-organization that is robust to cellular heterogeneity and plasticity. *Proceedings of the National Academy of Sciences* **112**. doi:10.1073/pnas.1410776112. (2015) (2015) (cit. on p. 7).
37. Wang, L. & Boyer, J. L. The maintenance and generation of membrane polarity in hepatocytes. *Hepatology* **39**. doi:10.1002/hep.20039 (2004) (cit. on pp. 7, 122).
38. Wodarz, A. & Näthke, I. Cell polarity in development and cancer. *Nature Cell Biology* **9**. doi:10.1038/ncb433 (2007) (cit. on p. 7).
39. De Gennes, P. G. & Prost, J. *The Physics of Liquid Crystals* 2nd ed. (Oxford University Press, New York, NY, USA, 1993) (cit. on pp. 9, 16–19, 21–25, 33, 46, 64, 90, 127, 128).
40. Kress, H., Stelzer, E. H. K., Holzer, D., Buss, F., Griffiths, G. & Rohrbach, A. Filopodia act as phagocytic tentacles and pull with discrete steps and a load-dependent velocity. *Proceedings of the National Academy of Sciences* **104**. doi:10.1073/pnas.0702449104 (2007) (cit. on p. 9).
41. Riedel-Kruse, I. H., Hilfinger, A., Howard, J. & Jülicher, F. How molecular motors shape the flagellar beat. *HFSP Journal* **1**. doi:10.2976/1.2773861 (2007) (cit. on p. 9).
42. Howard, J. *Mechanics of Motor Proteins & the Cytoskeleton* (Sinauer Associates, 2001) (cit. on p. 9).
43. Kressmann, S., Campos, C., Castanon, I., Fürthauer, M. & González-Gaitán, M. Directional Notch trafficking in Sara endosomes during asymmetric cell division in the spinal cord. *Nature Cell Biology* **17**. doi:10.1038/ncb3119 (2015) (cit. on p. 9).
44. Grill, S. W., Kruse, K. & Jülicher, F. Theory of Mitotic Spindle Oscillations. *Physical Review Letters* **94**. doi:10.1103/PhysRevLett.94.108104 (2005) (cit. on p. 9).

45. Zumdieck, A., Kruse, K., Bringmann, H., Hyman, A. A. & Jülicher, F.
Stress Generation and Filament Turnover during Actin Ring Constriction.
PLoS ONE **2**. doi:10.1371/journal.pone.0000696 (2007) (cit. on p. 9).
46. Robinson, D. N., Cavet, G., Warrick, H. M. & Spudich, J. A.
Quantitation of the distribution and flux of myosin-II during cytokinesis.
BMC Cell Biology **3**. doi:10.1186/1471-2121-3-4 (2002) (cit. on p. 9).
47. Depken, M., Galburt, E. A. & Grill, S. W.
The Origin of Short Transcriptional Pauses. *Biophysical Journal* **96**.
doi:10.1016/j.bpj.2008.12.3918 (2009) (cit. on p. 9).
48. Jülicher, F., Kruse, K., Prost, J. & Joanny, J.-F.
Active behavior of the Cytoskeleton. *Physics Reports* **449**.
doi:10.1016/j.physrep.2007.02.018 (2007) (cit. on p. 9).
49. Friedrich, B. M. & Safran, S. A. How cells feel their substrate: spontaneous
symmetry breaking of active surface stresses. *Soft Matter* **8**.
doi:10.1039/c2sm06450b (2012) (cit. on p. 9).
50. Otto, O. *et al.*
Real-time deformability cytometry: on-the-fly cell mechanical phenotyping.
Nature Methods **12**. doi:10.1038/nmeth.3281 (2015) (cit. on p. 9).
51. Fischer-Friedrich, E., Toyoda, Y., Cattin, C. J., Müller, D. J.,
Hyman, A. A. & Jülicher, F.
Rheology of the Active Cell Cortex in Mitosis. *Biophysical Journal* **111**.
doi:10.1016/j.bpj.2016.06.008 (2016) (cit. on pp. 9, 78).
52. Marchetti, M. C., Joanny, J. F., Ramaswamy, S., Liverpool, T. B.,
Prost, J., Rao, M. & Simha, R. A. Hydrodynamics of soft active matter.
Reviews of Modern Physics **85**. doi:10.1103/RevModPhys.85.1143 (2013)
(cit. on pp. 10, 11).
53. Tanaka, S. Simulation Frameworks for Morphogenetic Problems.
Computation **3**. doi:10.3390/computation3020197 (2015)
(cit. on pp. 10–12, 14).
54. Ranft, J. M.
Mechanics of Growing Tissues : A Continuum Description Approach
PhD thesis (Technical University Dresden & Pierre and Marie Curie
University Paris, 2012) (cit. on p. 10).

55. Lecuit, T. & Le Goff, L.
Orchestrating size and shape during morphogenesis. *Nature* **450**.
doi:10.1038/nature06304 (2007) (cit. on pp. 10, 16).
56. Steinberg, M. S. Differential adhesion in morphogenesis: a modern view.
Current Opinion in Genetics & Development **17**.
doi:10.1016/j.gde.2007.05.002 (2007) (cit. on p. 10).
57. Turing, A. M. The Chemical Basis of Morphogenesis.
Philosophical Transactions of the Royal Society B **237**.
doi:10.1098/rstb.1952.0012 (1952) (cit. on p. 10).
58. Newman, S. a. & Comper, W. D.
'Generic' physical mechanisms of morphogenesis and pattern formation.
Development **110** (1990) (cit. on p. 10).
59. Sampathkumar, A., Yan, A., Krupinski, P. & Meyerowitz, E. M.
Physical Forces Regulate Plant Development and Morphogenesis.
Current Biology **24**. doi:10.1016/j.cub.2014.03.014 (2014)
(cit. on p. 10).
60. Wartlick, O., Mumcu, P., Jülicher, F. & Gonzalez-Gaitan, M.
Understanding morphogenetic growth control — lessons from flies.
Nature Reviews Molecular Cell Biology **12**. doi:10.1038/nrm3169 (2011)
(cit. on pp. 10, 16, 59).
61. Wartlick, O., Jülicher, F. & Gonzalez-Gaitan, M. Growth control by a
moving morphogen gradient during Drosophila eye development.
Development **141**. doi:10.1242/dev.105650 (2014) (cit. on p. 10).
62. Werner, S., Stückemann, T., Beirán Amigo, M., Rink, J. C., Jülicher, F. &
Friedrich, B. M. Scaling and Regeneration of Self-Organized Patterns.
Physical Review Letters **114**. doi:10.1103/PhysRevLett.114.138101
(2015) (cit. on p. 10).
63. Boehm, B., Westerberg, H., Lesnicar-Pucko, G., Raja, S., Rautschka, M.,
Cotterell, J., Swoger, J. & Sharpe, J. The role of spatially controlled cell
proliferation in limb bud morphogenesis. *PLoS Biology* **8**.
doi:10.1371/journal.pbio.1000420 (2010) (cit. on p. 10).

64. Scianna, M., Bell, C. & Preziosi, L.
A review of mathematical models for the formation of vascular networks.
Journal of Theoretical Biology **333**. doi:10.1016/j.jtbi.2013.04.037
(2013) (cit. on pp. 10, 14).
65. Verdier, C., Etienne, J., Duperray, A. & Preziosi, L.
Review: Rheological properties of biological materials.
Comptes Rendus Physique **10**. doi:10.1016/j.crhy.2009.10.003 (2009)
(cit. on p. 11).
66. Rodriguez, E. K., Hoger, A. & McCulloch, A. D.
Stress-dependent finite growth in soft elastic tissues.
Journal of Biomechanics **27**. doi:10.1016/0021-9290(94)90021-3 (1994)
(cit. on p. 11).
67. Merkel, M. *From cells to tissues: Remodeling and polarity reorientation in epithelial tissues*
PhD thesis (Technical University Dresden, Dresden, 2014)
(cit. on pp. 11, 12, 15, 78).
68. Martin, P. C., Parodi, O. & Pershan, P. S.
Unified hydrodynamic theories of Crystals. *Physical Review A* **6**.
doi:10.1103/PhysRevA.6.2401 (1972) (cit. on p. 11).
69. Ramaswamy, S. The Mechanics and Statistics of Active Matter.
Annual Review of Condensed Matter Physics **1**.
doi:10.1146/annurev-conmatphys-070909-104101 (2010) (cit. on p. 11).
70. Perepelyuk, M., Chin, L., Cao, X., van Oosten, A., Shenoy, V. B.,
Janmey, P. A. & Wells, R. G.
Normal and Fibrotic Rat Livers Demonstrate Shear Strain Softening and
Compression Stiffening: A Model for Soft Tissue Mechanics.
PLOS ONE **11**. doi:10.1371/journal.pone.0146588 (2016)
(cit. on p. 11).
71. Miller, K. Constitutive modelling of abdominal organs.
Journal of Biomechanics **33**. doi:10.1016/S0021-9290(99)00196-7
(2000) (cit. on p. 11).

72. Popović, M., Nandi, A., Merkel, M., Etournay, R., Eaton, S., Jülicher, F. & Salbreux, G. Active dynamics of tissue shear flow. *New Journal of Physics* **19**. doi:10.1088/1367-2630/aa5756 (2017) (cit. on p. 11).
73. Nishii, K., Reese, G., Moran, E. C. & Sparks, J. L. Multiscale computational model of fluid flow and matrix deformation in decellularized liver. *Journal of the Mechanical Behavior of Biomedical Materials* **57**. doi:10.1016/j.jmbbm.2015.11.033 (2016) (cit. on pp. 11, 16).
74. Debbaut, C., Monbaliu, D. & Segers, P. Engineering Point of View on Liver Transplantation Strategies: Multi-Level Modeling of Hepatic Perfusion. *Transplantation Proceedings* **46**. doi:10.1016/j.transproceed.2014.09.167 (2014) (cit. on p. 11).
75. Schwartz, J.-M., Denninger, M., Rancourt, D., Moisan, C. & Laurendeau, D. Modelling liver tissue properties using a non-linear visco-elastic model for surgery simulation. *Medical Image Analysis* **9**. doi:10.1016/j.media.2004.11.002 (2005) (cit. on pp. 11, 16).
76. Anderson, A. R. A., Chaplain, M. A. J., Rejniak, K. A. & Fozard, J. A. Single-cell-based models in biology and medicine. *Mathematical Medicine and Biology* **25**. doi:10.1093/imammb/dqn008 (2008) (cit. on pp. 11, 12).
77. Smallwood, R. Computational modeling of epithelial tissues. *Wiley Interdisciplinary Reviews: Systems Biology and Medicine* **1**. doi:10.1002/wsbm.18 (2009) (cit. on p. 11).
78. Farhadifar, R. *Dynamics of Cell Packing and Polar Order in Developing Epithelia* PhD thesis (Technical University Dresden, Dresden, 2009) (cit. on p. 11).
79. Farhadifar, R., Röper, J.-C., Aigouy, B., Eaton, S. & Jülicher, F. The Influence of Cell Mechanics, Cell-Cell Interactions, and Proliferation on Epithelial Packing. *Current Biology* **17**. doi:10.1016/j.cub.2007.11.049 (2007) (cit. on pp. 11, 12).

80. Hufnagel, L., Teleman, A. A., Rouault, H., Cohen, S. M. & Shraiman, B. I. On the mechanism of wing size determination in fly development. *Proceedings of the National Academy of Sciences* **104**. doi:10.1073/pnas.0607134104 (2007) (cit. on p. 11).
81. Kruse, K. & Jülicher, F. Self-organization and mechanical properties of active filament bundles. *Physical Review E* **67**. doi:10.1103/PhysRevE.67.051913 (2003) (cit. on p. 12).
82. Lodish, H., Berk, A., Zipursky, S. L., Matsudaira, P., Baltimore, D. & Darnell, J. *Molecular Cell Biology* 4th ed. (W. H. Freeman, New York, NY, USA, 2000) (cit. on p. 12).
83. Staple, D. B., Farhadifar, R., Röper, J.-C., Aigouy, B., Eaton, S. & Jülicher, F. Mechanics and remodelling of cell packings in epithelia. *The European Physical Journal E* **33**. doi:10.1140/epje/i2010-10677-0 (2010) (cit. on pp. 12, 15, 16).
84. Alt, S., Ganguly, P. & Salbreux, G. Vertex models: from cell mechanics to tissue morphogenesis. *Philosophical Transactions of the Royal Society B* **372**. doi:10.1098/rstb.2015.0520 (2017) (cit. on p. 12).
85. Landsberg, K. P. *et al.* Increased Cell Bond Tension Governs Cell Sorting at the Drosophila Anteroposterior Compartment Boundary. *Current Biology* **19**. doi:10.1016/j.cub.2009.10.021 (2009) (cit. on p. 12).
86. Aliee, M., Röper, J.-C., Landsberg, K. P., Pentzold, C., Widmann, T. J., Jülicher, F. & Dahmann, C. Physical Mechanisms Shaping the Drosophila Dorsoventral Compartment Boundary. *Current Biology* **22**. doi:10.1016/j.cub.2012.03.070 (2012) (cit. on p. 12).
87. Aliee, M. *Dynamics and mechanics of compartment boundaries in developing tissues* PhD thesis (Technical University Dresden, 2013) (cit. on p. 12).
88. Aigouy, B., Farhadifar, R., Staple, D. B., Sagner, A., Röper, J.-C., Jülicher, F. & Eaton, S. Cell Flow Reorients the Axis of Planar Polarity in

- the Wing Epithelium of *Drosophila*. *Cell* **142**.
doi:10.1016/j.cell.2010.07.042 (2010) (cit. on pp. 12, 15, 16, 78).
89. Chu, Y.-S., Dufour, S., Thiery, J. P., Perez, E. & Pincet, F.
Johnson-Kendall-Roberts Theory Applied to Living Cells.
Physical Review Letters **94**. doi:10.1103/PhysRevLett.94.028102 (2005)
(cit. on p. 12).
90. Drasdo, D., Hoehme, S. & Block, M.
On the role of physics in the growth and pattern formation of multi-cellular
systems: What can we learn from individual-cell based models?
Journal of Statistical Physics **128**. doi:10.1007/s10955-007-9289-x
(2007) (cit. on p. 12).
91. Drasdo, D., Kree, R. & McCaskill, J. S.
Monte Carlo approach to tissue-cell populations. *Physical Review E* **52**.
doi:10.1103/PhysRevE.52.6635 (1995) (cit. on p. 12).
92. Palsson, E.
A three-dimensional model of cell movement in multicellular systems.
Future Generation Computer Systems **17**.
doi:10.1016/S0167-739X(00)00062-5 (2001) (cit. on p. 12).
93. Hoehme, S. *et al.*
Prediction and validation of cell alignment along microvessels as order
principle to restore tissue architecture in liver regeneration.
Proceedings of the National Academy of Sciences **107**.
doi:10.1073/pnas.0909374107 (2010) (cit. on pp. 14, 16, 81).
94. Ising, E. Beitrag zur Theorie des Ferromagnetismus.
Zeitschrift für Physik **31**. doi:10.1007/BF02980577 (1925) (cit. on p. 14).
95. Graner, F. & Glazier, J. A. Simulation of biological cell sorting using a
two-dimensional extended Potts model. *Physical Review Letters* **69**.
doi:10.1103/PhysRevLett.69.2013 (1992) (cit. on p. 14).
96. Glazier, J. A. & Graner, F. Simulation of the differential adhesion driven
rearrangement of biological cells. *Physical Review E* **47**.
doi:10.1103/PhysRevE.47.2128 (1993) (cit. on p. 14).

97. Metropolis, N., Rosenbluth, A. W., Rosenbluth, M. N., Teller, A. H. & Teller, E. Equation of State Calculations by Fast Computing Machines. *The Journal of Chemical Physics* **21**. doi:10.1063/1.1699114 (1953) (cit. on p. 14).
98. Ben-Isaac, E., Park, Y., Popescu, G., Brown, F. L. H., Gov, N. S. & Shokef, Y. Effective Temperature of Red-Blood-Cell Membrane Fluctuations. *Physical Review Letters* **106**. doi:10.1103/PhysRevLett.106.238103 (2011) (cit. on pp. 14, 92).
99. Merks, R. M., Brodsky, S. V., Goligorsky, M. S., Newman, S. A. & Glazier, J. A. Cell elongation is key to in silico replication of in vitro vasculogenesis and subsequent remodeling. *Developmental Biology* **289**. doi:10.1016/j.ydbio.2005.10.003 (2006) (cit. on p. 14).
100. Köhn-Luque, A., de Back, W., Yamaguchi, Y., Yoshimura, K., Herrero, M. A. & Miura, T. Dynamics of VEGF matrix-retention in vascular network patterning. *Physical Biology* **10**. doi:10.1088/1478-3975/10/6/066007 (2013) (cit. on p. 14).
101. Segerer, F. J., Thüroff, F., Piera Alberola, A., Frey, E. & Rädler, J. O. Emergence and Persistence of Collective Cell Migration on Small Circular Micropatterns. *Physical Review Letters* **114**. doi:10.1103/PhysRevLett.114.228102 (2015) (cit. on p. 14).
102. Marcinkevicius, E., Fernandez-Gonzalez, R. & Zallen, J. A. Q&A: Quantitative approaches to planar polarity and tissue organization. *Journal of Biology* **8**. doi:10.1186/jbio1191 (2009) (cit. on p. 15).
103. Salbreux, G., Barthel, L. K., Raymond, P. A. & Lubensky, D. K. Coupling Mechanical Deformations and Planar Cell Polarity to Create Regular Patterns in the Zebrafish Retina. *PLoS Computational Biology* **8**. doi:10.1371/journal.pcbi.1002618 (2012) (cit. on p. 16).
104. Bielmeier, C., Alt, S., Weichselberger, V., La Fortezza, M., Harz, H., Jülicher, F., Salbreux, G. & Classen, A.-K. Interface Contractility between Differently Fated Cells Drives Cell Elimination and Cyst Formation. *Current Biology* **26**. doi:10.1016/j.cub.2015.12.063 (2016) (cit. on p. 16).

105. Morales-Navarrete, H. *et al.* A versatile pipeline for the multi-scale digital reconstruction and quantitative analysis of 3D tissue architecture. *eLife* **4**. doi:10.7554/eLife.11214 (2015) (cit. on pp. 16, 26, 27, 70, 82, 86).
106. Yuste, R. Fluorescence microscopy today. *Nature Methods* **2**. doi:10.1038/nmeth1205-902 (2005) (cit. on p. 16).
107. Hoyer, P. *et al.* Breaking the diffraction limit of light-sheet fluorescence microscopy by RESOLFT. *Proceedings of the National Academy of Sciences* **113**. doi:10.1073/pnas.1522292113 (2016) (cit. on p. 16).
108. Chung, K. & Deisseroth, K. CLARITY for mapping the nervous system. *Nature Methods* **10**. doi:10.1038/nmeth.2481 (2013) (cit. on p. 16).
109. Ke, M.-T., Fujimoto, S. & Imai, T.
SeeDB: a simple and morphology-preserving optical clearing agent for neuronal circuit reconstruction. *Nature Neuroscience* **16**. doi:10.1038/nn.3447 (2013) (cit. on p. 16).
110. Debbaut, C. *et al.* Perfusion Characteristics of the Human Hepatic Microcirculation Based on Three-Dimensional Reconstructions and Computational Fluid Dynamic Analysis. *Journal of Biomechanical Engineering* **134**. doi:10.1115/1.4005545 (2012) (cit. on p. 16).
111. Debbaut, C., Vierendeels, J., Siggers, J. H., Repetto, R., Monbaliu, D. & Segers, P. A 3D porous media liver lobule model: the importance of vascular septa and anisotropic permeability for homogeneous perfusion. *Computer Methods in Biomechanics and Biomedical Engineering* **17**. doi:10.1080/10255842.2012.744399 (2014) (cit. on p. 16).
112. Schliess, F. *et al.*
Integrated metabolic spatial-temporal model for the prediction of ammonia detoxification during liver damage and regeneration. *Hepatology* **60**. doi:10.1002/hep.27136 (2014) (cit. on p. 16).
113. Chandrasekhar, S. *Liquid Crystals* doi:10.1017/CB09780511622496 (Cambridge University Press, Cambridge, 1992) (cit. on pp. 17, 26).

114. Dierking, I., Palangana, A. J., Vij, J. K., Kocot, A., Madsen, L. A. & Davidson, P. Characterisation. In *Biaxial Nematic Liquid Crystals* (John Wiley & Sons, Ltd, Chichester, UK, 2015). doi:10.1002/9781118696316.ch10 (cit. on p. 17).
115. Luckhurst, G. R. & Sluckin, T. J. Introduction. In *Biaxial Nematic Liquid Crystals* (John Wiley & Sons, Ltd, Chichester, UK, 2015). doi:10.1002/9781118696316.ch1 (cit. on pp. 19, 21, 22, 46, 49).
116. Carlsson, T. & Leslie, F. M. Behaviour of biaxial nematics in the presence of electric and magnetic fields. *Liquid Crystals* **10**. doi:10.1080/02678299108026279 (1991) (cit. on pp. 19, 55).
117. Doi, M. *Soft Matter Physics* (Oxford University Press, New York, NY, USA, 2013) (cit. on pp. 19, 21, 127).
118. Allender, D. W. & Lee, M. A. Landau Theory of Biaxial Nematic Liquid Crystals. *Molecular Crystals and Liquid Crystals* **110**. doi:10.1080/00268948408074514 (1984) (cit. on pp. 22, 24).
119. Straley, J. P. Ordered phases of a liquid of biaxial particles. *Physical Review A* **10**. doi:10.1103/PhysRevA.10.1881 (1974) (cit. on pp. 22, 24, 128).
120. Beris, A. N. & Edwards, B. J. *Thermodynamics of flowing systems with internal microstructure* (Oxford University Press, 1994) (cit. on p. 23).
121. Selinger, J. V. *Introduction to the Theory of Soft Matter* doi:10.1007/978-3-319-21054-4 (2016) (cit. on pp. 23, 90).
122. Cleaver, D. J. & Allen, M. P. Computer simulations of the elastic properties of liquid crystals. *Physical Review A* **43**. doi:10.1103/PhysRevA.43.1918 (1991) (cit. on p. 23).

123. Priest, R. G.
A Calculation of the Elastic Constants of a Nematic Liquid Crystal.
Molecular Crystals and Liquid Crystals **17**.
doi:10.1080/15421407208083836 (1972) (cit. on p. 23).
124. Singh, Y., Rajesh, K., Menon, V. J. & Singh, S. Molecular theory of elastic constants of liquid crystals. II. Application to the biaxial nematic phase.
Physical Review E **49**. doi:10.1103/PhysRevE.49.501 (1994)
(cit. on pp. 23, 91).
125. Landau, L. D. & Lifshitz, E. M. *Electrodynamics of Continuous Media* (Pergamon Press, Oxford, 1960) (cit. on p. 24).
126. Onsager, L. The Effects of Shape on the Interaction of Colloidal Particles.
Annals of the New York Academy of Sciences **51**.
doi:10.1111/j.1749-6632.1949.tb27296.x (1949) (cit. on p. 24).
127. Maier, W. & Saupe, A. Eine einfache molekulare Theorie des nematischen kristallinflüssigen Zustandes. *Zeitschrift für Naturforschung A* **13**.
doi:10.1515/zna-1958-0716 (1958) (cit. on pp. 24, 89).
128. Freiser, M. J. Ordered States of a Nematic Liquid.
Physical Review Letters **24**. doi:10.1103/PhysRevLett.24.1041 (1970)
(cit. on pp. 24, 128).
129. Belli, S., Patti, A., Dijkstra, M. & van Roij, R.
Polydispersity Stabilizes Biaxial Nematic Liquid Crystals.
Physical Review Letters **107**. doi:10.1103/PhysRevLett.107.148303
(2011) (cit. on p. 24).
130. Bates, M. A. & Frenkel, D. Influence of polydispersity on the phase behavior of colloidal liquid crystals: A Monte Carlo simulation study.
Journal of Chemical Physics **109**. doi:10.1063/1.477248 (1998)
(cit. on p. 24).
131. Alben, R. Liquid crystal phase transitions in mixtures of rodlike and platelike molecules. *The Journal of Chemical Physics* **59**.
doi:10.1063/1.1680625 (1973) (cit. on p. 24).

132. Stroobants, A. & Lekkerkerker, H. N. W. Liquid crystal phase transitions in a solution of rodlike and disklike particles.
The Journal of Physical Chemistry **88**. doi:10.1021/j150660a058 (1984)
(cit. on p. 24).
133. Masters, A. J. Hard Particle Theories. In *Biaxial Nematic Liquid Crystals* (John Wiley & Sons, Ltd, Chichester, UK, 2015).
doi:10.1002/9781118696316.ch4 (cit. on p. 24).
134. Vroege, G. J. Colloidal Systems. In *Biaxial Nematic Liquid Crystals* (John Wiley & Sons, Ltd, Chichester, UK, 2015).
doi:10.1002/9781118696316.ch12 (cit. on p. 24).
135. Van Roij, R. & Mulder, B. Demixing in a hard rod-plate mixture.
Journal de Physique II **4**. doi:10.1051/jp2:1994110 (1994)
(cit. on p. 24).
136. Camp, P. J., Allen, M. P., Bolhuis, P. G. & Frenkel, D.
Demixing in hard ellipsoid rod-plate mixtures.
The Journal of Chemical Physics **106**. doi:10.1063/1.474012 (1997)
(cit. on p. 24).
137. Varga, S., Galindo, A. & Jackson, G. Phase behavior of symmetric rod-plate mixtures revisited: Biaxiality versus demixing.
The Journal of Chemical Physics **117**. doi:10.1063/1.1519536 (2002)
(cit. on p. 24).
138. Alben, R. Phase Transitions in a Fluid of Biaxial Particles.
Physical Review Letters **30**. doi:10.1103/PhysRevLett.30.778 (1973)
(cit. on p. 24).
139. Allender, D. W., Lee, M. A. & Hafiz, N.
Landau Theory of Biaxial and Uniaxial Nematic Liquid Crystals.
Molecular Crystals and Liquid Crystals **124**.
doi:10.1080/00268948508079464 (1985) (cit. on p. 24).
140. Matteis, G. D.
Continuum Landau Model for Biaxial Nematic Liquid Crystals.
Molecular Crystals and Liquid Crystals **500**.
doi:10.1080/15421400802713678 (2009) (cit. on pp. 24, 55, 129, 139).

141. Majumdar, A. Equilibrium order parameters of nematic liquid crystals in the Landau-de Gennes theory.
European Journal of Applied Mathematics **21**.
doi:10.1017/S0956792509990210 (2010) (cit. on p. 24).
142. Longa, L. Landau Theory of Nematic Phases.
In *Biaxial Nematic Liquid Crystals*
(John Wiley & Sons, Ltd, Chichester, UK, 2015).
doi:10.1002/9781118696316.ch5 (cit. on p. 24).
143. Eppenga, R. & Frenkel, D. Monte Carlo study of the isotropic and nematic phases of infinitely thin hard platelets. *Molecular Physics* **52**.
doi:10.1080/00268978400101951 (1984) (cit. on p. 24).
144. Pasini, P. & Zannoni, C.
Advances in the Computer Simulations of Liquid Crystals
(eds Pasini, P. & Zannoni, C.) doi:10.1007/978-94-011-4225-0
(Springer Netherlands, Dordrecht, 2000) (cit. on p. 24).
145. Bates, M. A. & Luckhurst, G. R. Biaxial nematic phases and V-shaped molecules: A Monte Carlo simulation study. *Physical Review E* **72**.
doi:10.1103/PhysRevE.72.051702 (2005) (cit. on p. 24).
146. Nguyen, K. T., Sciortino, F. & De Michele, C.
Self-Assembly-Driven Nematization. *Langmuir* **30**.
doi:10.1021/1a500127n (2014) (cit. on p. 24).
147. Avendaño, C., Jackson, G., Müller, E. A. & Escobedo, F. A.
Assembly of porous smectic structures formed from interlocking high-symmetry planar nanorings.
Proceedings of the National Academy of Sciences **113**.
doi:10.1073/pnas.1604717113 (2016) (cit. on p. 24).
148. Friedel, G. Les états mésomorphes de la matière. *Annales de Physique* **9**.
doi:10.1051/anphys/192209180273 (1922) (cit. on p. 25).
149. Frank, F. C. I. Liquid crystals. On the theory of liquid crystals.
Discussions of the Faraday Society **25**. doi:10.1039/df9582500019 (1958)
(cit. on p. 25).

150. Gage, G. J., Kipke, D. R. & Shain, W.
Whole Animal Perfusion Fixation for Rodents.
Journal of Visualized Experiments. doi:10.3791/3564 (2012)
(cit. on p. 26).
151. Kalaidzidis, Y., Kalaidzidis, A., Marsico, G., Chernykh, M.,
Morales-Navarrete, H. & Klukowski, P. *MotionTracking* 2017.
<http://motiontracking.mpi-cbg.de> (cit. on p. 26).
152. Morales-Navarrete, H. *et al.* A versatile pipeline for the multi-scale digital reconstruction and quantitative analysis of 3D tissue architecture. *eLife* **4**. doi:10.7554/eLife.11214. (2016) (2015) (cit. on p. 28).
153. Fisher, R. Dispersion on a Sphere. *Proceedings of the Royal Society of London A: Mathematical, Physical and Engineering Sciences* **217**. doi:10.1098/rspa.1953.0064. (2016) (1953) (cit. on p. 32).
154. Snyder, J. P. *Map projections—A working manual* (2016)
(US Government Printing Office, Washington, 1987) (cit. on pp. 33, 129).
155. Matteis, G. D., Sonnet, A. M. & Virga, E. G. Landau theory for biaxial nematic liquid crystals with two order parameter tensors. *Continuum Mechanics and Thermodynamics* **20**. doi:10.1007/s00161-008-0086-9 (2008) (cit. on p. 45).
156. Virga, E. G. Molecular Field Theory. In *Biaxial Nematic Liquid Crystals* (John Wiley & Sons, Ltd, Chichester, UK, 2015). doi:10.1002/9781118696316.ch3 (cit. on pp. 45, 46, 54, 131, 132).
157. Freiser, M. J. Successive Transitions in a Nematic Liquid. *Molecular Crystals and Liquid Crystals* **14**. doi:10.1080/15421407108083564 (1971) (cit. on pp. 45, 49, 128).
158. De Matteis, G., Bisi, F., Virga, E. G., Matteis, G. D., Bisi, F. & Virga, E. G. Constrained stability for biaxial nematic phases. *Continuum Mechanics and Thermodynamics* **19**. doi:10.1007/s00161-007-0041-1 (2007) (cit. on pp. 46, 47).
159. Luckhurst, G. R.
Biaxial Nematics: Order Parameters and Distribution Functions.
In *Biaxial Nematic Liquid Crystals*

- (John Wiley & Sons, Ltd, Chichester, UK, 2015).
doi:10.1002/9781118696316.ch2 (cit. on p. 46).
160. Rosso, R.
Orientational order parameters in biaxial nematics: Polymorphic notation.
Liquid Crystals **34**. doi:10.1080/02678290701284303 (2007)
(cit. on pp. 46, 128, 134).
161. Berardi, R. & Zannoni, C. Computer Simulations of Biaxial Nematics.
In *Biaxial Nematic Liquid Crystals*
(John Wiley & Sons, Ltd, Chichester, UK, 2015).
doi:10.1002/9781118696316.ch6 (cit. on p. 49).
162. Fisher, N. I., Lewis, T. & Embleton, B. J. J.
Statistical analysis of spherical data doi:10.1017/CB09780511623059
(Cambridge University Press, Cambridge, 1987) (cit. on p. 49).
163. Alben, R., McColl, J. & Shih, C.
The characterization of order in nematic liquid crystals.
Solid State Communications **11**. doi:10.1016/0038-1098(72)90325-0
(1972) (cit. on p. 51).
164. Lewis, A. H. *et al.* Colloidal liquid crystals in rectangular confinement:
theory and experiment. *Soft Matter* **10**. doi:10.1039/C4SM01123F (2014)
(cit. on p. 59).
165. Chaikin, P. M. & Lubensky, T. C. *Principles of Condensed Matter Physics*
(Cambridge University Press, 2000) (cit. on p. 64).
166. Saurabh, S., Vidyarthi, A. S. & Prasad, D.
RNA interference: concept to reality in crop improvement. *Planta* **239**.
doi:10.1007/s00425-013-2019-5 (2014) (cit. on p. 78).
167. Stückemann, T. *et al.*
Antagonistic Self-Organizing Patterning Systems Control Maintenance and
Regeneration of the Anteroposterior Axis in Planarians.
Developmental Cell **40**. doi:10.1016/j.devcel.2016.12.024 (2017)
(cit. on p. 78).
168. Gilleron, J. *et al.* Image-based analysis of lipid nanoparticle-mediated
siRNA delivery, intracellular trafficking and endosomal escape.
Nature Biotechnology **31**. doi:10.1038/nbt.2612 (2013) (cit. on p. 78).

169. Elbaum-Garfinkle, S., Kim, Y., Szczepaniak, K., Chen, C. C.-H., Eckmann, C. R., Myong, S. & Brangwynne, C. P. The disordered P granule protein LAF-1 drives phase separation into droplets with tunable viscosity and dynamics. *Proceedings of the National Academy of Sciences* **112**. doi:10.1073/pnas.1504822112 (2015) (cit. on p. 78).
170. Broadhead, R. *et al.* Flagellar motility is required for the viability of the bloodstream trypanosome. *Nature* **440**. doi:10.1038/nature04541 (2006) (cit. on p. 78).
171. Pan, Y., Heemskerk, I., Ibar, C., Shraiman, B. I. & Irvine, K. D. Differential growth triggers mechanical feedback that elevates Hippo signaling. *Proceedings of the National Academy of Sciences* **113**. doi:10.1073/pnas.1615012113 (2016) (cit. on p. 78).
172. Cerchiari, A. E. *et al.* A strategy for tissue self-organization that is robust to cellular heterogeneity and plasticity. *Proceedings of the National Academy of Sciences* **112**. doi:10.1073/pnas.1410776112 (2015) (cit. on p. 78).
173. Bogorad, R. L., Yin, H., Zeigerer, A., Nonaka, H., Ruda, V. M., Zerial, M., Anderson, D. G. & Kotliansky, V. Nanoparticle-formulated siRNA targeting integrins inhibits hepatocellular carcinoma progression in mice. *Nature Communications* **5**. doi:10.1038/ncomms4869 (2014) (cit. on p. 78).
174. Waskom, M. *et al.* seaborn: v0.7.1 (June 2016). doi:10.5281/ZENODO.54844 (2016) (cit. on pp. 79, 131).
175. Weisstein, E. W. *Cross-Correlation Theorem* <http://mathworld.wolfram.com/Cross-CorrelationTheorem.html> (2017) (cit. on p. 86).
176. Champeney, D. C. *A Handbook of Fourier Theorems* (Cambridge University Press, Cambridge, UK, 1987) (cit. on p. 86).
177. Maier, W. & Saupe, A. Eine einfache molekular-statistische Theorie der nematischen kristallinflüssigen Phase. Teil I. *Zeitschrift für Naturforschung A* **14**. doi:10.1515/zna-1959-1005 (1959) (cit. on pp. 89, 127).

178. Maier, W. & Saupe, A. Eine einfache molekular-statistische Theorie der nematischen kristallinflüssigen Phase. Teil II.
Zeitschrift für Naturforschung A **15**. doi:10.1515/zna-1960-0401 (1960)
(cit. on p. 89).
179. Syga, S. *Nematic Order in Complex Tissues*
Bachelor Thesis (Technical University Dresden, 2014) (cit. on p. 89).
180. Lebwohl, P. a. & Lasher, G.
Nematic-Liquid-Crystal Order—A Monte Carlo Calculation.
Physical Review A **6**. doi:10.1103/PhysRevA.6.426 (1972) (cit. on p. 90).
181. Pasini, P., Chiccoli, C. & Zannoni, C.
Liquid Crystal Lattice Models I. Bulk Systems.
In *Advances in the Computer Simulations of Liquid Crystals*
(eds Pasini, P. & Zannoni, C.) (Springer Netherlands, Dordrecht, 2000).
doi:10.1007/978-94-011-4225-0_5 (cit. on p. 90).
182. Marguta, R. G., Martínez-Ratón, Y., Almarza, N. G. & Velasco, E.
Theory and simulation of the confined Lebwohl-Lasher model.
Physical Review E **83**. doi:10.1103/PhysRevE.83.041701 (2011)
(cit. on p. 90).
183. Saupe, A. Elastic and flow properties of biaxial nematics.
The Journal of Chemical Physics **75**. doi:10.1063/1.441903 (1981)
(cit. on p. 91).
184. Vissenberg, M. C. J. M., Stallinga, S. & Vertogen, G. Generalized
Landau–de Gennes theory of uniaxial and biaxial nematic liquid crystals.
Physical Review E **55**. doi:10.1103/PhysRevE.55.4367 (1997)
(cit. on p. 91).
185. Longa, L., Stelzer, J. & Dunmur, D. Density functional approach to study
the elastic constants of biaxial nematic liquid crystals.
The Journal of Chemical Physics **109**. doi:10.1063/1.476707 (1998)
(cit. on p. 91).
186. Stewart, I. W. Continuum Theory of Biaxial Nematic Liquid Crystals.
In *Biaxial Nematic Liquid Crystals*
(John Wiley & Sons, Ltd, Chichester, UK, 2015).
doi:10.1002/9781118696316.ch7 (cit. on p. 91).

187. Safran, S. A.
Statistical Thermodynamics of Surfaces, Interfaces and Membranes
(Addison-Wesley Publishing Company, Reading, MA, 1994)
(cit. on p. 110).
188. Barrat, J.-L. & Hansen, J.-P.
Basic Concepts for Simple and Complex Liquids
(Cambridge University Press, Cambridge, UK, 2003) (cit. on p. 110).
189. Steinberg, M. S. Reconstruction of Tissues by Dissociated Cells.
Science **141**. doi:10.1126/science.141.3579.401 (1963) (cit. on p. 110).
190. Breuer, D., Ivakov, A., Sampathkumar, A., Hollandt, F., Persson, S. & Nikoloski, Z. Quantitative analyses of the plant cytoskeleton reveal underlying organizational principles.
Journal of The Royal Society Interface **11**. doi:10.1098/rsif.2014.0362 (2014) (cit. on p. 122).
191. Hua, M., Zhang, W., Li, W., Li, X., Liu, B., Lu, X. & Zhang, H. Molecular mechanisms regulating the establishment of hepatocyte polarity during human hepatic progenitor cell differentiation into a functional hepatocyte-like phenotype. *Journal of Cell Science* **125**. doi:10.1242/jcs.110551 (2012) (cit. on p. 122).
192. Taniguchi, E., Sakisaka, S., Matsuo, K., Tanikawa, K. & Sata, M. Expression and Role of Vascular Endothelial Growth Factor in Liver Regeneration After Partial Hepatectomy in Rats.
Journal of Histochemistry & Cytochemistry **49**. doi:10.1177/002215540104900112 (2001) (cit. on p. 122).
193. Coultas, L., Chawengsaksophak, K. & Rossant, J. Endothelial cells and VEGF in vascular development. *Nature* **438**. doi:10.1038/nature04479 (2005) (cit. on p. 122).
194. Sugiyama, Y., Takabe, Y., Nakakura, T., Tanaka, S., Koike, T. & Shiojiri, N. Sinusoid development and morphogenesis may be stimulated by VEGF-Flk-1 signaling during fetal mouse liver development.
Developmental Dynamics **239**. doi:10.1002/dvdy.22162 (2010) (cit. on p. 122).

195. Asal, M. *Self-organization of biological transport networks*
Master thesis (Technical University Dresden, 2017) (cit. on p. 122).
196. Luckhurst, G. R. & Zannoni, C.
Why is the Maier–Saupe theory of nematic liquid crystals so successful?
Nature **267**. doi:10.1038/267412b0 (1977) (cit. on pp. 127, 128).
197. Humphries, R. L., James, P. G. & Luckhurst, G. R.
Molecular field treatment of nematic liquid crystals.
Journal of the Chemical Society, Faraday Transactions 2 **68**.
doi:10.1039/f29726801031 (1972) (cit. on p. 128).
198. Luckhurst, G., Zannoni, C., Nordio, P. & Segre, U.
A molecular field theory for uniaxial nematic liquid crystals formed by
non-cylindrically symmetric molecules. *Molecular Physics* **30**.
doi:10.1080/00268977500102881 (1975) (cit. on p. 128).
199. Galerne, Y. Biaxial Nematics. *Molecular Crystals and Liquid Crystals
Incorporating Nonlinear Optics* **165**. doi:10.1080/00268948808082199
(1988) (cit. on p. 128).
200. Sonnet, A. M., Virga, E. G. & Durand, G. E. Dielectric shape dispersion
and biaxial transitions in nematic liquid crystals. *Phys. Rev. E* **67**.
doi:10.1103/PhysRevE.67.061701 (2003) (cit. on p. 128).
201. Wussing, H. *The Genesis of the Abstract Group Concept* (ed Grant, H.)
(Dover Publications, Inc., Mineola, New York, USA, 2007) (cit. on p. 137).
202. Metropolis, N., Rosenbluth, A. W., Rosenbluth, M. N., Teller, A. H. &
Teller, E. Equation of State Calculations by Fast Computing Machines.
The Journal of Chemical Physics **21**. doi:10.1063/1.1699114 (1953)
(cit. on p. 142).
203. Jones, E., Oliphant, T., Peterson, P., *et al.*
SciPy: Open source scientific tools for Python 2001–.
<http://www.scipy.org/> (cit. on p. 145).
204. Behnel, S., Bradshaw, R., Citro, C., Dalcin, L., Seljebotn, D. S. &
Smith, K. Cython: The Best of Both Worlds.
Computing in Science & Engineering **13**. doi:10.1109/MCSE.2010.118
(2011) (cit. on p. 145).

Acknowledgements

First and foremost I wish to express my deepest appreciation and gratitude towards Benjamin Friedrich and Frank Jülicher for offering continuous guidance, motivation and encouragement throughout the development of this dissertation project.

The work presented in this thesis would not have been possible without the experimental data obtained in the group of Marino Zerial at the Max Planck Institute of Molecular Cell Biology and Genetics. In particular, I want to thank Hidenori Nonaka, Kirstin Meyer, Hernán Andrés Morales Navarrete, Fabián Segovia Miranda and Yannis Kalaidzidis for their expertise, stimulating discussions and introductions to the biological concepts related to this work. While pursuing my PhD, I also had the opportunity to guide a Bachelor student, Simon Syga and a Master student, Marius Asal, through their projects. I sincerely thank them for their trust, their contributions and new perspectives to the overall research project. For a critical reading of the thesis' manuscript, I thank Benjamin, Paul, Silvanus, Yannic, Jens, Gary, Annelie, Fabián and Tajana.

A core strength of the groups are the many scientific and not-so-scientific discussions going on with the brilliant people around. I would therefore like to thank all my colleagues at the two Max Planck Institutes, many of whom became true friends and made my stay a special, memorable and growing experience. In particular, I want to thank Christoph, who is not only an advocate of nurturing the mind but also of training the body. Silvanus, for giving me interesting problems to think about. The 1pm lunch group, which was always good for fun discussion about mushrooms, medieval history, politics and much more. Stephan and the non-linear dynamics guys for their weird but very intriguing topics. Franzi, Ben and Tom for the music we did together, which never failed to warm my heart.

Finally, I thank my parents, my sister and my friends for their continuing support and guidance in life. You are awesome and I should let you know that more often.

Eigenständigkeitserklärung

Hiermit versichere ich, dass ich die vorliegende Arbeit ohne unzulässige Hilfe Dritter und ohne Benutzung anderer als der angegebenen Hilfsmittel angefertigt habe; die aus fremden Quellen direkt oder indirekt übernommenen Gedanken sind als solche kenntlich gemacht. Die Arbeit wurde bisher weder im Inland noch im Ausland in gleicher oder ähnlicher Form einer anderen Prüfungsbehörde vorgelegt.

Die vorliegende Arbeit wurde im Zeitraum zwischen Mai 2013 und Januar 2018 unter der Betreuung von Prof. Dr. Frank Jülicher und Dr. Benjamin Friedrich am Max-Planck-Institut für Physik komplexer Systeme in Dresden angefertigt.

Ich versichere, dass ich bisher kein erfolgloses Promotionsverfahren unternommen habe. Ich erkenne die Promotionsordnung der Fakultät Mathematik und Naturwissenschaften der Technischen Universität an.

Dresden,